

Hydraulic Characteristics of Embedded Circular Culverts

by

Chris R. Magura

A Thesis

Submitted to the Faculty of Graduate Studies
in Partial Fulfillment for the Degree of

MASTER OF SCIENCE

Department of Civil Engineering

University of Manitoba

Winnipeg, Manitoba

© August 2007

Abstract

On small rivers and streams, culverts are the most common form of stream crossing in Manitoba. However, conflicting interests arise between the need to balance economical installations with proper stewardship of our aquatic resources, most notably fish and fish habitat. Current models intended to ensure that culvert installations include proper consideration for fish passage are based on conservative average velocity criteria because there are currently no methods to adequately predict the velocity distribution in culverts. Therefore, this report details a physical modeling study to investigate the flow characteristics of circular corrugated structural plate (CSP) culverts with 10% embedment and projecting end inlets using a 0.62 m diameter corrugated metal pipe under a range of flows ($0.064 \text{ m}^3/\text{s}$ to $0.254 \text{ m}^3/\text{s}$) and slopes (0%, 0.5% and 1.0%).

An automated sampling system was used to record detailed velocity measurements at cross-sections along the length of the model. The velocity data was then used to develop isovel plots and observations were made regarding the effect of water depth, average velocity, boundary roughness and inlet configuration on the velocity structure. Strong trends were observed when the percent flow area was related to velocity suggesting a regression based velocity prediction method may be feasible. The distribution of shear velocity and equivalent sand roughness was measured and the Manning's roughness coefficient of the model was determined. Existing methods to predict bed roughness and composite roughness were evaluated using the measured water surface profiles. Simulations made using HEC-RAS were found to agree well with model results although inlet losses were underestimated by an average of 9%. An analytical method was used to estimate an 11% reduction in maximum discharge caused by 10% embedment with a rough gravel bed.

Based on a review of existing literature and model results, recommendations are presented to focus future research and to highlight areas where a better understanding of the velocity structure in culverts may lead to design improvements for fish passage.

Acknowledgments

I would like to thank the following people/organisations for their contribution to this research:

- My supervisor, Dr. Jay Doering – for giving me this opportunity and for always making time for me whenever I asked for help,
- Manitoba Infrastructure and Transportation – for their generous funding which purchased the materials and technical support needed to complete this research. Specifically, I would like to thank Ron Richardson who brought the project to my attention and who, along with Tim Locke and Ninel Gonzalez, provided guidance for the project,
- Manitoba Hydro – for providing the remained of my funding that supported me throughout my graduate studies. Specifically I would like to thank my line advocate, Roy Bukowski, for his support and encouragement and my supervisor Wendy Love and Karl Reznichuk for supporting my efforts and giving me time to complete my thesis,
- Armtec Limited – who donated the culvert,
- Roy Hartle – whose machining skill and design suggestions were instrumental in constructing the automated sampling system,
- My fellow graduate students – including Shawn Clark, Rafael Murillo, Jared Malenchak, Karen Wong, Ming Wang and Fisaha Unduche for their friendship, ideas and support, and
- Dr. Mark Tachie – for his good advice and encouragement.

Dedication

I would like to dedicate this work to my wife, Maureen, whose endless love and support enabled me to complete my thesis, and to my daughter Jady, who has been patiently waiting for Daddy to play with her.

Table of Contents

Abstract.....	i
Acknowledgments.....	ii
Dedication.....	iii
Table of Contents.....	iv
List of Figures.....	vii
List of Tables.....	x
Nomenclature.....	xi
Chapter 1: Introduction.....	1
1.1 Background.....	1
1.2 Objectives.....	4
1.3 Overview.....	4
Chapter 2: Literature Review.....	6
2.1 Manning’s Equation.....	6
2.2 Composite Roughness.....	8
2.2.1 Equal Velocity Method.....	8
2.2.2 Sum of Forces Method.....	10
2.2.3 Conveyance Method.....	10
2.3 Velocity Distributions within Culverts.....	10
2.3.1 One Dimensional Velocity Prediction.....	10
2.3.2 Two Dimensional Velocity Prediction.....	12
2.4 Model Studies of Culverts.....	15
2.5 Culvert Baffle Fishways.....	19
Chapter 3: Laboratory Set-up and Sampling Methodology.....	21
3.1 Laboratory Facilities.....	21
3.2 Physical Model Design.....	21
3.2.1 Similitude for Open Channel Flow.....	22
3.2.2 Scaling the Culvert.....	23
3.2.3 Scaling the Roughness Elements.....	24
3.3 Model Construction.....	26

3.3.1	Headwater Box.....	26
3.3.2	The Culvert	29
3.3.3	Tailwater Box.....	32
3.4	Acoustic Doppler Velocimetry	33
3.5	Automated Sampling System.....	36
3.6	Supplemental Surface Velocity Sampling	40
Chapter 4:	Experimental Procedure and Data Processing	42
4.1	Experimental Procedure.....	42
4.1.1	Water Surface Elevations.....	42
4.1.2	Gradually Varied Flow	43
4.1.3	Detailed Velocity Measurements	43
4.1.4	Smooth-Walled Trials.....	44
4.2	Data Processin.....	45
4.2.1	ADV Files	45
4.2.2	Matlab Analysis Functions	45
Chapter 5:	Analysis of Results.....	48
5.1	Analysis Approach.....	48
5.1.1	Modelling the Cross-section in Matlab.....	48
5.1.2	Peripheral Velocities.....	49
5.1.3	Fit of Interpolated Data.....	52
5.1.4	Vertical Velocity Profiles	53
5.2	Cross-section Properties of Circular Embedded Culvert	54
5.3	Results Summary for Experimental Runs.....	56
5.4	Velocity Structure	58
5.4.1	Entrance Region.....	59
5.4.2	Culvert Barrel.....	62
5.4.3	Area-Velocity Comparison	65
5.4.4	Boundary Layer Development.....	68
5.4.5	Isolation of Bed Roughness Effect	71
5.4.6	Secondary Currents.....	73
5.5	Log Law Region	77

5.5.1	Calculation of Shear Velocity.....	77
5.5.2	Calculation of Equivalent Sand Roughness.....	81
5.5.3	Design Applications.....	83
5.6	Manning’s Roughness Coefficient.....	84
5.6.1	Prediction of Manning’s Roughness.....	84
5.6.2	Experimental Determination of Manning’s n.....	85
5.7	Evaluation of Composite Roughness Methods.....	87
5.7.1	Defining the Cross-section in Composite Roughness Terms.....	87
5.7.2	GVF Profiles.....	88
5.7.3	Comparison with HECRAS Beta 4.0 Simulation.....	94
5.8	Effect of Embedment on Maximum Discharge.....	96
5.9	Movement of Bed Material.....	98
Chapter 6: Summary and Recommendations.....		100
6.1	Summary of Experimental Results.....	101
6.2	Recommendations.....	108
6.2.1	Recommendations for further research.....	108
6.2.2	Recommendations for Immediate Application.....	109
References.....		110
Appendix A – Sample Motion Control Program and Output.....		117
Appendix B – Isovel Plots.....		125
Appendix C – Vertical Velocity Profiles.....		151
Appendix D – Shear Velocity Determination.....		197
Appendix E – Log Law Plots for k_s Determination.....		227
Appendix F – Individual k_s Values for Experimental Runs.....		257

List of Figures

Figure 2.1: Definition sketch for Los Angeles District and Colebatch methods.....	9
Figure 3.1: Projecting end outlet configuration (not to scale).	22
Figure 3.2: Corrugation profile for prototype and model culverts.....	24
Figure 3.3: Model layout and components (not to scale).....	26
Figure 3.4: Projecting inlet showing simulated road embankment and gravel bed.	27
Figure 3.5: Sharp crested weir showing nape splitters used for aeration demand.....	28
Figure 3.6: Calibration of Sharp Crested Weir Coefficient.	29
Figure 3.7: Assembly pattern for flanged nestable CSP used in model.....	29
Figure 3.8: Assembled cross-section shown bolt pattern.....	30
Figure 3.9: Flexible rubber collar connecting culvert to tailwater box.....	30
Figure 3.10: View facing upstream of culvert and supports (set at 0% slope).	31
Figure 3.11: Layout of culvert outlet, tailwater gate and tailwater box outlet.....	33
Figure 3.12: Definition of sample volume for three dimensional velocity measurements.	33
Figure 3.13: a) Side-looking ADV probe, b) Downward-looking ADV probe tip. Right hand axes are defined for each probe type.....	34
Figure 3.14: Stability of instantaneous streamwise velocity readings illustrated with cumulative averaging over a 40 second sampling period (central plane of S0Q221 – cross-section 10).	36
Figure 3.15: Schematic of the automated sampling system showing the motion control system integrated with the ADV.....	38
Figure 3.16: Progression of sampling on polar coordinate system.	39
Figure 3.17: Automated sampling system showing the sampling cart, control computers and sampling mast with ADV in fully withdrawn position (ADV is not visible). ...	39
Figure 3.18: Mast set up at cross-section 1 and angled to allow the ADV to sample the left side of the cross-section.....	40
Figure 3.19: Hypothetical cross-section shown zones of automated and supplemental sampling.....	41
Figure 4.1: Sample coordinate reference sketch.....	43

Figure 4.2: View of culvert looking downstream from the inlet with smooth-walled insert installed in the first six cross-sections.	44
Figure 5.1: Definition of core flow and region of extrapolation.....	49
Figure 5.2: Fit of data compared to the Log Law in extrapolated zone for $z = 0$ cm and $z = 18$ cm for XS20 of S5Q221.	52
Figure 5.3: Comparison of measured point velocities with interpolated data for S5Q221, XS20 for central profile (0 zero degree) and +40 degree sampling radial.....	53
Figure 5.4: Sampling vertical profiles from interpolated data.....	54
Figure 5.5: Definition of cross-section.	55
Figure 5.6: Isovel Plot for S0Q64 XS1, $y_o=0.310$ m, $A = 0.173$ m ² , $u_{avg} = 37.0$ cm/s.....	60
Figure 5.7: Isovel Plot for S0Q186 XS1, $y_o=0.502$ m, $A = 0.273$ m ² , $u_{avg} = 68.2$ cm/s.....	60
Figure 5.8: Isovel Plot for S0Q64 XS2, $y_o=0.304$ m, $A = 0.169$ m ² , $u_{avg} = 37.8$ cm/s.....	61
Figure 5.9: Isovel Plot for S0Q64 XS3, $y_o=0.303$ m, $A = 0.169$ m ² , $u_{avg} = 37.9$ cm/s.....	61
Figure 5.10: Isovel Plot for S0Q186 XS2, $y_o=0.492$ m, $A = 0.269$ m ² , $u_{avg} = 69.2$ cm/s....	61
Figure 5.11: Isovel Plot for S0Q186 XS3, $y_o=0.482$ m, $A = 0.265$ m ² , $u_{avg} = 70.2$ cm/s....	61
Figure 5.12: View upstream from cross-section 4. Significant entrance losses were observed causing a mounding effect in the water surface profile across the inlet....	62
Figure 5.13: Isovel Plot for S5Q145 XS20, $y_o=0.299$ m, $A=0.166$ m ² , $u_{avg}=87.2$ cm/s... 63	63
Figure 5.14: Isovel Plot for S5Q221 XS20, $y_o=0.448$ m, $A=0.250$ m ² , $u_{avg} = 88.5$ cm/s.. 63	63
Figure 5.15: Isovel Plot for S1Q150 XS12, $y_o=0.255$ m, $A=0.139$ m ² , $u_{avg}=107.9$ cm/s. 65	65
Figure 5.16: Isovel Plot for S5Q254 XS12, $y_o=0.381$ m, $A=0.215$ m ² , $u_{avg} = 118.3$ cm/s.65	65
Figure 5.17: Velocity-normalized isovel plot of XS12 for S0Q186 ($u_{avg} = 71.6$ cm/s).... 66	66
Figure 5.18: Aggregated percent area less than u/u_{avg} for all runs for XS6-26.	68
Figure 5.19: Water surface profiles and the estimation of boundary layer development using the criterion of $0.99u_{max}$	70
Figure 5.20: Isovel Plot for S5Q145s XS6, $y_o=0.306$ m, $A=0.166$ m ² , $V_{avg}=87.4$ cm/s. 73	73
Figure 5.21: Isovel Plot for S5Q221s XS6, $y_o=0.437$ m, $A=0.236$ m ² , $V_{avg}=93.8$ cm/s. 73	73
Figure 5.22: Hypothetical secondary currents in a circular embedded CSP culvert.	75
Figure 5.23: Quiver plot of v and w velocity components for XS6 of S0Q186 overlain on isovel plot. Arrow length implies relative magnitude.....	76

Figure 5.24: Quiver plot of v and w velocity components for XS20 of S0Q64 overlain on isovel plot. Arrow length implies relative magnitude.....	76
Figure 5.25: Logarithmic plot of central and non-central velocity profiles for determination of shear velocity - S0Q186, XS12.	78
Figure 5.26: a) Distribution of shear velocity (averaged over XS6-26) from $z = 0$ to 0.27 m for all experimental runs, b) normalized by global shear velocity (u_{*o}).	78
Figure 5.27 (a-f): Comparison of average bed ($z = 0$ to 0.18 m) and wall ($z = 0.24$ to 0.27 m) shear velocity with global shear velocity for all experimental runs.....	80
Figure 5.28: Velocity profiles fit to Log Law for determination of k_s - S0Q186, XS12. .	81
Figure 5.29: Distribution of equivalent sand roughness (averaged over XS6-26) from $z = 0$ to 0.27 m for all experimental runs.....	82
Figure 5.30: Equivalent sand roughness (averaged over all experimental runs) along the length of the culvert.	83
Figure 5.31: Experimental determination of composite Manning's coefficient (\bar{n}).	86
Figure 5.32: Definition sketch for area-dependent composite roughness methods.	88
Figure 5.33 (a-c): Fitting measured water surface profiles using Standard Step Method and Einstein/Horton composite roughness ($n_{CSP} = 0.023$ and $n_{bed} = 0.029$).	90
Figure 5.34: Details of the culvert inlet zone.....	92
Figure 5.35: Profile plot from HECRAS simulation of S5Q145 run with no tailwater control.	94
Figure 5.36: Comparison of HECRAS Beta 4.0 model simulations with measured water surface profiles with tailwater control.	95
Figure 5.37: Comparison of HECRAS Beta 4.0 model simulations with measured water surface profiles with no tailwater control.	96
Figure 5.38: Flow characteristics of a circular section with and without embedment of $0.1D_o$	97
Figure 5.39: Estimation of maximum discharge by variation of n with Q approach for an empty culvert and one with 10% embedment.....	98

List of Tables

Table 2.1: Experimental culverts used by Barber and Downs (1996).	15
Table 3.1: Froudian Scale Ratios.	23
Table 3.2: Target parameters for model and hypothetical prototype.	23
Table 3.3: Roughness scaling for model and hypothetical prototype.	25
Table 3.4: Model gravel bed material gradation.	26
Table 3.5: Calibration of Sharp Crested Weir Coefficient.	28
Table 3.6: Location of sampling cross-sections relative to culvert inlet.	31
Table 4.1: Detailed velocity measurement testing parameters.	42
Table 4.2: Sample parameter summary for smooth-walled trials	44
Table 5.1: Experimental results for 0% and 0.5% slope runs	57
Table 5.2: Experimental results for 1.0% slope runs	58
Table 5.3: Summary of area-velocity results for experimental runs	67
Table 5.4: Parameter summary for smooth wall runs - results are averaged for XS 2, 4 and 6 and are compared to regular 0.5% slope runs.	71
Table 5.5: Individual experimental results for smooth-walled trials at 0.5% slope.	72
Table 5.6: Calculation of global shear velocity for experimental runs	79
Table 5.7: Predicted values of Manning's n for prototype and model Class 350 rip rap, ranked in ascending order.	85
Table 5.8: Comparison of Max and Min Composite Roughness at cross-section 14.	90
Table 5.9: Comparison of Composite Roughness Methods Using $n_{bed} = 0.029$ and $n_{CSP} =$ 0.023	91
Table 5.10: Measured inlet losses compared to calculated values and HEC-RAS results.	95
Table 5.11: Estimation of Q_{max} and loss in conveyance caused by 10% embedment.	97

Nomenclature

Symbol	Definition
% Error Q_{int}	percentage error between Q_{int} and know discharge
3dQ10	fish passage design flow
A	flow area
A_{3dQ10}	area of flow when depth equals Y_{3dQ10}
A_b	cross-sectional area occupied by the bed
A_{cell}	area represented by one cell of the cross-section matrix
A_{flow}	$A_{total} - A_b$
a_i	subdivided flow area for calculation of composite roughness
A_{max}	maximum available flow area
A_{nbed}	area of flow affected by bed roughness
A_{nw}	area of flow affected by culvert wall roughness
A_o	full flow area
A_{sub}	portion of bed affected area projecting above the water surface
A_{total}	total cross-sectional area including A_b
b	$= (AR^{2/3})_{Q_{max}} S_o^{1/2}$
b_1, b_2	regression coefficients
B_1, B_2	regression coefficients
C	Chezy's roughness coefficient
C1, C2, C3 and C4	weir coefficients for individual calibration trails
C_m	Manning's constant
C_{sound}	speed of sound
CSP	corrugated steel pipe
C_{weir}	sharp crested weir coefficient
D	hydraulic depth

Symbol	Definition
d_{15}	15 th percentile of particle size distribution
d_{50}	average particle size
d_{75}	75 th percentile of particle size distribution
d_{84}	84 th percentile of particle size distribution
d_{90}	90 th percentile of particle size distribution
d_{100}	maximum particle size
d_b	depth of embedment
D_o	culvert diameter
e	natural log base (2.71828)
f	Darcy-Weisbach friction factor
F	Froude number
F_{Doppler}	change in frequency at the ADV receiver
F_{source}	transmitted frequency from ADV transducer
g	acceleration due to gravity
h	depth below the surface where u_{max} occurs
H_c	Height of CSP corrugation
HEC-RAS	Hydrologic Engineering Center - River Analysis System
h_L	head loss through the acceleration zone of the contraction
k_e	inlet head loss coefficient
k_s	Nikuradse's equivalent sand roughness
L	culvert length
L_c	Length of CSP corrugation
L_{cell}	linear distance represented by one cell of the cross-section matrix
logit Y_u	logit transformed cumulative percent area
M	dimensionless entropy parameter
n	Manning's coefficient
\bar{n}	composite Manning's roughness coefficient
\bar{n}_{meas}	composite roughness derived from flow and depth data

Symbol	Definition
NaN	Matlab designation for Not-a-Number
n_{bed}	Manning's roughness for bed material
n_{CSP}	Manning's coefficient of roughness for model CSP
$n_{inserts}$	Manning's coefficient of roughness for culvert inserts
P	wetted perimeter
p	non-exceedence probability of cumulative density function of Normal distribution
P_b	perimeter of the culvert subtended by the bed
p_i	subdivided wetted perimeter for calculation of composite roughness
P_{total}	$P_w + T_b$
P_w	wetted perimeter of the culvert wall
Q	discharge
Q_{75}	maximum overflow rate using the 75 Hp pump
Q_{int}	integrated flow calculated from cross-section matrix
Q_{max}	maximum possible discharge for a culvert of a given size and slope
Q_{model}	model discharge
Q_o	full flow discharge
$Q_{overflow}$	overflow rate of headtank
R	hydraulic radius
Re	Reynolds number
Re^*	roughness Reynolds number
R_o	full flow hydraulic radius
S_f	friction slope
S_o	bed slope
subscripted m	in reference to the model
subscripted p	in reference to the prototype
subscripted Q_{max}	in reference to the Q_{max}

Symbol	Definition
T	top width of the flow
T_b	top width (wetted perimeter) of the bed
u^*	shear velocity
u^*_o	global shear velocity
u, v, w	streamwise, lateral and vertical velocity (x,y,z) respectively
u_{avg}	average velocity
u_{entr}	maximum velocity through the culvert inlet contraction
u_i	velocity value associated with one cell of the cross-section matrix
u_{max}	maximum streamwise velocity
u_{pool}	average velocity of water in inlet pool/headwater box
u_t	normalized velocity $u_t = u - u_{avg}$
V_{3dQ10}	average velocity of 3dQ10 design flow
$V_{relative}$	relative velocity between source and ADV receiver
X	linear dimension
x	a value in a sample
XS	abbreviation of cross-section
y	depth
Y_{3dQ10}	depth at 3dQ10 design flow
y_d	height above the datum where velocity profile readings deviate from the Log Law
Y_{max}	maximum possible flow depth
y_o	average depth of flow
Y_u	cumulative percentage of the cross-section below a given velocity
y_z	height above the datum at a non-central plane
z	horizontal distance from central plane of culvert
z_o	half the top width of flow
β_1	velocity distribution coefficient

Symbol	Definition
δ	turbulent boundary layer thickness
ΔH	total head loss through the inlet zone
Δu_m	maximum deviation in velocity from the log law
λ	similarity scaling ratio
μ	sample mean
ν_k	kinematic viscosity of water
ζ	dimensionless position parameter
ζ_{\max}	maximum value of ζ
ζ_0	minimum value of ζ occurring on the channel bed
ρ	density of water
σ	standard deviation of the sample
τ_0	bed shear stress at relative distance z/z_0
τ_{00}	bed shear stress at the central plane
ω	test statistic for Normal distribution

Chapter 1: Introduction

1.1 Background

In Manitoba, there are a vast number of stream crossings over natural and man-made channels. On small rivers and streams, circular corrugated structural plate (CSP) culverts are the most economical method of installing these crossings. However, conflicting interests arise with the need to balance economical installations with proper stewardship of our aquatic resources, most notably fish and fish habitat. It is therefore necessary to develop design criteria which meet the structural requirements for a safe, economical design, without compromising the needs of valued fish species.

In Canada, the legislated requirements for fish passage are set out in very general terms in the Fisheries Act (R.S., 1985, c. F-14):

“20. (1) Every obstruction across or in any stream where the Minister determines it to be necessary for the public interest that a fish-pass should exist shall be provided by the owner or occupier with a durable and efficient fish-way or canal around the obstruction, which shall be maintained in a good and effective condition by the owner or occupier, in such place and of such form and capacity as will in the opinion of the Minister satisfactorily permit the free passage of fish through it.”

In the Manitoba Stream Crossing Guidelines for the Protection of Fish and Fish Habitat (Manitoba Natural Resources, 1996), this legislation is interpreted to mean that culverts must be designed such that fish desiring to proceed upstream do not experience a delay greater than 7 consecutive days once in each 50 year period. The Transportation Association of Canada's Guide to Bridge Hydraulics lists a delay greater than 3 days as acceptable with a frequency of 1 in 10 years (Neill, 2001). A flow which will produce a 3 day delay with a frequency of 1 in 10 years is commonly termed 3dQ10. The ability of fish to proceed upstream in a culvert depends upon a complex interaction of several

factors including water velocity occurring in the culvert, fish species, fish size, length of the culvert and other bio-physical parameters (Katopodis, 2005). If the flow velocity in a culvert is too high, it will act as a barrier to fish desiring to proceed upstream to spawn, feed or during other periods of upstream movement. Flow velocities can be reduced by increasing culvert size, roughness, burial depth, and by reducing culvert slope. Also, end treatments such as headwalls and wing-walls may be incorporated to provide smoother flow transitions into and out of culverts.

Despite the fact that they are considered the least desirable culvert for fish passage, circular (CSP) culverts are the stream crossing of choice in Manitoba as in many other places, due to their relatively low installation cost. The primary criticisms of circular culverts are that they: (1) concentrate flow velocities by forcing the flow through a smaller cross-sectional area, (2) cause loss of habitat and natural substrate (Manitoba Natural Resources, 1996), and (3) remove the irregularities in the natural stream bed that create zones of quiescent flow where fish can rest (Watts, 1974).

In an attempt to mitigate the 3rd criticism above, circular culverts are installed with a gradient as close to the natural stream bed as possible and are required to be embedded by 0.3 m or 10% of their diameter, whichever is greater. The embedded portion is then filled in with suitable granular material to the level of the natural stream bed. This serves the dual purpose of providing a more natural bed substrate and it increases the roughness of the culvert, reducing the average flow velocity which would occur in a non-embedded culvert of similar cross-sectional area.

In Manitoba, average flow velocities generally have to be maintained below 1.0 m/s for culverts shorter than 25 m and below 0.8 m/s for culverts longer than 25 m. (Manitoba Natural Resources, 1996). Velocities as low as 0.6 m/s may be required depending upon the fish species present. Even with a 10% embedment and the addition of a rough granular bed, culverts with uniform cross-section provide no resting places and fish are required to swim continuously while advancing upstream. Excessive water velocities will cause a fish to wash out of the culvert if it is unable to ascend the full length before it

becomes exhausted (Behlke et al., 1991). It is at this point where we must examine a key assumption made by current fish passage models.

Current fish passage models are one dimensional in that they relate the swimming ability of fish to the average flow velocity that occurs in a culvert (Behlke et al., 1991; Katopodis, 1992). However, it is believed that fish tend to seek the best locations for swimming (Behlke et al., 1991) and therefore it is unlikely that they would choose to swim against average water velocity when a significant portion of the cross-section has lower velocities. It is well understood that flow velocity attenuates as the boundary is approached and some models utilize flow reduction factors to attempt to account for this. However, there is currently no adequate method for predicting velocity distributions within culverts. (Barber and Down, 1996; Katopodis, 2005).

Requiring culverts to be countersunk with an aggregate bed further compounds the level of uncertainty for designers and may invalidate many existing design aids. There is no broadly applicable method to predict the effect of embedment on velocity distribution and conveyance within culverts. In addition, the effectiveness of current methods for calculating composite roughness is uncertain. This also has implications for risk assessment and liability related to flood events and structural failure of stream crossings. As a result, conservative design criteria based on average velocity are still used in Manitoba and construction costs may greatly exceed what is required for a safe design that meets the needs of affected fish species.

These factors alone indicate that detailed testing must be undertaken to quantify the hydraulic performance of embedded circular CSP culverts designed to meet fish passage criteria. Further motivation comes from recent research on fish swimming performance (Peake, in press). This research reveals that the swimming ability of four key fish species has been significantly underrated by existing fish passage models and suggests that systematic bias exists in the classic forced performance testing used to set velocity criteria. Once a thorough evaluation of culvert performance has been completed, the data should be combined with the most up-to-date knowledge of fish swimming performance.

Fish passage models used to set velocity criteria for culverts and fishways may then be updated to provide a better balance between economy and protection of fish resources.

1.2 Objectives

This report details a physical modeling study to investigate the flow characteristics of circular corrugated structural plate (CSP) culverts with 10% embedment and projecting end inlets under a range of flows and slopes.

The objectives of this research are:

- to perform a detailed investigation of the streamwise velocity distribution as it develops along the length of a model culvert,
- to describe the velocity structure observed and investigate the effect of flow velocity, depth and embedment on the shape of the velocity field
- to determine the effect of the projecting-end inlet on the flow,
- to observe the distribution of shear velocity and equivalent sand roughness across the width and along the length of the culvert,
- to evaluate existing methods of calculating composite roughness when applied to partially buried CSP culverts,
- to evaluate simulations of the model results using HEC-RAS Beta 4.0,
- to make observations of flow characteristics such as secondary currents, frictional losses, boundary layer development, as well as the reduction in maximum discharge caused by embedment,
- to provide guidance for further research on methods of predicting velocity distributions in partially buried culverts, and
- to highlight areas where a better understanding of the velocity structure in embedded culverts may lead to design improvements for fish passage.

1.3 Overview

The background and impetus behind this research are detailed in Chapter 1. Chapter 2 is a review of the current state of knowledge in several areas relating to culvert design.

Discussed are methods of predicting Manning's composite roughness and the uses and limitations of existing methods of predicting the velocity distribution in partially buried culverts under open channel flow conditions. Chapter 3 describes the laboratory facilities and design of the physical model including similitude considerations. The model components are described in detail and sections are included about the automated sampling methodology and instrumentation used. Chapter 4 summarises the experimental procedure for measuring water surface elevations, determination of Manning's roughness coefficient and detailed velocity measurements. The Matlab programs developed to assist with processing the data and create the isovel plots are also described. The analysis approach used in this study is detailed in Chapter 5, followed by a summary of the measured data and a discussion of the analysis performed, including velocity structure, boundary layer development, distribution of shear velocity and equivalent sand roughness. The Manning's roughness coefficient for the model is determined and existing methods for determining composite roughness are evaluated. In addition, the suitability of HECRAS for modelling flow in embedded circular culverts is investigated by evaluating HECRAS simulations against measured model results. This chapter also discusses the potential development of an area-velocity prediction method and the overall effect of embedment on culvert performance is examined. Finally, the results are summarized in Chapter 6 in the context of the study objectives and recommendations are made to focus related research.

Chapter 2: Literature Review

2.1 Manning's Equation

The most widely used equation for estimation of discharge under open channel flow conditions is Manning's equation (Chow, 1959). It has also been applied to flow through culverts, producing acceptable results despite the fact that uniform flow rarely occurs in culverts. The modern form of the equations is

$$u_{avg} = \frac{C_m}{n} R^{2/3} S_f^{1/2}, \quad (2.1)$$

where u_{avg} = average velocity in the channel, $C_m = 1.0$ for S.I. units ($C_m = 1.49$ for Imperial units), R is the hydraulic radius, S_f is the friction slope (usually taken to be equal to the bed slope) and n is Manning's roughness coefficient. By multiplying both sides of the equation by the flow area, A , discharge, Q , can be calculated as

$$Q = \frac{C_m}{n} A R^{2/3} S_f^{1/2}. \quad (2.2)$$

For natural channels, the most difficult part of applying Manning's equation is in estimating the roughness coefficient. The value of Manning's n typically ranges from 0.025 to 0.08 for natural streams (Chow, 1959). Several factors affect the value of the roughness coefficient including surface roughness, vegetation, channel irregularities, channel alignment, channel obstructions, channel size/shape, and stage/discharge. On the other hand, the roughness coefficients for corrugated metal culverts can be referenced in design manuals and range from 0.011 to 0.033 (Handbook of steel drainage and highway construction products, 2002).

Many empirical methods of estimating Manning's n have been devised for natural channels. In most cases, grain size, which affects surface roughness, is of primary importance. However, several methods consider other factors including hydraulic radius, water depth, bed slope, friction slope and even the Froude number. Some of the methods that have been proposed are

$$\text{Strickler (1923)} \quad n = \frac{d_{50}^{1/6}}{21.1}, \quad (2.3)$$

$$\text{Meyer-Peter and Muller (1948)} \quad n = \frac{d_{90}^{1/6}}{26}, \quad (2.4)$$

$$\text{Limerinos (1970)} \quad n = \frac{(0.113R^{1/6})}{\left(0.35 + 2.0 \log_{10} \left\{ \frac{R}{d_{50}} \right\}\right)}, \quad (2.5)$$

$$\text{Bray (1979)} \quad n = \frac{(0.113y_o^{1/6})}{\left(1.09 + 2.2 \log_{10} \left\{ \frac{y_o}{d_{50}} \right\}\right)}, \quad (2.6)$$

$$\text{Jarret (1984)} \quad n = \frac{0.39S_f^{0.38}}{R^{0.16}}, \quad (2.7)$$

$$\text{Abt et al. (1987)} \quad n = 0.0456(D_{50}S_o)^{0.159}, \quad (2.8)$$

$$\text{Bruschin (1985)} \quad n = \left(\frac{d_{50}^{1/6}}{12.38} \right) \left(\frac{RS_o}{d_{50}} \right)^{1/7}, \quad (2.9)$$

$$\text{Ugarte and Madrid (1994)} \quad n = \left[0.183 + \ln \left(\frac{1.7462S_f^{0.1581}}{F^{0.2631}} \right) \right] \left[\left(\frac{D_{84}^{1/6}}{g^{1/2}} \right) \right], \text{ and } (2.10)$$

$$\text{Julien (2002)} \quad n = 0.062d_{50}^{1/6}, \quad (2.11)$$

$$n = 0.046d_{75}^{1/6}, \quad (2.12)$$

$$n = 0.038d_{90}^{1/6}, \quad (2.13)$$

where d_{50} , d_{75} , d_{84} and d_{90} represent size fractions of the bed material associated with 50%, 75%, 84%, and 90% non-exceedence probability, respectively. The term y_o is

average water depth, S_o is channel bed slope, g is acceleration due to gravity and F is the Froude number. The Froude number is defined for open channel flow as

$$F = \frac{u_{avg}}{\sqrt{gD}}, \quad (2.14)$$

where D is the hydraulic depth.

The diversity of approaches used by researchers is evidence of the complexity involved in determining Manning's roughness coefficient and heavy reliance is placed upon the experience of the design engineer.

2.2 Composite Roughness

In Manitoba, circular CSP culverts are required to be embedded a total of 10% of their diameter or 0.3 m, whichever is greater. The culvert is then filled with suitable granular material to the level of the natural stream bed. This design modification is done to facilitate fish passage by slowing the average water velocity in the culvert. The Manning's roughness coefficient of the bed is greater than the rest of the wetted perimeter within the culvert. The addition of granular bed material now introduces some of the same uncertainties faced when attempting to determine the Manning's n in natural channels. The roughness of the bed material is dependent upon the material size distribution, which is difficult to determine in the field.

A further complication arises because the roughness of the culvert is now a composite of the bed and the culvert sides. There are three main methods currently in use for determining composite roughness. These methods are based on the assumption that the cross-section can be divided into discrete flow areas affected by the different roughness elements.

2.2.1 Equal Velocity Method

Cox (1973) tested three methods for determining composite roughness. A further assumption is made that the velocities in each segment of the area are equivalent and

equal to the average velocity for the channel. These methods are the Horton (1933) or Einstein (1934) method, the Colebatch (1941) method and the Los Angeles District (Cox, 1973) method.

$$\text{Horton or Einstein} \quad \bar{n} = \frac{\left(\sum_1^N p_i n_i^{1.5} \right)^{2/3}}{P^{2/3}} = \frac{\left(p_1 n_1^{1.5} + p_2 n_2^{1.5} + \dots + p_N n_N^{1.5} \right)^{2/3}}{P^{2/3}}, \quad (2.15)$$

$$\text{Colebatch} \quad \bar{n} = \frac{\left(\sum_1^N a_i n_i^{1.5} \right)^{2/3}}{A^{2/3}} = \frac{\left(a_1 n_1^{1.5} + a_2 n_2^{1.5} + \dots + a_N n_N^{1.5} \right)^{2/3}}{A^{2/3}}, \text{ and} \quad (2.16)$$

$$\text{Los Angeles District} \quad \bar{n} = \frac{\sum_1^N a_i n_i}{A} = \frac{\left(a_1 n_1 + a_2 n_2 + \dots + a_N n_N \right)}{A}, \quad (2.17)$$

where \bar{n} is the composite roughness, p_i and a_i are the individual wetted perimeters and areas affected by the different roughness elements (respectively), and P and A are the total wetted perimeter and flow area (respectively). The use of wetted perimeter in the denominator of the Horton method makes for stable computation at very low flow depths in that it prevents dividing by zero. Cox (1973) concluded that the Horton's method was less accurate than the Colebatch or Los Angeles District methods for use with rectangular or trapezoidal channels but its simplicity and programmability for complex cross-sections has made it popular with many designers. The cross-section definition sketch for the Los Angeles District and Colebatch methods is shown in Figure 2.1 for a rectangular channel.

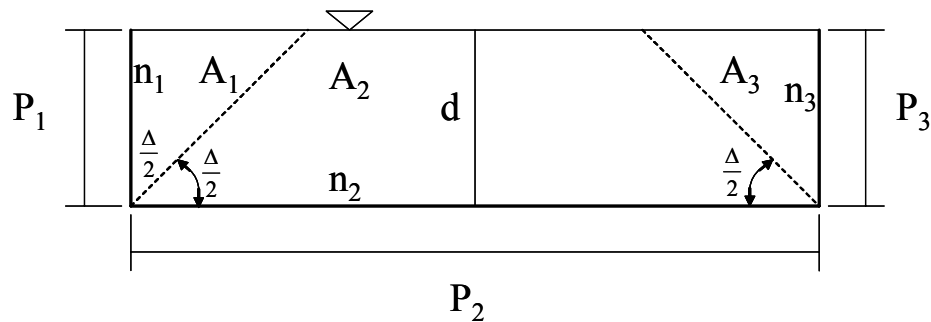


Figure 2.1: Definition sketch for Los Angeles District and Colebatch methods.

2.2.2 Sum of Forces Method

Einstein and Banks (1950) proposed the idea that the total resistance to the flow is equal to the sum of the forces acting in each flow area.

$$\text{Einstein and Banks} \quad \bar{n} = \frac{\left(\sum_1^N p_i n_i^2 \right)^{1/2}}{P^{1/2}} = \frac{\left(p_1 n_1^2 + p_2 n_2^2 + \dots + p_N n_N^2 \right)^{1/2}}{P^{1/2}} \quad (2.18)$$

2.2.3 Conveyance Method

Lotter (1933) assumed that the flow for a channel with composite roughness is equal to the flow occurring in the sub-divided cross-sectional areas.

$$\text{Lotter} \quad \bar{n} = \frac{PR^{5/3}}{\sum_1^N \frac{p_i R_i^{5/3}}{n_i}} = \frac{PR^{5/3}}{\frac{p_1 R_1^{5/3}}{n_1} + \frac{p_2 R_2^{5/3}}{n_2} + \dots + \frac{p_N R_N^{5/3}}{n_N}} \quad (2.19)$$

2.3 Velocity Distributions within Culverts

Velocity distributions for turbulent open channel flow have been modeled mathematically in both one and two dimensions.

2.3.1 One Dimensional Velocity Prediction

The Power Law formula was found by Roberson and Crowe (1990) to provide a valid estimation of the velocity profile in the turbulent boundary layer under open channel flow conditions for Reynolds numbers ranging from $10^5 < Re < 10^7$. The Power Law is commonly of the form

$$\frac{u}{u_{\max}} = \left(\frac{y}{\delta} \right)^{1/7}, \quad (2.20)$$

where u is velocity, u_{\max} is the maximum velocity, y is depth, and δ is the thickness of the turbulent boundary layer. Roberson and Crowe (1990) found the Power Law compared well to experimental results in the range of $0.1 < y/\delta < 1.0$.

The Prandtl-von Karman universal velocity distribution law (Chow, 1959) or Log Law was adapted by Schlichting (1979) to describe hydraulically smooth, transitional and completely rough flow regimes. The completely rough version is

$$\frac{u}{u_*} = 2.5 \ln \frac{y}{k_s} + 8.5, \quad (2.21)$$

where u is the streamwise velocity at a point, u_* is the shear velocity, and k_s is the Nikuradse equivalent sand roughness. Like Manning's roughness coefficient, numerous methods have been developed to relate k_s to the size distribution of gravel river beds. Some equations are as follows:

$$\text{Strickler (1923)} \quad k_s = D_{90} \quad (2.22)$$

$$\text{Charlton et al. (1978)} \quad 3D_{84} < k_s < 3D_{90} \quad (2.23)$$

$$\text{Bray (1979)} \quad k_s = 3.5D_{84} \quad (2.24)$$

$$\text{Hey (1979)} \quad k_s = 3.5D_{84} \quad (2.25)$$

It is widely accepted that in gravel bed rivers, the equivalent roughness, k_s , is often many times greater than the physical size of the roughness elements (Yalin, 1972).

Kane and Wellen (1985) utilized an equation adapted from Chow (1964) to predict the central velocity profile in highway culverts. Chow (1964) stipulates that the equation is applicable to turbulent open channel flow in a wide channel and that it does not apply near the bed or the water surface. The equation is

$$\frac{(u - V)C}{V\sqrt{8g}} = 2 \log \left(\frac{y}{y_o} \right) + 0.88, \quad (2.26)$$

where C is the Chezy roughness coefficient and y/y_o is the relative depth. Chezy's roughness coefficient is related to Manning's n by the following formula

$$C = \frac{R^{1/6}}{n}. \quad (2.27)$$

Substituting equation 2.27 into equation 2.26 and solving for the velocity at any point yields

$$u = \frac{(32g)^{1/2}(u_{avg})n}{R^{1/6}} \log\left(\frac{y}{y_o}\right) + \frac{0.88(8g)^{1/2}(u_{avg})n}{R^{1/6}} + u_{avg}. \quad (2.28)$$

Mountjoy (1986) utilized equation 2.28 to predict the central velocity profile in embedded culverts with gravel beds flowing under wide channel conditions (width to depth ratios of 10 to 20). By gathering constants, equation 2.28 was simplified to

$$u = B_1 \log\left(\frac{y}{y_o}\right) + B_2, \quad (2.29)$$

where $B_1 = \frac{(32g)^{1/2}(u_{avg})n}{R^{1/6}}$ and $B_2 = \frac{0.88(8g)^{1/2}(u_{avg})n}{R^{1/6}} + u_{avg}$. By correlating measured stream velocities at $y/y_o=0.6$ with coefficient B_2 , and then regressing B_1 with B_2 , Mountjoy developed a method of predicting the coefficients during the design phase. The study was based on velocity measurements taken from 49 culverts throughout Alaska and is based on the assumption that mean velocity occurs at a relative depth of 0.6.

2.3.2 Two Dimensional Velocity Prediction

White (1996) utilized a similar regression-based approach to predict velocity distributions in embedded culverts in Oregon. Using the assumption that at low to moderate flow, the aspect ratio of the flow area in the study culverts would approach a wide channel, he averaged multiple velocity profiles across each culvert cross section. He then applied this single velocity distribution across the width of the channel, thereby indirectly estimating a two dimensional velocity distribution. This distribution was then used to calculate the percent flow area that would be passable to fish. White's equation is of the form

$$\frac{u}{u_{avg}} = b_1 + b_2 \log\left(\frac{y}{D}\right), \quad (2.30)$$

where b_1 and b_2 are regression coefficients and D is hydraulic depth. White (1996) found that the computed percentage of the channel area below a given velocity was generally less than those interpreted from field measurements, making his approach conservative.

Chiu (1988) developed an entropy-based approach to predict the two-dimensional velocity distribution in open channel flows. Chiu (1993) adapted this approach to pipe flow studies, which have historically relied upon one dimensional velocity distribution equations. Chiu's equation is

$$\frac{u}{u_{max}} = \frac{1}{M} \ln \left[1 + (e^M - 1) \frac{\xi - \xi_o}{\xi_{max} - \xi_o} \right], \quad (2.31)$$

where u_{max} is the maximum velocity, M is a dimensionless entropy parameter, ξ is a dimensionless parameter related to the coordinate system, ξ_{max} is the maximum value of ξ occurring where $u = u_{max}$, and ξ_o is the minimum value of ξ that occurs on the channel bed where u equals zero. The parameter ξ is given by

$$\xi = \frac{y}{y_o - h} \exp \left(1 - \frac{y}{y_o - h} \right), \quad (2.32)$$

where h is the depth below the surface where u_{max} occurs. Chiu (1988) relates the entropy parameter, M to the ratio of u_{avg}/u_{max} by the following equation

$$\frac{u_{avg}}{u_{max}} = e^M (e^M - 1)^{-1} - \frac{1}{M}. \quad (2.33)$$

House et al. (2005) comment that it is necessary to have fore-knowledge of the velocity distribution to determine Chiu's entropy and positional parameters and that this makes equation 2.31 difficult to apply for design. House et al. (2005) also state that Chiu's coordinate system assumes a continually decreasing velocity profile and does not allow for local maxima and minima that frequently occur in the velocity distribution of culverts. Further, Barber and Downs (1996) state that Chiu's equation will always predict a velocity distribution that is symmetric about the centerline. However, it is interesting to note that Barber and Downs (1996) determined that Chiu's entropy parameter, M , could be calculated from u_{avg}/u_{max} (using equation 2.33), which can be estimated by the ratio *Corrugation Height/Pipe Diameter* for a given culvert. This may address the criticism stated by House et al. (2005) when attempting to apply Chiu's approach to culvert design.

In 2005, House et al. further refined the regression approach of White (1996) by first utilizing a logit function to transform the cumulative percent area variable, to produce a new variable *logit* Y_u .

$$\text{logit } Y_u = \ln\left(\frac{Y_u}{100 - Y_u}\right), \quad (2.34)$$

where Y_u is the cumulative percentage of the cross-section below a given velocity. The velocity values were then normalized (u_t) by subtracting the average velocity thus

$$u_t = u - u_{avg}, \quad (2.35)$$

Regression was used to determine the slope of each transformed velocity distribution as

$$\text{logit } Y_u = \beta_1 u_t, \quad (2.36)$$

and β_1 was termed the velocity distribution coefficient. The overall regression model for the velocity distribution coefficient is given as

$$\beta_1 = 14.11 - 5.26(A) + 3.67(Q) - 16.56(F) + 2.29\left(\frac{R}{k_s}\right), \quad (2.37)$$

where R/k_s is the relative roughness parameter. House et al. (2005) found the resulting model predicted measured the cumulative percent area based on velocity well, but like the equation produced by White (1996), tended to be conservative. House et al. (1996) also noted that the model assumed uniform flow and that a description of velocity distributions along the length of a culvert would be necessary to determine suitability for fish passage at the design stage.

Barber and Downs (1996) note the inadequacy of existing models to predict the true velocity distributions due to persistent asymmetry in flows occurring in both natural channels and in controlled laboratory experiments. As an example of this asymmetry, Barber and Downs (1996) cite studies by Replogle and Chow (1966) and Katopodis et al. (1978). Replogle and Chow (1966) studied the tractive-force and velocity distribution in circular pipes flowing partially full, revealing that the maximum velocity was often depressed below the surface and skewed to one side. They did not however, develop a

means for predicting the observed velocity field. Katopodis et al. (1978) performed a study of model and prototype culverts with baffle systems installed. On a 44.5 m long control culvert without baffles, they qualitatively described the two dimensional velocity distributions at two stations along the culvert length. Some of the isovel plots they developed show a distinct skew in the maximum velocity to the right side of the culvert (looking downstream). This kind of skew has been attributed to a misalignment of the culvert barrel with the stream bed (Behlke et al., 1991) but numerous authors have found evidence that even tiny perturbations in channel geometry can create secondary currents, which are believed to impact the velocity distribution (Chow, 1959; Replogle and Chow, 1966; Schlichting, 1979; Sterling and Knight, 2000; Ead et al., 2000).

2.4 Model Studies of Culverts

Barber and Downs (1996) evaluated the equations of Mountjoy (1986) and Chiu (1993) against velocity measurements data taken in 4 different circular culverts at laboratory facilities at Washington State University. Their primary aim was to measure the velocity profiles observed and find a means of extrapolating these results to larger size culverts. The culverts used in the experiment are detailed in Table 2.1.

Table 2.1: Experimental culverts used by Barber and Downs (1996).

Culvert #	Inside Diameter (m)	Length (m)	Corrugations (mm)
1	0.305	6.1	68 x 13
2	0.61	12.2	68 x 13
3	0.737	9.74	76 x 25
4	0.61	6.1	none

Detailed velocity measurements were taken at several stations along the length of all four culverts for a range of flows ($0.0052 \text{ m}^3/\text{s}$ to $0.1274 \text{ m}^3/\text{s}$), slopes (0.5% to 5.0%), and relative depths ($0.16D_o$ to $0.78D_o$) depending upon the culvert. A tailgate was used to control the flow depth in the culverts where needed.

Analysis of the velocity data showed a skew in several of the velocity cross-sections. For this reason, Barber and Downs (1996) felt it was not possible to accurately predict the exact shape of the velocity distributions. The effort to do so was abandoned and the approach of estimating cross-sectional area based on velocity used by Mountjoy (1986), White (1996) and House et al. (2005) was adopted. The authors state that there is no evidence to suggest that asymmetric velocity distributions pose a hindrance to fish passage, thereby providing justification for using a method to predict average thickness of velocity zones rather than the actual velocity profile at any given location in the culvert. Relative velocity contours (u/u_{max}) were produced from discrete velocity readings and the area of each contour (effective area) was calculated. From these results, a symmetric velocity profile comprised of the effective areas was reconstructed, preserving continuity. It is this “effective cross-section” profile that was used to evaluate the equations of Mountjoy (1986) and Chiu (1993).

The equation of Mountjoy (1986) and a one-dimensional application of Chiu (1993) were compared to the effective centerline profile derived from the four model culverts tested by Barber and Downs (1996). A statistical analysis of fit was performed on the results for the Mountjoy and Chiu equations including bias, mean absolute error and root mean square error. Sensitivity analysis was also performed for Chiu’s entropy parameter, M , and Manning’s n , for Mountjoy. Barber and Downs (1996) state that both equations provided reasonable fit to the experimental velocity profiles, but Mountjoy’s equation provided the best fit to the experimental data and was easier to apply for design purposes.

In order to address the inadequacy of existing models to predict the two-dimensional velocity distribution in a culvert, Ead et al. (2000) conducted a study of turbulent open channel flow in a culvert, Ead et al. (2000) conducted a study of turbulent open channel flow in a circular corrugated steel culvert. The authors utilized an 8 m long, 0.62 m diameter culvert with 68 mm by 12 mm corrugations with a range of flows ($0.030 \text{ m}^3/\text{s}$ to $0.200 \text{ m}^3/\text{s}$) and slopes (0.55%, 1.14% and 2.55%). Centerline velocity and water surface profiles were taken at 14 stations along the length of the culvert. Two stations, one near the entrance and one at the midpoint of the culvert, were selected for detailed velocity sampling. Velocity profiles were taken at six stations across half the width of

the culvert, from $z/z_o = 0$ to 0.88, where z = the horizontal distance from the center plane and z_o = half the top width of flow. The relative spacing of the vertical stations varied slightly for different runs. The shear velocity, u_* , was determined at the base of each vertical profile by plotting u vs. y on semi-log paper and determining the slope of the linear portion of the curve. Each vertical profile was then plotted as u/u_* vs. y/k_s and k_s was adjusted until the profiles fit the Log Law for rough turbulent flow (equation 2.21) (Schlichting, 1979),

$$\frac{u}{u_*} = 5.75 \log \frac{y}{k_s} + 8.5. \quad (2.21)$$

By this means, Ead et al. (2000) determined that k_s was equal to the height of the culvert corrugations, or 0.012 m. As a check, this procedure was applied to the velocity data from Katopodis et al. (1978) and k_s was again found to be equal to the corrugation height of the large, 4.27 m control culvert. As seen in many other culverts, the authors noted the maximum velocity was depressed below the water surface, commonly believed to be caused by secondary currents. All velocity profiles were found to have a logarithmic region (nearest the bed), but deviations in the velocity profile were strongly correlated with relative distance from the central plane (z/z_o). By non-dimensionalisation and correlation of various measured parameters, modifications were made to the Log Law to expand its application to account for deviations near the water surface and across the width of the cross-section. To make the equation applicable for design, the velocity distribution was related to average velocity rather than shear velocity. Ead et al. (2000) caution that equations 2.38 and 2.39 were developed using only a single culvert size and may not be universally applicable. The resulting equations are

$$\text{for } \quad y_z/k_s < y_d/k_s,$$

$$\frac{u}{u_{avg}} = \left[5.75 \log \left(\frac{y}{k_s} \right) + 8.5 \right] [f_3(z/z_o)]^{1/2} \left(\frac{Jg^{1/2}n}{R^{1/6}} \right), \quad (2.38)$$

$$\text{and for } \quad y_z/k_s > y_d/k_s,$$

$$\frac{u}{u_{avg}} = \left[5.75 \log \left(\frac{y}{k_s} \right) + 8.5 - \frac{(y_z/k_s) - f_1(z/z_o)}{(y_o/k_s) - f_1(z/z_o)} f_2(z/z_o) \right] \cdot [f_3(z/z_o)]^{1/2} \left(\frac{Jg^{1/2}n}{R^{1/6}} \right), \quad (2.39)$$

where

$$f_1(z/z_o) = (y_d/k_s) = -6.91(z/z_o)^2 - 2.05(z/z_o) + 9.00,$$

$$f_2(z/z_o) = (\Delta u_m/u_*) = 5.58(z/z_o) + 0.90,$$

$$f_3(z/z_o) = (\tau_o/\tau_{oo}) = -20.00(z/z_o - 0.60)^3 + 2.75(z/z_o - 0.60)^2 - 0.40(z/z_o - 0.60) + 1.00,$$

$$J = \frac{u_{*o}}{(gRS)^{1/2}},$$

and y_z is the height above the datum at a non-central plane, y_o is average depth of flow at a non-central plane in the uniform flow region, y_d is the height above the datum at which the velocity profile readings deviate from the Log Law, Δu_m is the maximum deviation in velocity from the log law in the upper region of flow, τ_o is the bed shear stress at relative distance z/z_o , and τ_{oo} is the bed shear stress at the central plane.

Sterling and Knight (2000) and Knight and Sterling (2000) studied the velocity profile, overall resistance and boundary shear in circular conduits flowing part full, with and without a flat bed. In both studies, the conduit used was a 0.244 m diameter by 19 m long plastic pipe and the ratio of bed depth to culvert diameter ranged from 0.0 to 0.664. The culvert slope was varied from 0.1% to 0.9% and a wide range of flows were investigated in both studies to simulate flow conditions that may occur in culverts, sewers, and hydropower tunnels. The bed and conduit walls were of the same material and Sterling and Knight (2000) found that Manning's n was independent of stage for all of the tests conducted. Velocity profiles were taken near the culvert outlet and the resulting contour plots showed strong evidence of secondary currents inferred from the

distortion of the isovels close to the channel wall and the depression of the maximum velocity below the water surface. The distortion of the isovels was more pronounced in tests with larger ratios of bed depth to culvert diameter. Knight and Sterling (2000) found the boundary shear stress around the wetted perimeter of the conduit was highly sensitive to cross-sectional shape. In general, the ratio of local to global shear stress ($\tau_o/\rho gRS_o$) varied widely (0.6 to 1.2), peaking at the central plane and decreasing as the water surface was approached. As the water depth was increased, the distribution of $\tau_o/\rho gRS_o$ around the wetted perimeter tended to flatten out to unity. The peak and the overall variability of the $\tau_o/\rho gRS_o$ distribution was exaggerated as the bed depth was increased, causing the cross-section to resemble a rectangular channel.

2.5 Culvert Baffle Fishways

Considerable work has been invested into developing and testing various baffle fishways for circular culverts in both field and laboratory settings (Behlke et al., 1991; Katopodis et al., 1978; Ead et al., 2002; Rajaratnam et al., 1988; Rajaratnam et al., 1990; Watts, 1974). The key concept behind baffle systems is that they provide regularly spaced low velocity zones where fish can rest between successive attempts to pass the shooting flow regime. Progress upstream is made utilizing a rapid swimming mode called burst speed (Katopodis, 1992), which can be maintained for short periods of time (e.g. 15 seconds), enough for a fish to pass to the next cell where it can rest and recuperate.

The research relating to baffled fishways is highly specific to the type of baffle system employed and the focus is on determining optimal baffle size, shape and spacing while minimizing losses to hydraulic efficiency due to increases in culvert roughness. Some work has been done to examine the velocity field primarily in the central plane of the culvert (Katopodis et al., 1978; Ead et al., 2002; Rajaratnam et al., 1988; Rajaratnam et al., 1990) but velocity structure in baffled culverts is very complex with alternating zones of high and low velocity as well as various plunging, streaming and shooting flow regimes. Unfortunately, design guidelines developed for baffle fishways have little application to partially buried culverts.

This begs the question, “Why not employ baffle fishways in Manitoba?” Despite their successful application in other areas, culvert fishways employing baffles are ill suited to the conditions prevalent throughout much of the Prairie Provinces. In the Manitoba Stream Crossing Guidelines for the Protection of Fish and Fish Habitat (Manitoba Natural Resources, 1996), culvert fishways are recommended only as a last resort, citing the need for regular maintenance and a tendency for the baffles to infill with sediment and catch large debris, leading to an increased risk of washouts and flooding.

Chapter 3: Laboratory Set-up and Sampling Methodology

3.1 Laboratory Facilities

Construction and testing of the model was conducted on the lower level of the Hydraulics Research and Testing Facility at the University of Manitoba. Water was supplied to the model by a 350 mm diameter PVC supply line from a constant head tank on the main level. The tank is supplied by two pumps (75 hp and 65 hp) and is capable of delivering a constant discharge of up to 0.485 m³/s. Two calibrated volumetric tanks are set below the head tank to measure discharge. Flow through the model is calculated by taking the difference between the maximum overflow rate (using one or both of the pumps) and the overflow rate when the model is in use.

3.2 Physical Model Design

To increase the applicability of the study, it was desirable to construct an undistorted model which was representative of a typical Manitoba highway culvert when designed to meet current fish passage criteria. Most circular highway culverts in Manitoba range in size from 2.1 m x 40 m to 6.0 m x 80 m, with 3 m being a typical diameter. In practice, these culverts are sized to pass a 2% flow with minimal head loss, usually less than 0.3 m. The diameter or number of barrels may then be increased to accommodate the 3dQ10 flow. Fish passage criteria typically require an average velocity ranging from 0.6 m/s to 1.0 m/s, depending upon the culvert length and fish species present. In Manitoba, culverts are embedded by 0.3 m or 10% of their diameter, whichever is greater, and filled with a suitable aggregate. This material is termed Class 350 rip rap and has the following size distribution: $d_{15} = 0.1$ m, $d_{50} = 0.2$ m and $d_{100} = 0.35$ m (Manitoba Infrastructure and Transportation, 2003). The typical inlet and outlet configuration is a projecting end, intercepting a road embankment slope of 3:1 at a distance of roughly $0.2D_o$ from the invert, shown in Figure 3.1.

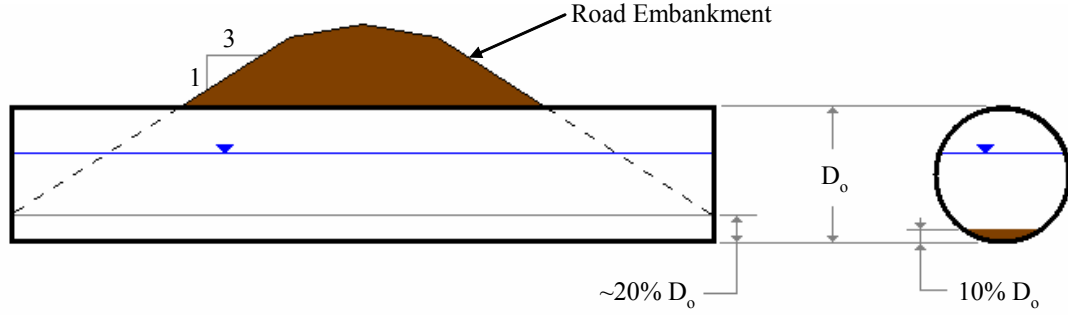


Figure 3.1: Projecting end outlet configuration (not to scale).

3.2.1 Similitude for Open Channel Flow

In open channel flow, the dominant forces are gravitational, with inertial and frictional forces playing a lesser role. This would suggest that both Froude (F) and Reynolds (Re) model scaling should be maintained as in

$$\frac{F_p}{F_m} \equiv \frac{u_p / \sqrt{g_p X_p}}{u_m / \sqrt{g_m X_m}} = \frac{Re_p}{Re_m} \equiv \frac{u_p X_p / \nu_p}{u_m X_m / \nu_m} = 1, \quad (3.1)$$

where ν is the kinematic viscosity of water and the subscripts p and m denote model and prototype, respectively. For calculation of the Froude number, X equal to the characteristic length, taken to be hydraulic depth. Belataos (1995) notes that since gravitational forces are equivalent for the model and prototype, equation 3.1 results in

$$\frac{(\nu_k)_p}{(\nu_k)_m} = \lambda^{1.5}, \quad (3.2)$$

where λ is the geometric scale factor, which relates the dimensions in the prototype to the dimensions in the model. The geometric scale factor is equal to

$$\lambda = \frac{X_p}{X_m}. \quad (3.3)$$

However, viscous effects are minimized and Reynolds independence can be assumed for completely rough flow regimes when the roughness Reynolds number (Re^*) is greater

than 70 ($Re^* = k_s u^* / \nu$). This was found to be the case for all flows tested in the model and the Froudian scale relations selected are shown in Table 3.1.

Table 3.1: Froudian Scale Ratios.

Parameter	Scaling Ratio
Length	λ
Area	λ^2
Velocity	$\lambda^{1/2}$
Discharge	$\lambda^{5/2}$
Manning's n	$\lambda^{1/6}$

3.2.2 Scaling the Culvert

Based on the applicable scale ratios, laboratory space constraints, commercially available culverts sizes and available laboratory flow, it was determined that a 5:1 scale model ($\lambda = 5$) would be the best choice for this study. Table 3.2 details the resulting parameters for the model and a hypothetical prototype created using Froudian scaling ratios. Design flow, depth and velocity listed for the prototype were used as a general guideline to create target parameters for the model and were not exactly replicated during testing.

Table 3.2: Target parameters for model and hypothetical prototype.

Parameter	Prototype	Model
Diameter (D_o)	3.10 m	0.62 m
Length (L)	71.40 m	14.28 m
Available Flow Area (A_{max})	7.155 m ²	0.286 m ²
Embedment (d_b)	0.310 m	0.062 m
Area of Bed (A_b)	0.400 m ²	0.016 m ²
Design Flow ($3dQ_{10}$)	3.578 m ³ /s	0.062 m ³ /s
Design Depth ($Y_{3dQ_{10}} \sim D_o/2$)	1.55 m	0.31 m
Design Flow Area ($A_{3dQ_{10}}$)	4.336 m ²	0.173 m ²
Design Velocity ($V_{3dQ_{10}}$)	0.800 m/s	0.357 m/s

3.2.3 Scaling the Roughness Elements

Circular culverts with diameters exceeding 1.5 m are usually constructed of structural plate with a nominal corrugation profile of 152 mm x 51 mm (Handbook of steel drainage and highway construction products, 2002). The culvert used for the study had a nominal corrugation profile of 68 mm x 13 mm. Details are shown in Figure 3.2.

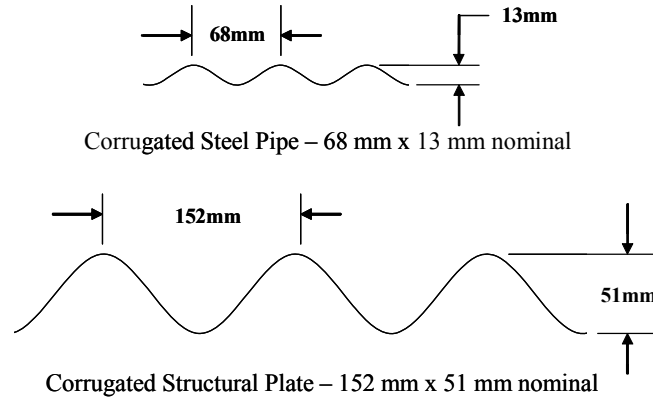


Figure 3.2: Corrugation profile for prototype and model culverts.

At a scale factor of 5, the corrugation length (L_c) and height (H_c) scale as

$$\frac{L_{c_p}}{L_{c_m}} = \frac{2.24}{1} \text{ and } \frac{H_{c_p}}{H_{c_m}} = \frac{3.92}{1},$$

which does not preserve perfect geometric similarity. However, the Manning's n for prototype and model are well known and scale exactly for $\lambda = 5$ (Table 3.3).

$$n_p = 0.030 = \lambda^{1/6} n_m = 5^{1/6} \cdot 0.023$$

Determining how to scale the granular material in the bed is a more complex matter. Belataos (1995) states that since the Froude number and slope are equivalent in both the model and prototype, this implies that the Darcy-Weisbach friction factor for both should also be equal, based on

$$f = \frac{8S_o}{F^2}. \quad (3.4)$$

Also, if the model and prototype flows are independent of the Reynolds number, then the friction factor depends only on the relative roughness, R/k_s , which means that the equivalent sand roughness should be scaled by the geometric scale factor ($\lambda = 5$) like other linear dimensions in the model. It has been demonstrated that equivalent sand roughness is proportional to particle size (Strickler, 1923; Charlton et al., 1978; Bray, 1979; Hey, 1979). Therefore, as shown in Table 3.3, the gravel mix used for the model was scaled directly from specifications for Class 350 rip rap (Manitoba Infrastructure and Transportation, 2003) while the Manning's n for the bed material was estimated from published values for similar size aggregate (USACE, 1994).

Table 3.3: Roughness scaling for model and hypothetical prototype.

Parameter	Prototype	Model
Manning's n for Culvert	0.030	0.023
Manning's n for Bed	0.035-0.041	0.027-0.031
Gravel d_{15}	0.100 m	0.020 m
Gravel d_{50}	0.200 m	0.040 m
Gravel d_{100}	0.350 m	0.070 m

To recreate the gravel mix, it was assumed that the particle sizes would be normally distributed, therefore the probability that any particle will exceed the d_{15} is $p = 0.15$, and the variance of the size distribution was estimated as $z @ p = 0.15$ equals -1.0364. The ω statistic is related to the normal distribution by

$$\omega = \frac{x - \mu}{\sigma}, \quad (3.5)$$

where x = a value in the sample, μ = the mean and σ = the standard deviation. Using equation 3.5, the standard deviation of the model gravel sizes was determined as

$$\sigma_m = \frac{d_{15m} - d_{50m}}{z} = \frac{0.02m - 0.04m}{-1.0364} = 0.0193.$$

Commercially available river-wash gravel was then used to recreate a well graded 5:1 scale mix (shown in Table 3.4). The size fractions were proportioned by mass and sufficient material was purchased and mixed to fill the model bed to a depth of $0.1D_o$.

Table 3.4: Model gravel bed material gradation.

Size Fraction (%)	0-4	4-8	8-14	14-46	46-72	72-100
Size Range (mm)	0-6	6-13	13-19	19-38	38-51	51-70

3.3 Model Construction

The model consisted of three major components: a headwater box, the culvert, and a tailwater box. The layout and components of the model are shown in Figure 3.3.

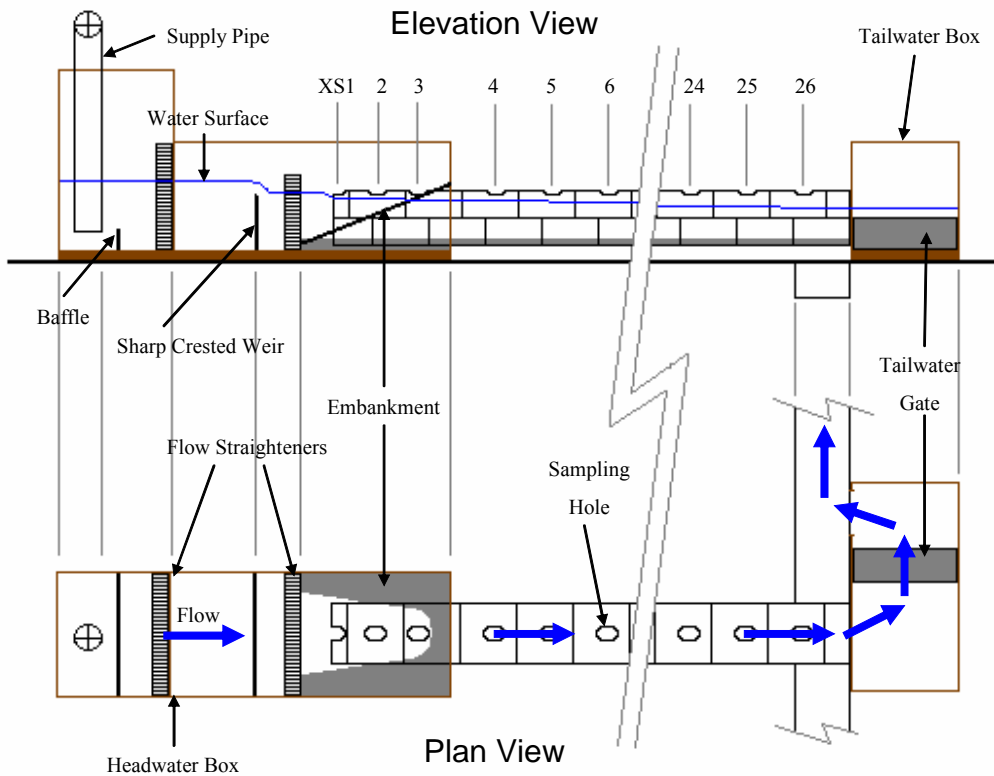


Figure 3.3: Model layout and components (not to scale).

3.3.1 Headwater Box

The headwater box was constructed of $\frac{3}{4}$ inch thick high density overlay and framed in using standard, 2x6 inch dimensional lumber. It measured 1.23 m wide by 1.23 m deep by 4.9 m long. All joints were supported along their full length, gapped by 5 mm and filled with clear silicon caulking to prevent leakage. The flow from the supply pipe

entered the upstream portion of the headwater box and passed through a flow straightener consisting of a layer of industrial furnace filter and a layer of stacked, 50 mm diameter by 300 mm central vacuum tubing. The flow then passed over a sharp crested weir, calibrated to a stilling well and then through a second flow straightener before entering the culvert inlet (Figure 3.4). The inlet projected from a simulated road embankment built from plywood. To save space and because slope stability was not an issue, the embankment was built at a slope of 2:1. The bed of the approach channel was filled with gravel to the level of the culvert bed. Headwater elevations were measured with a manometer just downstream of the second flow straightener. The elevation of the manometer was tied to the invert of the culvert.



Figure 3.4: Projecting inlet showing simulated road embankment and gravel bed.

A sharp crested weir (shown in Figure 3.5) was built to allow rapid and precise flow estimation, rather than relying on the lengthy process of estimating flow using the laboratory's volumetric tanks. The discharge over a sharp crested weir can be calculated by the equation

$$Q = C_{weir} H^{1.5} L_{weir} \quad (3.6)$$

where Q is the flow over the weir, C_{weir} is the weir coefficient, H is the head relative to the weir crest and L_{weir} is the length of the weir (equal to the width of the headwater box = 1.229 m). By taking a range of flow and head measurements, the weir coefficient can be calculated, thus calibrating the weir. This was done as shown in Table 3.5, where Q_{75} is the maximum overflow rate using the 75 Hp pump, $Q_{overflow}$ is the overflow rate when there is model flow, Q_{model} is the flow through the model, and $C1$, $C2$, $C3$ and $C4$ are the weir coefficients for the individual trials.



Figure 3.5: Sharp crested weir showing nappe splitters used for aeration demand.

Table 3.5: Calibration of Sharp Crested Weir Coefficient.

Trial	H (m)	$Q_{overflow}$	$Q_{75} - Q_{overflow} = Q_{model}$ (m^3/s)	C
1	0.041	0.266	0.021	2.102
2	0.086	0.223	0.065	2.087
3	0.139	0.159	0.129	2.020
4	0.197	0.065	0.223	2.067
$Q_{75} =$	0.288 m^3/s		Average C_{weir}	2.069

Figure 3.6 shows that there is close agreement between flows calculated using the average weir coefficient and those calculated using the weir coefficients from the individual trials.

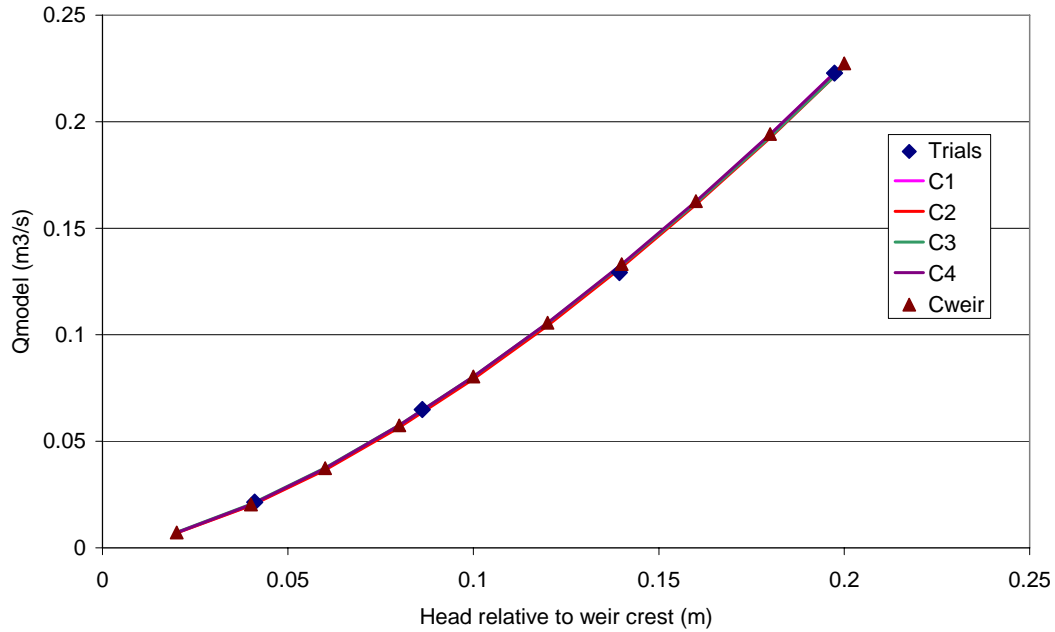


Figure 3.6: Calibration of Sharp Crested Weir Coefficient.

3.3.2 The Culvert

The culvert was constructed from 51 full pieces and 2 half pieces flanged nestable corrugated steel pipe donated by Armtec Ltd. The diameter of the pipe was 0.63 m in the trough of each corrugation and 0.61 m at the peak. The average diameter of the pipe was therefore taken to be 0.62 m. The pipe was assembled with two corrugations overlapping as shown in Figure 3.7.

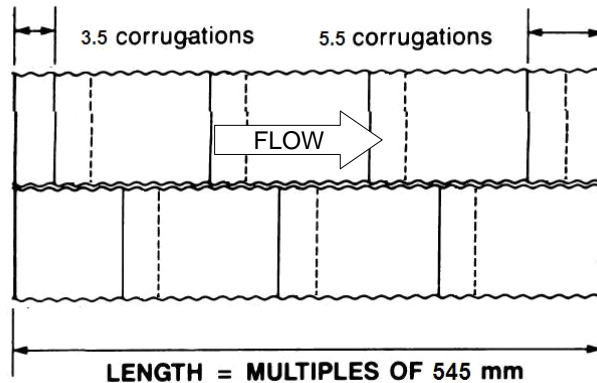


Figure 3.7: Assembly pattern for flanged nestable CSP used in model.

In addition, each joint was sealed with a custom fabricated rubber gasket and bolted together along the flanges, creating a continuous culvert with uniform cross-section, as shown in Figure 3.8.

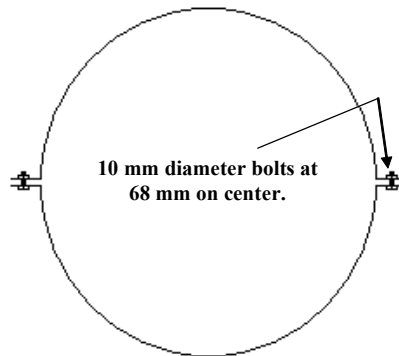


Figure 3.8: Assembled cross-section shown bolt pattern.

The culvert was connected to the headwater and tailwater boxes (as shown in Figure 3.9) using flexible rubber collars, preventing leaks and allowing for rotation as the slope of the culvert was adjusted.

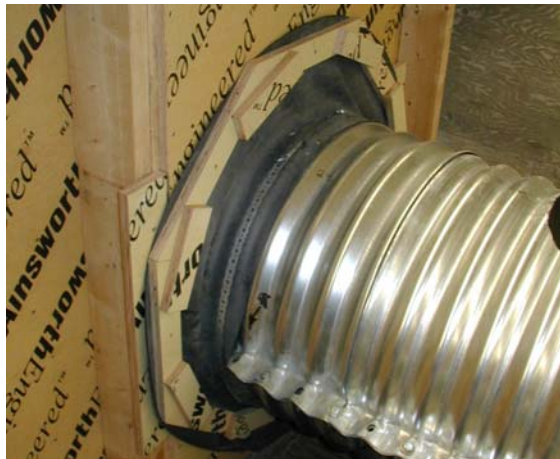


Figure 3.9: Flexible rubber collar connecting culvert to tailwater box.

Sampling stations 1 to 3 were located in the headwater box, and holes were cut in the obvert of the culvert at 0.415 m on center, starting at 0.050 m from the inlet to provide access for instrumentation. Along the rest of the culvert access holes were cut in the

center of each upper culvert section, at 0.545 m on center. The location of each sampling station is detailed in Table 3.6.

Table 3.6: Location of sampling cross-sections relative to culvert inlet.

XS	Dist d/s (m)	Elev Adj (m)	XS	Dist d/s (m)	Elev Adj (m)
HW	-1.000	0.004	14	7.060	0.000
1	0.050	0.004	15	7.605	-0.001
2	0.465	0.004	16	8.150	-0.001
3	0.875	0.003	17	8.695	-0.001
4	1.610	0.004	18	9.240	-0.002
5	2.165	0.004	19	9.785	-0.002
6	2.710	0.003	20	10.330	-0.003
7	3.255	0.003	21	10.870	-0.004
8	3.805	0.003	22	11.415	-0.004
9	4.345	0.002	23	11.960	-0.005
10	4.885	0.001	24	12.505	-0.005
11	5.430	0.000	25	13.050	-0.005
12	5.970	0.001	26	13.665	-0.005
13	6.515	0.000	TW	14.500	-0.005

The culvert was mounted on plywood bunks spaced 0.545 m on center and positioned beneath each overlap joint. The bunks were hung on wooden stringers as part of a series of 3 independent rigid supports along the length of the culvert. A set of adjustable legs was positioned at approximately every 1.1 m. The left side of the model is shown in Figure 3.10.



Figure 3.10: View facing upstream of culvert and supports (set at 0% slope).

Elevations of the culvert invert were surveyed using a Nikon AE7 automatic level and the legs were adjusted to set an initial slope of 0%. For subsequent trials, the slope was changed by raising the entire headwater box and adjusting each of the support legs on the culvert until the desired slope was achieved. A set of rails was attached on either side of the culvert and referenced to the culvert invert to provide a datum for instrumentation. Table 3.6 also shows the elevation adjustment at each sampling station which accounts for a slight downward slope of the datum rails relative to the culvert invert. The elevation of the rails at cross-section 14 was taken as the “true” datum, with an elevation adjustment of zero.

Once the culvert had been levelled, the gravel bed was placed to an estimated average depth of 6 cm. A small board was used to retain the gravel bed in the culvert and was positioned just below the upper surface of the bed material, at an elevation of 0.06 m above the invert (Figure 3.11). Once the initial placement of the bed was complete, water was passed through the culvert and then allowed to drain out to the level of the board. Once the water ceased to flow, the water surface became truly level and could be used as an accurate datum. The bed material was then repositioned until the author deemed a uniform average depth of 0.06 m was achieved.

3.3.3 Tailwater Box

The tailwater box was constructed similarly to the headwater box and measured 1.23 m wide by 2.45 m long. Flow in the culvert discharged into a tailwater box through an outlet mounted flush to the head wall. A projecting outlet was not used because the outlet configuration would have little impact upon flow velocity in the culvert barrel. Tailwater elevations were measured with a manometer mounted on the headwall to the right of the outlet. Manometer readings were protected from fluctuations in water surface elevation using a stilling well mounted over the manometer port. The elevation of the manometer was tied to the invert of the culvert. The tailwater depth was controlled by a tailwater gate, shown in Figure 3.11. The flow exited the tailwater box into a channel in the floor of the laboratory and returned back to the main sump for recirculation.



Figure 3.11: Layout of culvert outlet, tailwater gate and tailwater box outlet.

3.4 Acoustic Doppler Velocimetry

Velocity measurements were made using SonTek acoustic Doppler velocimeters (ADV) which measured the three components of the velocity (u , v and w) at 25 Hz. The measurement technique employed by an ADV is quasi-non-invasive as it takes velocity measurements in a remote sampling volume located 57 mm away from the excitation transducer. The ADV sampling volume used was a cylinder 5 mm in diameter and 6 mm high as shown in Figure 3.12.

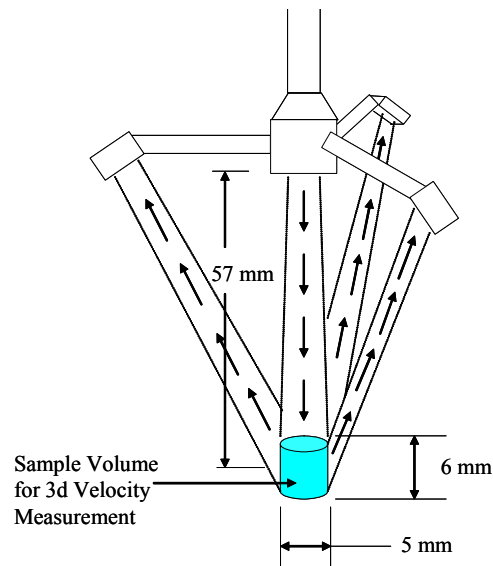


Figure 3.12: Definition of sample volume for three dimensional velocity measurements.

The ADV measures the velocity of water using a principle called Doppler shift. Sound waves are emitted by the excitation transmitter and are reflected back to a receiver from particles entrained in the water. The particles are moving relative to the receiver and therefore induce a shift in the frequency of the reflected sound relative to the transmit frequency. This principle is illustrated in equation 3.7

$$F_{Doppler} = -2F_{source} \frac{V_{relative}}{C_{sound}}, \quad (3.7)$$

where $V_{relative}$ is the relative velocity between source (suspended particulates) and receiver, C_{sound} is the speed of sound, $F_{Doppler}$ is the change in frequency at the receiver, and F_{source} is the transmitted frequency (SonTek, 1997). The electronics in the ADV are calibrated for the individual probe geometry and use the Doppler shift at the receivers to calculate the three components of the velocity.

Two different ADVs were used; one with a downward-looking probe tip and one with a side-looking probe tip (shown in Figure 3.13). The side-looking probe was used to measure velocities close to the water surface and in areas of the cross-section not reachable by the downward-looking probe.

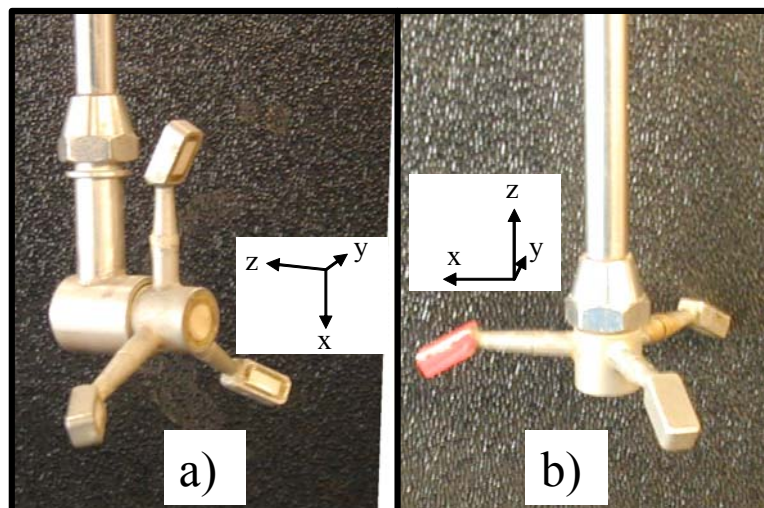


Figure 3.13: a) Side-looking ADV probe, b) Downward-looking ADV probe tip. Right hand axes are defined for each probe type.

Before velocity sampling begins, the range of expected velocities must be set. The ADV sampling ranges are ± 3 cm/s, ± 10 cm/s, ± 30 cm/s, ± 100 cm/s and ± 250 cm/s. SonTek advises the user to select the smallest velocity range which will suit because the velocity measurements are accurate to within 1% of the selected velocity range. For example, when the range is set to ± 100 cm/s, the expected error is ± 1.0 cm/s.

Liu et al. (2002) tested the accuracy of ADV measurements taken at 50 Hz in the bubbly-two phase flow created by a hydraulic jump. They found that the error of the ADV measurements increased linearly with air concentration. They also studied the boundary effect on ADV accuracy. Sontek claims that under good conditions, accurate velocity measurements may be acquired when the leading edge of the sample volume is within 0.5 mm of the boundary. Liu et al. (2002) found a significant effect when the sample volume was less than 30 mm from the boundary and at a distance of 5 mm, the error ranged from 12 to 25%. The accuracy of the ADV for measuring turbulence characteristics was tested independently by Voulgaris and Trowbridge (1998). They found that ADV measurements of mean velocity and Reynolds stress were within 1% of the value measured with a Laser Doppler Velocimeter. From these varying results, it is clear that the testing environment exerts a strong influence on the quality of ADV measurements.

The ADV also records a number of parameters which can be used to measure the quality of the data collected. For each receiver, the ADV records the Signal to noise ratio, the percent correlation and the standard deviation (in cm/s). The signal to noise ratio is a function of the sampling environment and the ambient noise levels in the electronics. Correlation is expressed as a percent with 100% under perfect conditions and 0% when the output velocity value is based on an incoherent signal. Ideally, the correlation should be between 70-100% but average velocities can be attained accurately at correlations as low as 40%. SonTek's Data Acquisition System (ADV Version 2.3) was used to record the sample data. At the start of recording, the software will provide an estimate of the distance from the sampling volume to the boundary if the distance is within the range of 2 to 25 cm. To minimise the effect of changes in temperature on the ADV measurements, the water temperature was input into the control software at the start of each run.

3.5 Automated Sampling System

To achieve a detailed picture of the velocity distribution, it was necessary to have a dense sampling grid with 60 to 120 sampling locations in each cross-section depending upon water depth. It was determined from earlier tests that average streamwise velocity readings in turbulent flow became stable after 30 seconds of continuous measurement with an ADV (as shown in Figure 3.14). With the 40 second sampling duration used, manual sampling of a single cross-section could take several hours. Therefore, an automated sampling system was devised to take the detailed velocity measurements necessary and provide consistency and repeatability of sampling between cross sections.

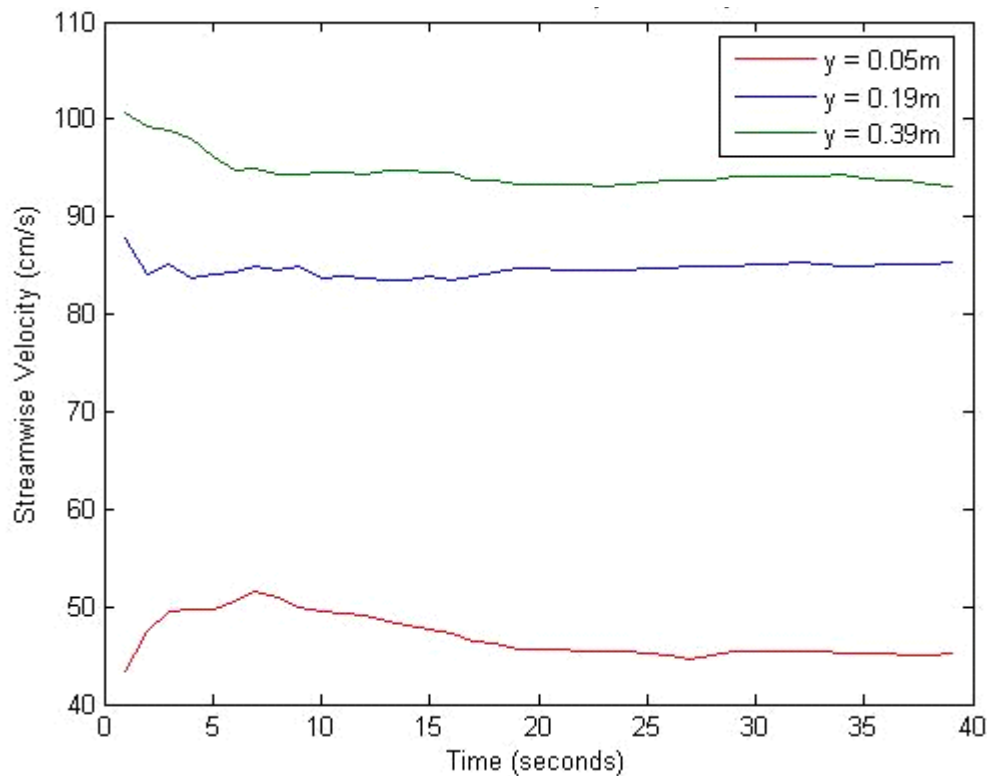


Figure 3.14: Stability of instantaneous streamwise velocity readings illustrated with cumulative averaging over a 40 second sampling period (central plane of S0Q221 – cross-section 10).

The system comprises the following components:

- one PC to run the Galil SmartTERM motion control software,
- one Galil DMC-1020 two-axis motion control PC card,

- one Galil controller bus,
- two Electrocraft BDC-25 amplifiers (X and Y),
- two Electrocraft E-3626 brushless servo-motors (X and Y),
- one sampling cart with a tilting mast,
- one downward-looking ADV, and
- a second PC to run the ADV data acquisition software Ver. 2.3 (DOS operating system).

The integration of these components is shown in Figure 3.15. The Galil SmartTERM software used was a Windows based interface with numerous advantages over its DOS based predecessor including color coded syntax help and echoing of commands as they were executed. The software controlled the two motors using custom ASCII files (hereafter referred to as DMC files) created by the user. The files contained a series of commands to control such parameters as motor velocity, acceleration, deceleration, torque limits, error limits and absolute or relative position. For each sample location, commands were used to relay timing and positional data to a cache which could be accessed and saved for reference. A sample of a DMC file used for a water depth of 0.468 m is provided in Appendix A. Attached to each motor was an optical encoder disk which emitted 1000 pulses per revolution. The controller interpreted these pulses in quadrature, dividing one revolution into 4000 counts. The motors were connected directly to leads screws with a 5 mm/revolution thread size giving a resolution of 0.00125 mm/count.

This motion control system has been employed with success previously using a Cartesian coordinate based sampling system (Hans, 1997). However, for automated sampling with a Cartesian coordinate system, there must be access across the full width of the cross-section. If enough of the culvert obvert is removed to allow this access, it will severely limit the depth of flow attainable in the culvert. Therefore, a polar coordinate sampling system was developed to allow sampling of the entire cross-section through a small opening in the culvert obvert. The size of the opening still allowed a relative depth of $0.938y/D_o$, the depth at which maximum discharge occurs in a circular culvert.

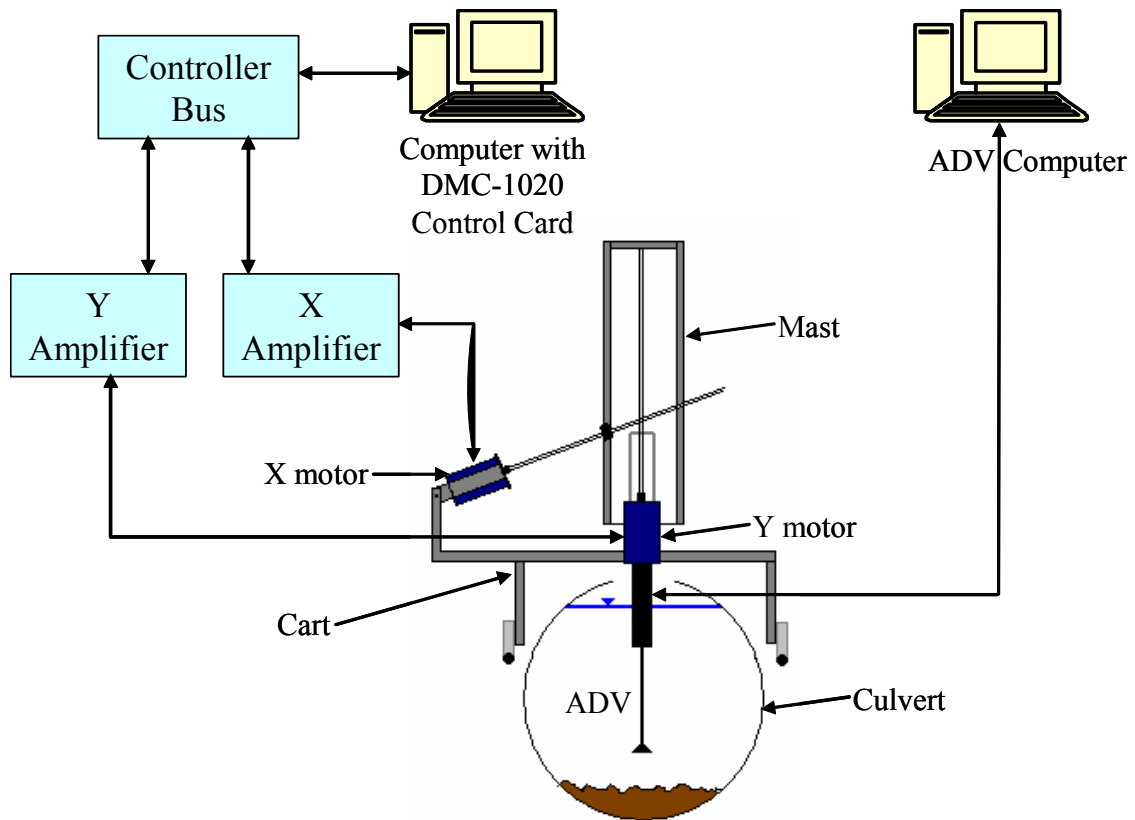


Figure 3.15: Schematic of the automated sampling system showing the motion control system integrated with the ADV.

Figure 3.16 shows a schematic of the sampling progression using a polar coordinate system. Only the downward looking ADV was used for automated sampling. Sampling began nearest the bed on radial #1. After each sample was complete, the ADV was advanced toward the water surface until the uppermost sample in the radial was completed. The mast was then tilted to the next radial and the ADV was lowered to the sampling location closest to the bed. This pattern was repeated until the full cross-section had been sampled. The number of radials and samples varied with the specific DMC file selected for the water depth. A different DMC file was created for each water depth ranging from 0.228 m to 0.508 m in increments of 0.01 m. This was done to optimize the arrangement of sample points, to allow flexibility in sampling and to minimize sampling time.

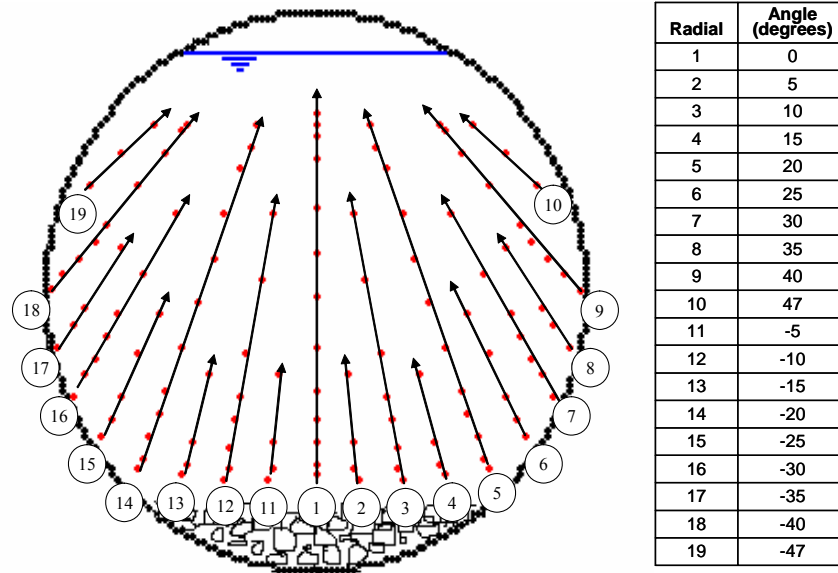


Figure 3.16: Progression of sampling on polar coordinate system.

The apparatus used to position the ADV consisted of two main components; a cart supported on rails (the datum) and a mast which could tilt ± 47 degrees from vertical, allowing the ADV to be positioned nearly anywhere in the cross-section (Figure 3.17). The tilt angle of the mast was controlled by motor X and the insertion of the ADV was controlled by motor Y (Figure 3.15).



Figure 3.17: Automated sampling system showing the sampling cart, control computers and sampling mast with ADV in fully withdrawn position (ADV is not visible).



Figure 3.18: Mast set up at cross-section 1 and angled to allow the ADV to sample the left side of the cross-section.

Checking the calibration of motor X and Y confirmed that 4000 counts was equivalent to 5 mm linear displacement. However, the tilt angle of the mast was not a linear function of the count so tilt angle was calibrated using an analog inclinometer with a 0.5 degree resolution. The inclinometer was also used to ensure the apparatus was returned fully to its home position before the sampling began at each cross-section. There was not enough room in the headwater box to accommodate the cart and the mast, so the mast was also designed to be mounted to a fixed frame for cross-sections 1 to 3. Figure 3.18 shows the mast set up at cross-section 1 and angled to allow the ADV to sample the left side of the cross-section. Due to space restrictions, the tilt angle was limited within the headwater box and therefore, automated sampling on the 40 and 47 degree radials was not possible.

3.6 Supplemental Surface Velocity Sampling

The primary focus of this study was the zone from a depth of maximum velocity, down to the bed. However, for a more complete picture of the velocity structure, surface velocities were collected for the experimental runs at 0% slope using a manually positioned side-looking ADV. Velocity readings were taken close to the water surface

and near the culvert walls where the downward looking ADV could not reach. A typical sampling pattern is shown in Figure 3.19.

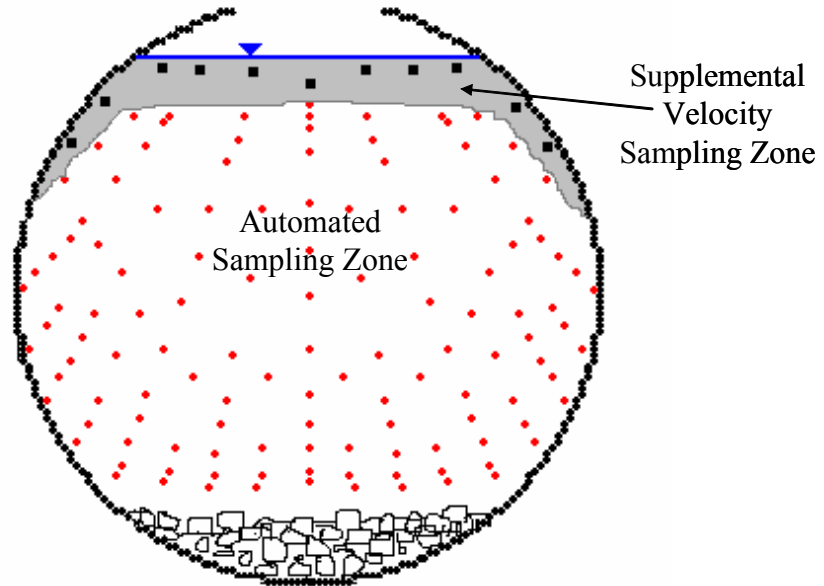


Figure 3.19: Hypothetical cross-section shown zones of automated and supplemental sampling.

Chapter 4: Experimental Procedure and Data Processing

4.1 Experimental Procedure

The model was tested using three slopes, each with two different flow conditions. Each slope was tested with a low flow case (with $y \sim D_o/2$) and a high flow case, where the conveyance of the culvert was maximized without surcharging at the inlet. The rationale was to examine an extreme range of flows for each slope, thereby inducing a diverse velocity structure for study. All flows tested were subcritical because supercritical flow is rarely a desirable design goal in culverts when fish passage is a consideration. The first test at 0% slope and $Q = 0.064 \text{ m}^3/\text{s}$ was conducted to simulate conditions which may occur under 3dQ10 flow at a depth of approximately $D_o/2$. Table 4.1 provides a summary of the testing parameters used for detailed velocity measurements.

Table 4.1: Detailed velocity measurement testing parameters.

Slope	Flow (m^3/s)	Code	Average Depth (m)	Average Froude #
0%	0.064	S0Q64	0.299	0.235
	0.186	S0Q186	0.472	0.291
0.5%	0.145	S5Q145	0.305	0.514
	0.221	S5Q221	0.449	0.387
1.0%	0.150	S1Q150	0.260	0.700
	0.254	S1Q254	0.386	0.517

4.1.1 Water Surface Elevations

For detailed velocity testing, water surface elevations were recorded at each sampling station along the length of the culvert using a point gauge attached to the sampling cart. The tailwater gate was set to minimize variation in flow depth. In the headwater box (cross-sections 1 to 3), water surface elevations were measured with a point gauge attached to the sampling frame. Headwater and tailwater elevations were measured using built in manometers. All elevations and positional data used to locate velocity readings in the cross-section were recorded relative to the ADV probe tip. Figure 4.1 provides a

reference sketch defining the cross-section relative to the ADV probe tip. The vertical distance from the probe to the water surface was referred to as Y_{tip} .

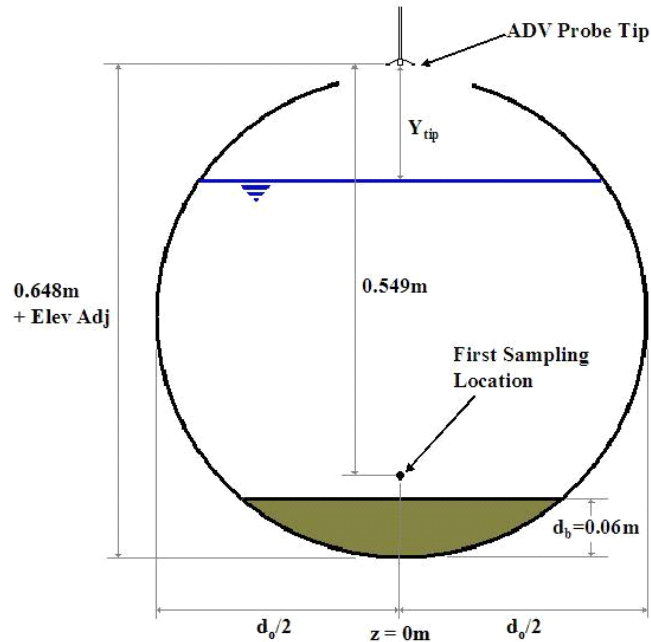


Figure 4.1: Sample coordinate reference sketch.

4.1.2 Gradually Varied Flow

In order to assess the suitability of the available composite roughness calculation methods, it was necessary to measure the water surface profile occurring in the culvert under gradually varied flow conditions. For each combination of slope and flow listed in Table 4.1, the tailwater gate was lowered completely allowing an M2 profile to develop in the culvert. Water surface elevations were recorded using a point gauge at each sampling station. Headwater and tailwater elevations were also recorded.

4.1.3 Detailed Velocity Measurements

Detailed velocity measurements were taken at cross-sections 1, 2, 3, 4, 6, 8, 10, 12, 14, 17, 20, 23 and 26 for all experimental runs listed in Table 4.1. The sampling stations were more closely spaced near the culvert inlet, in an attempt to capture the rapidly

changing flow structure in this region. Supplemental surface velocity readings were also taken for experimental runs S0Q64 and S0Q186 at each cross-section where detailed velocity measurements were taken.

4.1.4 Smooth-Walled Trials

In an effort to isolate the effect of the bed material on the velocity structure, the corrugation roughness was removed by using a smooth plastic insert to line the first six cross-sections of the culvert for the 0.5% slope trials. The 4 mm thick insert was affixed tightly to the inside of the culvert as shown in Figure 4.2. This reduced the diameter of the culvert to 0.60 m, a reduction in available flow area of 5.7% and the DMC files did not require modification for use with smooth-walled testing. Detailed velocity measurements were taken at stations 2, 4 and 6 for flows of 0.145 m³/s and 0.221 m³/s. The run parameters are summarised in Table 4.2.



Figure 4.2: View of culvert looking downstream from the inlet with smooth-walled insert installed in the first six cross-sections.

Table 4.2: Sample parameter summary for smooth-walled trials

Slope	Flow (m ³ /s)	Run	Average Depth (m)	Average Froude #
0.5%	0.145	S5Q145s	0.305	0.527
	0.221	S5Q221s	0.433	0.423

4.2 Data Processing

4.2.1 ADV Files

During sampling of a cross-section, the ADV was left to record continuously, producing a single ADV file of up to 150,000 instantaneous velocity readings for each of the three velocity components. In order to isolate the velocity readings from individual sampling points, it was necessary to determine the timing of each sample based upon the specific DMC file used to position the ADV probe. The DMC files were designed to output the position of each motor and the time as the system came to rest at each sampling point. A sample of the output for $Y_{iip} \sim 120\text{mm}$ ($y \sim 0.468\text{ m}$) is presented in Appendix A. By prerecording the timing and positional output, a sampling index was created for each DMC file. Due to limitations in the range of motion possible in the headwater box (mentioned in section 3.5), a separate set of DMC files was created for use with cross-sections 1 to 3. Timing and position output was also recorded for these DMC files covering the full range of possible water depths along the length of the model. Sampling with the ADV was initiated manually when the motion control system reached the first sampling location.

The files created by the ADV data acquisition system were read using a program called WinADV produced by the Bureau of Reclamation of the U.S. Department of the Interior. WinADV is shareware available as a 32-bit program for Windows 95/98/NT 4.0/2000/XP systems. The program provides an interface for viewing and analysis of all three velocity components. WinADV was used primarily to convert unfiltered data into a semi-colon delimited format (.vu – velocity unfiltered) that could be easily imported into MS Excel and Matlab.

4.2.2 Matlab Analysis Functions

A suite of Matlab functions was created to process the ADV files and to create isovel plots of the velocity distribution in each cross-section. The following is a brief description of the analysis suite and the individual functions it comprises.

Culvert - This is the main function and calls the sub-functions. Graphical user interfaces (GUIs) are provided to select the desired sampling run distinguished by slope, flow and cross-section number. Options for use of supplemental data, surface velocity profiles, editing options, labelling of contours, and creation of jpeg images can be specified through several GUIs. Batch processing options are also available and all relevant data is output to the Matlab workspace for use in further analysis.

MakeTandP.m - Opens the timing and position files generated for each DMC file and extracts the time stamp for each sampling location. Counts from the X and Y motor are interpreted as polar coordinates and these are transformed into Cartesian coordinates and located within the cross section.

timingAdjust.m – In order to rapidly create all the timing and position files, the DMC files were run with a sampling time of 0 seconds. This subroutine expands the timing and position files to accommodate a 40 seconds sampling time.

getmeans.m - Uses the timing files generated in MakeTandP.m to extract the mean velocities at each sampling point. The timing files are corrected for irregularities caused by the Windows 98 environment and the samples are truncated by 50 data points at the beginning and end, ensuring the probe was stationary during sampling.

suppl.m – Supplemental surface velocity data is inserted into the cross-sections for the S0Q64 and S0Q186 runs. Average velocities and positional data for each sampling point are created from manually recorded timing and position files unique to each sampling set.

makeXsection.m - Creates the cross-section boundary template and inserts the measured velocities at the correct sample locations. The culvert cross-section is discretised into a matrix of 101 by 101 cells. Each cell or pixel is equivalent to 6.14 mm by 6.14 mm, roughly equivalent to the frontal area of the ADV sample volume. For 0% slope runs, supplemental surface velocity data may be selected. For 0.5% and 1.0% runs, horizontal surface velocity profiles may be estimated.

Interpolate.m - Uses internal Matlab functions to perform 2-D interpolation between the measured point velocities within the cross-section.

AdjustBoundary.m – Peripheral velocity values are extrapolated to the boundary using the Karman Power Law.

ContPlot2.m - Plots the velocity distribution as color filled isovels. Labelling options for the isovels include “manual”, “automatic” and “none”. A JPEG image from the plot may be created.

Chapter 5: Analysis of Results

5.1 Analysis Approach

This study places a heavy reliance upon the ability to estimate the velocity at any point within the region of the cross-section where point velocity measurements were taken. To achieve this, the sampling density was highest near the boundaries where the highest velocity gradients were anticipated. A lower sampling density was used in the central region of the flow where velocity is generally more uniform. This economical sampling approach is widely used in open channel flow studies to save time and reduce the computational burden (Katopodis et al., 1978; Mountjoy, 1986; Barber and Down, 1996). However, it was not possible to sample all areas of the cross-section and the velocity in these zones was estimated. Checks were performed that confirmed the validity of this approach, including comparisons of the measured and interpolated velocity data and a continuity check for each cross-section. Extrapolated data is therefore used in a qualitative way to make observations about the velocity structure. It should be noted that parameters such as shear velocity and equivalent sand roughness were calculated using interpolated data from within the sampling region only.

5.1.1 Modelling the Cross-section in Matlab

Matlab was used to create a contoured velocity distribution plot or isovel plot for each cross-section where detailed velocity sampling was undertaken. To achieve this, a template matrix was created consisting of 101 rows and 101 columns to represent the flow area within the culvert cross-section including the gravel bed and culvert walls. Each cell within the matrix represented an area equivalent to

$$A_{cell} = \left(\frac{D_o}{101} \right)^2 = \left(\frac{620mm}{101} \right)^2 = 37.7 \text{ mm}^2,$$

or a linear distance of

$$L_{cell} = \left(\frac{D_o}{101} \right) = \left(\frac{620mm}{101} \right) = 6.14 \text{ mm}.$$

Therefore, a cell was comparable to the frontal area of the ADV sample volume (5 mm by 6 mm). Velocity readings were located within the cross-section by converting positional data to row and column indices. This carried a potential error of up to $\pm L_{cell}/2$ or 3.07 mm. Due to the high degree of uncertainty involved in determining the true zero flow boundary of the gravel bed, this tolerance was deemed acceptable.

5.1.2 *Peripheral Velocities*

In the cross-section template matrix, cells outside the wetted perimeter and above the water surface were designated as “Not-a-Number” (NaN), thereby delimiting the flow area. The measured velocities including any manual surface velocity readings were then located in the cross-section creating a non-uniformly spaced vector. To create isovels, the two-dimensional interpolation function “griddata.m” was used to generate a surface encompassing all the velocity measurements. This surface can be termed the “core flow” and is represented in Figure 5.1. In runs S0Q64 and S0Q186, where surface velocity measurements were made, the core flow extends almost to the water surface. The velocity value associated with each cell within the cross-section is assumed to be the average velocity for the area represented by the cell.

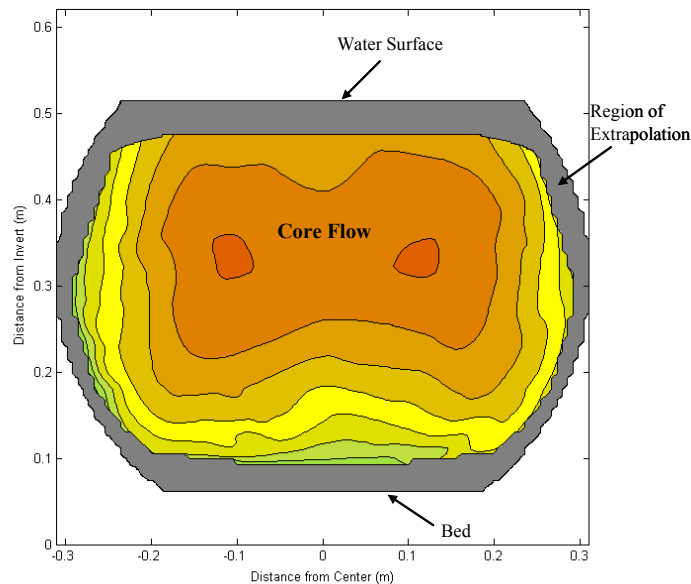


Figure 5.1: Definition of core flow and region of extrapolation.

The unsampled region of the cross-section between the core flow and the boundaries is referred to in Figure 5.1 as the “region of extrapolation”. When sampling near the water surface, flow separation around the ADV shaft caused air to be drawn down to the probe tip, spoiling the sample. The depth at which this separation would occur was a function of water velocity. The thickness of the region of extrapolation between the core flow and the water surface is therefore also a function of water velocity. This phenomenon made surface velocity sampling infeasible for the 0.5% and 1.0% runs, even with the side-looking ADV. The thickness of the region of extrapolation adjacent to the culvert bed and walls was determined primarily by the limits of approach assigned to the automated sampling system. The effective (average) bed depth was estimated to be 6 cm but certain roughness elements may have projected 1-2 cm above this elevation. As the mobility of the gravel bed was uncertain, it was decided to begin sampling at a safe distance from the boundary to avoid damaging the ADV. Therefore, the sampling was initiated an average of 3.3 cm from the bed. Velocity sampling was conducted more closely to the culvert walls.

In the experimental runs where surface velocity measurements were not taken, horizontal velocity profiles developed from the 0% slope runs were used as a proxy. The surface velocities of the S0Q64 and S0Q186 runs were normalized by their respective u_{avg} values. Due to the similarity in velocity structure and flow depth, the normalized surface velocity profile from the S0Q64 run was applied to S5Q145 and S1Q150. Similarly, the normalized surface velocity profile from the S0Q186 run was applied to S5Q221 and S1Q254. Two approaches were evaluated to estimate the velocity profile in the region of extrapolation: (1) extrapolation with the Karman power law, and (2) allowing `griddata.m` to interpolate between the edge of the core flow and a zero flow boundary. In both cases, velocity values in the region of extrapolation were compared to those predicted by the Log Law (equation 2.2).

With approach (1), the outermost velocity values of the “core flow” were extrapolated to the flow boundaries using the Karman power law. This procedure is widely used in performance testing of hydroelectric generating stations and is detailed in the 1975 ISO

Testing Code 3354: “Measurement of clean water flow in closed conduits - Velocity-area method using current-meters.” The zero flow boundary is assumed to be adjacent to the outer cells of the region of extrapolation and is not included on the isovels. The exponent of the power law was customized to provide the “best fit” to the data. Figure 5.2 demonstrates the fit estimated with the power law at cross-section 20 of the S5Q221 run. Profiles are shown for the central plane ($z = 0$ cm) and close to edge of the bed ($z = 18$ cm).

Generally, the extrapolated data fit the Log Law well. However, for some cross-sections, slight irregularities were noticed in the values at the edge of core flow near the center of the bed. These edge anomalies may cause the velocities in the extrapolated region to deviate from the values predicted by the Log Law, as seen in the $z = 0$ cm data series in Figure 5.2. In cross-sections where it was present, this effect was strongest near the central plane ($z = 0$), becoming negligible by $z = \pm 6$ cm. Where the deviation occurred, it always produced velocities lower than those predicted by the Log Law. This error should have produced only small errors in the continuity check as it occurred in a very localised area and in the region of lowest velocity.

The other approach to estimating the peripheral velocities that was evaluated was to allow griddata.m to interpolate between the edge of the core flow and a zero flow boundary. It was found that this method underestimated the velocity in the region of extrapolation by 10-90%. The deviation from the Log Law can be seen in Figure 5.2 for the data series “ $z=0$ cm w Zero Flow Boundary” and “ $z=18$ cm w Zero Flow Boundary”. Therefore, using the Karman power law was selected as the most reasonable means of estimating the velocity distribution in the region of extrapolation.

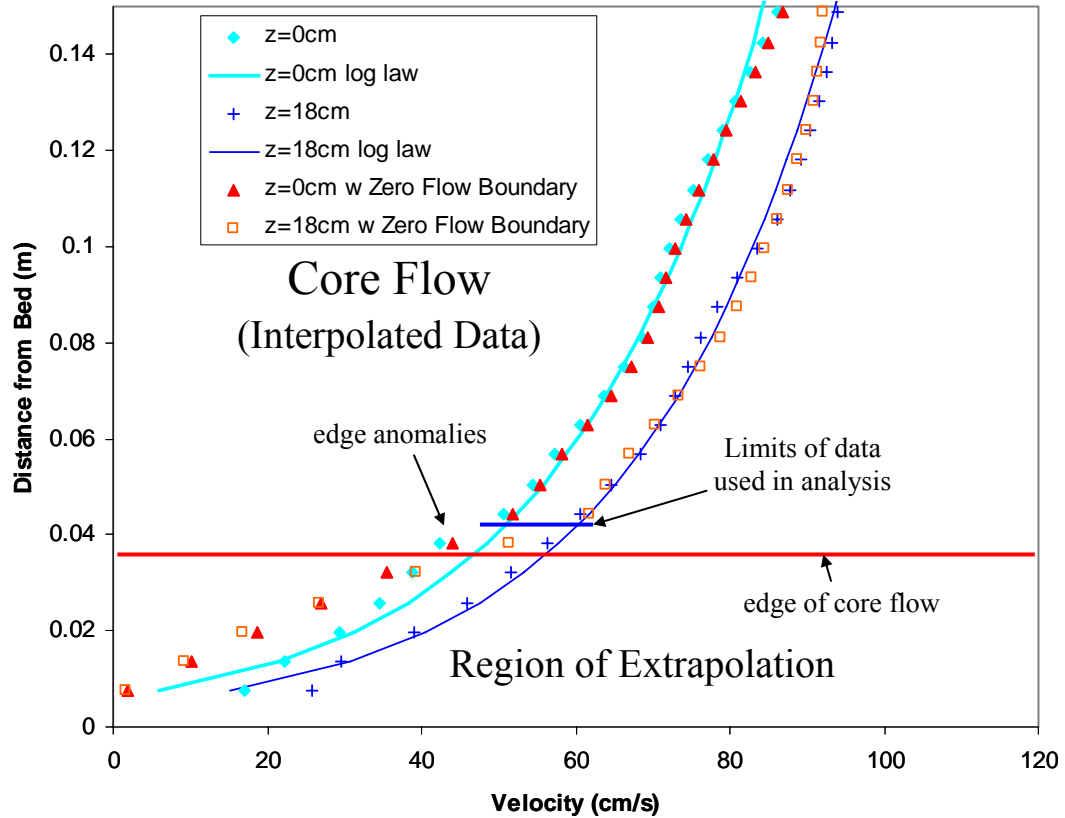


Figure 5.2: Fit of data compared to the Log Law in extrapolated zone for $z = 0$ cm and $z = 18$ cm for XS20 of S5Q221.

5.1.3 Fit of Interpolated Data

Figure 5.3 shows the fit of the interpolated data when overlain on the measured point velocities for the 0 degree and +40 degree sampling radial of experimental run S5Q221 at cross-section 20. The interpolation method used by `griddata.m` is a triangle-based cubic interpolation. The technical documentation provided with Matlab Version 7.0.0 states that the surface created always passes through all the data points. For all experimental runs, good agreement was found between measured and interpolated data along the sampling radials. A high sampling density is relied upon to minimize the distance between sampling radials. The results of the interpolation check suggest that the interpolation method used by the Matlab function `griddata.m` provides an accurate estimate of the velocity at any point in the sampling region.

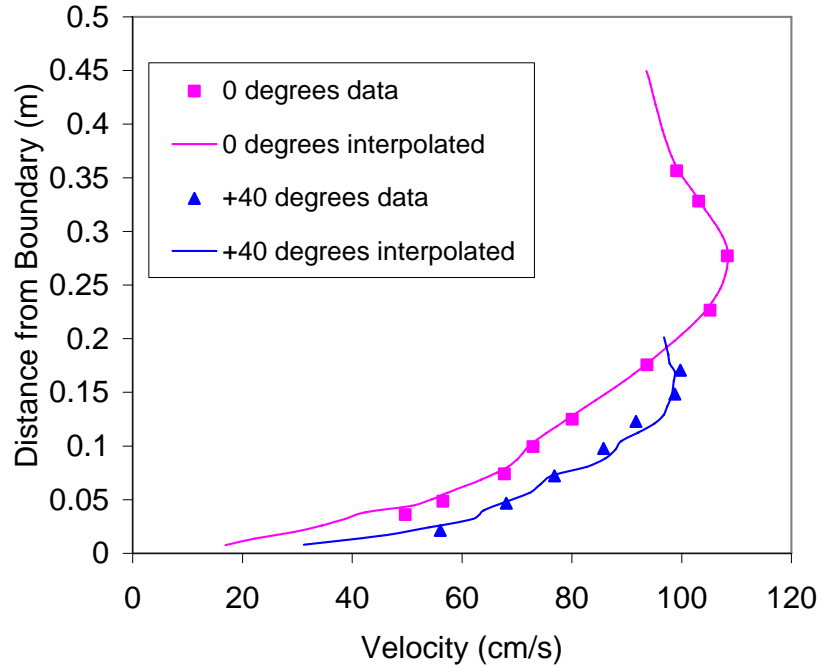


Figure 5.3: Comparison of measured point velocities with interpolated data for S5Q221, XS20 for central profile (0 zero degree) and +40 degree sampling radial.

5.1.4 Vertical Velocity Profiles

The polar coordinate sampling grid used in the automated sampling system design created non-uniformly spaced data points in each cross-section. A two dimensional interpolation of the non-uniformly spaced data was then performed to create a uniformly spaced matrix of point velocity values, thus filling in the flow area of the cross-section. From this interpolated cross-section, 11 vertical velocity profiles were extracted as shown in Figure 5.4. Verticals were extracted at $z = 0$ m, $z = \pm 0.06$ m, $z = \pm 0.12$ m, $z = \pm 0.18$ m, $z = \pm 0.24$ m and $z = \pm 0.27$ m. Ead et al. (2000) used a similar approach, sampling a series of vertical profiles across roughly 88% of the width of a 0.62 m diameter corrugated metal culvert. The velocity profiles from corresponding non-central verticals (for example $z = 0.06$ m and $z = -0.06$ m) were averaged to compensate for transient asymmetry. Generally, though, the velocity distributions were very symmetrical. The averaged velocity profiles were then truncated so that they contained only those values from the sampled region, or core flow.

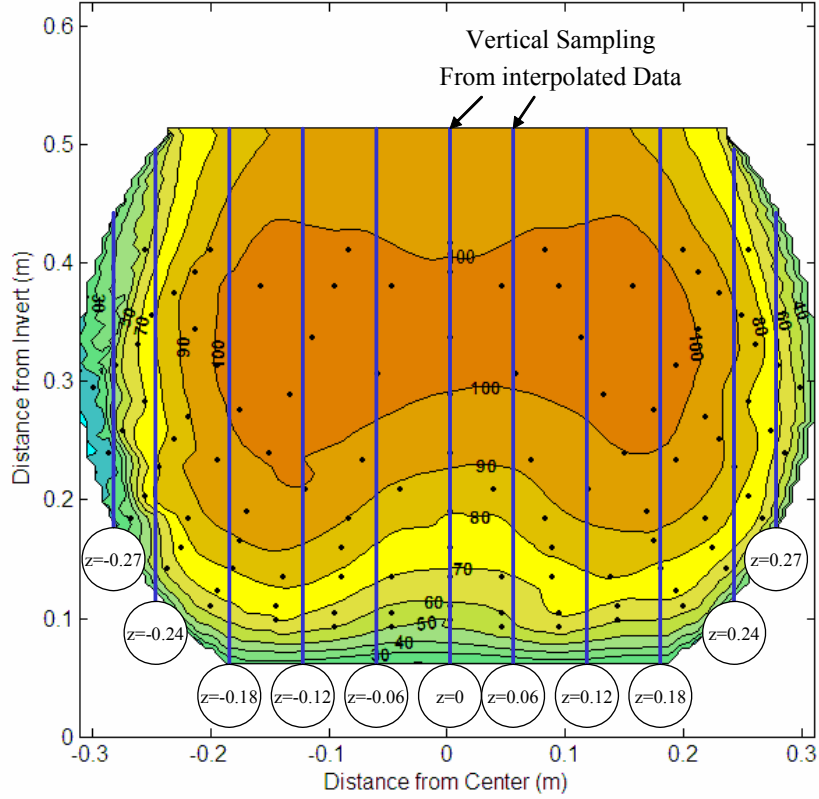


Figure 5.4: Sampling vertical profiles from interpolated data.

5.2 Cross-section Properties of Circular Embedded Culvert

For most of the analysis performed in this study, it was necessary to determine the geometric elements of the cross-section including the area, wetted perimeter, hydraulic radius and top width of the flow area. Figure 5.5 defines the cross-section and illustrates graphically some of the nomenclature used. Based on these definitions, the following cross-section properties may be calculated:

Area:
$$A_{flow} = A_{total} - A_b \quad (5.1)$$

$$A_{total} = \frac{D_o^2}{8} (\varphi - \sin \varphi) \quad (5.2)$$

$$A_b = \frac{D_o^2}{8} (\theta - \sin \theta) \quad (5.3)$$

Wetted Perimeter: $P_{total} = P_w + T_b$ (5.4)

$$P_w = \frac{(\varphi - \theta)D_o}{2} \quad (5.5)$$

$$T_b = \sin\left(\frac{\theta}{2}\right)D_o \quad (5.6)$$

$$P_b = \frac{\theta D_o}{2} \quad (5.7)$$

Top width: $T = \sin\left(\frac{\varphi}{2}\right)D_o$ (5.8)

Hydraulic Radius: $R = \frac{A_{flow}}{P_{flow}}$ (5.9)

Hydraulic Depth: $D = \frac{A_{flow}}{T}$ (5.10)

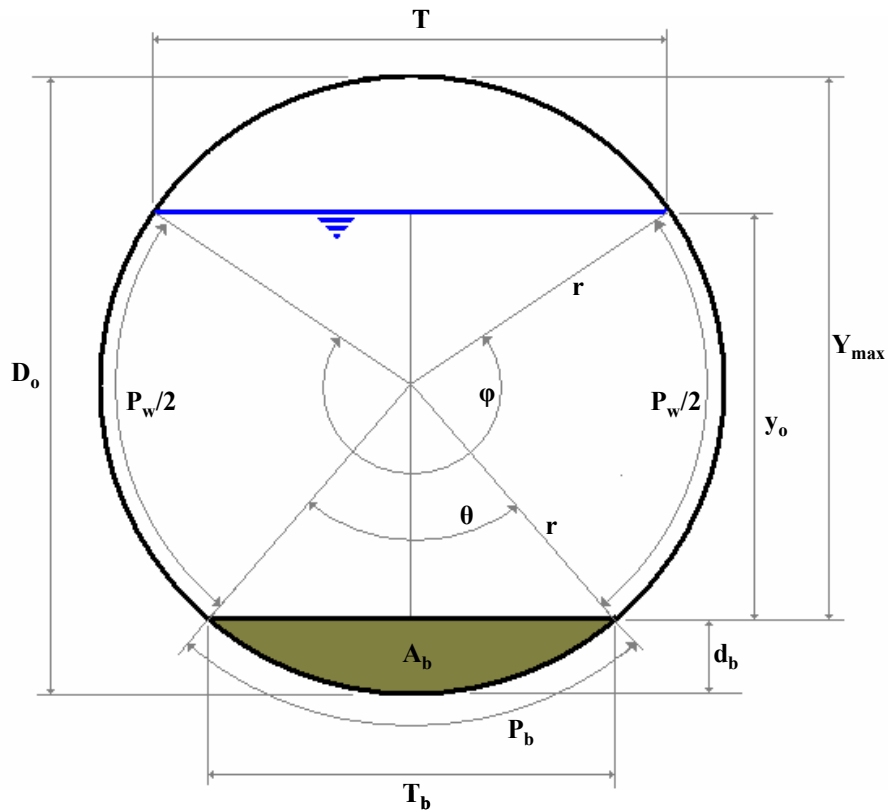


Figure 5.5: Definition of cross-section.

5.3 Results Summary for Experimental Runs

This section provides a brief discussion of the experimental results calculated for each cross-section where detailed velocity measurements were taken. The results for the 0%, 0.5% and 1.0% runs are summarized in Table 5.1 and Table 5.2. For each run, the tailwater gate was adjusted to approximate a uniform flow depth (to simulate backwater conditions normally encountered in Manitoba). This limited the variation in depth along the culvert to a maximum of $\pm 6\%$ of average depth, except in the first two cross-sections, which were strongly affected by the entrance losses. The flow was subcritical along the full length of the culvert for all runs.

The validity of the modeling approach used in Matlab was also tested with a continuity check. For each cross-section, the integrated flow (Q_{int}) was calculated by summing the velocity of each cell multiplied by the area it represents as follows:

$$Q_{int} = \sum_1^N u_i A_{cell} \cdot \quad (5.11)$$

The error was then determined by comparing Q_{int} to the know discharge calculated from the sharp crested weir in the headwater box as follows:

$$\% Error Q_{int} = \frac{(Q_{int} - Q)}{Q} \cdot 100\% . \quad (5.12)$$

As seen in Table 5.1 and Table 5.2, the largest errors occur in cross-sections 1, 2 and 26, where the velocity structure is affected by inlet disturbances and surging in the tailwater box. When all cross-sections are considered, the error ranges from -10.2% to 2.8% with an average of -4.1%. When cross-sections 3, 4, 6, 8, 10, 12, 14, 17, 20 and 23 are considered exclusively, the error ranges from -6.9% to 0% with an average of -3.9%. These results are comparable to the results of other studies that use area-integration as a continuity check. Barber and Downs (1996) conducted a series of velocity profiling experiments on four different size pipes and obtained $\% Error Q_{int}$ values ranging from -10.2% to 22.1% with an average of 1.1%. Sterling and Knight (2000) also conducted detailed velocity measurement in a circular pipe with a flat bed under open channel flow conditions. Their $\% Error Q_{int}$ ranged from $\pm 3.0\%$ with an overall average of 2.5%.

Table 5.1: Experimental results for 0% and 0.5% slope runs

Run	XS	Depth (m)	y/D _o	Area (m ²)	V _{avg} (m/s)	Q _{int} (m ³ /s)	% Error of Q _{int}
S0Q64 S = 0% Q = 0.064 m ³ /s	1	0.310	0.500	0.173	0.370	0.062	-3.1
	2	0.304	0.490	0.169	0.378	0.061	-4.0
	3	0.303	0.489	0.169	0.379	0.060	-6.6
	4	0.305	0.492	0.170	0.377	0.061	-5.4
	6	0.302	0.487	0.168	0.381	0.062	-3.4
	8	0.302	0.487	0.168	0.381	0.061	-4.3
	10	0.300	0.484	0.167	0.384	0.061	-4.9
	12	0.300	0.484	0.167	0.384	0.061	-5.0
	14	0.296	0.477	0.164	0.389	0.060	-6.9
	17	0.295	0.476	0.164	0.391	0.060	-5.7
	20	0.293	0.473	0.163	0.394	0.061	-5.3
	23	0.289	0.466	0.160	0.400	0.060	-6.7
	26	0.289	0.466	0.160	0.400	0.058	-9.4
S0Q186 S = 0% Q = 0.186 m ³ /s	1	0.502	0.810	0.273	0.682	0.174	-6.4
	2	0.492	0.794	0.269	0.692	0.177	-4.7
	3	0.482	0.777	0.265	0.702	0.174	-6.5
	4	0.485	0.782	0.266	0.699	0.178	-4.5
	6	0.481	0.776	0.265	0.703	0.178	-4.5
	8	0.479	0.773	0.264	0.705	0.179	-3.6
	10	0.473	0.763	0.261	0.712	0.179	-3.9
	12	0.470	0.758	0.260	0.716	0.179	-3.7
	14	0.466	0.752	0.258	0.721	0.178	-4.0
	17	0.461	0.744	0.256	0.727	0.179	-3.7
	20	0.455	0.734	0.253	0.735	0.178	-4.4
	23	0.447	0.721	0.249	0.746	0.179	-4.0
	26	0.442	0.713	0.247	0.753	0.178	-4.6
S5Q145 S = 0.5% Q = 0.145 m ³ /s	1	0.310	0.500	0.173	0.838	0.137	-5.2
	2	0.315	0.508	0.176	0.824	0.146	1.0
	3	0.303	0.489	0.169	0.860	0.136	-6.3
	4	0.313	0.505	0.175	0.830	0.142	-2.4
	6	0.308	0.497	0.172	0.844	0.144	-0.9
	8	0.306	0.494	0.171	0.850	0.143	-1.5
	10	0.302	0.487	0.168	0.863	0.139	-4.1
	12	0.301	0.485	0.167	0.866	0.140	-3.7
	14	0.300	0.484	0.167	0.869	0.140	-3.4
	17	0.301	0.485	0.167	0.866	0.141	-2.5
	20	0.299	0.482	0.166	0.872	0.139	-3.9
	23	0.300	0.484	0.167	0.869	0.143	-1.7
	26	0.303	0.489	0.169	0.860	0.139	-4.0
S5Q221 S = 0.5% Q = 0.221 m ³ /s	1	0.469	0.756	0.259	0.852	0.198	-10.2
	2	0.446	0.719	0.249	0.888	0.208	-5.7
	3	0.450	0.726	0.251	0.881	0.207	-6.4
	4	0.448	0.723	0.250	0.885	0.208	-5.9
	6	0.446	0.719	0.249	0.888	0.207	-6.3
	8	0.445	0.718	0.248	0.890	0.207	-6.6
	10	0.443	0.715	0.247	0.893	0.208	-5.7
	12	0.443	0.715	0.247	0.893	0.209	-5.3
	14	0.447	0.721	0.249	0.886	0.211	-4.7
	17	0.449	0.724	0.250	0.883	0.211	-4.8
	20	0.448	0.723	0.250	0.885	0.212	-4.1
	23	0.449	0.724	0.250	0.883	0.211	-4.4
	26	0.449	0.724	0.250	0.883	0.209	-5.2

Table 5.2: Experimental results for 1.0% slope runs

Run	XS	Depth (m)	y/D _o	Area (m ²)	V _{avg} (m/s)	Q _{int} (m ³ /s)	% Error of Q _{int}
S1Q150 S = 1.0% Q = 0.150 m ³ /s	1	0.294	0.474	0.163	0.919	0.154	2.4
	2	0.232	0.374	0.125	1.202	0.139	-7.0
	3	0.252	0.406	0.137	1.093	0.142	-5.6
	4	0.259	0.418	0.142	1.060	0.145	-3.2
	6	0.262	0.423	0.143	1.046	0.150	0.0
	8	0.261	0.421	0.143	1.050	0.148	-1.0
	10	0.259	0.418	0.142	1.060	0.148	-1.5
	12	0.255	0.411	0.139	1.079	0.146	-2.4
	14	0.255	0.411	0.139	1.079	0.147	-2.0
	17	0.260	0.419	0.142	1.055	0.148	-1.1
	20	0.261	0.421	0.143	1.050	0.149	-0.7
	23	0.263	0.424	0.144	1.041	0.149	-0.4
	26	0.271	0.437	0.149	1.007	0.145	-3.7
S1Q254 S = 1.0% Q = 0.254 m ³ /s	1	0.431	0.695	0.241	1.052	0.241	-5.0
	2	0.324	0.523	0.181	1.400	0.230	-9.5
	3	0.384	0.619	0.216	1.174	0.242	-4.8
	4	0.384	0.619	0.216	1.174	0.241	-5.0
	6	0.384	0.619	0.216	1.174	0.244	-4.1
	8	0.387	0.624	0.218	1.165	0.247	-2.9
	10	0.384	0.619	0.216	1.174	0.244	-3.9
	12	0.381	0.615	0.215	1.183	0.246	-3.1
	14	0.380	0.613	0.214	1.186	0.247	-2.7
	17	0.391	0.631	0.220	1.153	0.245	-3.4
	20	0.392	0.632	0.221	1.150	0.249	-2.0
	23	0.393	0.634	0.221	1.147	0.247	-2.6
	26	0.408	0.658	0.230	1.107	0.247	-2.6

5.4 Velocity Structure

The Matlab analysis suite was used to plot isovels for each cross-section where detailed velocity measurements were taken (cross-sections 1, 2, 3, 4, 6, 8, 10, 12, 14, 17, 20, 23 and 26). Using the interpolated velocity data, 11 vertical velocity profiles were extracted at each cross-section as described in section 5.1.4. The complete set of isovel plots and vertical profiles for each run are located in Appendix B and C respectively. For ease of viewing, isovel velocities are given in cm/s with increments of 10 cm/s. Color coding of the isovels is consistent for all plots. The vertical velocity profiles are used primarily for determination of shear velocity and equivalent sand roughness but they also provide a level of detail not resolvable from the isovel plots. This additional information was useful in assessing such details as boundary layer growth and the location of the maximum velocity within the cross-section.

Generally, all plots showed good symmetry even close to the inlet. This suggests that the addition of a rough gravel bed may encourage flow symmetry, considering open channel flow is notoriously asymmetrical, even in circular pipes under carefully controlled laboratory experiments (Chow, 1959; Replogle and Chow, 1966, Barber and Downs, 1996). Knight and Sterling (2000) presented symmetric isovels resulting from a series of experiments using a circular pipe with a flat bed under open channel flow conditions. However, the symmetry of the isovels they present is perfect to the smallest detail, suggesting that velocity measurements were taken from only half of the cross-section and symmetry was assumed.

5.4.1 Entrance Region

The isovels for the first three cross-sections of the 0% slope trials are shown in Figure 5.6 to Figure 5.11. The most striking feature of both the low and high flow condition is the contraction effect and flow separation associated with it. Having exited the flow straightener only 1 m upstream of the inlet, the velocity was nearly uniform through the central portion of the inlet. To pass through the reduced cross-section of the culvert, the flow is forced to accelerate, converting potential energy into kinetic energy in the form of a head loss. The isovels for cross-section 1 reveal that flow first accelerates in the region adjacent to the “dead zone” created by the contraction, forming two nearly symmetrical “velocity pillars”. Due to limitations in the range of motion of the sampling mast within the headwater box, some of the velocity values on the right hand side of cross-section 1 to 3 have been mirrored from the left side. However, this only applies to the high flow cases where the water depth exceeded 0.4 m and the majority of the velocity structure on the right hand side of cross-section 1 to 3 has been measured directly. Only the upper edge of the pillar on the right hand side of cross-sections 1 to 3 is affected and therefore, the overall symmetry and form of the flow structure is genuine. The velocity distribution in the inlet was found to be strikingly similar for all trials, regardless of the slope or discharge.

The extent of the contraction and its effect on the entrance region is consistent with observations of prototype culverts. Behlke et al. (1991) state that the flow area through the contraction will be approximately three-quarters that of the flow area downstream in the barrel for culvert inlets projecting into an inlet pool, which is at least twice as wide as the culvert diameter. As the approach channel was almost exactly twice the width of the culvert, this agrees well with the size of the contraction observed in all trials. In fact, the width of the contraction at cross-section 1 appears to be roughly $0.75D_o$, regardless of water velocity. Determining the exact location and extent of maximum contraction would have required more detailed testing near the inlet.

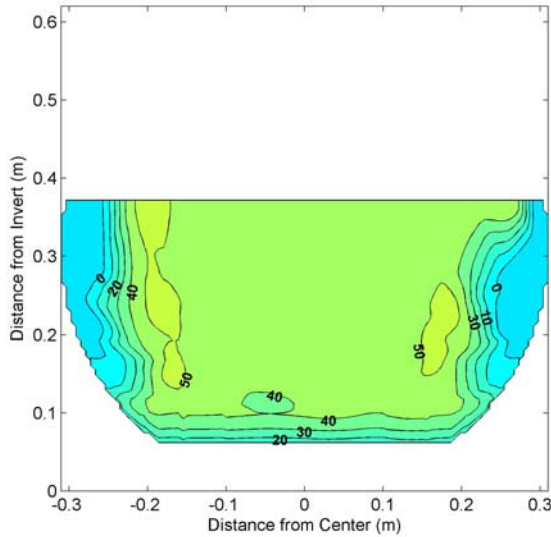


Figure 5.6: Isovel Plot for S0Q64 XS1,
 $y_o=0.310$ m, $A=0.173$ m², $u_{avg}=37.0$ cm/s.

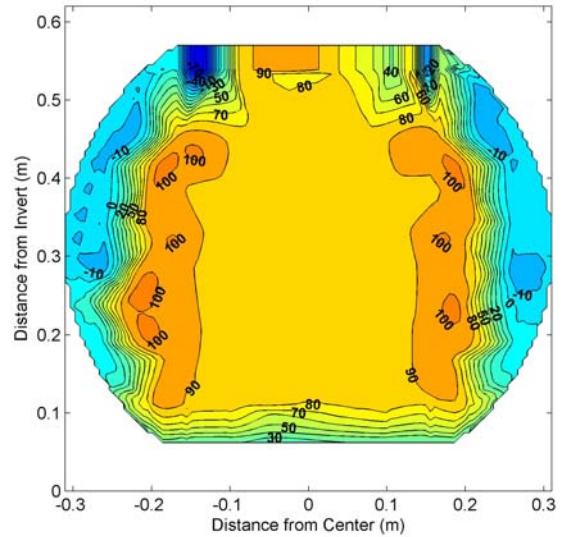


Figure 5.7: Isovel Plot for S0Q186 XS1,
 $y_o=0.502$ m, $A=0.273$ m², $u_{avg}=68.2$ cm/s.

Behlke et al. (1991) also mention that while the contraction itself occurs over a very short distance, the deceleration zone after the contraction can persist for several culvert diameters downstream. In all trials, the effect of the contraction was found to disappear by cross-section 4 or 2.6 diameters downstream from the inlet. Once past the contraction, the velocity gradient becomes more gradual near the bed as the bed roughness affects the developing profile. The central portion of the flow becomes almost triangular in shape as the contraction dissipates toward the water surface. The waviness of the lower 90 cm/s

contour in Figure 5.11 is likely related to the interpolation procedure and is not a true representation of the contour. Similar limitations have been observed in commercially available graphing packages (Knight and Sterling, 2000).

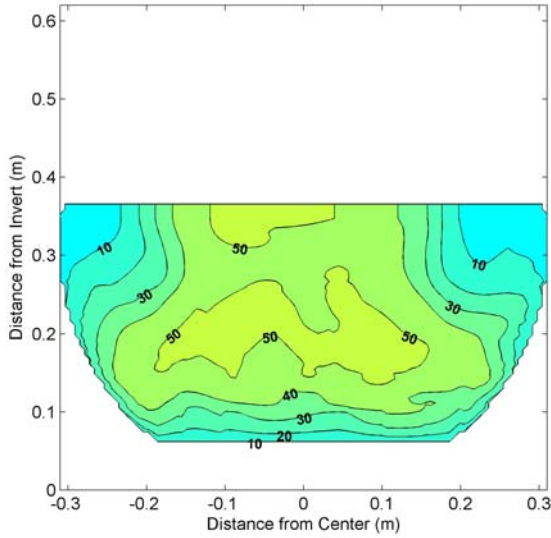


Figure 5.8: Isovel Plot for S0Q64 XS2,
 $y_o=0.304$ m, $A=0.169$ m², $u_{avg}=37.8$ cm/s.

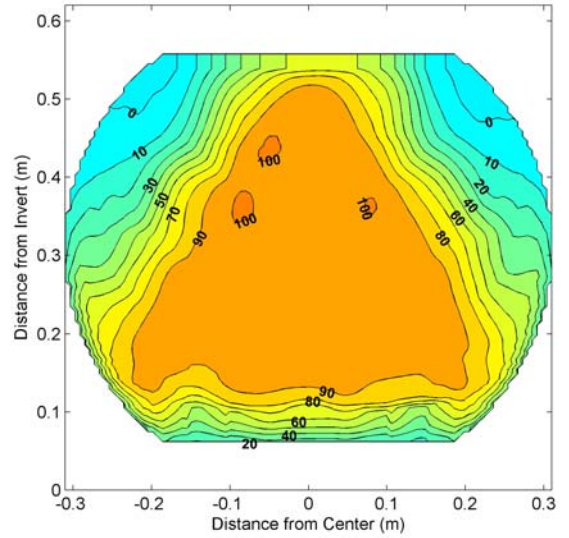


Figure 5.10: Isovel Plot for S0Q186 XS2,
 $y_o=0.492$ m, $A=0.269$ m², $u_{avg}=69.2$ cm/s.

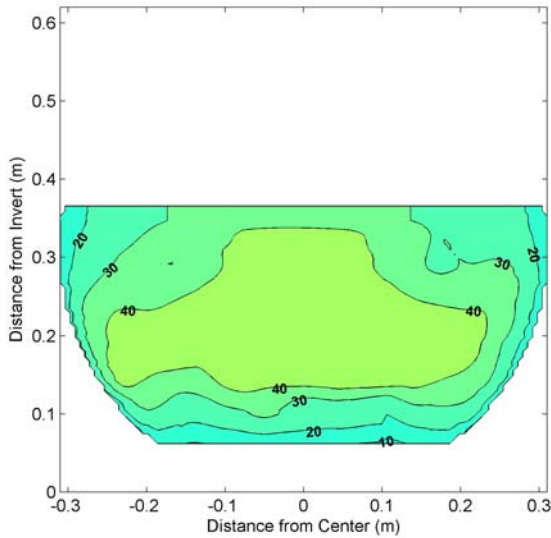


Figure 5.9: Isovel Plot for S0Q64 XS3,
 $y_o=0.303$ m, $A=0.169$ m², $u_{avg}=37.9$ cm/s.

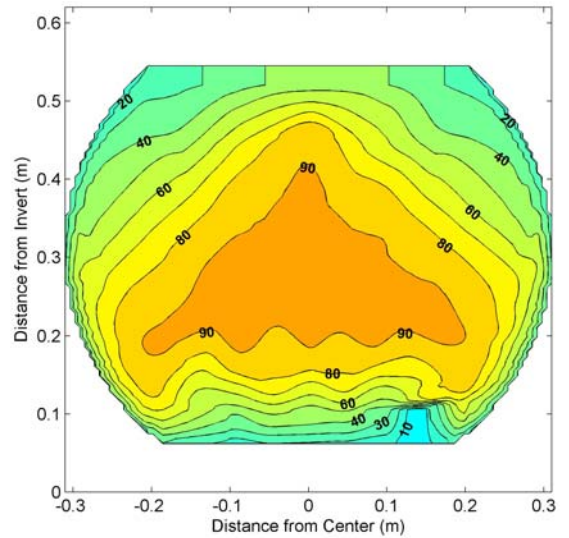


Figure 5.11: Isovel Plot for S0Q186 XS3,
 $y_o=0.482$ m, $A=0.265$ m², $u_{avg}=70.2$ cm/s.

In the eddy of the contraction, mild adverse currents were apparent in all runs except S1Q150. However, supplemental velocity measurements taken during the 0% slope trials have revealed strong adverse currents in cross-section 1 near the water surface of S0Q186 which are up to 70% of u_{max} in magnitude. These localised eddies are associated with the rapidly varied flow caused by the inlet head losses (Figure 5.12). The number of sampling points near the water surface is insufficient to fully describe the structure of these localized eddies but does clearly demonstrate their presence and the chaotic nature of the flow structure in a projecting inlet under high flow conditions. In all the isovel plots, the water surface is represented as level. This was generally reasonable except in the first cross-section as shown in Figure 5.12.

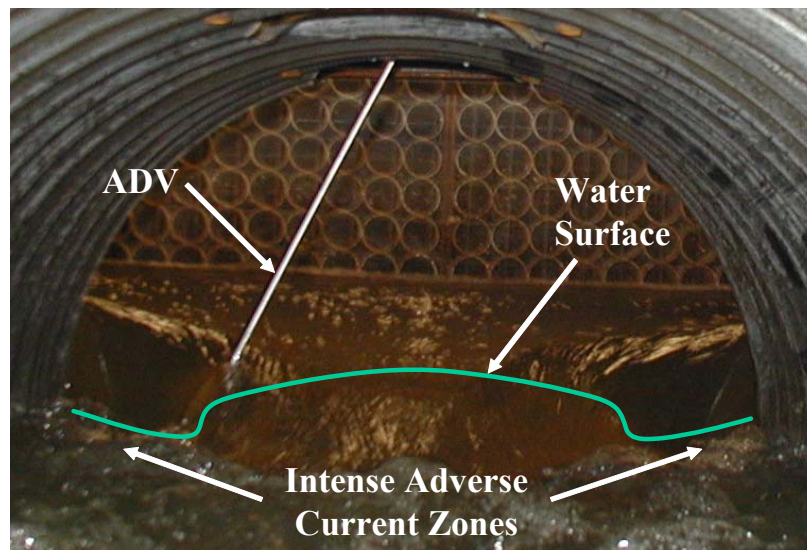


Figure 5.12: View upstream from cross-section 4. Significant entrance losses were observed causing a mounding effect in the water surface profile across the inlet.

5.4.2 Culvert Barrel

For all runs, the general shape of the isovels seems to have stabilised by cross-section 6 (4.4 diameters downstream), shifting slightly along the length of the culvert. Generally, the velocity gradient normal to the bed is less than the velocity gradient normal to the culvert walls. However, the degree by which they differ varies from run to run. From observations of the isovels, there seems to be three factors that strongly affect the overall

shape of the velocity distribution. These factors are water depth, velocity, and distance downstream.

5.4.2.1 *Effect of Depth on Isovel Shape*

In the low flow cases, where water depth ranged from $0.42y/D_o$ to $0.49 y/D_o$, the isovels are roughly parallel to the cross-section boundaries, forming a nearly convex shape as in Figure 5.13. The maximum velocity generally occurs in the central plane of the cross-section within a depth of $0.5y/y_o$ to $0.6 y/y_o$, where y_o is the average depth of the culvert. For all three low flow runs, the velocity gradient normal to the culvert walls is higher than for the bed, as is expected with the smoother wall surface (Chow, 1959).

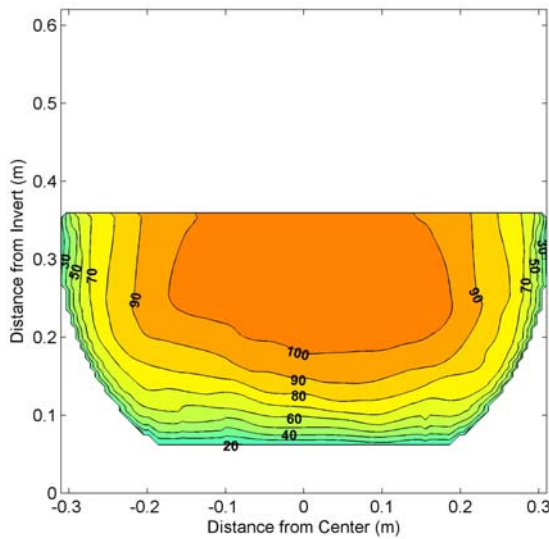


Figure 5.13: Isovel Plot for S5Q145 XS20, $y_o=0.299$ m, $A=0.166$ m², $u_{avg}=87.2$ cm/s.

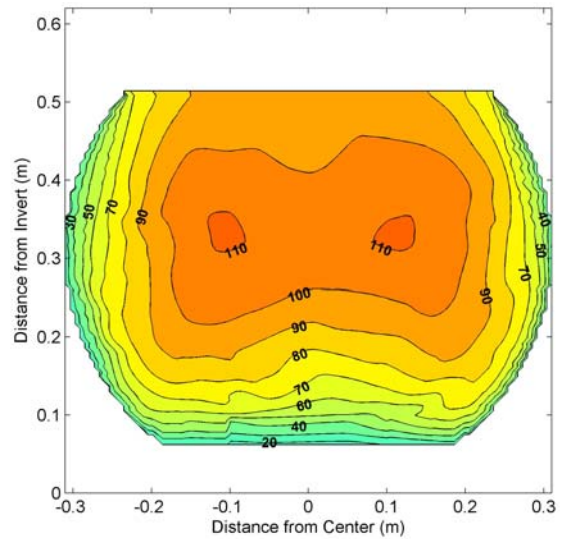


Figure 5.14: Isovel Plot for S5Q221 XS20, $y_o=0.448$ m, $A=0.250$ m², $u_{avg}=88.5$ cm/s.

In the high flow cases, where water depth ranged from $0.62y/D_o$ to $0.76 y/D_o$, the difference in the bed and wall velocity gradient is greatly increased. The isovels veer away from the bed sharply, forming a distinct zone of lower velocity water affected by the bed. This bed-affected region protrudes into the central flow of the culvert, imparting a relatively symmetrical dual-lobed shape upon the isovels as can be clearly seen in Figure 5.14. For all three high flow cases, the u_{max} occurred within a depth of $0.6y/y_o$ to $0.7 y/y_o$. Initially, the u_{max} of S1 Q254 occurred at the central plane, but by cross-section

8 (6 diameters downstream) u_{max} was nearly uniform across a width of $-0.12 \text{ m} < z < +0.12 \text{ m}$ from the central plane. For the S0Q186 and S5Q221 runs, u_{max} occurred in the central plane only in cross-section 4, after which the localized maximum velocity occurred simultaneously at $z = \pm 0.12 \text{ m}$. For S0Q186, this condition persisted until cross-section 17, or for a distance of 14 diameters downstream. For S5Q221, the dual u_{max} persisted along the full length of the culvert. In both S0Q186 and S5Q221, the velocity profile along the culvert continued to shift toward a more concentric structure as seen in S1Q254

5.4.2.2 Effect of Velocity on Isovel Shape

As the average velocity of the flow increases, the extent of bed affected region diminishes and the maximum velocity becomes more localized in the center plane. The isovels are parallel to the culvert boundaries in the S0Q64 run along nearly the full length of the culvert, showing a slight dip toward the bed by cross-section 26. This trend occurs sooner and to a greater degree as the average velocity in the low flow cases is increased. In Figure 5.15 the isovels for S1Q150 can be seen to dip towards the bed, creating a high velocity gradient centered over the bed and diminishing towards the sides. The most extensive zones of low velocity water are near the corner where the bed and wall meet.

This effect has been observed in other studies of circular pipes flowing partly full with a flat bed (Knight and Sterling, 2000). They investigated a wide range of flow and simulated embedment depths. In runs where there was significant embedment and the cross-section became roughly rectangular; Knight and Sterling observed compression of the isovels in the region of the corners. They attributed this to secondary currents, as described in Schlichting (1979). In their experiments the bed and sidewall of the test pipe had uniform roughness. As the isovels in S1Q150 took on a similar shape to those described by Knight and Sterling's experiments, this may suggest that as the velocity in an embedded culvert increases, the relative effect of the bed roughness on the shape of the isovels decreases, while the effect of secondary currents increases.

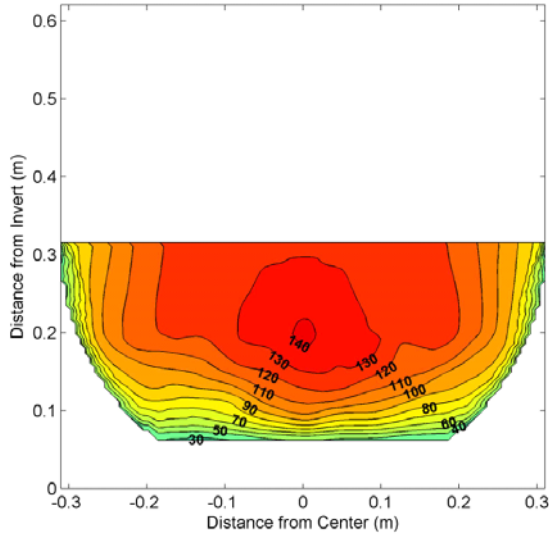


Figure 5.15: Isovel Plot for S1Q150 XS12, $y_o=0.255$ m, $A=0.139$ m², $u_{avg}=107.9$ cm/s.

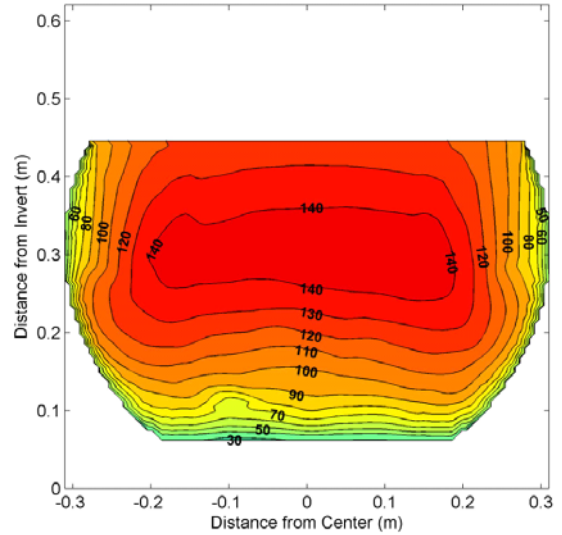


Figure 5.16: Isovel Plot for S5Q254 XS12, $y_o=0.381$ m, $A=0.215$ m², $u_{avg}=118.3$ cm/s.

The isovels for cross-section 12 of S1Q254 are shown in Figure 5.16. In the high flow cases, the bed affected region becomes less distinct as the average velocity increases. This effect is even more pronounced than in the low flow cases. Also, the isovels in Figure 5.16 are nearly parallel to the culvert boundaries without the distinctive dual-lobed shape seen in S0Q186 and S5Q221. Consequently, as the velocity increases, the region of highest velocity becomes more localized toward the central plane and more concave in shape. In S1Q254, the flow depth is roughly 17% shallower than the other high flow cases. This shallower depth may have contributed somewhat to the change in isovel shape, but the velocity effect is suspected to be of primary importance.

5.4.3 Area-Velocity Comparison

The complexity of open channel flow in embedded culverts and the limitations of existing methods of predicting two-dimensional velocity distribution have lead to the development of regression-based methods to predict the percentage of flow area below a given velocity (White, 1996; and House et al., 2005). However, in these studies the width to depth ratio of the flow area approached a wide open channel and the roughness

of culvert walls had little influence on the velocity structure. Barber and Downs (1996) developed another regression-based velocity-area prediction method for a range of pipe sizes with a large range of relative flow depths from $0.17D_o$ to $0.79D_o$, but none of the pipes tested were embedded as required by current fish passage criteria. It then becomes worth while to investigate if a regression-based area-velocity method might be applicable to embedded circular CSP culverts.

The consistency of isovel shape along the barrel of the culvert for each run and within the high and low flow cases suggests that this may be possible. Therefore, an investigation was performed to see how the normalized velocity distributions compared across all experiments when related to percent flow area. For each cross-section, the measured velocity values were normalized by dividing by the average velocity and the complete flow area filled in as before using the Matlab function, `griddata.m`. The isovel plot of XS12 for S0Q186 resulting of this procedure is shown in Figure 5.17. The normalized velocity range was divided into increments of $0.1u/u_{max}$ and the number of cells for each category was divided by the total number of cells representing the flow area.

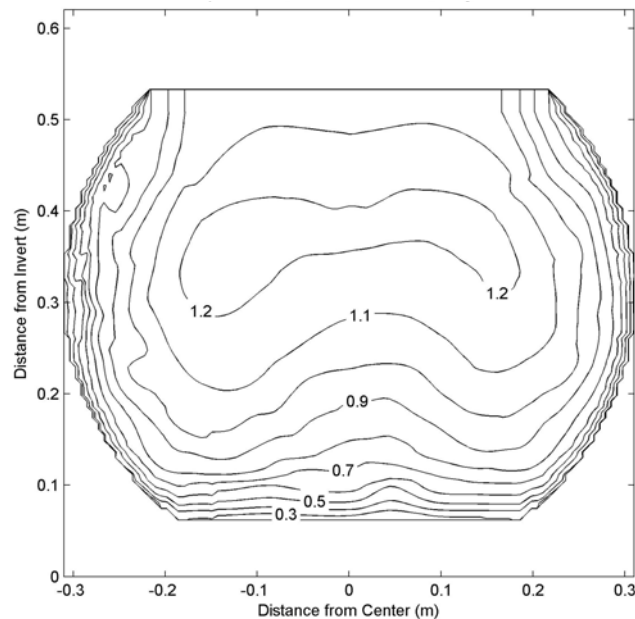


Figure 5.17: Velocity-normalized isovel plot of XS12 for S0Q186 ($u_{avg} = 71.6$ cm/s).

The resulting percentage flow areas (average of cross-section 6 to 26) for each velocity category are tabulated in Table 5.3. All relative velocities fall in the range $0.10 < u/u_{avg} < 1.40$ and despite large differences in relative depth, are fairly uniform across all experiments. For u/u_{avg} less than 0.9, the percent area varies by 5.0% or less. The average percent area at or below average velocity ($u/u_{avg} = 1.0$) is $46\% \pm 3.2\%$ across all runs. As the slope increases and higher velocities are attained, the difference between the average and maximum velocity approaches 15% between the experimental runs.

Table 5.3: Summary of area-velocity results for experimental runs.

u/u_{avg}	Percent of Flow Area Less Than u/u_{avg} for Average of XS6-26					
	S0Q64	S0Q186	S5Q145	S5Q221	S1Q150	S1Q254
0.10	0.0%	0.0%	0.0%	0.0%	0.0%	0.0%
0.20	0.1%	0.2%	0.1%	0.3%	0.1%	0.1%
0.30	1.9%	1.7%	1.7%	1.7%	1.5%	1.6%
0.40	5.3%	4.7%	4.9%	4.8%	4.8%	4.4%
0.50	9.0%	7.4%	8.0%	7.7%	8.0%	7.4%
0.60	13.9%	10.9%	11.9%	11.5%	12.1%	11.1%
0.70	20.0%	15.5%	16.7%	16.2%	16.8%	15.7%
0.80	27.6%	22.8%	23.4%	23.0%	23.2%	22.6%
0.90	37.0%	33.2%	33.2%	32.8%	32.7%	33.0%
1.00	49.8%	46.4%	45.3%	46.0%	43.5%	45.5%
1.10	69.0%	66.4%	60.2%	71.7%	56.5%	64.7%
1.20	96.1%	89.6%	97.2%	95.0%	83.6%	86.2%
1.30	100.0%	100.0%	100.0%	100.0%	99.8%	100.0%
1.40	100.0%	100.0%	100.0%	100.0%	100.0%	100.0%
1.50	100.0%	100.0%	100.0%	100.0%	100.0%	100.0%

To examine the effect of the variation between cross-sections, the individual results for all runs were aggregated and plotted in Figure 5.18. The trend is seen to diverge somewhat at relative velocities above 1.0. Again, this is related to the distortion of the velocity profile that occurs at higher velocities. A portion of the scatter also comes from variation within individual runs. Through the inlet region of the culvert, the proportion of area containing very low and high velocities decreases rapidly as the contraction effect fades and the velocity structure typical of the barrel develops. For this reason, only cross-section 6 to 26 were included in this analysis. Despite the wide variation in flow depth and velocity represented in Figure 5.18, the strong trend in the data suggests that a regression-based method of predicting percent flow area at a given velocity may be feasible, but is outside the scope of the current study.

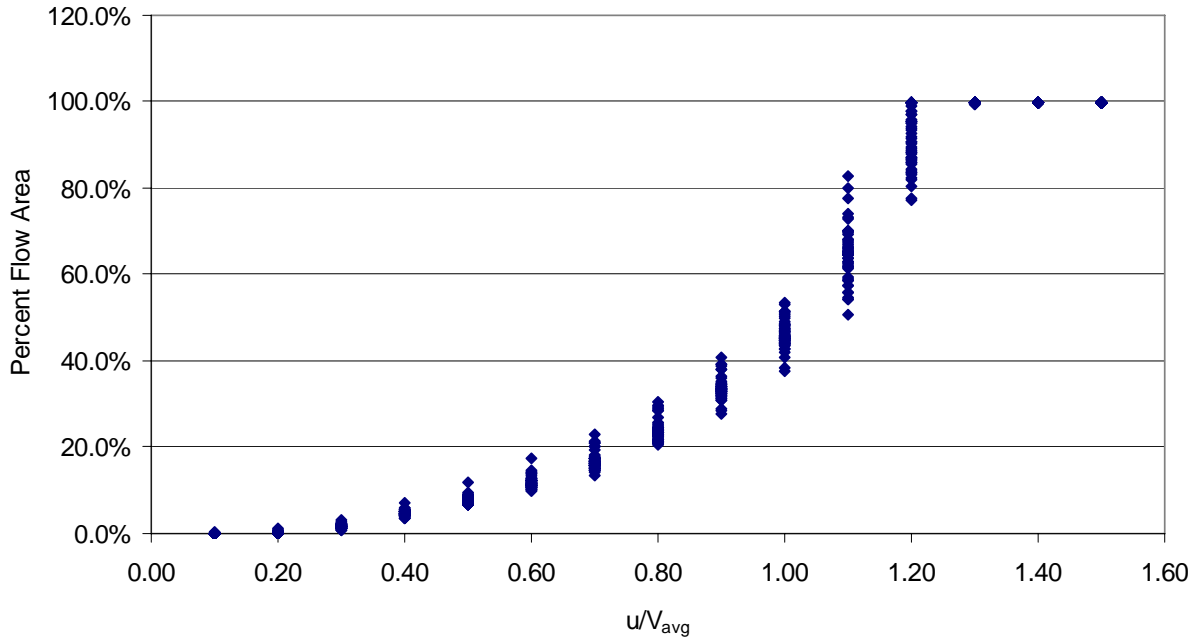


Figure 5.18: Aggregated percent area less than u/u_{avg} for all runs for XS6-26.

5.4.4 Boundary Layer Development

The water flowing into the culvert from the headwater box had a nearly uniform velocity distribution, as seen in the isovel plots and vertical velocity profiles for cross-section 1 of each run (Appendix B and C). Upon encountering the culvert walls and bed, the shearing forces acting on the water immediately start to alter the velocity profile. The shape of the velocity profile is usually well described by the Log Law (equation 2.21) within a region termed the turbulent boundary layer. In theory, this layer will continue to grow in thickness until it reaches the water surface. At this point the velocity profile should become stable and the flow is considered to be full developed (Chow, 1959).

Due to the difficulty in determining the exact thickness of the boundary layer, an arbitrary criteria $0.99u_{max}$ is commonly used. Unfortunately, this approach is seldom applicable in culverts where the location of u_{max} is often depressed below the water surface. Under these conditions, the velocity profile appears to develop from two directions at once; from the culvert bed upward and from the water surface downward.

However, the criterion of $0.99u_{max}$ can still be used to estimate the distance downstream where the velocity profile becomes stable and therefore the flow is fully developed.

Thus, the growth of the boundary layer was examined for all runs and the position of $0.99u_{max}$ is plotted in Figure 5.19 for the centerline velocities and at the edge of the gravel bed ($z = 0.18$ m). Both locations were considered due to the dual-lobed nature of many of the isovels, caused by the low velocities in the bed-affected region. Only velocity data from within the sampled region of the each cross-section was used. In the low flow cases, the depth of $0.99u_{max}$ becomes roughly constant by cross-section 6 or 4.4 diameters downstream from the inlet. It should be noted that the exact location of the maximum velocity is uncertain for cross-sections 6 to 20 in S1Q150 because separation around the ADV probe made sampling ineffective above $0.6y/D_o$. In the high flow cases, the location of $0.99u_{max}$ becomes roughly constant by cross-section 8 or 6.1 diameters downstream. In some runs, the velocity profile at $z = 18$ cm appears to take slightly longer to develop, most notably, in the 5% slope runs.

Ead et al. (2000) tested an identical circular CSP culvert without a gravel bed and found that for a run with slope equal to 0.55% and a flow of $0.160 \text{ m}^3/\text{s}$, the flow became fully developed within 1.6 diameters downstream of the inlet. The flow depth in their culvert was similar to the low flow cases tested here and boundary layer development was based on centerline velocity profiles only. However, these results are not directly comparable. The centerline velocity profiles measured by Ead et al. (2000) appeared to be logarithmic in nature even at the inlet of the culvert, while those measured here exhibited a nearly uniform velocity distribution, having passed through the flow straightener 1.0 m upstream from the inlet. For this reason, these results may be more representative of the boundary layer development that would occur when water enters a culvert with uniform velocity, as from a deep inlet pool. Also, it is likely that the projecting inlet configuration used in this experiment affects how the flow develops, as the effect of the contraction is dissipated downstream. However, these results do not definitively suggest that the inlet configuration delays flow development.

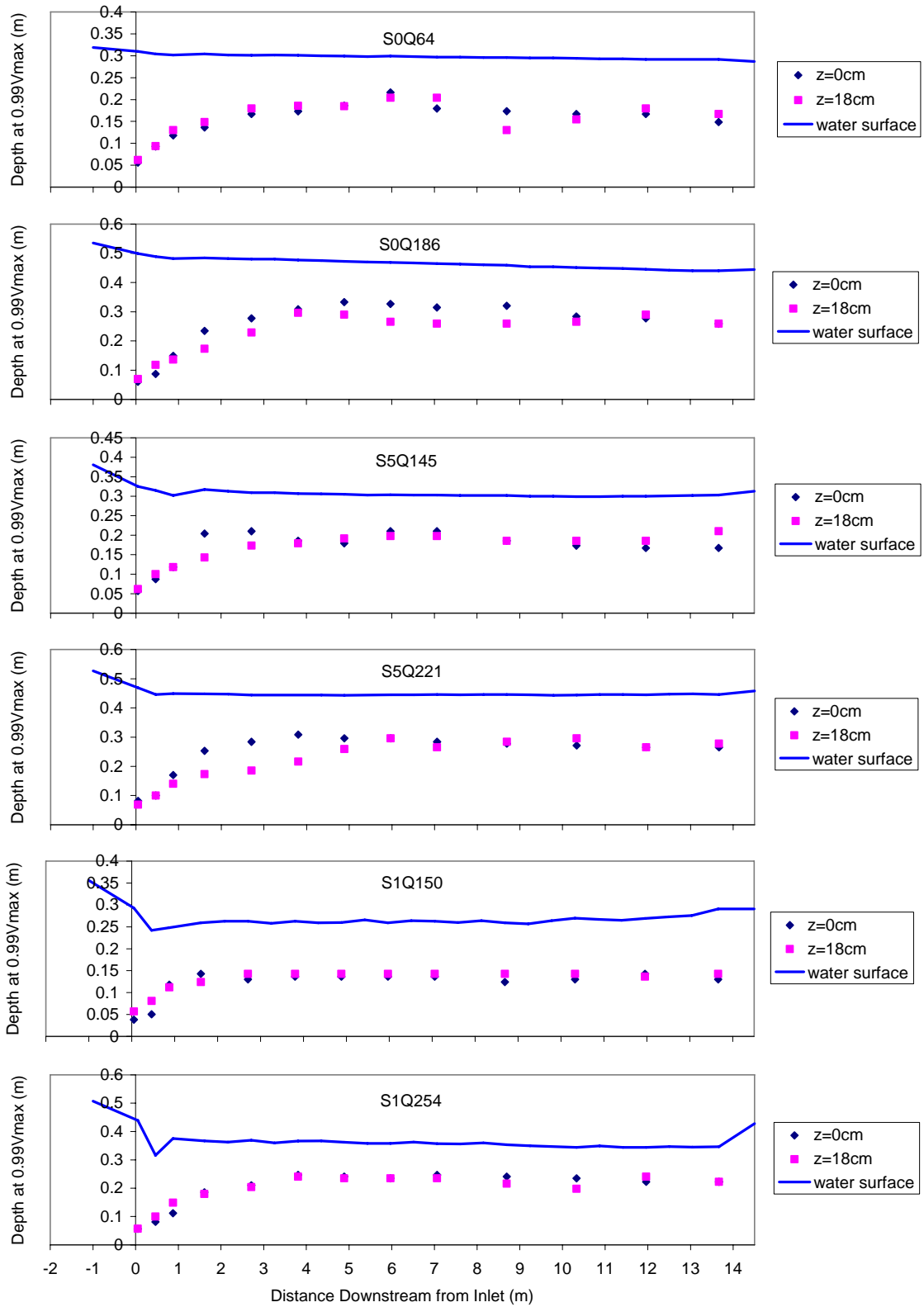


Figure 5.19: Water surface profiles and the estimation of boundary layer development using the criterion of $0.99u_{max}$.

5.4.5 Isolation of Bed Roughness Effect

In an effort to qualitatively determine the effect of the gravel bed on the velocity distribution, a method was devised to remove the corrugation roughness in the first 3.0 m of the culvert (up to and including cross-section 6). Flexible plastic sheets were inserted and affixed to the inner circumference of the culvert and their edges were recessed below the gravel bed. The Manning's roughness for the inserts ($n_{inserts}$) was assumed to be similar to acrylic pipe ($n = 0.012$). The roughness of the culvert is known to be equal to 0.023 and based on the scaling ratio for similitude of roughness as follows:

$$\frac{n_{inserts}}{n_{CSP}} = \lambda^{1/6}. \quad (5.13)$$

This equates to a change in the scaling ratio of $\lambda = 1/50$, effectively removing the roughness of the corrugations. The 4 mm thick inserts reduced the inside diameter of the culvert to 0.60 m and reduced the flow area by 5.7%.

The culvert was then tested at 0.145 m³/s and 0.221 m³/s with the headwater elevation set as close as possible to the conditions in the S5Q145 and S5Q221 experimental runs. The results from the smooth wall trials are compared to the corresponding 0.5% slope runs in Table 5.4 and detailed experimental results are listed in Table 5.5. At a flow of 0.145 m³/s, the smooth-walled inserts caused the average depth from cross-section 6 to 26 to decrease by 2.2% while the velocity and Froude number increased by 5.4% and 2.5% respectively. At a flow of 0.221 m³/s, the depth decreased by 3.1% while the velocity and Froude number increased by 6.5% and 9.3%, respectively.

Table 5.4: Parameter summary for smooth wall runs - results are averaged for XS 2, 4 and 6 and are compared to regular 0.5% slope runs.

Slope	Flow (m ³ /s)	Run	Average Depth (m)	u_{avg} (m/s)	Average Froude #
0.5%	0.145	S5Q145	0.312	0.833	0.514
		S5Q145s	0.305	0.878	0.527
	0.221	S5Q221	0.447	0.887	0.387
		S5Q221s	0.433	0.945	0.423

Table 5.5: Individual experimental results for smooth-walled trials at 0.5% slope.

Run	XS	Depth (m)	y/D _o	Area (m ²)	V _{avg} (m/s)	Q _{int} (m ³ /s)	% Error of Q _{int}
S5Q145s S = 0.5% Q = 0.145 m ³ /s	2	0.297	0.495	0.161	0.903	0.129	-11.2
	4	0.312	0.520	0.169	0.856	0.143	-1.1
	6	0.306	0.510	0.166	0.874	0.144	-0.6
S5Q221s S = 0.5% Q = 0.221 m ³ /s	2	0.426	0.710	0.231	0.959	0.211	-4.5
	4	0.437	0.728	0.236	0.938	0.207	-6.2
	6	0.437	0.728	0.236	0.938	0.208	-6.1

The flow conditions in the regular and smooth wall runs were considered similar enough for qualitative comparison of the velocity structure and detailed velocity measurements were taken at cross-section 2, 4, and 6. The % Error Q_{int} for the two smooth-walled runs was found to be comparable to the other runs at an average of -4.3% for S5Q145s and -5.6% for S5Q221s. The isovels for cross-section 6 of S5Q145s and S5Q221s are illustrated in Figure 5.20 and Figure 5.21. A complete set of isovel plots for the smooth-walled trials is provided at the end of Appendix B.

There are a number of similarities and differences between the results of the regular runs and the smooth-walled trials. The shape of the isovel plot for cross-section 2 is very similar for the regular and smooth-walled trials for both the high and low flow cases, suggesting that the velocity distribution is still dominated by the contraction effect. By cross-section 4, the high velocity flow has approached near to the now smooth culvert walls and a distinct low velocity zone centered over the bed has created the familiar dual-lobed shape in both S5Q145s and S5Q221s, effectively creating two localized areas of maximum velocity centered above the edges of the gravel bed. The reduced roughness in the smooth-walled trials provoked a significantly greater change in the shallower S5Q145s run relative to S5Q221s. This result suggests that the roughness of the bed relative to the walls is as important as water depth or velocity with respect to isovel shape and therefore velocity distribution. By manipulating the roughness of the bed relative to the culvert walls, it may eventually be possible to significantly customise the shape of the velocity distribution to the behavioural preferences of the fish species using the culvert as a fishway.

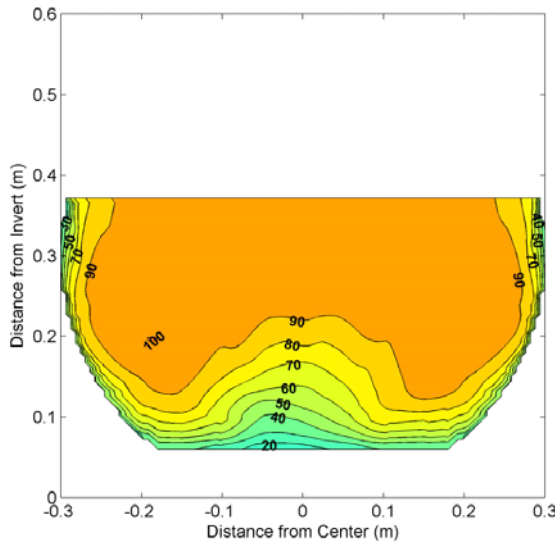


Figure 5.20: Isovel Plot for S5Q145s XS6, $y_o=0.306$ m, $A=0.166$ m², $V_{avg}=87.4$ cm/s.

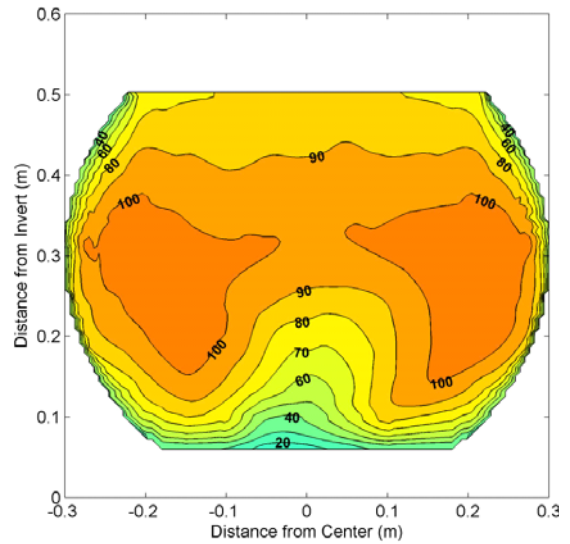


Figure 5.21: Isovel Plot for S5Q221s XS6, $y_o=0.437$ m, $A=0.236$ m², $V_{avg}=93.8$ cm/s.

5.4.6 Secondary Currents

Secondary currents are often touted as the primary cause of perturbations in the velocity structure of open channel flows (Chow, 1959; Schlichting, 1979; Barber and Downs, 1996; Ead et al., 2000). However, virtually no research has been conducted to investigate secondary currents in culverts installed in the field or even on large scale models of culverts. Observations of secondary currents has traditionally been associated with sophisticated micro-scale investigations using laser Doppler and particle image velocimetry in carefully controlled laboratory settings. However, with the advancement of ADV technology, direct measurement of turbulence characteristics such as turbulence intensity and Reynolds stress has become feasible in a wide range of settings (Voulgaris and Trowbridge, 1998). Although point measurements with an ADV cannot capture a complete snapshot of micro-scale turbulence the way laser velocimetry can, it may still be possible to infer patterns in secondary currents on a scale that is more relevant to fish passage. More specifically, fish are most strongly affected by turbulence on a scale that approaches their body size (Mufeed et al., 2002). It should be possible to assess these

larger, more coherent secondary flows using three dimensional velocity measurements recorded with an ADV.

To test this idea, the Matlab analysis suite was used to develop interpolated flow matrices for the v and w velocity components (horizontal and vertical respectively). This was done for selected cross-sections of the S0Q64 and S0Q186 runs using the function `griddata.m`. Only these runs were chosen because they were most thoroughly sampled. The Matlab function `quiver.m` was then applied to the resulting arrays of v and w velocity components. This function displays the resultant vector of the v and w components as an arrow in the corresponding position within the interpolated flow matrix. The length of the arrows represents the relative magnitude of the resultant velocity vector and `quiver.m` automatically scales them to fit within the grid. Arrow length can then be adjusted with a scaling factor to enable easier viewing and is not relatable between different plots.

Due to the large size of the cross-section template matrix (101 by 101 cells), the arrows were too small to be easily viewed and increasing the scale factor only caused them to interfere with each other making the plot unintelligible. Therefore, a 3 by 3 averaging filter was passed over each of the interpolated flow matrices for the u and v components reducing the matrix sizes to 33 by 33 cells. The `quiver.m` function was then applied and the resulting plots examined. Some of the plots appeared to relate very clearly to the isovel structure of the corresponding streamwise velocity component, while others had a less coherent pattern. Most of the quiver plots were highly symmetrical about the center plane of the cross-section and the right side of two of them are shown in Figure 5.23 and Figure 5.24, overlain on their corresponding isovel plots.

Schlichting (1979) explains that secondary currents exist in pipes under both full flow and open channel flow conditions. He states that these flows often occur along the bisector of the angle between the sides and carry momentum to the corners, thereby resulting in comparatively high velocities in the corners. A hypothetical flow pattern based on observations by Schlichting (1979) is presented in Figure 5.22. An analogous pattern can be seen in the quiver plot of cross-section 20 for S0Q186 (Figure 5.23).

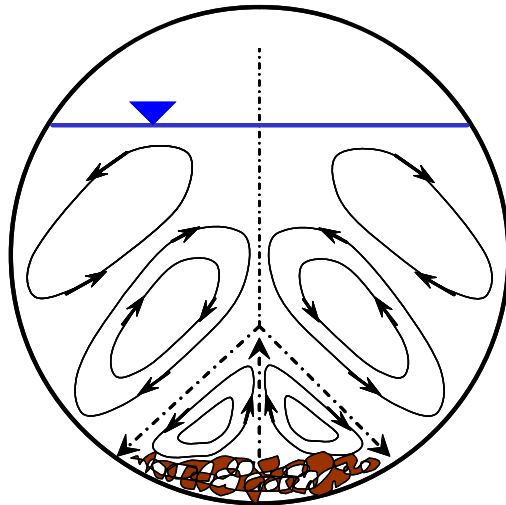


Figure 5.22: Hypothetical secondary currents in a circular embedded CSP culvert.

The strongest arrows are seen to originate from the bed region (lowest velocity), flowing upwards towards the center and curving into the corners. This pattern is mirrored almost exactly in form along a line roughly parallel to the isovel contours forming the bed affected region. These arrows are seen to originate near the upper culvert walls, becoming concentrated towards the center and corners. These results are a strong indicator that secondary currents are responsible for the high velocity region near the center of the culvert and the comparatively high velocities in the corners near the bed. The overall pattern matches well with the isovels, but it is difficult to discern closed circulation cells as expected. It is likely that detailed sampling nearer to the culvert boundaries would reveal a more complete picture of the flow structure.

The quiver plot in Figure 5.24 may offer some explanation as to why the bed affected region is not nearly as distinct in the low flow cases where the relative depth approaches $0.5D_o$. Rather than flowing away from the bed, the arrows flow from the central region and walls of the culvert towards the bed. The shift in secondary flows from the S0Q186 to the S0Q64 quiver plots may be responsible for higher relative velocities near the bed. Despite their limitations, the insight offered by this data may serve to encourage the use of ADVs in other more detailed studies of secondary currents and will provide an initial assessment of the three dimensional nature of flows within embedded culverts.

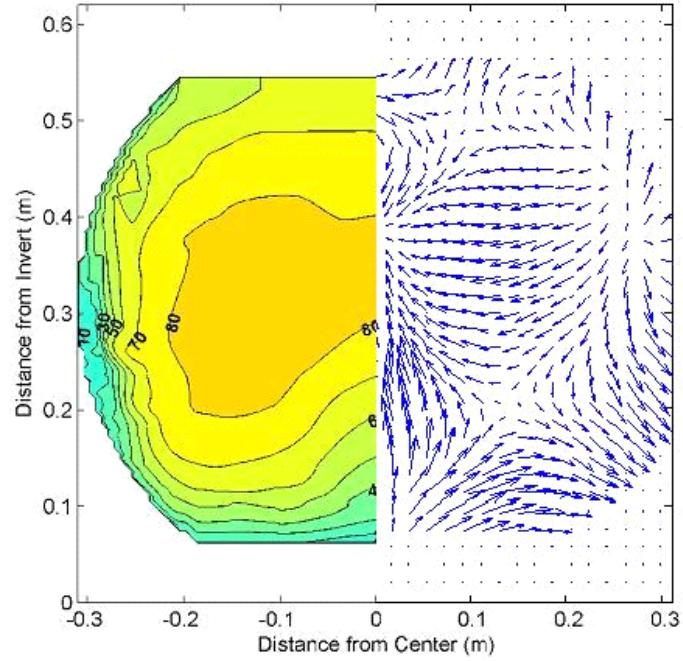


Figure 5.23: Quiver plot of v and w velocity components for XS6 of S0Q186 overlain on isovel plot. Arrow length implies relative magnitude.

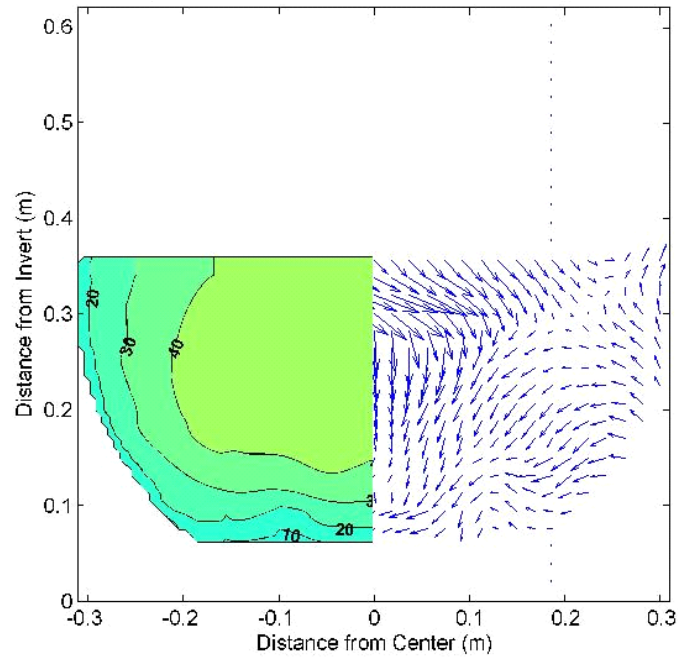


Figure 5.24: Quiver plot of v and w velocity components for XS20 of S0Q64 overlain on isovel plot. Arrow length implies relative magnitude.

5.5 Log Law Region

The vertical velocity profiles extracted from each interpolated flow cross-section were used to determine the shear velocity (u_*) and equivalent sand roughness (k_s) at $z = 0$ m, ± 0.06 m, ± 0.12 m, ± 0.18 m, ± 0.24 m and ± 0.27 m from the central plane. The corresponding non-central velocity profiles were averaged and the distribution of u_* and k_s was assumed to be symmetrical about the central plane. Only interpolated values from within the sampled region of the cross-section were used for this analysis.

5.5.1 Calculation of Shear Velocity

For each cross-section the central and averaged velocity profiles were plotted semi-logarithmically and a trend line was fit to the linear portion of each. The profiles in Figure 5.25 are typical for all the plots from cross-sections 6 to 26. The results from cross-section 1 to 4 were found to be highly erratic, owing to the inlet disturbance and the contraction effect. For this reason, only the results from cross-section 6 to 26 are reported. These plots are provided in Appendix D. By rearranging equation 2.21 as follows:

$$u = (2.5u_*) \ln \frac{y}{k_s} + 8.5u_*, \quad (2.21)$$

we see that u_* may be calculated by dividing the slope of the trend line by 2.5. This method was used previously by Ead et al. (2000) and depends only upon the assumption that u varies linearly with $\ln y$.

For each run, the shear velocity was found to vary consistently with distance from the central plane. This is demonstrated in Figure 5.26 a) where the distribution of shear velocity across the culvert bed is shown averaged over cross-section 6 to 26. The shape of the profile is consistent between runs, with u_* increasing with water velocity and the maximum u_* occurring typically between $z = 0.06$ m to 0.12 m. The center plane shear velocity is always somewhat lower than the peak, reflecting the low velocity zone created by the bed. Moving toward the culvert wall, the shear velocity drops off significantly, approaching 20 to 50% of the peak, depending upon the run.

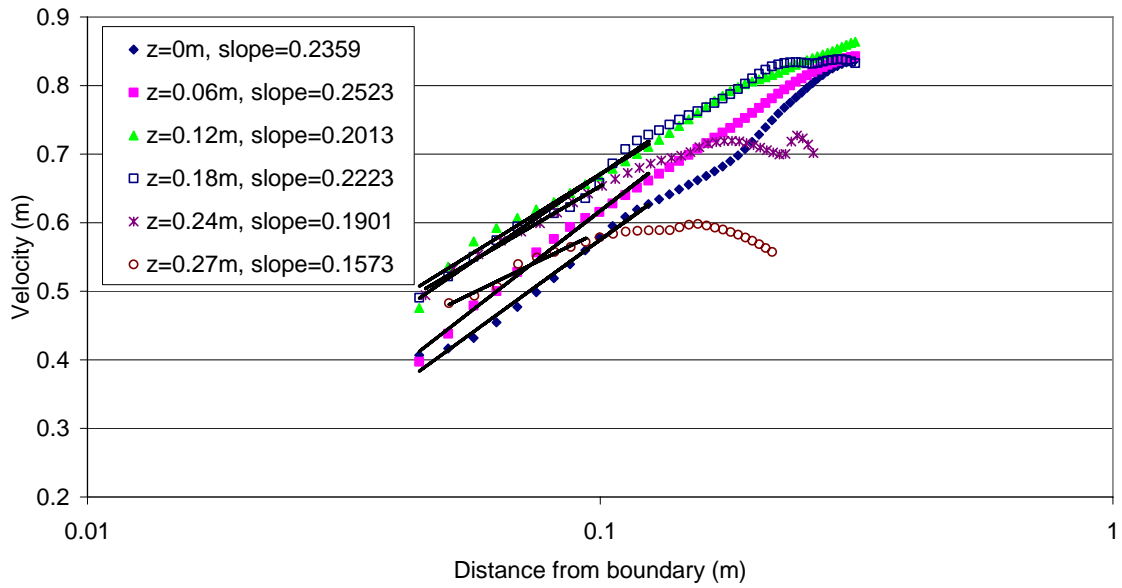


Figure 5.25: Logarithmic plot of central and non-central velocity profiles for determination of shear velocity - S0Q186, XS12.

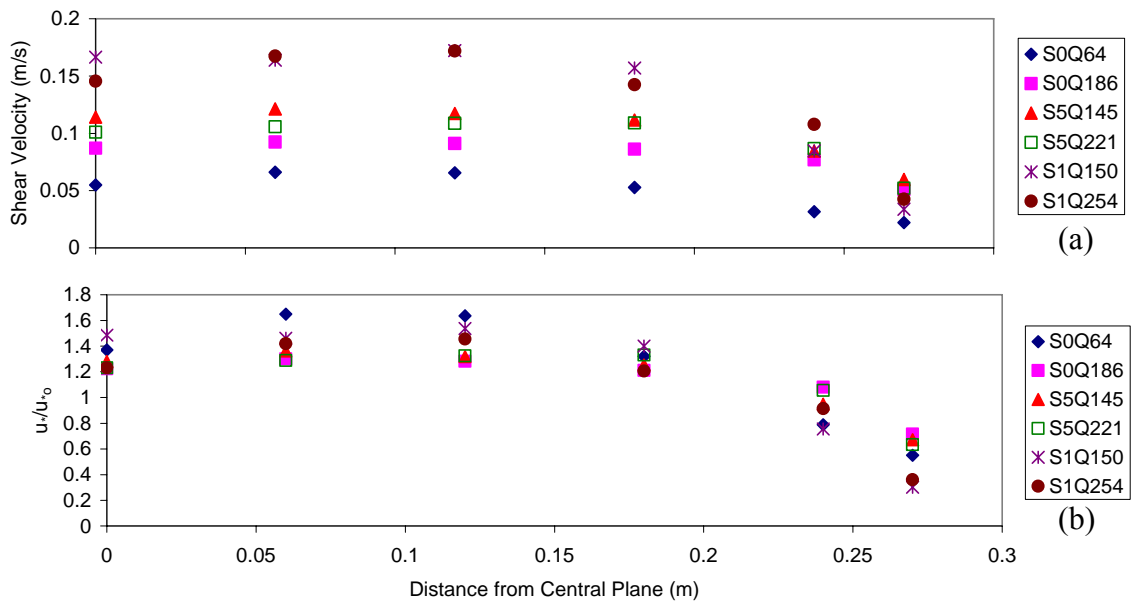


Figure 5.26: a) Distribution of shear velocity (averaged over XS6-26) from $z = 0$ to 0.27 m for all experimental runs, b) normalized by global shear velocity (u_{*o}).

The relative magnitude of the shear velocity between experimental runs is most strongly related to average velocity but also varies somewhat across the culvert bed. This demonstrates the dependence of shear velocity upon velocity gradient, and therefore isovel shape, which is in turn influenced by water depth, velocity and variation in boundary roughness as discussed in section 5.4. Figure 5.26 b) shows that the shear velocity distributions collapse significantly when normalized by the global shear velocity for each run (Table 5.6). Global shear velocity is calculated as

$$u_{*o} = \sqrt{gRS_f}, \quad (5.14)$$

where the friction slope is calculated as

$$S_f = \frac{u^2 n^2}{R^{4/3}}. \quad (5.15)$$

Table 5.6: Calculation of global shear velocity for experimental runs.

Slope	Flow (m ³ /s)	Run	Depth (m)	Friction Slope	R (m)	Global Shear Velocity
0%	0.064	S0Q64	0.299	0.0010	0.159	0.040
	0.186	S0Q186	0.472	0.0029	0.181	0.071
0.5%	0.145	S5Q145	0.305	0.0050	0.160	0.089
	0.221	S5Q221	0.449	0.0038	0.178	0.082
1.0%	0.150	S1Q150	0.260	0.0087	0.147	0.112
	0.254	S1Q254	0.386	0.0081	0.177	0.118

In general, the results in Table 5.6 are consistent with those of Ead et al. (2000) and Knight and Sterling (2000). However, Knight and Sterling investigated the distribution of boundary shear in detail for circular pipes flowing partly full. They used a Preston tube calibrated to measure shear stress directly and found that the local to global shear stress ratio peaked in the middle of the flat bed. The magnitude of this peak became more pronounced as the depth of burial was increased or the water depth was decreased. The bed and walls of the pipe used by Knight and Sterling were of uniform roughness and there was no significant bed-affected zone of low velocity water as seen in the isovels described in section 5.4. Likely, this bed-affected zone is responsible for the consistent dip in the center-plane shear velocity seen in Figure 5.26.

The shear velocity also showed no significant trend along the length of the culvert as seen in Figure 5.27, making the averaged distributions in Figure 5.26 more credible. In most cross-sections, the shear velocity over the bed is greater than the global shear and the shear velocity measured on the walls is less. However, some cross-over does occur and may be influenced by errors due to the difficulty in determining shear velocity from the velocity profiles, especially near the culvert walls.

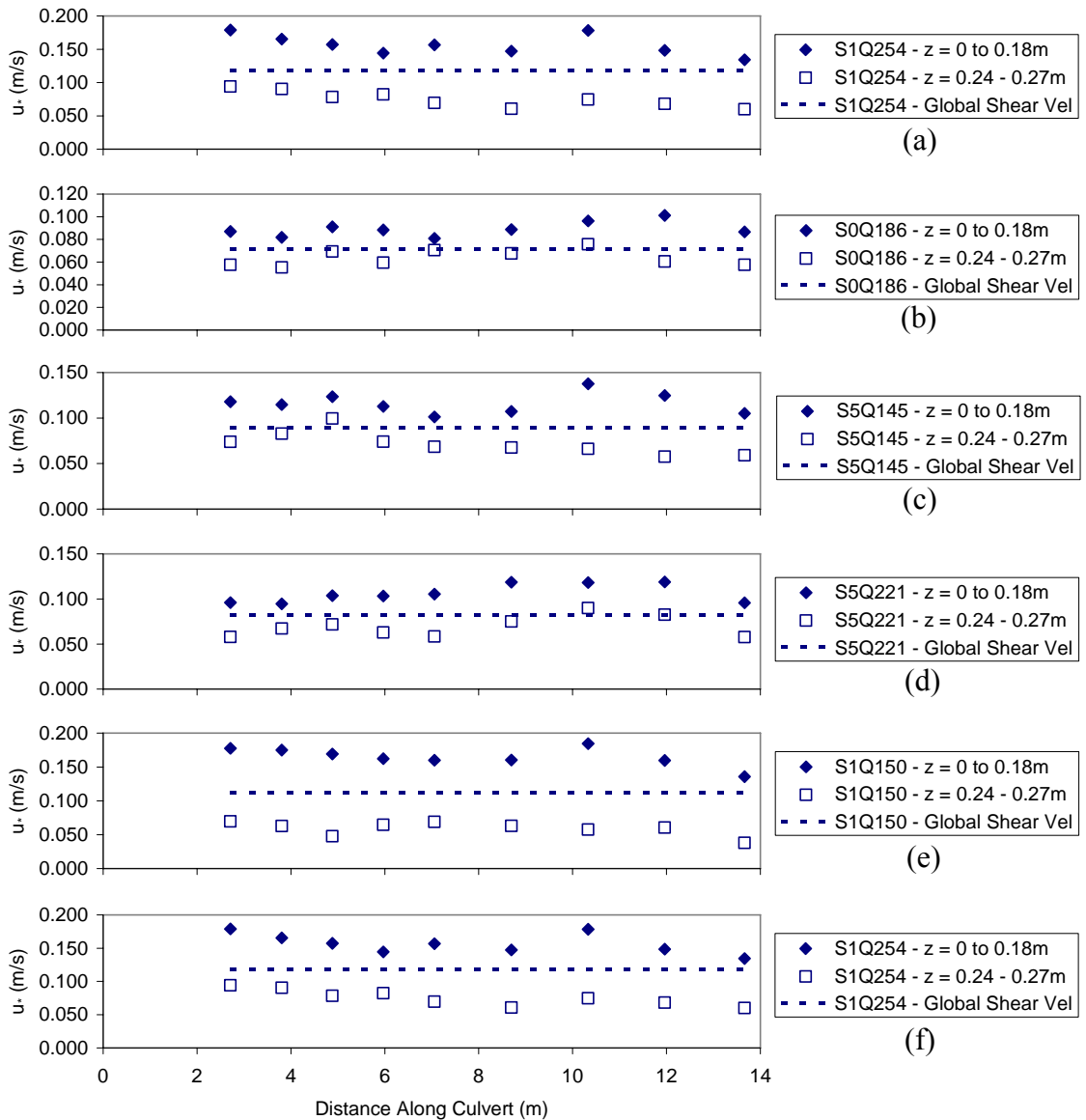


Figure 5.27 (a-f): Comparison of average bed ($z = 0$ to 0.18 m) and wall ($z = 0.24$ to 0.27 m) shear velocity with global shear velocity for all experimental runs.

5.5.2 Calculation of Equivalent Sand Roughness

After calculating the shear velocity at the base of each vertical profile, the velocity profiles were plotted again as u/u_* versus y/k_s and fit to the Prandtl-von Karman universal velocity distribution law (equation 2.21 - referred to here as the Log Law). The equivalent sand roughness was determined by adjusting the value of k_s to align the logarithmic portion of each profile with the Log Law (Figure 5.28). Like shear velocity, only the results from cross-section 6 to 26 are reported. These plots are provided in Appendix E and individual k_s results for each run are provided in Appendix F.

The deviation of the velocity profiles below the Log Law is due to the depression of the maximum velocity below the water surface, and is often attributed to secondary currents as discussed in section 5.4.5. The wake-like structure above the Log Law is often seen in the central and near-central plane profiles. It is formed when the slower velocities of the bed-affected region are aligned with the Log Law. This feature is most commonly associated with the high flow cases with deeper water and a distinct bed-affected region as discussed in section 5.4.2.

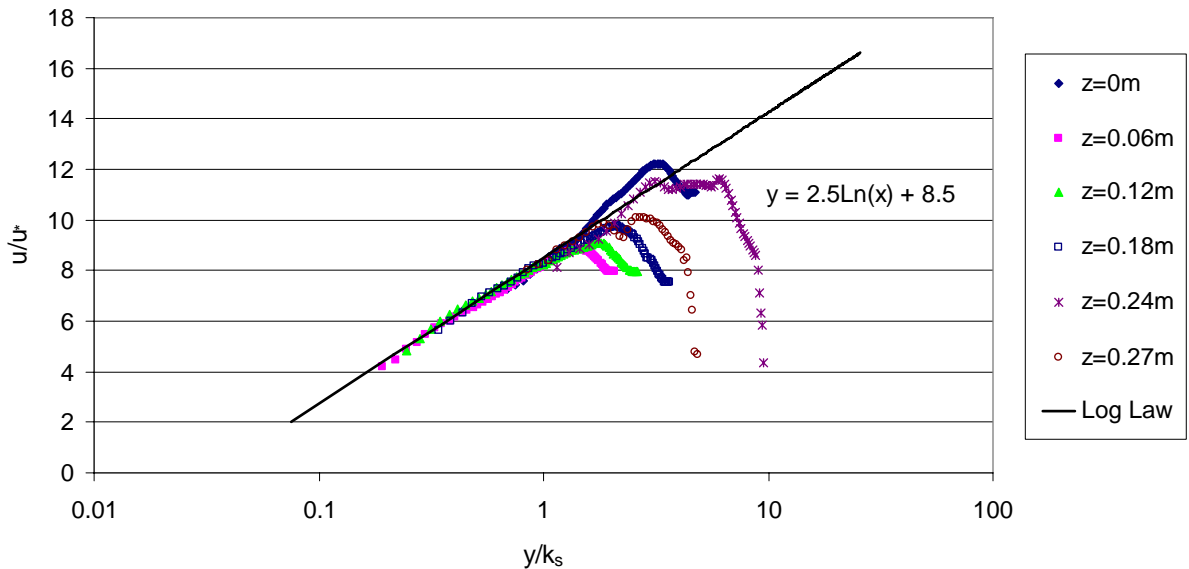


Figure 5.28: Velocity profiles fit to Log Law for determination of k_s - S0Q186, XS12.

Equivalent sand roughness is a fitting parameter with no direct physical representation. For this reason, it is useful to compare the value of k_s determined from these experiments with a range of predicted values. Numerous methods have been proposed to relate roughness to the grain size of bed material in gravel rivers. Some of these methods were listed in Chapter 2 as follows:

$$\text{Strickler (1923)} \quad k_s = D_{90} \quad (2.1)$$

$$\text{Charlton et al. (1978)} \quad 3D_{84} < k_s < 3D_{90} \quad (2.2)$$

$$\text{Bray (1979)} \quad k_s = 3.5D_{84} \quad (2.3)$$

$$\text{Hey (1979)} \quad k_s = 3.5D_{84} \quad (2.4)$$

It is widely accepted that the equivalent roughness in gravel-bed rivers is often many times greater than the physical size of the roughness elements (Yalin, 1972). For this reason, the latter three methods were used to predict the following range of k_s values: $0.178 \text{ m} < k_s < 0.207 \text{ m}$. Figure 5.29 shows the value of k_s for each experimental run from $z = 0 \text{ m}$ to 0.27 m and averaged over cross-section 6 to 26. There was significant variation in k_s along the culvert as seen in Figure 5.30. This is due primarily to the difficulty in accurately determining both the shear velocity and the highly variable surface of the gravel bed, which prevented the distance to the boundary from being determined exactly. However, as Figure 5.30 shows no discernable trend along the length of the culvert, mean k_s values are reported from cross-section 6 to 26.

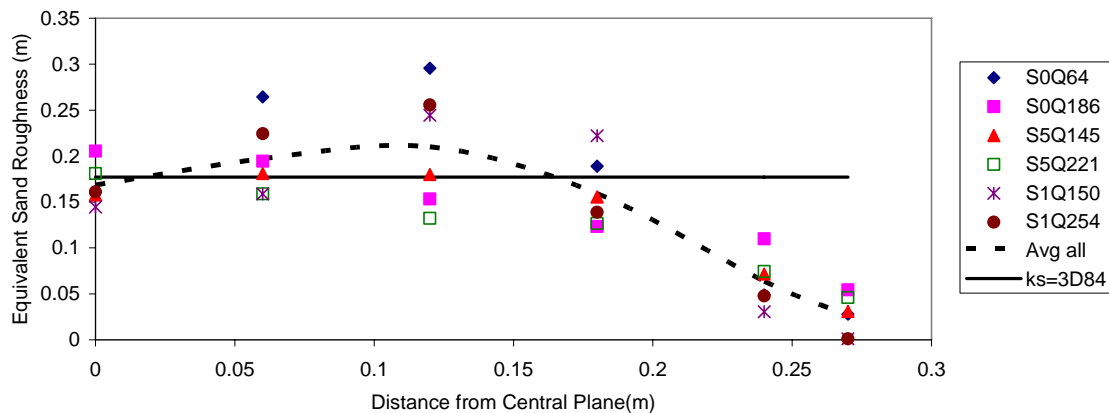


Figure 5.29: Distribution of equivalent sand roughness (averaged over XS6-26) from $z = 0$ to 0.27 m for all experimental runs.

For reference, $k_s = 3D_{84}$ is plotted in both Figure 5.29 and Figure 5.30. As seen in Figure 5.29, the average value from all experiments is bounded by the predicted range of k_s for much of the width of the gravel bed ($z = 0$ m to 0.18 m), falling off sharply in the vicinity of the culvert wall ($z > 0.18$ m). This is expected as Ead et al. (2000) determined the k_s value of an identical culvert without a gravel bed to be equivalent to the corrugation height, or 0.012 m. Therefore, near the edge of the bed, the value of k_s is affected by both the bed and wall roughness and would likely approach a value of 0.012 m at some point along the culvert wall if the flow depth was great enough.

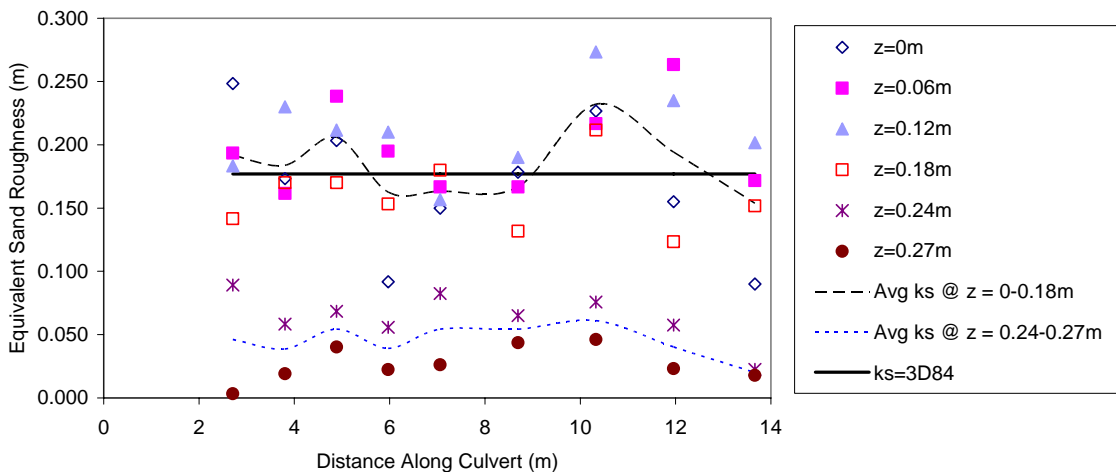


Figure 5.30: Equivalent sand roughness (averaged over all experimental runs) along the length of the culvert.

5.5.3 Design Applications

A major limitation of the Log Law is the difficult in applying it for design purposes without foreknowledge of the shear velocity and equivalent sand roughness. Therefore, a number of strictly empirical methods have been developed to relate velocity distribution to predictable parameters such as average velocity (Mountjoy, 1986; White, 1996; House, 2005) or global shear velocity (Chow, 1959) or both (Ead et al., 2000). However, the trends demonstrated herein suggest that shear velocity and equivalent sand roughness may have a predictable distribution around the wetted perimeter of an embedded culvert and that with additional study, a robust predictive method may be foreseeable.

5.6 Manning's Roughness Coefficient

Manning's equation (equation 2.1) is a widely used equation for estimation of discharge (Chow, 1959). Many culvert design aids including nomographs (Handbook of Steel Drainage and Highway Construction Products, 2002) and simulation programs like HEC-RAS (Brunner, 2002) are utilise Manning's equation and require a knowledge of Manning's roughness coefficient (n). Manning's n can be effectively determined in HEC-RAS by calibration to measured water surface elevations. Also, the roughness coefficients of commercially available culverts are well studied. However, for new installations of embedded culverts, prediction of Manning's n is problematic. This may lead to an increased risk of design failure or overly conservative sizing of culverts to compensate for the uncertainty in determining Manning's coefficient.

5.6.1 Prediction of Manning's Roughness

The Manning's coefficient for a 0.62 m diameter culvert with 68 mm x 12 mm corrugations is listed as 0.023 in the Handbook of Steel Drainage and Highway Construction Products (2002). This value was confirmed independently by Ead et al. (2000) using the combined results from a wide range of discharges at three different bed slopes. However, prediction of Manning's n for the gravel bed is a more complicated task, as evidenced by the numerous approaches that exist (Strickler, 1923; Meyer-Peter and Muller, 1948; Limerinos, 1970; Bray, 1979; Bruschin, 1985; Abt et al., 1987; Ugarte and Madrid, 1994; Julien, 2002). These predictive methods were developed primarily for use in gravel-bed rivers and produce widely varying results when applied to Class 350 rip rap (Manitoba Infrastructure and Transportation, 2003) specified for use as bed material in partially buried culverts.

Table 5.7 summarises results from a number of methods that have been proposed to estimate Manning's n from the size of the bed material. Estimated values are given for both Class 350 rip rap and the 5:1 scale gravel mix used in this study. The methods proposed by Bruschin (1985), Strickler (1923), Julien (2002) and Bray (1979) produced reasonable values and are highlighted in Table 5.7. In practice, calibrated n values for

Class 350 rip rap used in HEC-RAS have ranged from 0.035 to 0.041 for embedded culverts in Manitoba. This translates to a predicted model range of $0.027 < n < 0.031$ when the bed material is scaled by the geometric scale factor, λ .

Table 5.7: Predicted values of Manning's n for prototype and model Class 350 rip rap, ranked in ascending order.

Method to Calculate Manning's n	Equation #	$(n_{bed})_p$	$(n_{bed})_m$
Abt et al. (1987)	2.8	0.015	0.012
Julien (2002)	2.13	0.031	0.024
Meyer-Peter and Muller (1948)	2.4	0.032	0.024
Bruschin (1985)	2.9	0.035	0.027
Strickler (1923)	2.3	0.036	0.028
Julien (2002)	2.12	0.037	0.028
Bray (1979)	2.6	0.040	0.031
Julien (2002)	2.11	0.047	0.036
Ugarte and Madrid (1994)	2.10	0.053	0.041
Limerinos (1970)	2.5	0.071	0.054

5.6.2 Experimental Determination of Manning's n

The embedment of a culvert with known roughness adds uncertainty to prediction of the effective Manning's \bar{n} , also called composite roughness. It was important to experimentally assess the \bar{n} of the embedded model culvert to provide a basis against which to evaluate the existing methods for predicting composite roughness (discussed in the next section). This test was conducted when the model was set at 1% slope and the water surface elevation at cross-section 14 was measured for discharges ranging from $0.025 \text{ m}^3/\text{s}$ to $0.250 \text{ m}^3/\text{s}$ in $0.025 \text{ m}^3/\text{s}$ increments. Manning's \bar{n} for the culvert was then determined by plotting $AR^{2/3}S^{1/2}$ versus Q as shown in Figure 5.31. The slope of this line yields $\bar{n}_{meas} = 0.0238$, somewhat higher than the results reported by Ead et al. (2000) for the culvert alone. However, in a culvert where the bed roughness is greater than the roughness of the walls, the composite roughness will not be constant as water depth changes. Rather, it will decrease as the depth increases (Chow, 1959).

Further examination of Figure 5.31 reveals that below a depth of $y = 0.233$ m, the slope of the points yields $\bar{n} = 0.0256$ and for $y > 0.233$ m, $\bar{n} = 0.023$. This suggests that no single roughness coefficient will adequately predict discharge through an embedded culvert with bed roughness different from the wall roughness. Chow (1959) describes how the Manning's n of even a pipe of uniform roughness can vary as much as 28% simply due to changes in flow depth. Therefore, a suitable method must be found to predict composite roughness with respect to changes in water depth.

It is worth noting that some methods for predicting composite roughness in gravel bed rivers have been developed to take the effect of bed slope into account (Jarret, 1984; Bruschin, 1985; Abt et al., 1987; Ugarte and Madrid, 1994), though slope is not classically considered to affect roughness (Chow, 1959). Support of this approach may come from the results presented by Ead et al. (2000). Their calculated value of $n_{CSP} = 0.023$ is based on measured water surfaces combined from slopes of 0.55%, 1.14% and 2.55%. The points form distinctly different trends and when Manning's n is calculated using each slope separately and the resulting range is roughly $0.018 < n_{CSP} < 0.024$.

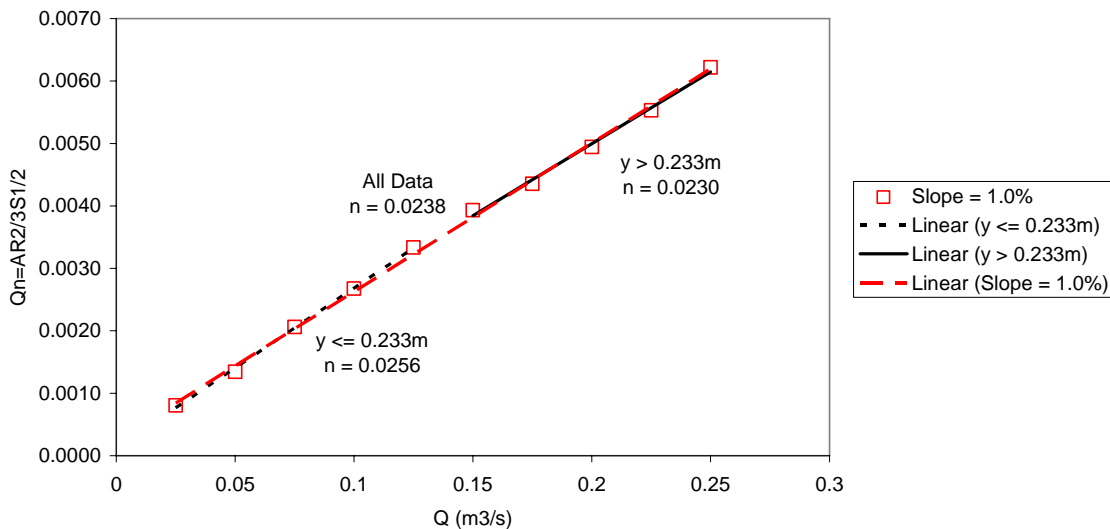


Figure 5.31: Experimental determination of composite Manning's coefficient (\bar{n}).

5.7 Evaluation of Composite Roughness Methods

Three main approaches (5 methods in total) for predicting composite roughness were evaluated as follows:

1. Equal velocity methods:
 - Einstein (1933) and Horton (1934)
 - Colebatch (1941)
 - Los Angeles District (Cox, 1973)
2. Sum of forces method
 - Einstein and Banks (1950)
3. Conveyance method
 - Lotter (1933)

The details for each method are provided in section 2.2. To compare the methods, each was used in conjunction with the Standard Step Method (Chow, 1959) to compute the water surface profile of each run as measured with the tailwater gate fully lowered. Before the composite roughness could be calculated, the cross-section of the culvert was re-defined to divide the flow area into regions affected by the bed and walls.

5.7.1 Defining the Cross-section in Composite Roughness Terms

The five composite roughness methods evaluated were originally developed for use with rectangular or trapezoidal channels and all three approaches assume that the flow can be divided into discrete areas affected by the bed and sides of the channel. In rectangular or trapezoidal channels, this was done by bisecting the angle between bed and channel side. Previous studies to evaluate their accuracy have not included culverts with a flat bed and therefore an alternative method of dividing the flow area must be developed. The method used in this study is detailed in Figure 5.32 and was originally proposed in a graduation project by Clayton (1997). Clayton proposed that the area affected by the bed roughness (A_{nbed}) should be represented by a triangle with a base equal to the width of the culvert bed and a maximum height of half the maximum flow depth ($Y_{max}/2$). If $y < Y_{max}/2$, then

A_{nbed} becomes trapezoidal in shape and the area projecting above the water surface (A_{sub}) must be subtracted out. The area affected by the walls may then be calculated as $A_{nw} = A_{total} - A_{nbed}$.

This method of dividing the flow areas is somewhat arbitrary but it does fit well with the general shape of the bed affected region especially apparent in the isovels for S0Q186 and S5Q221 (section 5.4.2). As the water depth exceeds half the flow depth, A_{nbed} reaches a maximum value and the relative contribution of the bed roughness to the composite n (\bar{n}) declines. As the flow depth decreases, the contribution of the bed to the overall roughness increases. An alternative method of dividing the area might be to assign a fixed angle to the sides of A_{nbed} , making it easier to program.

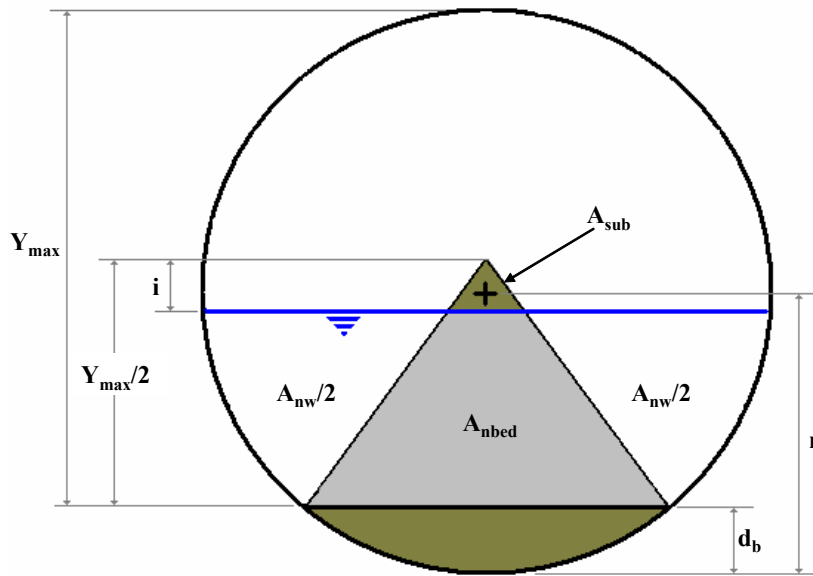


Figure 5.32: Definition sketch for area-dependent composite roughness methods.

5.7.2 Gradually Varied Flow Profiles

Water surface elevations were recorded with a point gauge attached to the sampling cart at each of the 26 sampling stations along the culvert for all of the experimental runs. In addition, each slope and flow combination was repeated with the tailwater gate fully

lowered and the resulting water surface profiles were used as a basis to evaluate 5 methods of computing composite roughness. The established value of $n_{CSP} = 0.023$ was used for the culvert walls and $n_{bed} = 0.029$ was initially picked as it represented the middle of the range estimated for the bed material in Table 5.7. The configuration of the tailwater box was such that the flow exiting the culvert was forced into a 90 degree bend. Mounding of the water surface due to surging in the tailwater box caused the tailwater elevations to be overestimated in the stilling well. Therefore, calculation of the gradually varied flow profile for each run commenced at cross-section 26 for the 0% slope runs and cross-section 25 for the 0.5% and 1.0% slope runs.

In all cases the flow was subcritical and calculations proceeded upstream using Microsoft Excel to compute the flow profile with the Standard Step Method (Chow, 1959). All slopes and discharges tested exhibited M2 profiles as seen in Figure 5.33 (a – c). However, the outlet of the tailwater box was somewhat undersized leading to staging at discharges over $0.221 \text{ m}^3/\text{s}$ that approached the normal depth of flow. When the tailwater gate was fully lowered, the control shifted from the gate to the tailwater box outlet. Fortunately, backwatering does not appear to have occurred as the water depth decreases continuously proceeding downstream for all runs conducted with the tailwater gate fully lowered. Each worksheet was programmed allowing the desired composite roughness method to be selected. The composite roughness was recalculated for each change in water depth and the resulting profiles were compared to the measured water surface elevations. The results for the Einstein/Horton method are shown in Figure 5.33 (a – c).

For all runs, the conveyance method proposed by Lotter resulted in the lowest composite roughness value along the full length of the culvert. The largest value of \bar{n} was given by the Einstein and Banks method for all cases except when the relative depth approached $0.25D_o$ near the outlet for S0Q64 where Colebatch was the highest. In all runs, the composite roughness values along the full length of the culvert differed by 1.5% to 4.9% of the experimentally measured value $\bar{n}_{meas} = 0.0238$. As a further illustration, Table 5.8 lists the difference between the \bar{n} values for cross-section 14 calculated using the Lotter and Einstein/Banks methods and compares them to the \bar{n}_{meas} .

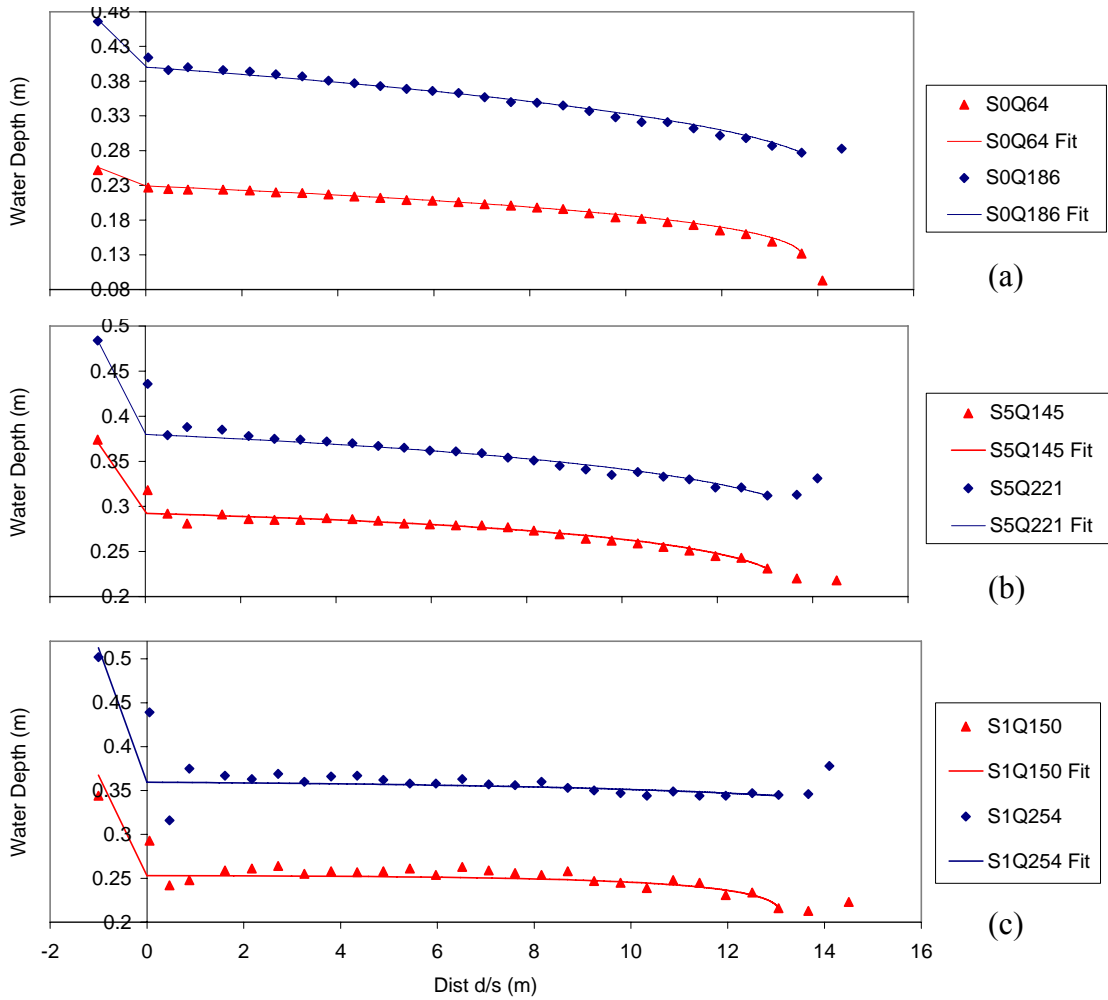


Figure 5.33 (a-c): Fitting measured water surface profiles using Standard Step Method and Einstein/Horton composite roughness ($n_{CSP} = 0.023$ and $n_{bed} = 0.029$).

Table 5.8: Comparison of Max and Min Composite Roughness at cross-section 14.

Method	S0Q64	S1Q186	S5Q145	S5Q221	S1Q150	S1Q254
Einstein/Banks	0.02575	0.02504	0.02536	0.02504	0.02548	0.02505
Lotter	0.02537	0.02390	0.02460	0.02391	0.02489	0.02394
Difference	0.00037	0.00114	0.00076	0.00113	0.00059	0.00111

The similarity between the methods made the task of evaluating them very difficult; complicated by the fact that n_{bed} was originally estimated. Through trial and error, it was confirmed that $n_{bed} = 0.029$ provided a good fit for all runs. As a further check, the n_{bed} was tailored to optimize the fit of each profile. The average of these custom fit n_{bed}

values was 0.0292. All 5 methods produce reasonable results, differing by millimetres. The Lotter method consistently produced the lowest water elevations as expected while Einstein/Banks produced the highest. The three most commonly applied methods are the equal velocity methods. These produced elevations in between Lotter and Einstein/Banks. In ascending order, they are: Los Angeles District, Colebatch and Einstein/Horton. This result is consistent with the findings of Cox (1973) who tested all three equal velocity methods. Cox concluded that in prismatic channels with a bed roughness greater than that of the sides, the Einstein/Horton method was less accurate and less conservative than the Colebatch or Los Angeles District methods. However, these results are not necessarily applicable to embedded circular culverts. Table 5.9 compares all 5 methods using the average elevation in the inlet region as a target. Based on these results, the Einstein/Banks and Einstein/Horton methods performed equally well, producing the smallest amount of variation from the target elevations.

Table 5.9: Comparison of Composite Roughness Methods Using $n_{bed} = 0.029$ and $n_{CSP} = 0.023$.

Run	Target Elev (m)	Difference From Target Elevation (m)				
		Ein/Banks	Ein/Hort	Colebatch	LAD	Lotter
S0Q64	0.227	0.002	0.002	0.003	0.002	0.001
S0Q186	0.400	0.001	0.000	-0.002	-0.002	-0.006
S5Q145	0.292	0.001	0.000	-0.001	-0.001	-0.004
S5Q221	0.384	-0.004	-0.004	-0.007	-0.007	-0.012
S1Q150	0.254	0.000	-0.001	-0.001	-0.002	-0.004
S1Q254	0.364	-0.004	-0.004	-0.008	-0.008	-0.014

For the 0.5% and 1.0% slope runs, the entrance loss was large, requiring estimation of the average elevation near the culvert inlet. The troughs and peaks of the standing wave created by the inlet loss can be clearly seen in Figure 5.33 b) and c), reducing in amplitude as it is propagated downstream. Observations of the S1Q254 profile show that the trough of the standing wave created by the inlet loss was so severe, that the flow depth dropped well below the normal depth, recovering to a uniform flow depth along the rest of the culvert length.

5.7.2.1 Inlet Losses

By far the most significant head losses at any point in the culvert occurred as a result of the projecting inlet. To fully describe the water surface, it was necessary to calculate these losses using an energy approach. The inlet losses shown in Figure 5.33 (a – c) were calculated considering all losses occurring between the inlet pool and the point of maximum expansion after the contraction. To do so accurately, it is necessary to calculate the velocity in the contracted section (u_{ctr}). As the sampling locations for cross-section 1 to 3 were fixed, it is not certain that the point of maximum contraction was sampled. As an alternative, a method described by Behlke et al. (1991) was used to estimate the inlet losses based on the velocity occurring in the barrel downstream from the contraction. The details used in this calculation are shown in Figure 5.34.

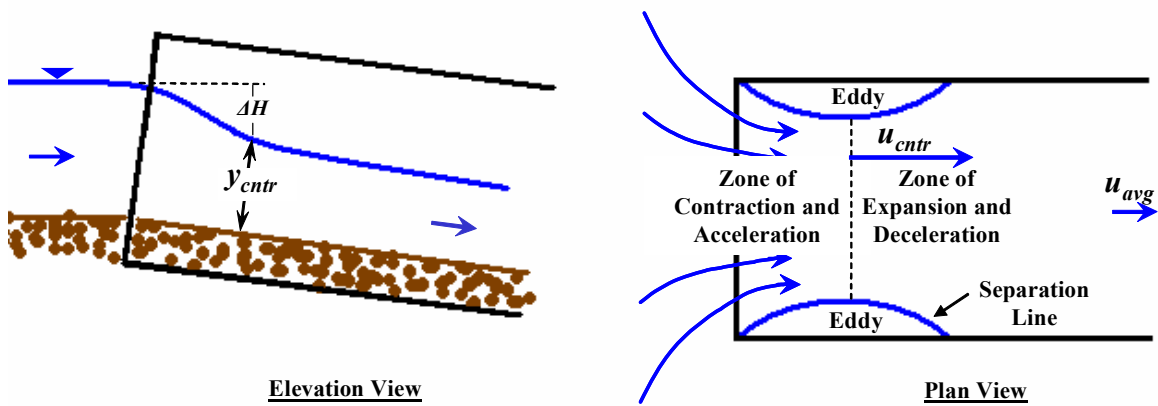


Figure 5.34: Details of the culvert inlet zone.

The inlet loss through the acceleration zone of the contraction may be written as

$$h_L = k_e \frac{(u_{avg})^2}{2g}, \quad (5.16)$$

where h_L is the head loss through the acceleration zone, k_e is the inlet loss coefficient and u_{avg} is the average velocity in the barrel roughly one diameter downstream of the inlet. The losses occurring in the flow acceleration zone are usually small and it is assumed that they can be ignored. The losses through the expansion zone may be written as

$$h_L = \frac{(u_{ctr})^2}{2g} - \frac{(u_{avg})^2}{2g}, \quad (5.17)$$

where u_{ctr} is the velocity at the point of maximum contraction (start of the expansion zone). Combining equations 5.16 and 5.17 yields

$$\frac{(u_{ctr})^2}{2g} = \frac{(1+k_e)(u_{avg})^2}{2g}. \quad (5.18)$$

Ignoring frictional losses, the energy equation can be written between the inlet pool and the point of maximum contraction as

$$\frac{(u_{ctr})^2}{2g} = \frac{(u_{pool})^2}{2g} + \Delta H, \quad (5.19)$$

where u_{pool} is the velocity in the inlet pool and ΔH is the total head loss through the inlet. If the velocity head in the inlet pool is negligible, equation 5.19 can be simplified and combined with equation 5.18 giving

$$\Delta H = \frac{(1+k_e)(u_{avg})^2}{2g}. \quad (5.20)$$

The Handbook of Steel Drainage and Highway Construction Products (2002) lists $k_e = 0.9$ for corrugated metal culverts with a projecting end as used in this study. Equation 5.20 was used to predict the inlet losses in conjunction with the Standard Step Method calculations of the water surface profile. Generally, the results were within 15% of the inlet losses measured between the headwater box and the average water surface in the inlet zone. However, as the width of the headwater box was roughly $2D_o$, equation 5.20 tended to overestimate inlet losses by an average of +7.3%, as seen clearly in Figure 5.33 c). Better results were obtained when the inlet pool velocity was accounted for as follows:

$$\Delta H = \frac{(1+k_e)(u_{avg})^2}{2g} - \frac{(u_{pool})^2}{2g}. \quad (5.21)$$

Inlet losses calculated with equation 5.21 were within 8.8% of measured values, overestimating them by an average of +0.3%.

5.7.3 Comparison with HECRAS Beta 4.0 Simulation

HEC-RAS is one of the most widely used design tools in the world for calculating stage and discharge through rivers, canals and stream crossing structures. As such, it was undertaken to evaluate the ability of HEC-RAS to accurately simulate the experimental runs using the measured water surface profiles. The geometric and steady flow data were entered to match the physical model and experimental conditions as closely as possible including the dimensions of the inlet pool and projecting inlet configuration. The Manning's roughness was set to 0.023 for the culvert and 0.029 for the gravel bed. HEC-RAS uses the Direct Step Method for computing the water surface profile and the Einstein/Horton Method for computing composite roughness, so this exercise was also a valuable check of the Standard Step profile calculations detailed in section 5.7.2. A profile plot is shown in **Figure 5.35** for the S5Q145 run with the tailwater gate fully lowered. The vertical scale is greatly exaggerated to make the water surface and energy grade-line easier to read. The HEC-RAS Beta 4.0 User's Manual (Brunner, 2006) states that the road embankment (shown with a 2:1 slope in **Figure 5.35**) is not used in the flow calculations and is for visualization purposes only.

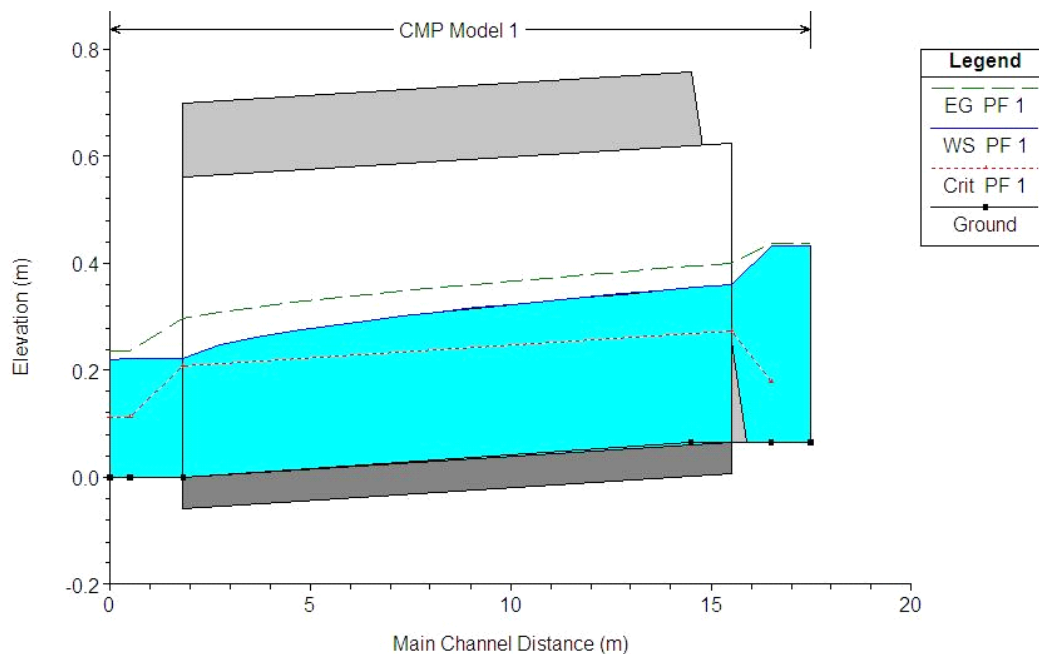


Figure 5.35: Profile plot from HECRAS simulation of S5Q145 run with no tailwater control.

As see in Figure 5.36 and Figure 5.37, the HEC-RAS results for the model runs with and without tailwater control show very good agreement with the measured water surface profiles, usually within 5 mm of the target elevation. As mentioned earlier, the tailwater elevations should be disregarded due to limitations of the tailwater box layout. Naturally, HEC-RAS failed to predict the large standing wave or surface undulations seen near the inlet of all runs at 0.5% slope or greater. Inlet losses were consistently underestimated by HEC-RAS as shown in Table 5.10 and differed from the measured values by 5.8% to 19.5% with an average of 9.0%. Table 5.10 also shows the inlet losses calculated using the method described by Behlke et al. (1991) with the inlet pool velocities accounted for (equation 5.21). The calculated values differed from the measured inlet losses by -8.8% to +8.5% with an average of +0.3%. There were also some overestimation of the water surface elevations near the outlet for S5Q221 and S1Q150 caused by difficulties with placing known water surface elevations inside the culvert.

Table 5.10: Measured inlet losses compared to calculated values and HEC-RAS results.

Inlet Loss (m)	S0Q64	S0Q186	S5Q145	S5Q221	S1Q150	S1Q254
Measured	0.025	0.066	0.082	0.100	0.102	0.138
Calculated	0.026	0.063	0.075	0.098	0.111	0.144
HEC-RAS	0.024	0.061	0.066	0.089	0.096	0.130

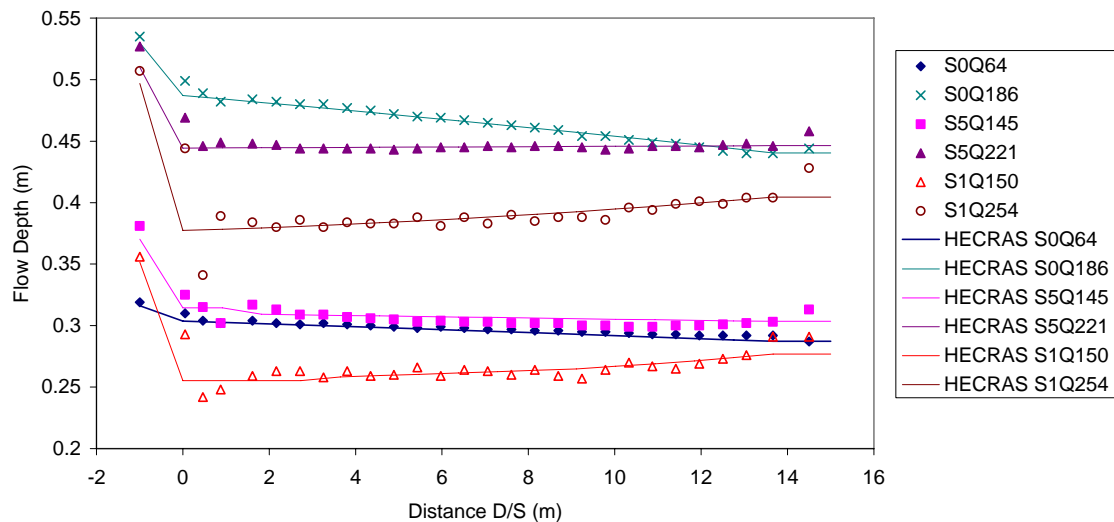


Figure 5.36: Comparison of HECRAS Beta 4.0 model simulations with measured water surface profiles with tailwater control.

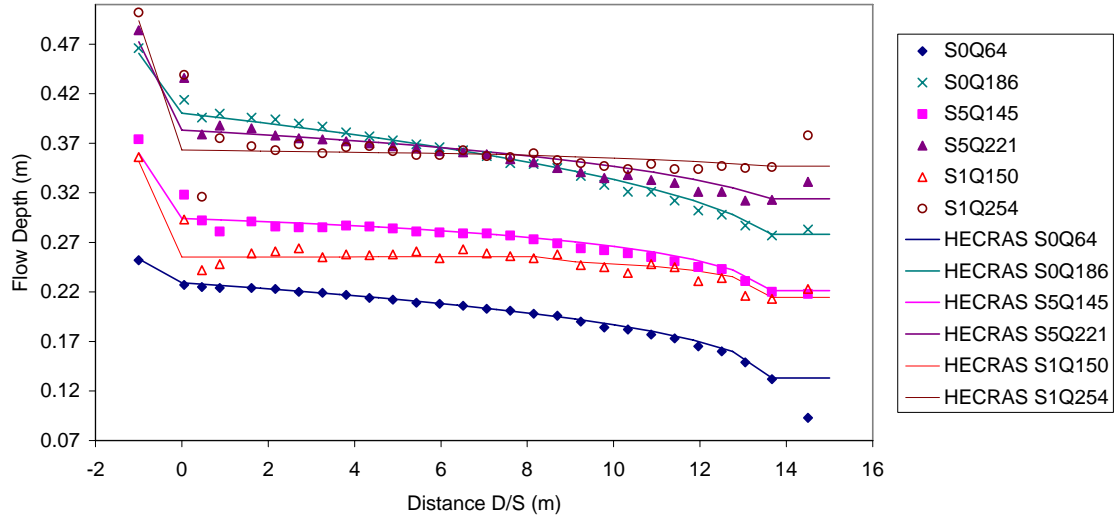


Figure 5.37: Comparison of HECRAS Beta 4.0 model simulations with measured water surface profiles with no tailwater control.

5.8 Effect of Embedment on Maximum Discharge

The maximum discharge in a circular culvert under open channel flow conditions occurs at a relative depth of $0.938y/D_o$ (Chow, 1959). The addition of a gravel bed will reduce the capacity of a culvert due to the reduction in flow area and the increase in composite roughness. If inlet losses are minimized with a carefully constructed transition, it should be possible to directly measure the maximum capacity in a culvert with and without embedment. However, with a projecting inlet, inlet losses will tend to cause surcharged conditions and an unstable water surface long before maximum discharge can be attained in the culvert. Therefore, the approach of varying n with Q was used to estimate analytically the effect of 10% embedment on maximum discharge.

To determine if the relative depth associated with Q_{max} is affected by embedment, y/y_{max} was plotted versus $Q/Q_o = AR^{2/3}/A_oR_o^{2/3}$ for a circular cross-section with and without 10% embedment, where Q_o , A_o and R_o are associated with full flow. As seen in Figure 5.38, no appreciable change was noted and Q_{max} was shown to occur at $0.94y/D_o$. Next, the composite roughness of the model culvert was determined to be $\bar{n} = 0.0244$ at a relative depth of $0.94D_o$ and based on $n_{bed} = 0.029$ and $n_{CSP} = 0.023$. The variation of n with Q

was then plotted in Figure 5.39 by assuming that at maximum discharge, the value of $(AR^{2/3})_{Q_{max}}$ is a constant. By assuming that the slope is also constant, Manning's equation can be reduced to

$$Q = b/n, \tag{5.22}$$

where $b = (AR^{2/3})_{Q_{max}} S_o^{1/2}$. This was done for a culvert with and without 10% embedment at both 0.5% and 1.0% slope. Horizontal lines were then plotted on Figure 5.39 for $\bar{n} = 0.0244$ and $n_{CSP} = 0.023$ as would occur at $y = 0.94D_o$.

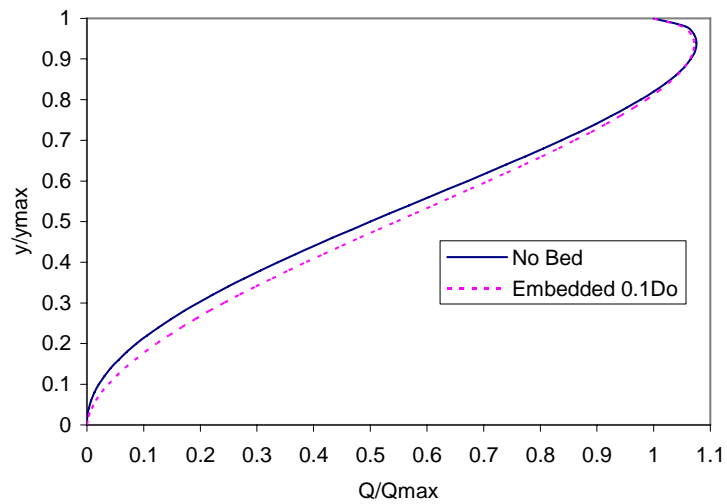


Figure 5.38: Flow characteristics of a circular section with and without embedment of $0.1D_o$.

The intersection of these lines with the $n-Q$ curves gives the maximum discharge for 0.62 m diameter culvert with and without 10% embedment. As shown in Table 5.11, 10% embedment of a CSP culvert is estimated to reduce its capacity by roughly 11% for both a 0.5% and 1.0% slope installation.

Table 5.11: Estimation of Q_{max} and loss in conveyance caused by 10% embedment.

Q_{max} (m ³ /s)	S=0.5%	S=1.0%
No Bed	0.290	0.411
10% Embedded	0.258	0.364
% Reduction	11.0%	11.4%

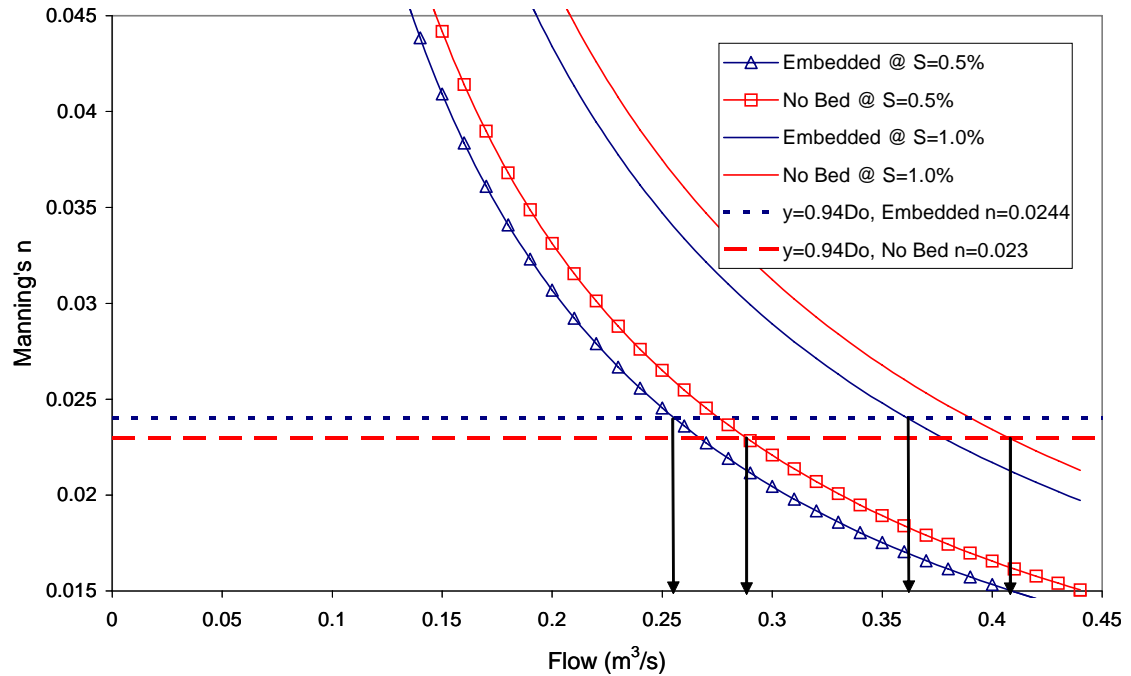


Figure 5.39: Estimation of maximum discharge by variation of n with Q approach for an empty culvert and one with 10% embedment.

5.9 Movement of Bed Material

The grade of bed material used was a 1:5 scale reduction of the Class 350 aggregate specified by Manitoba Infrastructure and Transportation's Specifications for Stone Rip Rap (2003) designed for use in culverts. The particle distribution was scaled using the geometric scale factor ($\lambda = 5$) as recommended by Belataos (1995) but mobility of the bed material was uncertain and qualitative observations of bed movement were made during testing. Very little movement of bed material occurred at all flows and slopes other than slight re-settlement of individual units to a more stable position. The larger size gravel was observed to form an armour layer, preventing movement of any of the smaller particles. No material was transported out of the culvert and into the tailwater box.

Some movement the bed material was observed immediately upstream and through the contraction region of the culvert inlet during 1.0% slope runs where velocities in excess of 1.6 m/s were recorded. The movement consisted of rolling or tumbling of some of the

larger armour units as well as the smaller particle they protected. Transport occurred over a distance of less than 1 m and no bed-forms were seen to develop anywhere in the culvert barrel. The displaced bed material was repositioned each day before testing commenced.

Chapter 6: Summary and Recommendations

Circular corrugated structural plate (CSP) culverts are the most common form of stream crossing on small rivers in Manitoba due to their relatively low cost and ease of installation. However, they are also considered the least desirable form of stream crossing from a fish passage perspective because they inevitably concentrate the flow, resulting in higher velocities than would occur in the natural channel. If the velocity in a culvert exceeds a certain level, it may act as a barrier to fish attempting to ascend upstream. Flow velocities can be reduced by increasing culvert size, roughness, burial depth, and by reducing culvert slope. Therefore, in an effort to control flow velocities in circular CSP culverts, Manitoba law requires that they be embedded by 0.3 m or 10% of their diameter (whichever is greater) and filled with a suitably graded rock to the level of the natural stream bed. They must also be sized so that fish desiring to proceed upstream do not experience a delay greater than 3 days, once every 10 years.

Assuming the hydrology of a river is known accurately, the two key elements to achieving an economical design for a culvert stream crossing are knowledge of the velocity distribution within the culvert and accurate data on the swimming abilities and behaviour of affected fish species. It is well understood that low velocity zones exist near the flow boundaries that may be used by fish traveling upstream. Unfortunately, no methods currently exist to accurately predict the effect of embedment on the velocity distribution in circular culverts under open channel flow conditions. As well, little research has been done to examine the effect of embedment on composite roughness in circular CSP culverts, adding further uncertainty to velocity prediction efforts. As a result, current fish passage models are based on average velocity and may be overly conservative. In addition, a growing body of research suggests that velocity criteria based on forced performance testing may significantly underestimate the swimming ability of fish (Peake, in press).

Further research is required to bridge the knowledge gap surrounding both prediction of velocity distributions and fish behavioural science with regard to fish passage considerations. In an effort to address the former, this report details a physical modeling study conducted to investigate the flow characteristics of an embedded circular CSP culvert under a range of flows and slopes. The model culvert was constructed of a 0.62 m diameter corrugated metal pipe and was intended to be a 5:1 scale reproduction of a 3 m diameter prototype culvert with 10% embedment, as required by the Manitoba Stream Crossing Guidelines for the Protection of Fish and Fish Habitat (MNR, 1996). The model was constructed with a projecting end inlet as this is the most commonly used inlet configuration in Manitoba. An automated sampling system using acoustic Doppler velocimetry was developed to conduct detailed sampling of flow velocities along the full length of the model under roughly uniform flow conditions.

6.1 Summary of Experimental Results

Experimental testing was conducted with slopes of 0%, 0.5% and 1.0% and with flows ranging from 0.064 m³/s to 0.254 m³/s, with subcritical flow conditions occurring in all cases. Each slope was tested with a low and high flow case producing a range of average relative depths from 0.42D_o to 0.76D_o with the tailwater gate adjusted to approximate uniform flow depth along the length of the culvert barrel. Detailed velocity measurements were made at 13 sampling locations along the length of the culvert for those runs with tailwater control. Water surface profiles were recorded for each experimental run, with and without tailwater control.

A Matlab analysis suite developed for this project was used to interpolate point velocity data, producing isovel plots of the velocity distribution at each sampling location. Examination of the isovel plots and vertical velocity profiles revealed that the velocity structure is strongly influenced by the contraction effect of the inlet, the water depth, and the average velocity. In all experimental runs, a strong contraction effect was measured; producing eddies with adverse currents occupying roughly 25% of the flow area immediately downstream from the inlet. Measured velocities within the contraction reached as high as 150% of the average inlet velocity. However, the full extent of the

contraction was not determined as the sampling locations were fixed. The contraction effect appeared to dissipate by roughly 3 diameters downstream from the inlet for all runs.

For all flow depths, the velocity gradient normal to the culvert walls was greater than the velocity gradient over the gravel bed, though the extent by which they differed varied greatly. At relative depths approaching $0.5D_o$, the isovel contours are roughly parallel to the culvert bed and walls. At relative depths closer to $0.75D_o$, a distinct low velocity zone developed over gravel bed, protruding into the flow towards the center of the culvert and creating a dual-lobed appearance to the isovel structure. Local velocity maxima were observed on both sides of the culvert.

As the average flow velocity increased, this bed-affected region of low velocity water became less distinct, with the isovels beginning to dip towards the center of the bed in the low flow runs. The maximum velocity became more localized in the center of the flow region and in the low flow cases, the most extensive zones of low velocity water were near the corner where the bed and wall meet. The effect of isolating the bed roughness was investigated by installing smooth plastic inserts, greatly reducing the culvert wall roughness. It was discovered that doing so produced the dual-lobed isovel shape previously seen only in the deeper high flow cases. The low velocity zone in the smooth wall trials was less extensive laterally and more localised over the bed than in the corresponding run with unaltered wall roughness. However, the vertical extent of the bed affected region was greater, owing to the redistributing of the flow towards the smooth culvert wall. This phenomenon may have implications relating to fish passage, sediment transport and scour in the design of embedded concrete culverts, where the bed roughness greatly exceeds that of the walls. This result suggests that the roughness of the bed relative to the walls is as important as water depth or velocity with respect to isovel shape and therefore velocity distribution and it may be possible to deliberately customize the shape of velocity field to suit the needs of affected fish species.

A number of researchers have observed that in circular CSP culverts, juvenile and weak swimming fish utilize the low velocity zones adjacent to the culvert wall and water surface (Behlke et al., 1991; Barber and Downs, 1996, Kane and Wellen, 1985). These zones are often attributed to the presence of secondary currents and tend to become smaller or disappear once the flow depth in the culvert becomes greater than half the diameter.

An interesting observation may be made from this relating to fish passage in embedded culverts. The Manitoba Stream Crossing Guidelines for the Protection of Fish and Fish Habitat (Manitoba Natural Resources, 1996) state that the flow depth in culverts is not to exceed half the diameter of the pipe during fish migration periods, presumably to ensure that the low velocity migration zones will be present. Based on qualitative observations of model results, the low velocity zones that develop near the bed appear to provide equally favourable conditions when compared to the "migration zones" near the wall. Therefore, unless a behavioral or biological basis exists that requires juvenile and weak swimming fish to exclusively use these surface migration zones, then they will also be able to ascend upstream using the low velocity zones created by the rough gravel bed. Hence, the continued relevance of stipulated maximum water depths as part of fish passage criteria should be critically reviewed in light of embedment requirements for culverts.

As mentioned earlier, secondary currents associated with turbulent open channel flow are believed to be responsible for unexpected changes in velocity structure (Chow, 1959; Schlichting, 1979; Barber and Downs, 1996; Ead et al., 2000). In addition, fish are most strongly affected by turbulence on a scale that approaches their body size. Therefore, the suitability of using 3 dimensional ADV velocity measurements to describe relevantly scaled secondary currents was investigated. Quiver (vector) plots of the v and w velocity components showed a strong correlation with the streamwise velocity structure. In the high flow cases with deeper water, secondary currents moved strongly from the bed and side-walls toward the culvert center and into the corners where relatively high velocities were observed. At lower flow depths, secondary currents moved from the walls, towards

the center of the culvert and towards the bed, possibly explaining the lack of a distinct bed-affected region of low velocity water. Though a crude effort, these results provide preliminary insight into the structure of secondary currents occurring in embedded circular CSP culverts. In light of the increasing importance placed upon turbulence with respect to fish passage, the ADV appears to be a useful tool for further investigation of secondary currents and potentially more detailed turbulence measurements.

Taking inspiration from work done by Barber and Downs (1996), White (1996) and House et al. (2005), an investigation was performed to see how the normalized velocity distributions compared across all experiments when related percent flow area. The results showed a strong correlation between cross-sectional flow area and relative velocity (u/u_{avg}) downstream of the zone affected by the contraction, irrespective of the average flow velocity and depth. The strong trend in the data suggests that a regression-based method of predicting percent flow area at a given velocity may be a feasible alternative to explicit velocity prediction and merits further study.

Unlike the traditionally held view, the turbulent boundary layer appears to develop from the bed upward and from the water surface downward, obscuring the concept of flow development somewhat. Despite large variations in the vertical velocity profile across the flow width, the central and non-central profiles appear to stabilize at roughly the same distance downstream within each experimental run. Generally, the distance downstream at which the flow became fully developed increased with flow depth. Based on the stability of the overall flow profile, the flow appeared to develop fully by 4.4 and 6.1 diameters downstream in the low flow and high flow cases respectively. However, some shifting in the velocity profiles was observed along the remainder of the culvert in all experimental runs, likely due to minor perturbations in the culvert cross-section, alignment, bed roughness and associated secondary currents. Flow development has implications for fish passage relating to the extent of the low velocity zone near the bed relative to longitudinal location in the culvert. It is unclear from these results whether the projecting end inlet delays turbulent boundary layer development in embedded circular CSP culverts.

By cross-section 6, roughly 4.4 diameters downstream from the inlet, the vertical velocity profiles were generally well described by the Log Law up to the depth where u_{max} occurred, with the profiles measured over the culvert wall showing a greatly reduced logarithmic region. At depths above u_{max} , the velocity profiles dip downward, due to the depression of u_{max} below the water surface. The logarithmic portion of the profiles were used to determine the distribution of shear velocity (u^*) and equivalent sand roughness (k_s) across the width of flow and along the length of the culvert barrel. For each run, significant variation occurred in the distribution of both parameters along the culvert barrel in the region of fully developed flow, more so with k_s than with u^* . Likely, this variation was due to the difficulty in accurately determining individual shear velocities from velocity profiles. Accurate measurement of k_s across each cross-section was further hindered by the high variability of the gravel bed surface. As no clear trend was observed along the culvert barrel, the results of each run were averaged for the region of fully developed flow and strong trends emerged in the distribution of both parameters across the width of flow.

The shape of the u^* profiles were consistent between runs, and the individual curves collapsed significantly when normalized by global shear velocity (i.e. u^*/u_{*o}). Shear velocity tended to increase with average water velocity, with peak values ranging from $1.28u_{*o}$ to $1.64u_{*o}$ occurring between $z = 0.06$ m to 0.12 m. The center plane shear velocity was always somewhat lower than the peak ($1.23u_{*o}$ to $1.48u_{*o}$), reflecting the low velocity zone created by the bed. Toward the culvert wall, the shear velocity dropped off significantly, approaching $0.2u_{*o}$ to $0.6u_{*o}$, depending upon the run. The trend in k_s was similar, though more variable between experimental runs, as mentioned above. The k_s value averaged across all runs fell between the predicted range of $3D_{84}$ to $3.5D_{84}$ across most of the gravel bed. Over the culvert wall, the average k_s dropped rapidly, approaching a value equivalent to the corrugation height, as previously determined by Ead et al. (2000). The trends demonstrated herein suggest that shear velocity and equivalent sand roughness may have a predictable distribution around the wetted perimeter of an embedded culvert. An understanding of the distribution of these

parameters may have applications in the development of a robust velocity prediction model.

Manning's equation is the most widely applied of all existing methods for estimating discharge under open channel flow conditions. The greatest uncertainty in applying Manning's equation lies in determining the roughness coefficient. A number of methods for predicting the Manning's n of the gravel bed were examined and based on model results, it was found that the methods of Bruschin (1985) and Bray (1979) bracketed the range of $0.035 < n < 0.041$ typically applied to Class 350 rip rap, when used as a bed material for embedded culverts in Manitoba. In composite roughness environments such as embedded culverts, determination of Manning's n becomes even more difficult as the common assumption that n is invariant with depth no longer applies (Chow, 1959). Therefore, a number of existing methods for determining composite roughness were evaluated.

As a basis for differentiating between them, the composite roughness of the model culvert was determined experimentally to be roughly 0.024, only slightly higher than for the culvert alone (0.023). However, as the composite n value is affected by water depth, it varied over a range of $0.0230 < \bar{n} < 0.0256$ when the lower and upper parts of the $AR^{2/3}S^{1/2}$ versus Q curve were considered separately. Gradually varied flow profiles were then calculated for each run using the Standard Step Method in conjunction with each composite roughness method and these were compared to measured water surface profiles. By trial and error, it was determined that $n_{bed} = 0.029$ provided a good fit for all experimental runs. For all runs, the conveyance method proposed by Lotter resulted in the lowest composite roughness value and lowest water surface elevation along the full length of the culvert. The largest \bar{n} and elevation values were given by the Einstein and Banks method for all cases except when the relative depth approached $0.25D_o$, where Colebatch was the highest. It was found that all 5 methods produced reasonable results, ranging from 101% to 108% of the experimentally determined value and differing by a maximum of 3.9% from the target elevations at the inlet. The Einstein/Banks and Einstein/Horton methods performed marginally better, producing the smallest amount of

variation from the target elevations across all experimental runs. However, these results cannot conclusively recommend one method over another.

By far the most significant head losses at any point in the culvert occurred as a result of the projecting inlet. It was found that if the water velocity in the inlet is small, then inlet losses can be estimated by the following equation:

$$\Delta H = \frac{(1 + k_e)(u_{avg})^2}{2g} . \quad (5.20)$$

However, as the width of the headwater box was roughly $2D_o$, equation 5.20 tended to overestimate inlet losses by as much as 15%. The inlet losses were predicted within 8.8% of measured values the inlet pool velocity was accounted for as follows:

$$\Delta H = \frac{(1 + k_e)(u_{avg})^2}{2g} - \frac{(u_{pool})^2}{2g} . \quad (5.21)$$

HEC-RAS is one of the most widely used design tools in the world for calculating stage and discharge through rivers, canals and stream crossing structures. As such, it was undertaken to evaluate the ability of HEC-RAS Beta 4.0 to accurately simulate the measured water surface profile from each of the experimental runs. The Manning's roughness was set to 0.023 for the culvert and 0.029 for the gravel bed. HEC-RAS uses the Direct Step Method for computing water surface profiles and the Einstein/Horton Method for computing composite roughness, so this exercise was also a valuable check of the Standard Step profile calculations performed. HEC-RAS produced results within 1% of the target inlet elevation for all runs but tended to underestimate inlet losses by an average of 9%.

The maximum discharge in a circular culvert under open channel flow conditions occurs at a relative depth of $0.938y/D_o$ (Chow, 1959). The addition of a gravel bed will reduce the maximum capacity of a culvert due to the reduction in flow area and the increase in composite roughness. However, the resulting reduction in capacity is hard to predict. Therefore, the approach of varying n with Q was used to estimate analytically the effect

of 10% embedment on maximum discharge. The results predict an 11% reduction in maximum discharge for a 3.0 m diameter circular CSP culvert when embedded by 10% using Class 350 rip rap as the bed material.

6.2 Recommendations

Based on a review of existing literature and the results of this study, several recommendations are proposed to provide guidance for future research and to highlight areas where changes to current regulations may improve the performance of embedded CSP culverts for fish passage.

6.2.1 Recommendations for further research

- Acoustic Doppler velocimetry is recommended as a tool for studying streamwise velocity structure, secondary currents and turbulence characteristics in embedded culverts,
- Continue the current study varying the average size of the bed material (D_{50}) and depth of bury (d_b) and culvert size (D_o) over a wide range of values,
- Develop dimensionless parameters relating d_b/D_o and D_{50}/D_o to the distribution of equivalent sand roughness across the bed and around the wetted perimeter,
- Relate d_b/D_o and D_{50}/D_o to relative depth and the distribution of shear velocity around the wetted perimeter for a given discharge,
- Investigate the feasibility of developing a method of predicting the velocity distribution using the Log Law in conjunction with predicted distributions of shear velocity and equivalent sand roughness,
- Develop a method of predicting the % area-velocity distribution using regression based analysis,
- Continue the current study to investigate the effect other inlet configurations on the velocity structure and fully describe the resulting contraction effect,
- Continue the current study to investigate the velocity structure in embedded box culverts,

- Continue the current study to investigate the effect of surcharged conditions on flow structure,
- Utilize alternative ADV probe configurations to allow velocity sampling very near to the water surface and prevent flow separation from interfering with sample collection,
- Investigate existing composite roughness methods over a wider range of relative water and bed depths and with a range of bed material sizes,

6.2.2 Recommendations for Immediate Application

- The continued relevance of stipulated maximum water depths as part of fish passage criteria should be critically reviewed in light of embedment requirements for culverts.
- The 5 composite roughness methods investigated produced highly comparable results over a range of relative depths $0.42 < y/D_o < 0.76$. In ascending order from most conservative to least, the composite roughness methods rank as Lotter, Los Angeles District, Colebatch, Einstein/Horton and Einstein/Banks. Einstein/Horton may be preferred due to its calculation stability at low flow depths.
- HEC-RAS Beta 4.0 is recommended for use with embedded circular CSP culverts, producing average water surface profiles within a few percent of measured values.
- Designers can expect a reduction in maximum discharge of roughly 11% when circular CSP culverts are embedded by $0.1D_o$ and Class 350 rip rap is used as the bed material.

References

Abt, S. R., Ruff, J. F., Doehring, F. K., and Donnell, C.A. (1987) "Influence of Culvert Shape on Outlet Scour," *Journal of Hydraulic Engineering*, ASCE, (113)(3), 393-400

Barber, M.E., and Downs, R.C. (1996) "Investigation of culvert hydraulics related to juvenile fish passage." Washington State Department of Transportation Report. WA-RD 388.2

Behlke, C.E., Kane, D.L., McLean, R.F., and Travis, M.D. (1991) "Fundamentals of culvert design for passage of weak-swimming fish." U.S. Department of Transportation Report No. FHWA-AK-RD-90-10. 153p

Belataos, S. (1995) "River Ice Jams." Water Resources Publications, Highlands Ranch, Colorado

Bray, D.I. (1979) "Estimating average velocity in gravel-bed rivers." *Journal of Hydraulics Division*. ASCE. 105(HY9), 1103-1122.

Brunner, G.W. (2002) "HEC-RAS River Analysis System – Hydraulic Reference Manual." Version 3.1, United States Army Corps of Engineers, Hydrologic Engineering Center, Report No. CPD-69, Davis, CA. 350pp

Brunner, G.W. (2006) "HEC-RAS River Analysis System – User's Manual." Version 4.0, United States Army Corps of Engineers, Hydrologic Engineering Center, Report No. CPD-68, Davis, CA. 420pp

Bruschin, J. (1985) "Discussion on Brownlie (1983): Flow depth in sand-bed channels." *Journal of Hydraulic Engineering*. ASCE, 111, 736-739

Canadian Department of Fisheries and Ocean and Manitoba Natural Resources. (1996) "Manitoba stream crossing guidelines for the protection of fish and fish habitat." 48 pp. + app.

Charlton, F.G., Brown, P.M., and Benson, R.W. (1978) "The hydraulic geometry of some gravel rivers in Britain." H.R. Wallingford, Report No. IT180

Chiu, C-L. (1989) "Velocity distribution in open-channel flow." Journal of Hydraulic Engineering, ASCE, 115(5), 615-628

Chiu, C-L., Lin, G-F., and Lu, J-M. (1993) "Application of probability and entropy concepts in pipe-flow study." Journal of Hydraulic Engineering, ASCE, 119(6), 742-755

Chow, V.T. (1959) "Open-Channel Hydraulics." McGraw-Hill, New York, N.Y., 680p

Chow, V.T. (1964) "Handbook of Applied Hydrology. A Compendium of Water Resource Technology ." McGraw-Hill Book Company, New York, N.Y., 572p

Clayton, B. (1997) "Estimating Flows in Composite Roughness Environments." Graduation project. Department of Civil Engineering, University of Manitoba, Winnipeg, MB.

Colebatch, G.T. (1941) "Model tests on the Liawenee Canal roughness coefficients." Journal of the Institute of Engineers, 13(2), 27-32

Cox, R.G. (1973) "Effective hydraulic roughness for channels having bed roughness different from bank roughness." U.S. Army Corps of Engineers, Paper No. H-73-2. Vicksburg, M.S.

Ead, S.A., Rajaratnam, N., Katopodis, C., and Ade, F. (2000) "Turbulent open-channel flow in circular corrugated culverts." Journal of Hydraulic Engineering, 126(10), 750-757

Ead, S.A., Rajaratnam, N., and Katopodis, C. (2002) "Generalized study of hydraulics of culvert fishways." *Journal of Hydraulic Engineering*, 128(11), 1018-1022

Einstein, H.A. (1934) "Der hydraulische oder profil-radius (The hydraulic radius or cross section radius)." *Schweizerische Bauzeitung*, Zurich, 103(8), 89-91

Einstein, H.A., and Banks, R.B., (1950) "Fluid Resistance of Composite Roughness." *Transactions of the American Geophysical Union*, 31(4), 603-610

Handbook of steel drainage and highway construction products. (2002) 2nd Canadian Edition, American Iron and Steel Institute, Washington, D.C.

Hans, P. (1997) "Discharge Calculation Techniques for Low Head Hydroelectric Plants." M.S. Thesis, Department of Civil Engineering, University of Manitoba, Winnipeg, Manitoba

Hey, R.D. (1979) "Flow resistance in gravel bed rivers." *Journal of the Hydraulics Division, ASCE*. 107(7), 899-918

Horton, R. E. (1933) "Separate roughness coefficients for channel bottom and sides." *Engineering News-Record*, 111(22), 652-653.

House, M.R., Pyles, M.R., and White, D. (2005) "Velocity distributions in streambed simulation culverts used for fish passage." *Journal of the American Water Resources Association*, 41(1), 209-217

Hydraulic Design of Flood Control Channels (1994) U.S. Army Corps of Engineers. EM 1110-2-1601. Washington, D.C.

International Standard (ISO) 3354 (1975) "Measurement of clean water flow in closed

conduits - Velocity-area method using current-meters.” ISO 3354-1975 (E)

Jarrett, R.D. (1984). “Hydraulics of high-gradient streams.” *Journal of Hydraulic Engineering*, ASCE, 110(11), 1519-1539

Julien, P.Y. (2002) “River Mechanics.” Cambridge University Press, New York, N.Y., 434p

Kane, D.L. and Wellen, P.M. (1985) “A hydraulic evaluation of fish passage through roadway culverts in Alaska.” Institute of Water Resources, University of Alaska-Fairbanks, Fairbanks, AK; State of Alaska, Department of Transportation and Public Facilities, Research Section, Fairbanks, AK., 54p

Katopodis, C., Robinson, P.R., and Sutherland, B.G. (1978) “A study of model and prototype culvert baffling for fish passage.” Canadian Fisheries and Marine Service. Technical Report No. 828. 78p

Katopodis, C. (1992) “Introduction to fishway design.” Working Document, Freshwater Institute, Fisheries and Oceans Canada, Winnipeg, MB. 67p

Katopodis, C. (2005) “Developing a toolkit for fish passage, ecological flow management and fish habitat works.” *Journal of Hydraulic Research*, 43(5), 451-467

Knight, D.W., and Sterling, M. (2000) “Boundary shear in circular pipes running partially full.” *Journal of Hydraulic Engineering*. 126(4), 263-275

Limerinos, J.T. (1970) “Determination of the manning coefficient from measured bed roughness in natural channels.” U.S. Geological Survey Water Supply Paper 1898-B, pB1-B47.

Liu, M., Zhu, D.Z., and Rajaratnam, N. (2002) "Evaluation of ADV measurements in bubbly two-phase flows." Hydraulic Measurements and Experimental Methods Conference Paper. American Society of Civil Engineers.

Lotter, G.K. (1933) "Considerations on hydraulic design of channels with different roughness of walls." Transactions, All-Union Scientific Research Institute of Hydraulic Engineering, 7, 238-241

Manitoba Infrastructure and Transportation (2003) "Standard Construction Specifications." Specifications for Stone Rip Rap, No. 1297, July 2003.

Meyer-Peter, E. and Muller, R. (1948) "Formulas for bed-load transport." 3rd Meeting of IAHR. International Association of Hydraulic Engineering and Research. Stockholm, Sweden, 39-64

Mountjoy, P.K. (1986) "Velocity profile prediction in culverts for fish passage design considerations." M.S. Thesis, University of Alaska, Fairbanks, AK.

Mufeed, O., Noreika, J.F., Haro, A., Maynard, A., Castro-Santos, T., and Cada, G.F. (2002) "Evaluation Of The Effects Of Turbulence On The Behavior Of Migratory Fish." U.S. Geological Survey and Oak Ridge National Laboratory, Report to Bonneville Power Administration, BPA Report# DOE/BP-00000022-1, 55pp

Neill, C.R. (2001) "Guide to Bridge Hydraulics." 2nd Ed., Transportations Association of Canada. 200p

Peake, S. (in press) "Passage performance of walleye, northern pike, and white sucker in an experimental culvert." North American Journal of Fisheries Management.

Rajaratnam, N., Katopodis, C., and Lodewyk, S. (1988) "Hydraulics of offset baffle culvert fishways." Canadian Journal of Civil Engineering, 15, 1043-1051

Rajaratnam, N., and Katopodis, C. (1990) "Hydraulics of culvert fishways III." Canadian Journal of Civil Engineering, 17, 558-568

Replogle, J.A., and Chow, V.T. (1966) "Tractive-force distribution in open channels." Journal of the Hydraulics Division, ASCE, 92(HY2), 169-191

Roberson, J.A. and Crow, C.T. (1990) "Engineering Fluid Mechanics." Houghton Mifflin Company, Boston, MA.

Schlichting, H. (1979) "Boundary Layer Theory." 7th Ed., McGraw-Hill, New York, N.Y., 817p

SonTek. (1997) "Acoustic Doppler Velocimeter Technical Documentation." Version 4.0, San Diego, California

Sterling, M., and Knight, D.W. (2000) "Resistance and boundary shear in circular conduits with flat beds running part full." Proceedings of the Institution of Civil Engineers. Water, maritime and energy. 142(4), 229-240

Strickler, A. (1923) "Beitraege zur Frage der Geschwindigkeitsformel und der Rauheitszahlen fuer Stroeme Kanaele und geschlossene Leitungen." Mitteilungen des Eidgenoessischer Amtes fuer Wasserwirtschaft, Bern, Switzerland, 16 (in German) (Translated as "Contributions to the question of a velocity formula and roughness data for streams, channels and closed pipelines" by Roesgan, T. and Brownlie, W.R.).

Ugarte, A. and M. Madrid (1994) "Roughness Coefficient in Mountain Rivers," Proceedings National Conference on Hydraulic Engr., ASCE, 652-656.

Voulgaris, G., and Trowbridge, J.H. (1998) "Evaluation of acoustic Doppler velocimeter (ADV) for turbulence measurements." *Journal of atmospheric and oceanic technology*. 15(1), 272-289

Watts, F.J., (1974) "Design of culvert fishways." Water Resources Research Institute. University of Idaho, Moscow, Idaho. 68p

White, D. (1996) "Hydraulic performance of countersunk culverts in Oregon." M.S. Thesis, Department of Forestry Engineering, Oregon State University, Corvallis, OR.

Yalin, M.S. (1972) "Mechanics of Sediment Transport." Pergamon, Oxford, 290 pp

Appendix A – Sample Motion Control Program and Output

DMC File for Station 4-26: Ytip~120 mm (water depth~0.468 mm)

The program is presented in two columns to conserve space. With each paired command, the first number refers to the X motor, and the second refers to the Y motor.

```
#FRT120MM
TR 0; KI 1,1
TL 9.5,9.5
ER 10000,10000
OE 1,1
AC 15000,15000
DC 15000,15000
SP 15000,15000
MG "XS4 TO XS26 ONLY!!"
MG "USE FOR YTIP=120MM"
MG " "
MG "CHECK CART SETUP"
MG "PRESS 1 TO CONTINUE"
MG "PRESS 99 TO ABORT"
IN "FOLLOWED BY 'ENTER'",N
MG " "
JP #ABORT,N<>1
MG " "
MG "START ADV AND PROGRAM"
MG "SIMULTANEOUSLY"
MG " "
MG "PRESS 1 TO CONTINUE"
MG "PRESS 99 TO ABORT"
IN "FOLLOWED BY 'ENTER'",N
MG " "
JP #ABORT,N<>1
MG " "
MG "10 SECONDS TO START"
WT 10000; DP 0,0; C=1
#0DEG
MG " "
MG "SAMPLING THE "
MG "0 DEGREE TRANSECT"
MG " "
PA 0,387500; BG;
AM;T=TIME-T0;T=
T=TIME-T0;T=
TP; WT 40000;
PA 0,377500;BG;
AM;T=TIME-T0;T=
TP; WT 40000;
PA 0,357500;BG;
AM;T=TIME-T0;T=
TP; WT 40000;
PA 0,337500;BG;
AM;T=TIME-T0;T=
TP; WT 40000;
PA 0,317500;BG;
AM;T=TIME-T0;T=
TP; WT 40000;
PA 0,277500;BG;
AM;T=TIME-T0;T=
TP; WT 40000;
PA 0,237500;BG;
AM;T=TIME-T0;T=
TP; WT 40000;
PA 0,197500;BG;
AM;T=TIME-T0;T=
TP; WT 40000;
PA 0,157500;BG;
AM;T=TIME-T0;T=
TP; WT 40000;
PA 0,137500;BG;
AM;T=TIME-T0;T=
TP; WT 40000;
PA 0,110000;BG;
AM;T=TIME-T0;T=
TP; WT 40000;
#5DEG
MG " "
MG "SAMPLING THE "
MG "5 DEGREE TRANSECT"
MG " "
PA 28000,392500;BG;
AM;T=TIME-T0;T=
TP; WT 40000;
PA 28000,382500;BG;
AM;T=TIME-T0;T=
TP; WT 40000;
PA 28000,362500;BG;
AM;T=TIME-T0;T=
TP; WT 40000;
PA 28000,302500;BG;
AM;T=TIME-T0;T=
TP; WT 40000;
#10DEG
MG "SAMPLING THE "
MG "10 DEGREE TRANSECT"
MG " "
PA 58500,397500;BG;
```

```

AM;T=TIME-T0;T=
TP; WT 40000;
PA 58500,387500;BG;
AM;T=TIME-T0;T=
TP; WT 40000;
PA 58500,367500;BG;
AM;T=TIME-T0;T=
TP; WT 40000;
PA 58500,347500;BG;
AM;T=TIME-T0;T=
TP; WT 40000;
PA 58500,327500;BG;
AM;T=TIME-T0;T=
TP; WT 40000;
PA 58500,287500;BG;
AM;T=TIME-T0;T=
TP; WT 40000;
PA 58500,227500;BG;
AM;T=TIME-T0;T=
TP; WT 40000;
PA 58500,167500;BG;
AM;T=TIME-T0;T=
TP; WT 40000;
#15DEG
MG "SAMPLING THE "
MG "15 DEGREE TRANSECT"
MG " "
PA 88000,402500;BG;
AM;T=TIME-T0;T=
TP; WT 40000;
PA 88000,392500;BG;
AM;T=TIME-T0;T=
TP; WT 40000;
PA 88000,372500;BG;
AM;T=TIME-T0;T=
TP; WT 40000;
PA 88000,312500;BG;
AM;T=TIME-T0;T=
TP; WT 40000;
#20DEG
MG "SAMPLING THE "
MG "20 DEGREE TRANSECT"
MG " "
PA 119000,407500;BG;
AM;T=TIME-T0;T=
TP; WT 40000;
PA 119000,397500;BG;
AM;T=TIME-T0;T=
TP; WT 40000;
PA 119000,377500;BG;
AM;T=TIME-T0;T=
TP; WT 40000;
PA 119000,357500;BG;
AM;T=TIME-T0;T=
TP; WT 40000;
PA 119000,337500;BG;
AM;T=TIME-T0;T=
TP; WT 40000;
TP; WT 40000;
PA 119000,297500;BG;
AM;T=TIME-T0;T=
TP; WT 40000;
PA 119000,257500;BG;
AM;T=TIME-T0;T=
TP; WT 40000;
PA 119000,217500;BG;
AM;T=TIME-T0;T=
TP; WT 40000;
PA 119000,177500;BG;
AM;T=TIME-T0;T=
TP; WT 40000;
PA 119000,137500;BG;
AM;T=TIME-T0;T=
TP; WT 40000;
PA 119000,127500;BG;
AM;T=TIME-T0;T=
TP; WT 40000;
#25DEG
MG "SAMPLING THE "
MG "25 DEGREE TRANSECT"
MG " "
PA 150000,397500;BG;
AM;T=TIME-T0;T=
TP; WT 40000;
PA 150000,377500;BG;
AM;T=TIME-T0;T=
TP; WT 40000;
PA 150000,357500;BG;
AM;T=TIME-T0;T=
TP; WT 40000;
PA 150000,317500;BG;
AM;T=TIME-T0;T=
TP; WT 40000;
PA 150000,277500;BG;
AM;T=TIME-T0;T=
TP; WT 40000;
#30DEG
MG "SAMPLING THE "
MG "30 DEGREE TRANSECT"
MG " "
PA 182500,377500;BG;
AM;T=TIME-T0;T=
TP; WT 40000;
PA 182500,357500;BG;
AM;T=TIME-T0;T=
TP; WT 40000;
PA 182500,337500;BG;
AM;T=TIME-T0;T=
TP; WT 40000;
PA 182500,317500;BG;
AM;T=TIME-T0;T=
TP; WT 40000;
PA 182500,297500;BG;
AM;T=TIME-T0;T=
TP; WT 40000;

```

```

PA 182500,257500;BG;
AM;T=TIME-T0;T=
TP; WT 40000;
PA 182500,197500;BG;
AM;T=TIME-T0;T=
TP; WT 40000;
#35DEG
MG "SAMPLING THE "
MG "35 DEGREE TRANSECT"
MG " "
PA 215000,347500;BG;
AM;T=TIME-T0;T=
TP; WT 40000;
PA 215000,327500;BG;
AM;T=TIME-T0;T=
TP; WT 40000;
PA 215000,307500;BG;
AM;T=TIME-T0;T=
TP; WT 40000;
PA 215000,247500;BG;
AM;T=TIME-T0;T=
TP; WT 40000;
#40DEG
MG "SAMPLING THE "
MG "40 DEGREE TRANSECT"
MG " "
PA 247000,317500;BG;
AM;T=TIME-T0;T=
TP; WT 40000;
PA 247000,297500;BG;
AM;T=TIME-T0;T=
TP; WT 40000;
PA 247000,277500;BG;
AM;T=TIME-T0;T=
TP; WT 40000;
PA 247000,257500;BG;
AM;T=TIME-T0;T=
TP; WT 40000;
PA 247000,237500;BG;
AM;T=TIME-T0;T=
TP; WT 40000;
PA 247000,197500;BG;
AM;T=TIME-T0;T=
TP; WT 40000;
PA 247000,177500;BG;
AM;T=TIME-T0;T=
TP; WT 40000;
PA 247000,167000;BG;
AM;T=TIME-T0;T=
TP; WT 40000;
#47DEG
MG "SAMPLING THE "
MG "47 DEGREE TRANSECT"
MG " "
PA 290000,227500
BG Y; AM; BG X;
AM;T=TIME-T0;T=
TP; WT 40000;
PA 290000,192500;BG;
AM;T=TIME-T0;T=
TP; WT 40000;
#N5DEG
MG "SAMPLING THE "
MG "-5 DEGREE TRANSECT"
MG " "
PA -27500,392500;
BG X; AM; BG Y;
AM;T=TIME-T0;T=
TP; WT 40000;
PA -27500,382500;BG;
AM;T=TIME-T0;T=
TP; WT 40000;
PA -27500,362500;BG;
AM;T=TIME-T0;T=
TP; WT 40000;
PA -27500,302500;BG;
AM;T=TIME-T0;T=
TP; WT 40000;
#N10DEG
MG "SAMPLING THE "
MG "-10 DEGREE TRANSECT"
MG " "
PA -54500,397500;BG;
AM;T=TIME-T0;T=
TP; WT 40000;
PA -54500,387500;BG;
AM;T=TIME-T0;T=
TP; WT 40000;
PA -54500,367500;BG;
AM;T=TIME-T0;T=
TP; WT 40000;
PA -54500,347500;BG;
AM;T=TIME-T0;T=
TP; WT 40000;
PA -54500,327500;BG;
AM;T=TIME-T0;T=
TP; WT 40000;
PA -54500,287500;BG;
AM;T=TIME-T0;T=
TP; WT 40000;
PA -54500,227500;BG;
AM;T=TIME-T0;T=
TP; WT 40000;
PA -54500,167500;BG;
AM;T=TIME-T0;T=
TP; WT 40000;
#N15DEG
MG "SAMPLING THE "
MG "-15 DEGREE TRANSECT"
MG " "
PA -80500,402500;BG;
AM;T=TIME-T0;T=
TP; WT 40000;
PA -80500,392500;BG;

```

```

AM;T=TIME-T0;T=
TP; WT 40000;
PA -80500,372500;BG;
AM;T=TIME-T0;T=
TP; WT 40000;
PA -80500,312500;BG;
AM;T=TIME-T0;T=
TP; WT 40000;
#N20DEG
MG "SAMPLING THE "
MG "-20 DEGREE TRANSECT"
MG " "
PA -104000,407500;BG;
AM;T=TIME-T0;T=
TP; WT 40000;
PA -104000,397500;BG;
AM;T=TIME-T0;T=
TP; WT 40000;
PA -104000,377500;BG;
AM;T=TIME-T0;T=
TP; WT 40000;
PA -104000,357500;BG;
AM;T=TIME-T0;T=
TP; WT 40000;
PA -104000,337500;BG;
AM;T=TIME-T0;T=
TP; WT 40000;
PA -104000,297500;BG;
AM;T=TIME-T0;T=
TP; WT 40000;
PA -104000,257500;BG;
AM;T=TIME-T0;T=
TP; WT 40000;
PA -104000,217500;BG;
AM;T=TIME-T0;T=
TP; WT 40000;
PA -104000,177500;BG;
AM;T=TIME-T0;T=
TP; WT 40000;
PA -104000,137500;BG;
AM;T=TIME-T0;T=
TP; WT 40000;
PA -104000,127500;BG;
AM;T=TIME-T0;T=
TP; WT 40000;
#N25DEG
MG "SAMPLING THE "
MG "-25 DEGREE TRANSECT"
MG " "
PA -127000,397500;BG;
AM;T=TIME-T0;T=
TP; WT 40000;
PA -127000,377500;BG;
AM;T=TIME-T0;T=
TP; WT 40000;
PA -127000,357500;BG;
AM;T=TIME-T0;T=
TP; WT 40000;
PA -127000,317500;BG;
AM;T=TIME-T0;T=
TP; WT 40000;
PA -127000,277500;BG;
AM;T=TIME-T0;T=
TP; WT 40000;
PA -127000,257500;BG;
AM;T=TIME-T0;T=
TP; WT 40000;
#N30DEG
MG "SAMPLING THE "
MG "-30 DEGREE TRANSECT"
MG " "
PA -146500,377500;BG;
AM;T=TIME-T0;T=
TP; WT 40000;
PA -146500,357500;BG;
AM;T=TIME-T0;T=
TP; WT 40000;
PA -146500,337500;BG;
AM;T=TIME-T0;T=
TP; WT 40000;
PA -146500,317500;BG;
AM;T=TIME-T0;T=
TP; WT 40000;
PA -146500,297500;BG;
AM;T=TIME-T0;T=
TP; WT 40000;
PA -146500,257500;BG;
AM;T=TIME-T0;T=
TP; WT 40000;
PA -146500,197500;BG;
AM;T=TIME-T0;T=
TP; WT 40000;
#N35DEG
MG "SAMPLING THE "
MG "-35 DEGREE TRANSECT"
MG " "
PA -166500,347500;BG;
AM;T=TIME-T0;T=
TP; WT 40000;
PA -166500,327500;BG;
AM;T=TIME-T0;T=
TP; WT 40000;
PA -166500,307500;BG;
AM;T=TIME-T0;T=
TP; WT 40000;
PA -166500,247500;BG;
AM;T=TIME-T0;T=
TP; WT 40000;
#N40DEG
MG "SAMPLING THE "
MG "-40 DEGREE TRANSECT"
MG " "
PA -185000,317500;BG;
AM;T=TIME-T0;T=
TP; WT 40000;
PA -185000,297500;BG;
AM;T=TIME-T0;T=

```



```

TP; WT 40000;
PA -185000,277500;BG;
AM;T=TIME-T0;T=
TP; WT 40000;
PA -185000,257500;BG;
AM;T=TIME-T0;T=
TP; WT 40000;
PA -185000,237500;BG;
AM;T=TIME-T0;T=
TP; WT 40000;
PA -185000,197500;BG;
AM;T=TIME-T0;T=
TP; WT 40000;
PA -185000,177500;BG;
AM;T=TIME-T0;T=
TP; WT 40000;
PA -185000,167500;BG;
AM;T=TIME-T0;T=
TP; WT 40000;
#N47DEG
MG "SAMPLING THE "
MG "-47 DEGREE TRANSECT"
MG " "
PA -210000,227500;BG Y;
AM; BG X;
AM;T=TIME-T0;T=
TP; WT 40000;
PA -210000,192500;BG;
AM;T=TIME-T0;T=
TP; WT 40000;
MG " "
MG "TOTAL TIME ="
T=TIME-T0;T=
MG "RETURNING TO HOME"
PA 0,0; BG X;
AM; BG Y;
MG "TURN OFF THE ADV"
MG " "
AM;
MG "SAMPLING COMPLETE!!!"
M=99
JP #END, M=99
#ABORT
MG "PROGRAM ABORTED"
#END
EN

```

DMC Output for Station 4-26: Ytip ~120 mm (water depth~0.468 mm)

The output is presented in two columns to conserve space. Each line of the output is a set consisting of a time (seconds) and a pair of positional data (counts). The first of the paired numbers refers to the X motor, and the second refers to the Y motor.

```
XS4 TO XS26 ONLY!!           0000027999, 0000382508
USE FOR YTIP=120MM           0000053916.0000
                               0000028000, 0000362502
CHECK CART SETUP             0000059068.0000
PRESS 1 TO CONTINUE          0000028000, 0000302499
PRESS 99 TO ABORT           SAMPLING THE
FOLLOWED BY 'ENTER'         10 DEGREE TRANSECT

START ADV AND PROGRAM        0000066610.0000
SIMULTANEOUSLY              0000058500, 0000397509
                               0000068308.0000
PRESS 1 TO CONTINUE          0000058500, 0000387502
PRESS 99 TO ABORT           0000070730.0000
FOLLOWED BY 'ENTER'         0000058500, 0000367504
                               0000073152.0000
10 SECONDS TO START         0000058500, 0000347504
                               0000075574.0000
SAMPLING THE                 0000058500, 0000327502
0 DEGREE TRANSECT           0000079362.0000
                               0000058500, 0000287508
0000000000.0000             0000084514.0000
0000000000, 0000387500      0000058500, 0000227500
0000001698.0000             0000089666.0000
0000000000, 0000377500      0000058500, 0000167482
0000004118.0000             SAMPLING THE
0000000000, 0000357499      15 DEGREE TRANSECT
0000006538.0000
0000000000, 0000337483      0000106766.0000
0000008958.0000             0000088000, 0000402520
0000000000, 0000317479      0000108464.0000
0000012744.0000             0000088000, 0000392506
0000000000, 0000277478      0000110886.0000
0000016530.0000             0000088000, 0000372503
0000000000, 0000237481      0000116038.0000
0000020316.0000             0000088000, 0000312502
0000000000, 0000197478      SAMPLING THE
0000024102.0000             20 DEGREE TRANSECT
0000000000, 0000157480
0000026522.0000             0000123580.0000
0000000000, 0000137478      0000119000, 0000407509
0000029454.0000             0000125278.0000
0000000001, 0000109982      0000119000, 0000397499
                               0000127700.0000
SAMPLING THE                 0000119000, 0000377497
5 DEGREE TRANSECT           0000130122.0000
                               0000119000, 0000357485
0000049796.0000             0000132544.0000
0000028001, 0000392498      0000119000, 0000337498
0000051494.0000             0000136332.0000
```

0000119000, 0000297490
0000140120.0000
0000119000, 0000257484
0000143908.0000
0000119000, 0000217481
0000147696.0000
0000119000, 0000177492
0000151484.0000
0000119000, 0000137482
0000153182.0000
0000119000, 0000127484
SAMPLING THE
25 DEGREE TRANSECT

0000172670.0000
0000150000, 0000397498
0000175092.0000
0000150000, 0000377497
0000177514.0000
0000150000, 0000357481
0000181302.0000
0000150000, 0000317497
0000185090.0000
0000150000, 0000277482
SAMPLING THE
30 DEGREE TRANSECT

0000192974.0000
0000182500, 0000377498
0000195396.0000
0000182501, 0000357490
0000197818.0000
0000182500, 0000337499
0000200240.0000
0000182500, 0000317498
0000202662.0000
0000182500, 0000297495
0000206450.0000
0000182500, 0000257482
0000211602.0000
0000182500, 0000197478
SAMPLING THE
35 DEGREE TRANSECT

0000222898.0000
0000215000, 0000347507
0000225320.0000
0000215000, 0000327503
0000227742.0000
0000215000, 0000307504
0000232894.0000
0000215000, 0000247507
SAMPLING THE
40 DEGREE TRANSECT

0000238730.0000
0000247000, 0000317493

0000241152.0000
0000247000, 0000297480
0000243574.0000
0000247000, 0000277483
0000245996.0000
0000247000, 0000257493
0000248418.0000
0000247000, 0000237481
0000252206.0000
0000247000, 0000197478
0000254628.0000
0000247000, 0000177481
0000256368.0000
0000247000, 0000166981

SAMPLING THE
47 DEGREE TRANSECT
0000265544.0000
0000290002, 0000227500
0000268990.0000
0000290000, 0000192502
SAMPLING THE
-5 DEGREE TRANSECT

0000306430.0000
-0000027500, 0000392499
0000308128.0000
-0000027500, 0000382507
0000310550.0000
-0000027500, 0000362510
0000315702.0000
-0000027500, 0000302488
SAMPLING THE
-10 DEGREE TRANSECT

0000323244.0000
-0000054500, 0000397506
0000324942.0000
-0000054500, 0000387506
0000327364.0000
-0000054500, 0000367503
0000329786.0000
-0000054500, 0000347505
0000332208.0000
-0000054500, 0000327504
0000335996.0000
-0000054500, 0000287500
0000341148.0000
-0000054500, 0000227501
0000346300.0000
-0000054500, 0000167483
SAMPLING THE
-15 DEGREE TRANSECT

0000363400.0000
-0000080500, 0000402513
0000365098.0000

-0000080500, 0000392502
0000367520.0000
-0000080500, 0000372508
0000372672.0000
-0000080500, 0000312503
SAMPLING THE
-20 DEGREE TRANSECT

0000380214.0000
-0000103999, 0000407508
0000381912.0000
-0000104000, 0000397502
0000384334.0000
-0000104000, 0000377499
0000386756.0000
-0000104000, 0000357498
0000389178.0000
-0000104000, 0000337501
0000392966.0000
-0000104000, 0000297483
0000396754.0000
-0000104000, 0000257484
0000400542.0000
-0000104001, 0000217482
0000404330.0000
-0000104000, 0000177481
0000408118.0000
-0000104000, 0000137478
0000409816.0000
-0000104000, 0000127520
SAMPLING THE
-25 DEGREE TRANSECT

0000429304.0000
-0000127000, 0000397508
0000431726.0000
-0000127001, 0000377497
0000434148.0000
-0000127000, 0000357496
0000437936.0000
-0000127000, 0000317498
0000441724.0000
-0000127000, 0000277502
SAMPLING THE
-30 DEGREE TRANSECT

0000449608.0000
-0000146500, 0000377500
0000452030.0000
-0000146500, 0000357500
0000454452.0000
-0000146500, 0000337497
0000456874.0000
-0000146500, 0000317501
0000459296.0000
-0000146500, 0000297500
0000463084.0000

-0000146500, 0000257503
0000468236.0000
-0000146500, 0000197479
SAMPLING THE
-35 DEGREE TRANSECT

0000479532.0000
-0000166500, 0000347499
0000481954.0000
-0000166500, 0000327504
0000484376.0000
-0000166500, 0000307502
0000489528.0000
-0000166500, 0000247499
SAMPLING THE
-40 DEGREE TRANSECT

0000495364.0000
-0000185000, 0000317500
0000497786.0000
-0000185000, 0000297486
0000500208.0000
-0000185000, 0000277483
0000502630.0000
-0000185000, 0000257483
0000505052.0000
-0000185000, 0000237484
0000508840.0000
-0000185000, 0000197480
0000511262.0000
-0000185000, 0000177482
0000512960.0000
-0000185000, 0000167482
SAMPLING THE
-47 DEGREE TRANSECT

0000520874.0000
-0000210017, 0000227500
0000524320.0000
-0000210000, 0000192502

TOTAL TIME =
0000524322.0000
RETURNING TO HOME
TURN OFF THE ADV

SAMPLING COMPLETE!!!

Appendix B – Isovel Plots

SOQ64

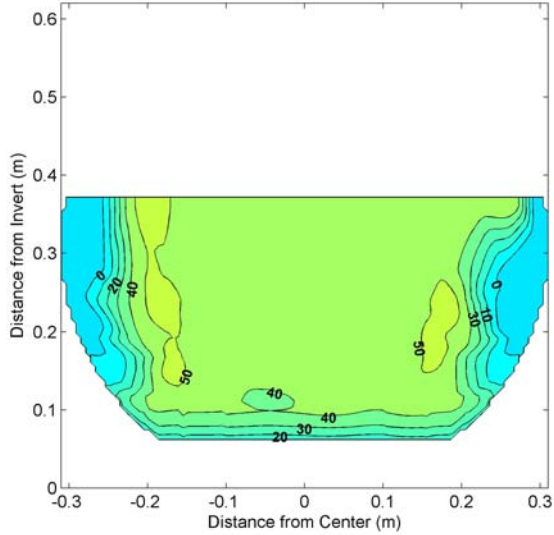


Figure B - 1: $S=0\%$, $Q=0.064 \text{ m}^3/\text{s}$ XS1,
 $y_o=0.310 \text{ m}$, $A=0.173 \text{ m}^2$, $u_{avg}=37.0 \text{ cm/s}$

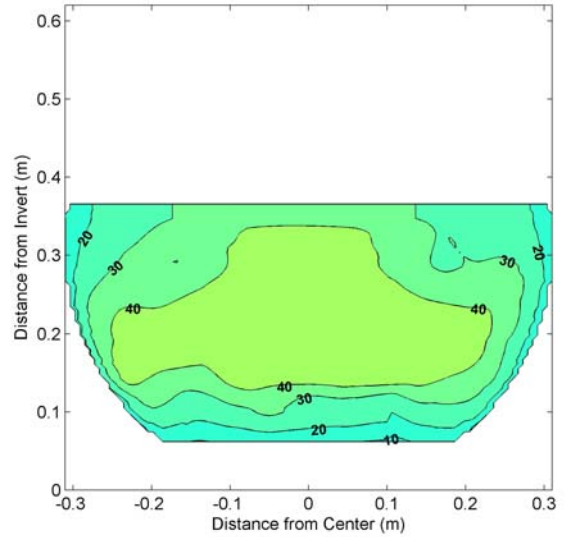


Figure B - 3: $S=0\%$, $Q=0.064 \text{ m}^3/\text{s}$ XS3,
 $y_o=0.303 \text{ m}$, $A=0.169 \text{ m}^2$, $u_{avg}=37.9 \text{ cm/s}$

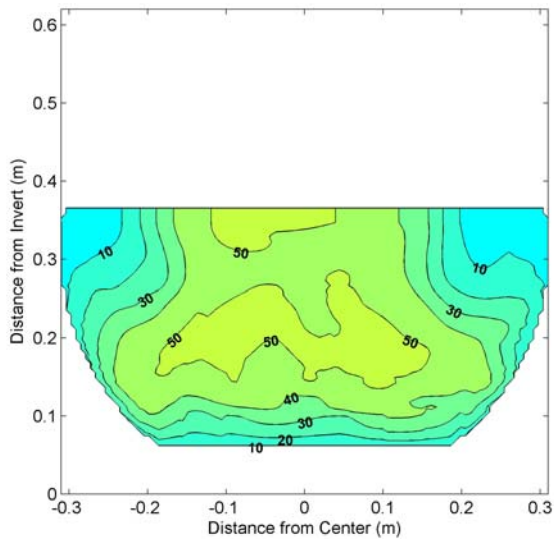


Figure B - 2: $S=0\%$, $Q=0.064 \text{ m}^3/\text{s}$ XS2,
 $y_o=0.304 \text{ m}$, $A=0.169 \text{ m}^2$, $u_{avg}=37.8 \text{ cm/s}$

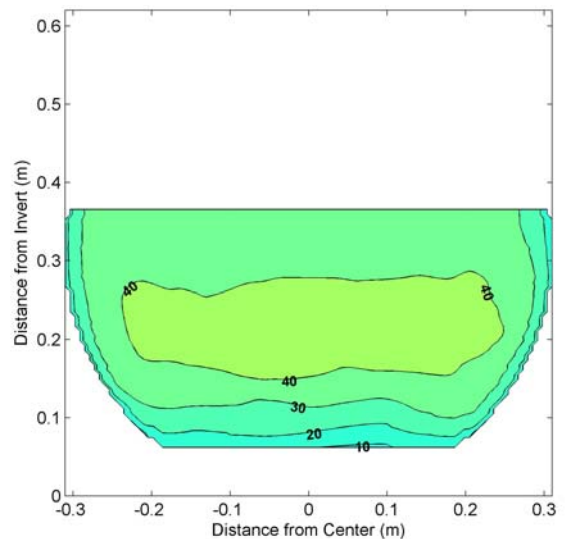


Figure B - 4: $S=0\%$, $Q=0.064 \text{ m}^3/\text{s}$ XS4,
 $y_o=0.305 \text{ m}$, $A=0.170 \text{ m}^2$, $u_{avg}=37.7 \text{ cm/s}$

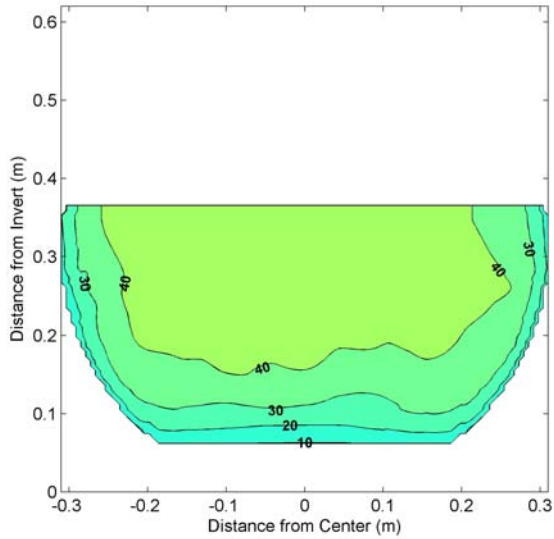


Figure B - 5: $S=0\%$, $Q=0.064 \text{ m}^3/\text{s}$ XS6,
 $y_o=0.302 \text{ m}$, $A=0.168 \text{ m}^2$, $u_{avg}=38.1 \text{ cm/s}$

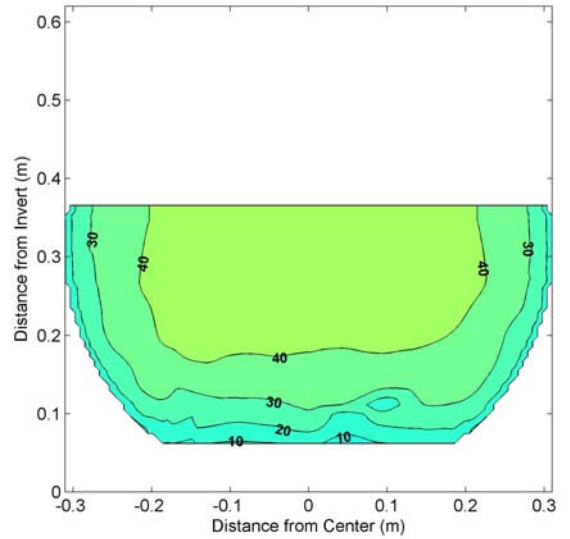


Figure B - 7: $S=0\%$, $Q=0.064 \text{ m}^3/\text{s}$ XS10,
 $y_o=0.300 \text{ m}$, $A=0.167 \text{ m}^2$, $u_{avg}=38.4 \text{ cm/s}$

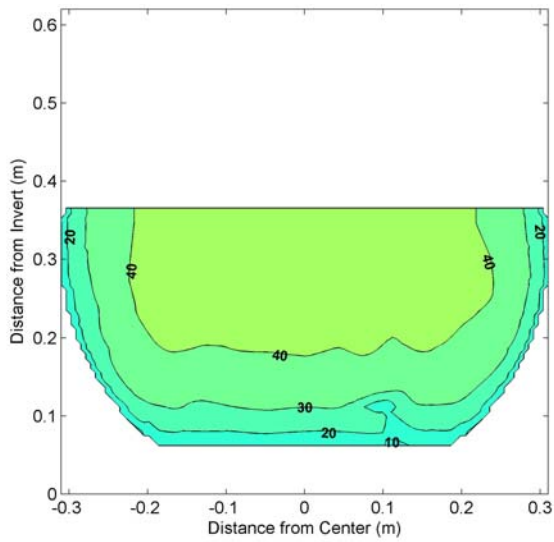


Figure B - 6: $S=0\%$, $Q=0.064 \text{ m}^3/\text{s}$ XS8,
 $y_o=0.302 \text{ m}$, $A=0.168 \text{ m}^2$, $u_{avg}=38.1 \text{ cm/s}$

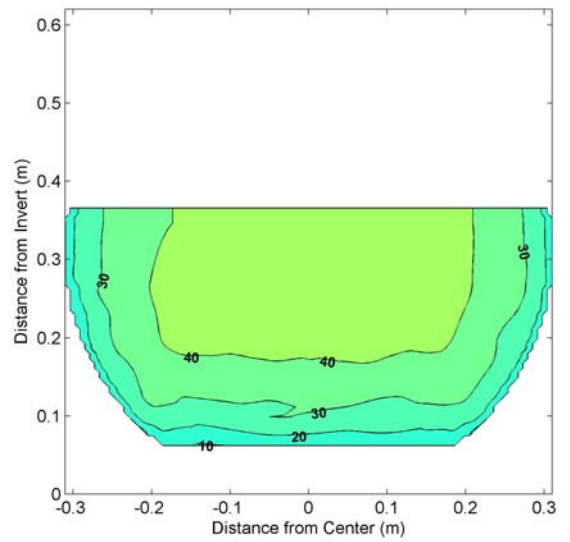


Figure B - 8: $S=0\%$, $Q=0.064 \text{ m}^3/\text{s}$ XS12,
 $y_o=0.300 \text{ m}$, $A=0.167 \text{ m}^2$, $u_{avg}=38.4 \text{ cm/s}$

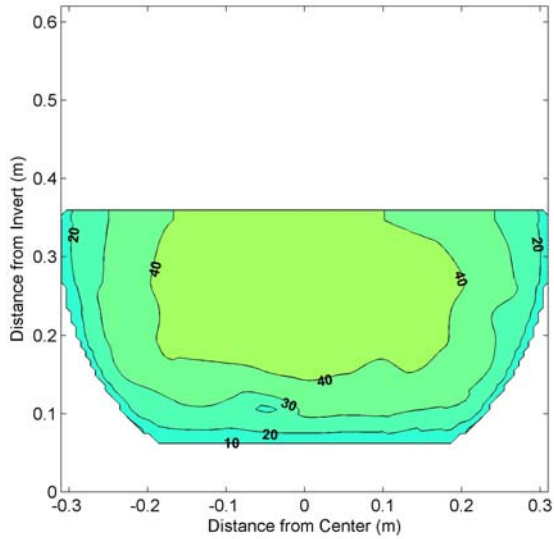


Figure B - 9: $S=0\%$, $Q=0.064 \text{ m}^3/\text{s}$ XS14,
 $y_o=0.296 \text{ m}$, $A=0.164 \text{ m}^2$, $u_{avg}=38.9 \text{ cm/s}$

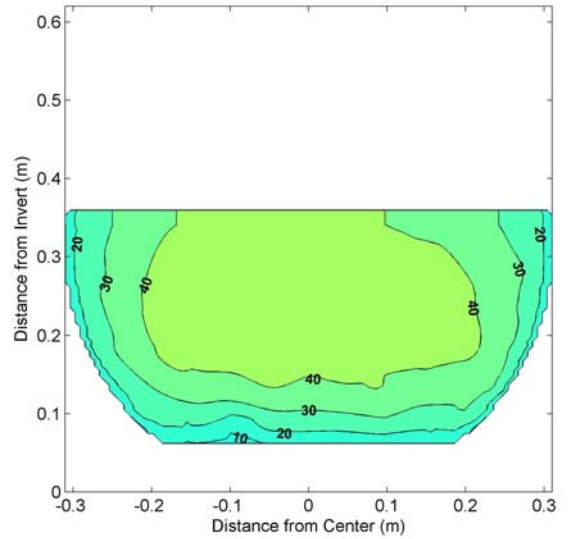


Figure B - 11: $S=0\%$, $Q=0.064 \text{ m}^3/\text{s}$ XS20,
 $y_o=0.293 \text{ m}$, $A=0.163 \text{ m}^2$, $u_{avg}=39.4 \text{ cm/s}$

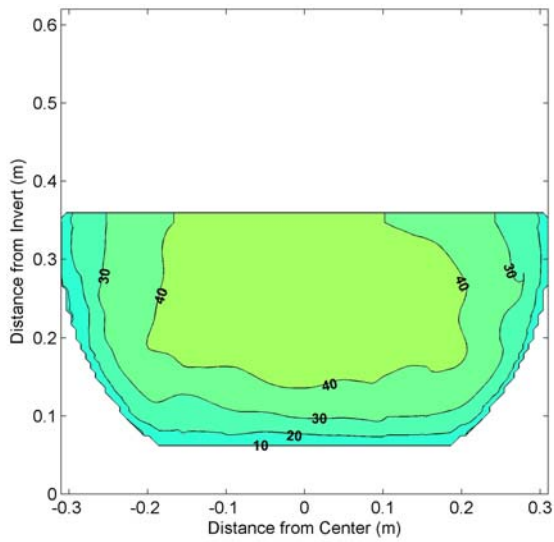


Figure B - 10: $S=0\%$, $Q=0.064 \text{ m}^3/\text{s}$ XS17,
 $y_o=0.295 \text{ m}$, $A=0.164 \text{ m}^2$, $u_{avg}=39.1 \text{ cm/s}$

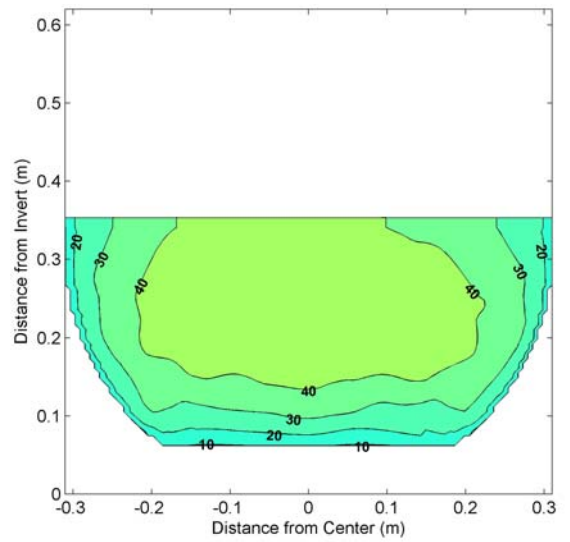


Figure B - 12: $S=0\%$, $Q=0.064 \text{ m}^3/\text{s}$ XS23,
 $y_o=0.289 \text{ m}$, $A=0.160 \text{ m}^2$, $u_{avg}=40.0 \text{ cm/s}$

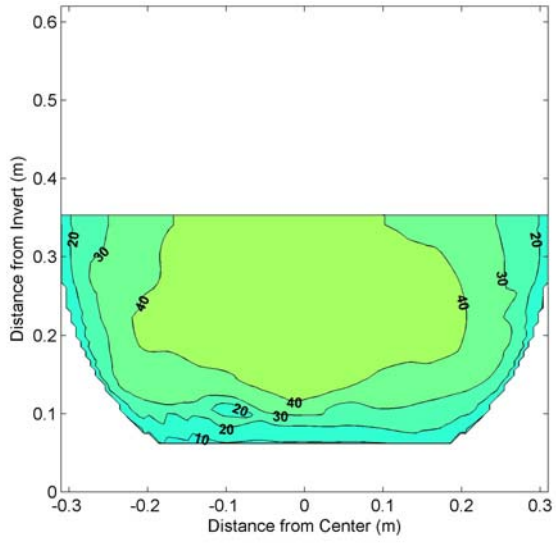


Figure B - 13: $S=0\%$, $Q=0.064 \text{ m}^3/\text{s}$ XS26,
 $y_o=0.289 \text{ m}$, $A=0.160 \text{ m}^2$, $u_{avg}=40.0 \text{ cm/s}$

S0Q186

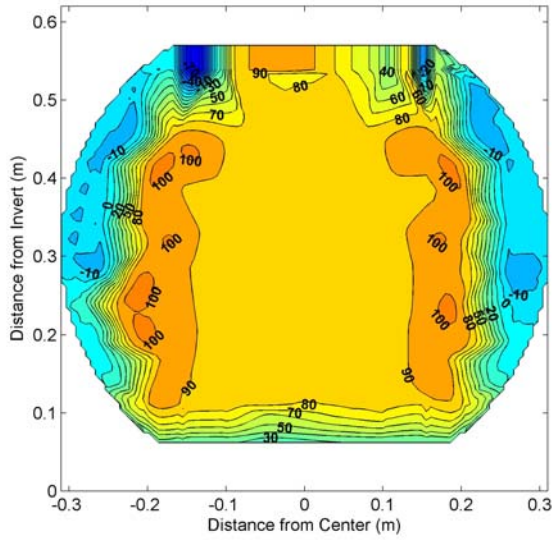


Figure B - 14: $S=0\%$, $Q=0.186\text{m}^3/\text{s}$ XS1,
 $y_o=0.502\text{ m}$, $A=0.273\text{ m}^2$, $u_{avg}=68.2\text{ cm/s}$

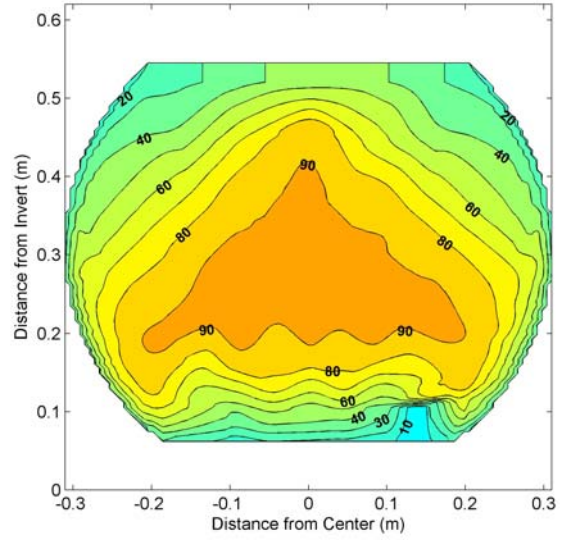


Figure B - 16: $S=0\%$, $Q=0.186\text{m}^3/\text{s}$ XS3,
 $y_o=0.482\text{ m}$, $A=0.265\text{ m}^2$, $u_{avg}=70.2\text{ cm/s}$

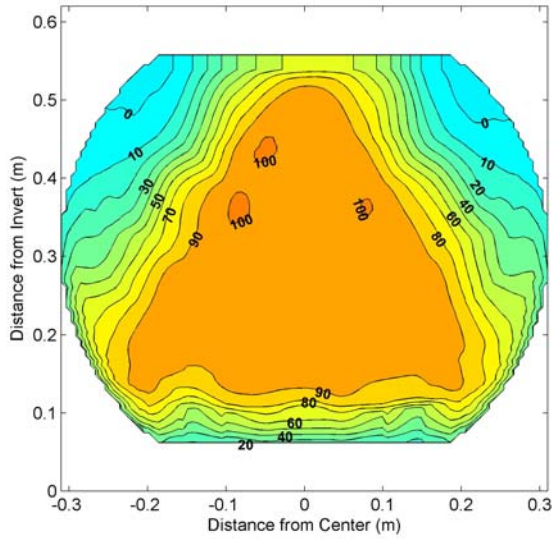


Figure B - 15: $S=0\%$, $Q=0.186\text{m}^3/\text{s}$ XS2,
 $y_o=0.492\text{ m}$, $A=0.269\text{ m}^2$, $u_{avg}=69.2\text{ cm/s}$

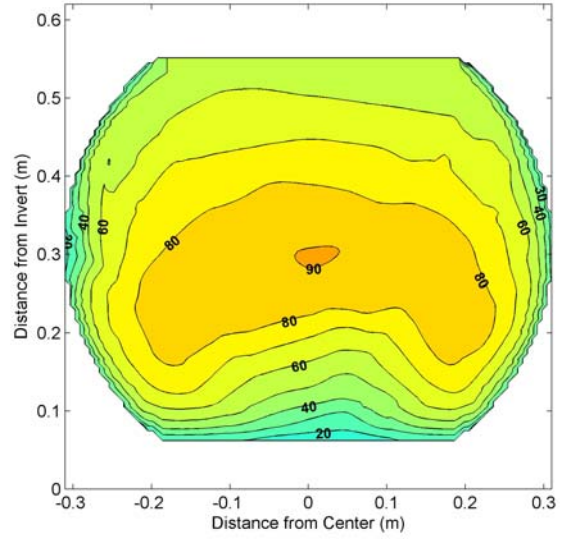


Figure B - 17: $S=0\%$, $Q=0.186\text{m}^3/\text{s}$ XS4,
 $y_o=0.485\text{ m}$, $A=0.266\text{ m}^2$, $u_{avg}=69.9\text{ cm/s}$

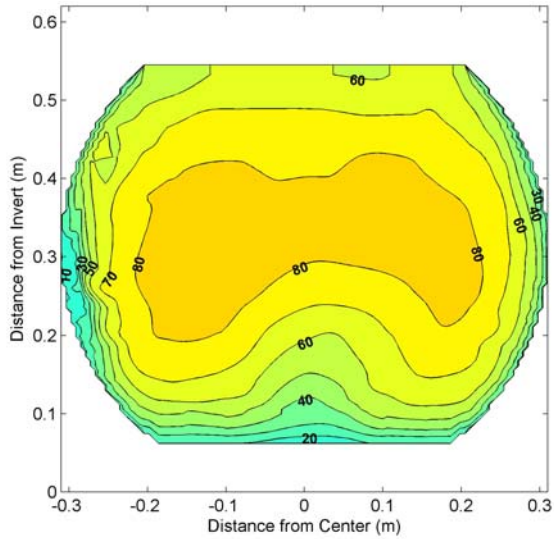


Figure B - 18: $S=0\%$, $Q=0.186\text{m}^3/\text{s}$ XS6,
 $y_o=0.481\text{ m}$, $A=0.265\text{ m}^2$, $u_{avg}=70.3\text{ cm/s}$

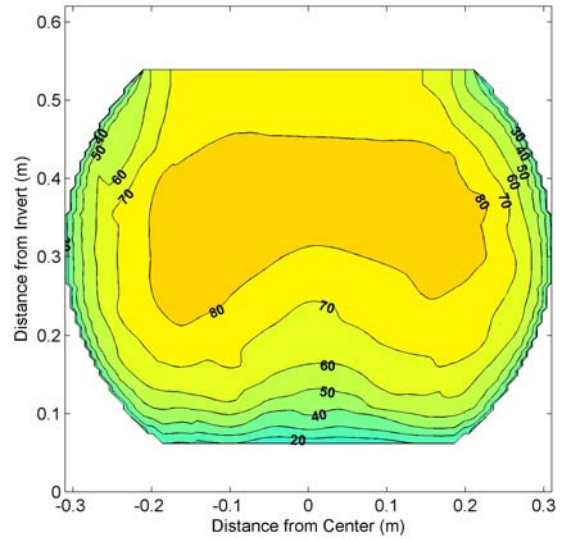


Figure B - 20: $S=0\%$, $Q=0.186\text{m}^3/\text{s}$ XS10,
 $y_o=0.473\text{ m}$, $A=0.261\text{ m}^2$, $u_{avg}=71.2\text{ cm/s}$

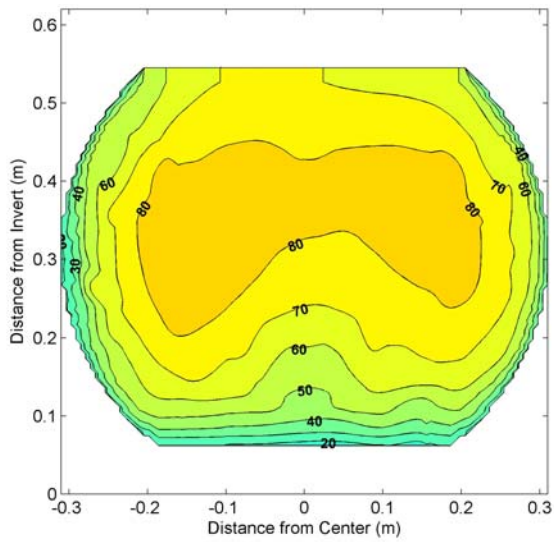


Figure B - 19: $S=0\%$, $Q=0.186\text{m}^3/\text{s}$ XS8,
 $y_o=0.479\text{ m}$, $A=0.264\text{ m}^2$, $u_{avg}=70.5\text{ cm/s}$

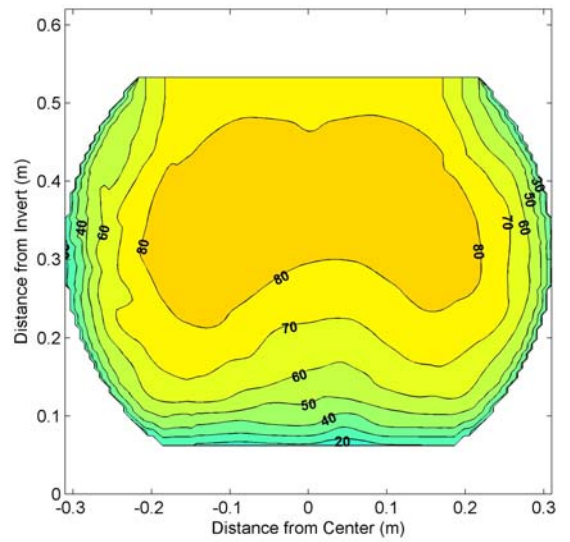


Figure B - 21: $S=0\%$, $Q=0.186\text{m}^3/\text{s}$ XS12,
 $y_o=0.470\text{ m}$, $A=0.260\text{ m}^2$, $u_{avg}=71.6\text{ cm/s}$

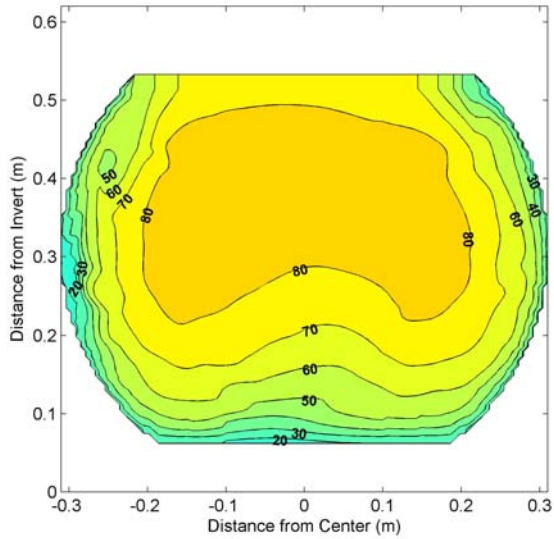


Figure B - 22: $S=0\%$, $Q=0.186\text{m}^3/\text{s}$ XS14,
 $y_o=0.466\text{ m}$, $A=0.258\text{ m}^2$, $u_{avg}=72.1\text{ cm/s}$

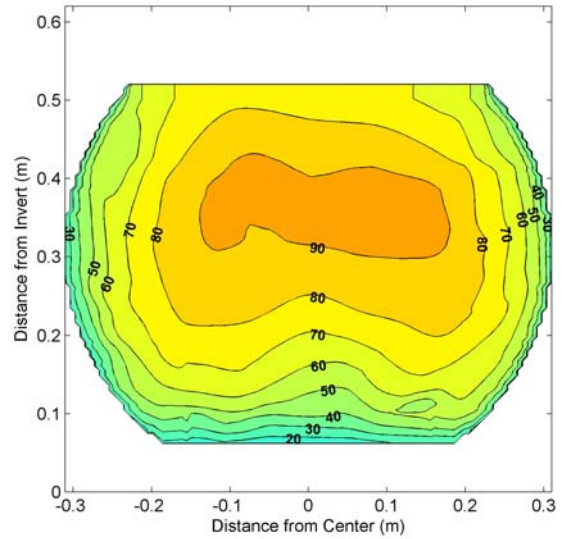


Figure B - 24: $S=0\%$, $Q=0.186\text{m}^3/\text{s}$ XS20,
 $y_o=0.455\text{ m}$, $A=0.253\text{ m}^2$, $u_{avg}=73.5\text{ cm/s}$

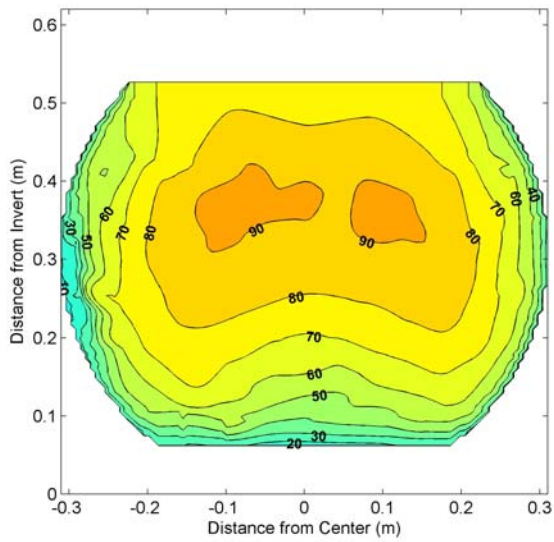


Figure B - 23: $S=0\%$, $Q=0.186\text{m}^3/\text{s}$ XS17,
 $y_o=0.461\text{ m}$, $A=0.256\text{ m}^2$, $u_{avg}=72.7\text{ cm/s}$

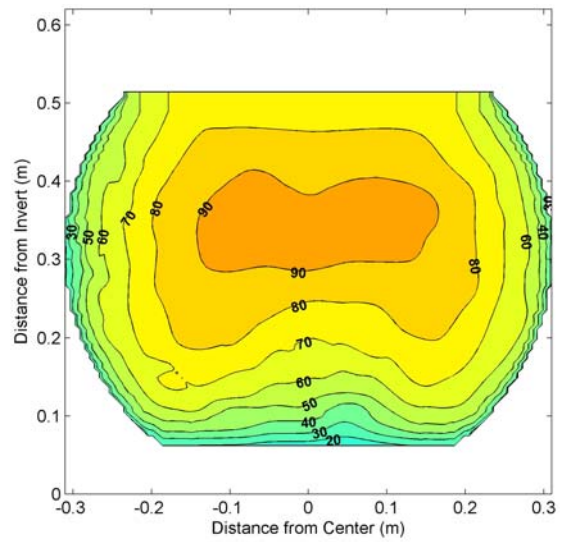


Figure B - 25: $S=0\%$, $Q=0.186\text{m}^3/\text{s}$ XS23,
 $y_o=0.447\text{ m}$, $A=0.249\text{ m}^2$, $u_{avg}=74.6\text{ cm/s}$

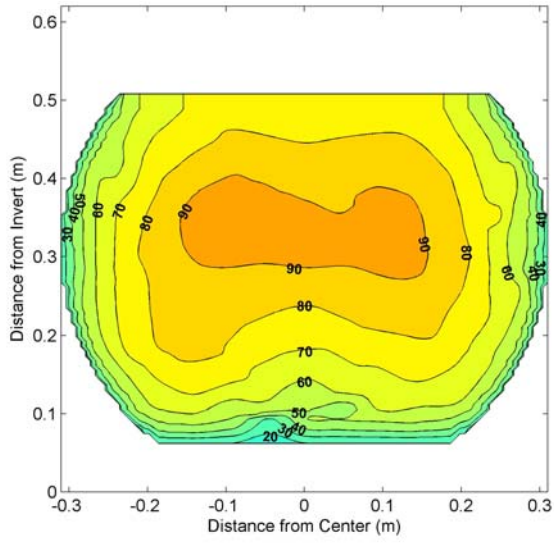


Figure B - 26: $S=0\%$, $Q=0.186\text{m}^3/\text{s}$ XS26,
 $y_o=0.442\text{ m}$, $A=0.247\text{ m}^2$, $u_{avg}=73.5\text{ cm/s}$

S5Q145

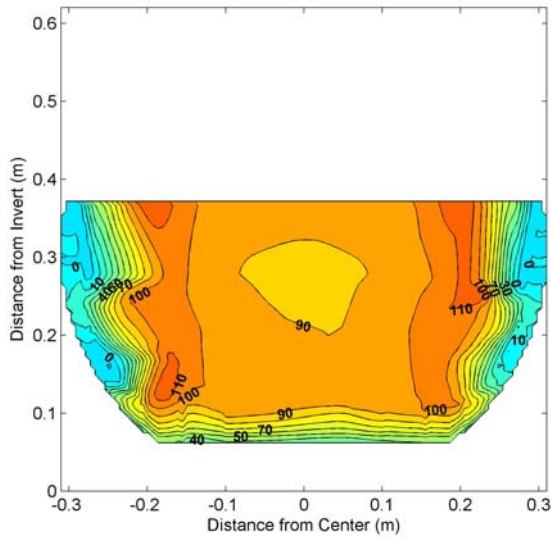


Figure B - 27: $S=0.5\%$, $Q=0.145\text{m}^3/\text{s}$ XS1,
 $y_o=0.310\text{ m}$, $A=0.173\text{ m}^2$, $u_{avg}=83.8\text{ cm/s}$

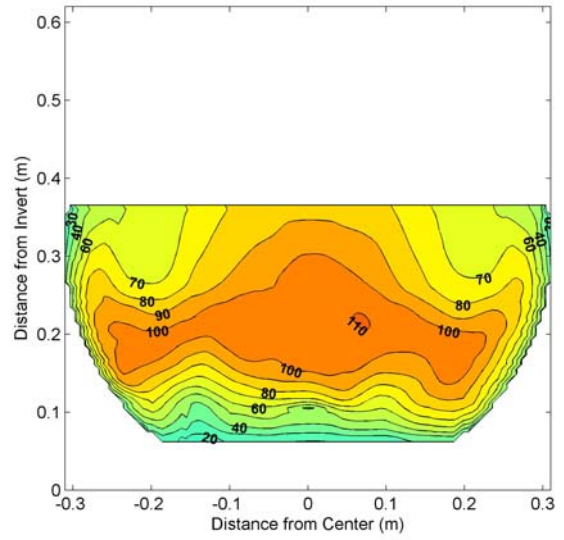


Figure B - 29: $S=0.5\%$, $Q=0.145\text{m}^3/\text{s}$ XS3,
 $y_o=0.303\text{ m}$, $A=0.169\text{ m}^2$, $u_{avg}=86.0\text{ cm/s}$

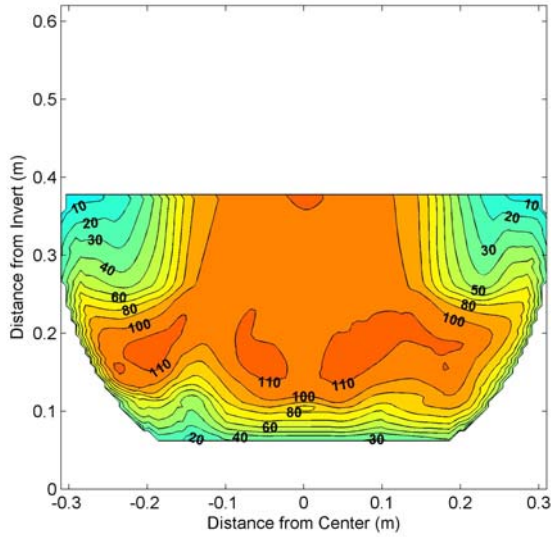


Figure B - 28: $S=0.5\%$, $Q=0.145\text{m}^3/\text{s}$ XS2,
 $y_o=0.315\text{ m}$, $A=0.176\text{ m}^2$, $u_{avg}=82.4\text{ cm/s}$

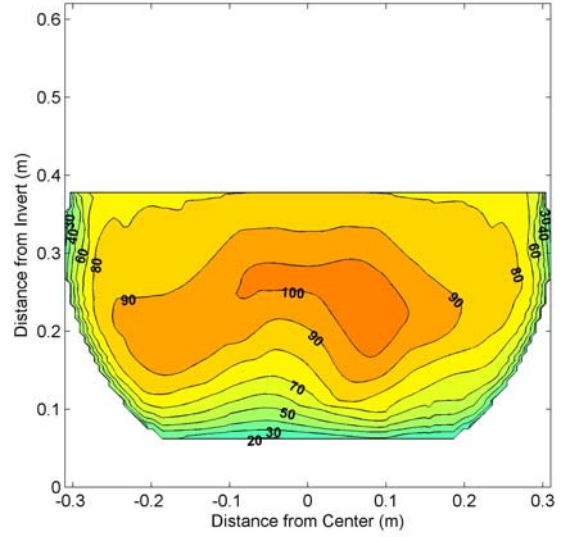


Figure B - 30: $S=0.5\%$, $Q=0.145\text{m}^3/\text{s}$ XS4,
 $y_o=0.313\text{ m}$, $A=0.175\text{ m}^2$, $u_{avg}=83.0\text{ cm/s}$

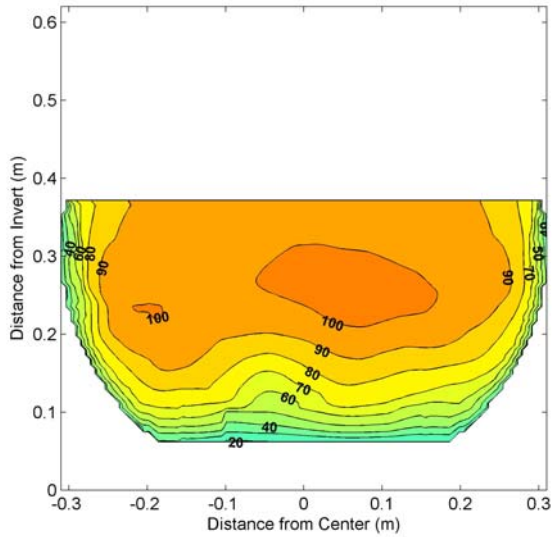


Figure B - 31: $S=0.5\%$, $Q=0.145\text{m}^3/\text{s}$ XS6,
 $y_o=0.308\text{ m}$, $A=0.172\text{ m}^2$, $u_{avg}=84.4\text{ cm/s}$

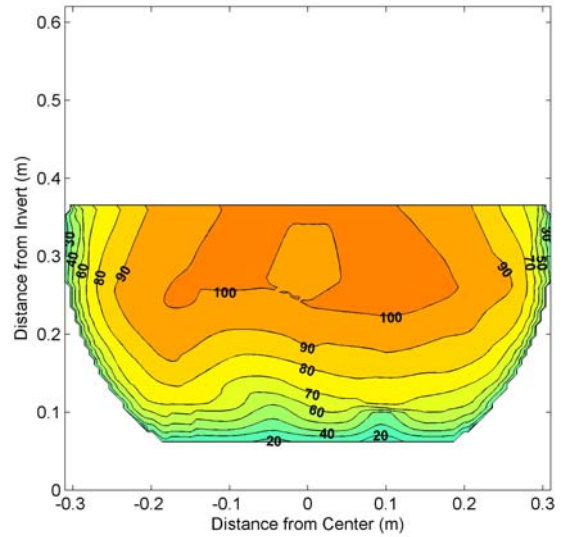


Figure B - 33: $S=0.5\%$, $Q=0.145\text{m}^3/\text{s}$ XS10,
 $y_o=0.302\text{ m}$, $A=0.168\text{ m}^2$, $u_{avg}=86.3\text{ cm/s}$

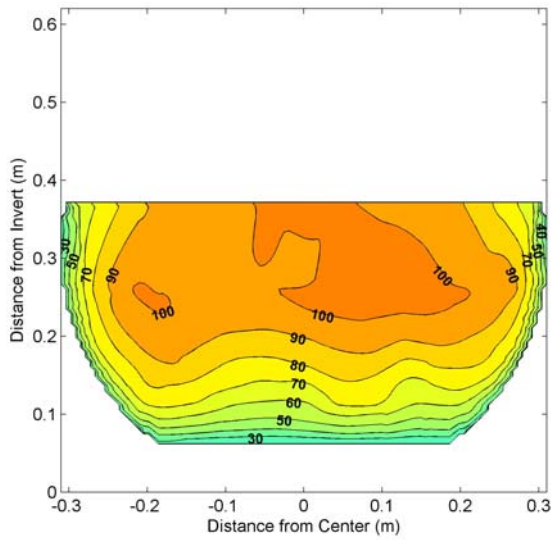


Figure B - 32: $S=0.5\%$, $Q=0.145\text{m}^3/\text{s}$ XS8,
 $y_o=0.306\text{ m}$, $A=0.171\text{ m}^2$, $u_{avg}=85.0\text{ cm/s}$

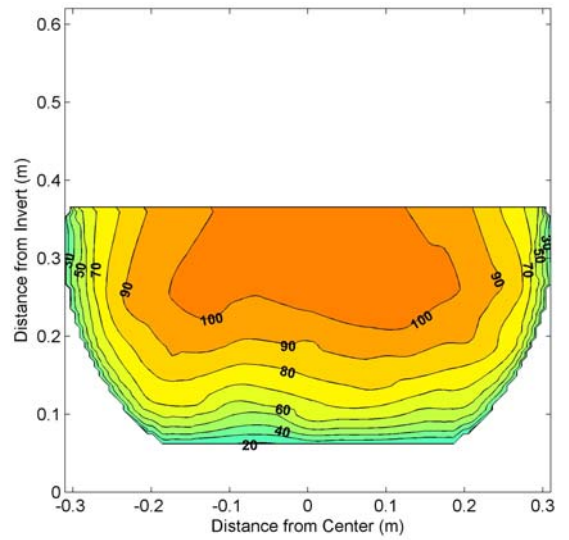


Figure B - 34: $S=0.5\%$, $Q=0.145\text{m}^3/\text{s}$ XS12,
 $y_o=0.301\text{ m}$, $A=0.167\text{ m}^2$, $u_{avg}=86.6\text{ cm/s}$

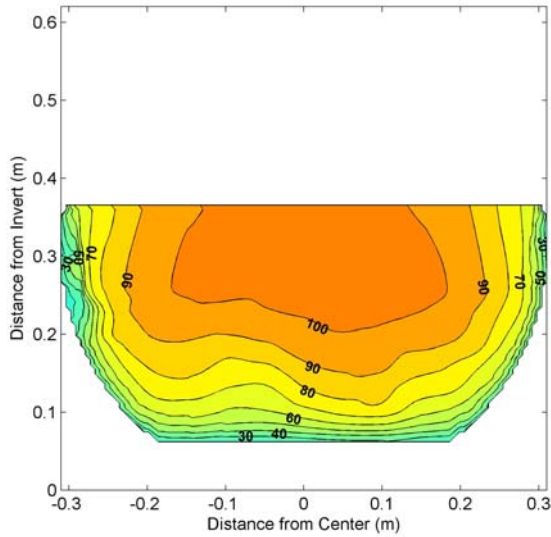


Figure B - 35: $S=0.5\%$, $Q=0.145\text{m}^3/\text{s}$ XS14,
 $y_o=0.300\text{ m}$, $A=0.167\text{ m}^2$, $u_{avg}=86.9\text{ cm/s}$

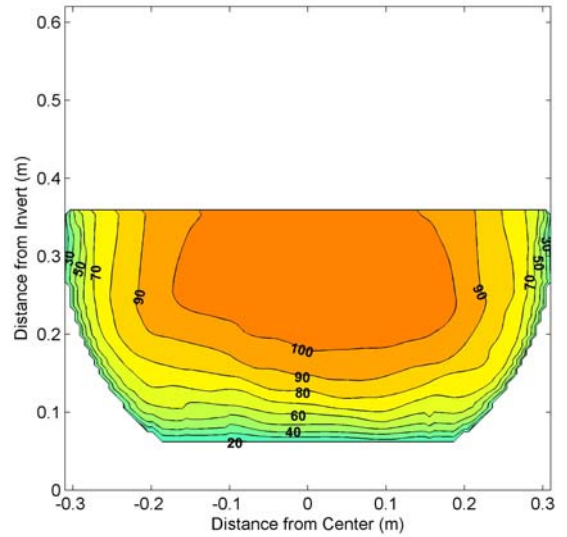


Figure B - 37: $S=0.5\%$, $Q=0.145\text{m}^3/\text{s}$ XS20,
 $y_o=0.299\text{ m}$, $A=0.166\text{ m}^2$, $u_{avg}=87.2\text{ cm/s}$

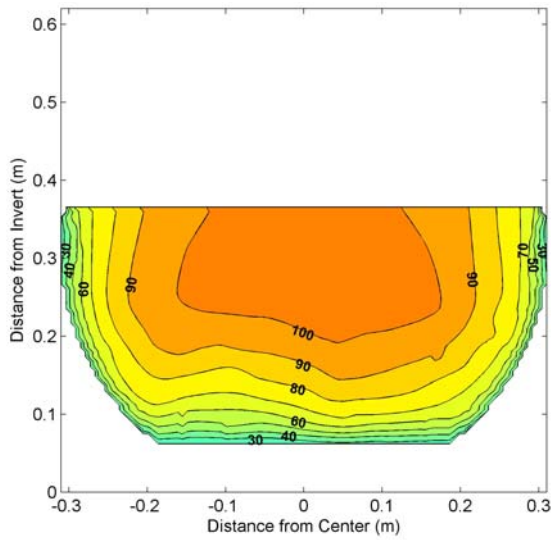


Figure B - 36: $S=0.5\%$, $Q=0.145\text{m}^3/\text{s}$ XS17,
 $y_o=0.301\text{ m}$, $A=0.167\text{ m}^2$, $u_{avg}=86.6\text{ cm/s}$

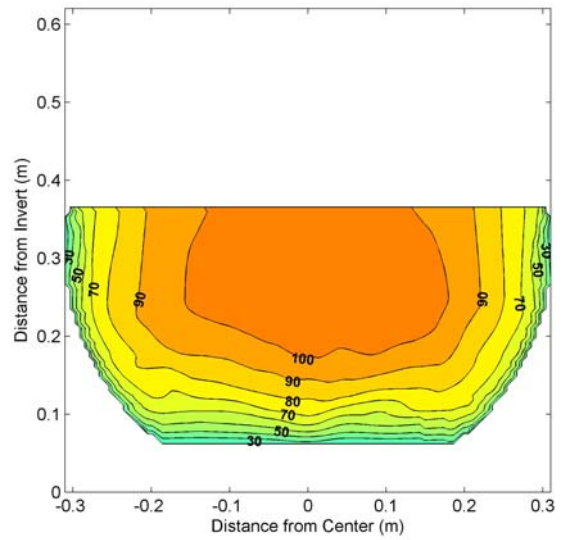


Figure B - 38: $S=0.5\%$, $Q=0.145\text{m}^3/\text{s}$ XS23,
 $y_o=0.300\text{ m}$, $A=0.167\text{ m}^2$, $u_{avg}=86.9\text{ cm/s}$

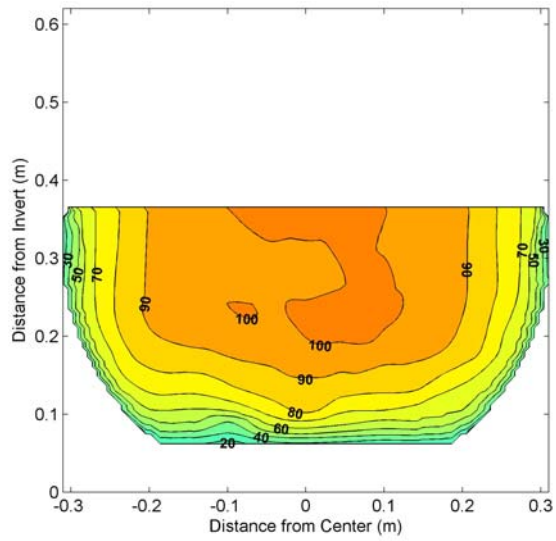


Figure B - 39: $S=0.5\%$, $Q=0.145\text{m}^3/\text{s}$ XS26,
 $y_o=0.303\text{ m}$, $A=0.169\text{ m}^2$, $u_{avg}=86.0\text{ cm/s}$

S5Q221

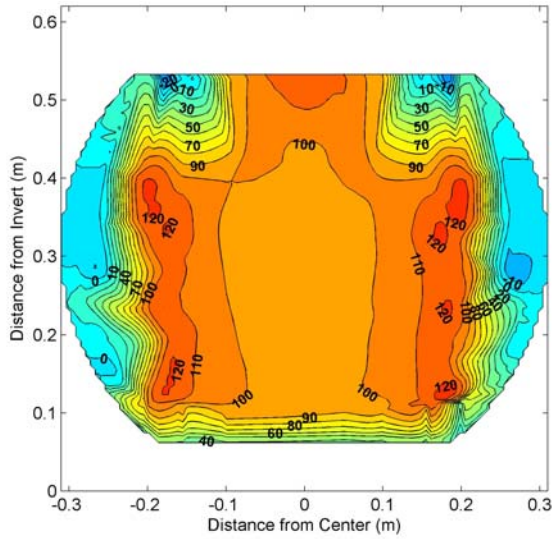


Figure B - 40: $S=0.5\%$, $Q=0.221\text{m}^3/\text{s}$ XS1,
 $y_o=0.469\text{ m}$, $A=0.259\text{ m}^2$, $u_{avg}=85.2\text{ cm/s}$

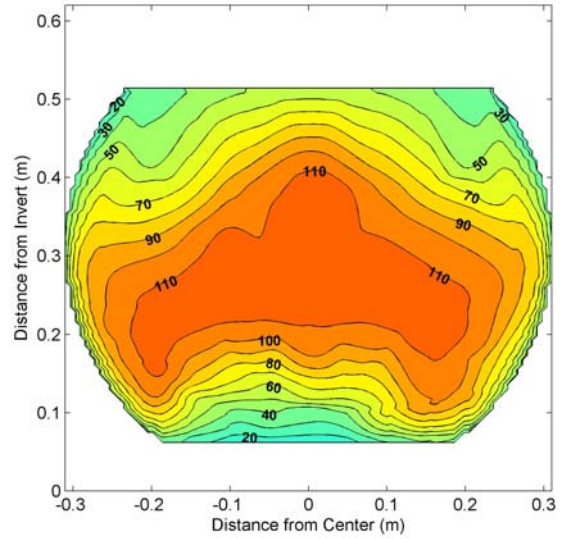


Figure B - 42: $S=0.5\%$, $Q=0.221\text{m}^3/\text{s}$ XS3,
 $y_o=0.450\text{ m}$, $A=0.251\text{ m}^2$, $u_{avg}=88.1\text{ cm/s}$

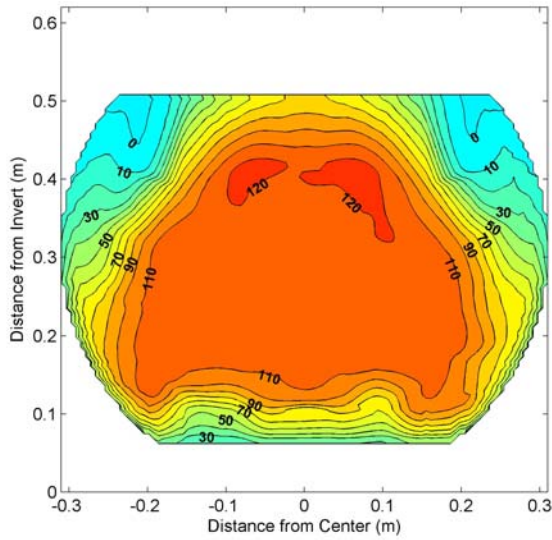


Figure B - 41: $S=0.5\%$, $Q=0.221\text{m}^3/\text{s}$ XS2,
 $y_o=0.446\text{ m}$, $A=0.249\text{ m}^2$, $u_{avg}=88.8\text{ cm/s}$

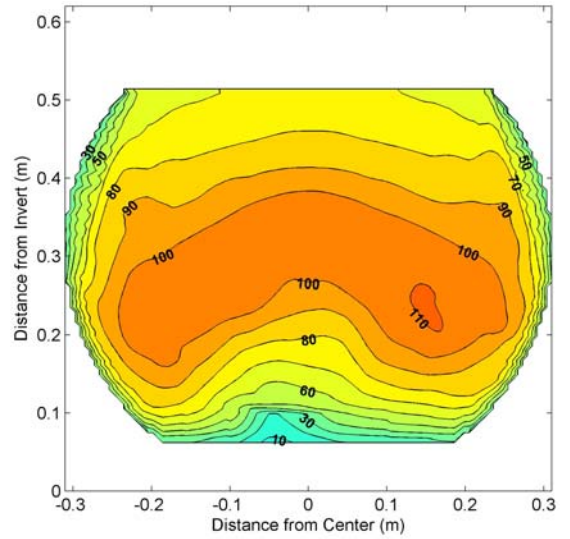


Figure B - 43: $S=0.5\%$, $Q=0.221\text{m}^3/\text{s}$ XS4,
 $y_o=0.448\text{ m}$, $A=0.250\text{ m}^2$, $u_{avg}=88.5\text{ cm/s}$

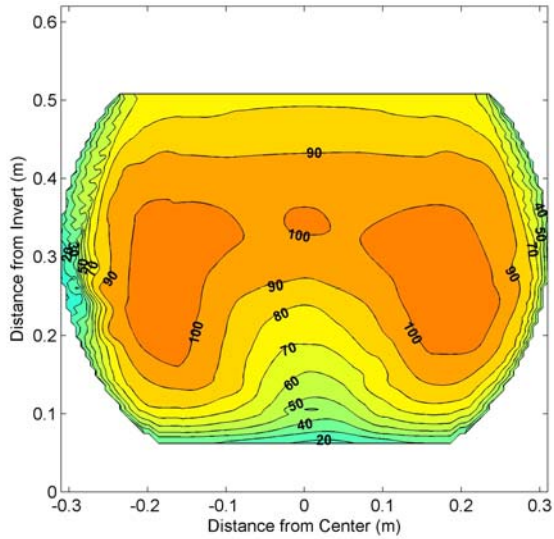


Figure B - 44: $S=0.5\%$, $Q=0.221\text{m}^3/\text{s}$ XS6,
 $y_o=0.446\text{ m}$, $A=0.249\text{ m}^2$, $u_{avg}=88.8\text{ cm/s}$

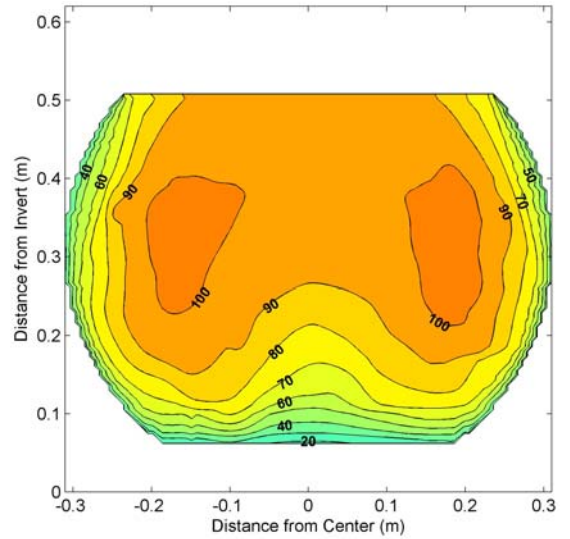


Figure B - 46: $S=0.5\%$, $Q=0.221\text{m}^3/\text{s}$ XS10,
 $y_o=0.443\text{ m}$, $A=0.247\text{ m}^2$, $u_{avg}=89.3\text{ cm/s}$

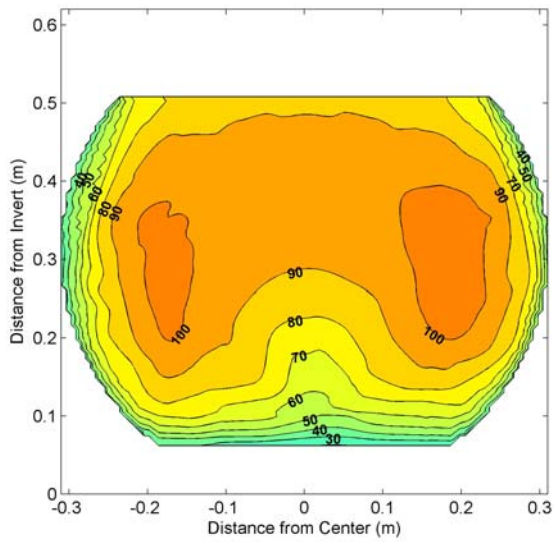


Figure B - 45: $S=0.5\%$, $Q=0.221\text{m}^3/\text{s}$ XS8,
 $y_o=0.445\text{ m}$, $A=0.248\text{ m}^2$, $u_{avg}=89.0\text{ cm/s}$

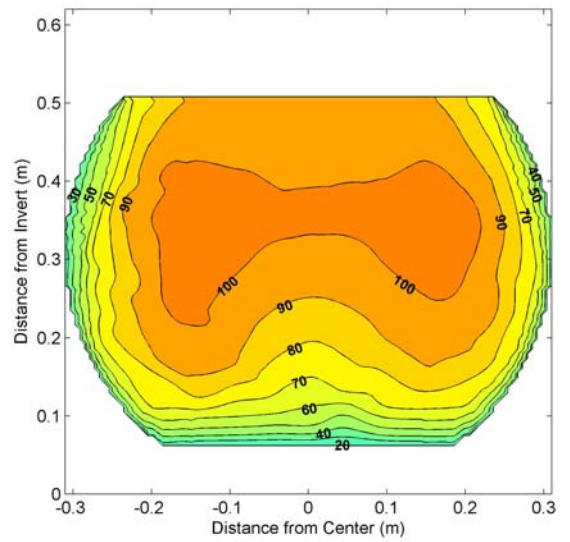


Figure B - 47: $S=0.5\%$, $Q=0.221\text{m}^3/\text{s}$ XS12,
 $y_o=0.443\text{ m}$, $A=0.247\text{ m}^2$, $u_{avg}=89.3\text{ cm/s}$

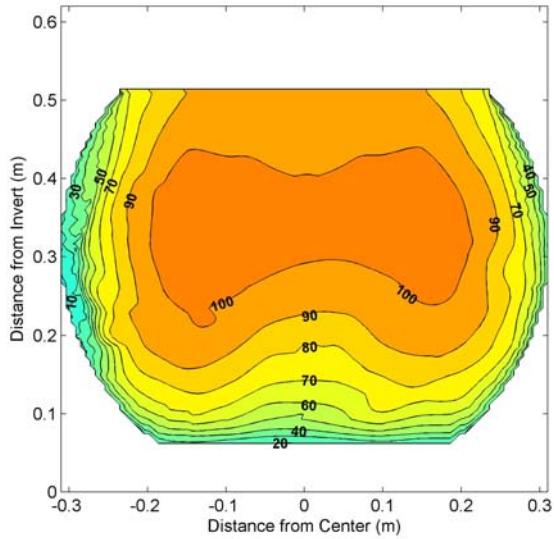


Figure B - 48: $S=0.5\%$, $Q=0.221\text{m}^3/\text{s}$ XS14,
 $y_o=0.447\text{ m}$, $A=0.249\text{ m}^2$, $u_{avg}=88.6\text{ cm/s}$

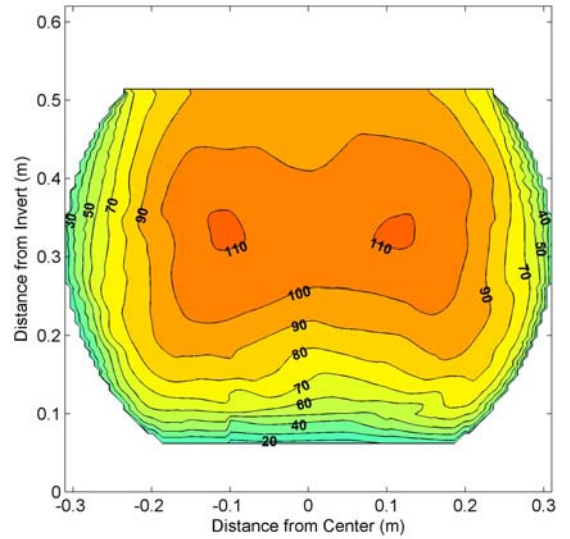


Figure B - 50: $S=0.5\%$, $Q=0.221\text{m}^3/\text{s}$ XS20,
 $y_o=0.448\text{ m}$, $A=0.250\text{ m}^2$, $u_{avg}=88.5\text{ cm/s}$

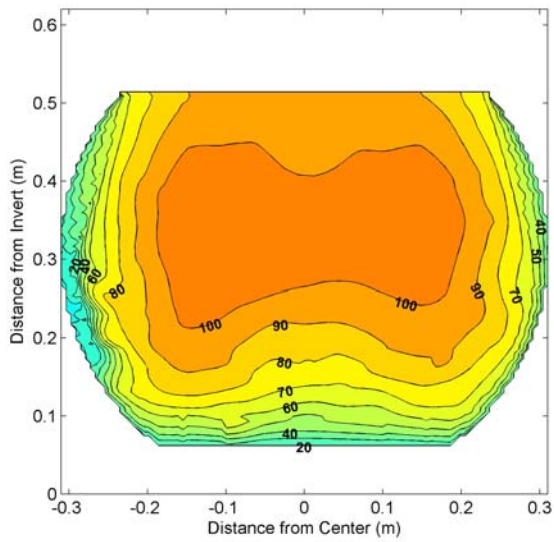


Figure B - 49: $S=0.5\%$, $Q=0.221\text{m}^3/\text{s}$ XS17,
 $y_o=0.449\text{ m}$, $A=0.250\text{ m}^2$, $u_{avg}=88.3\text{ cm/s}$

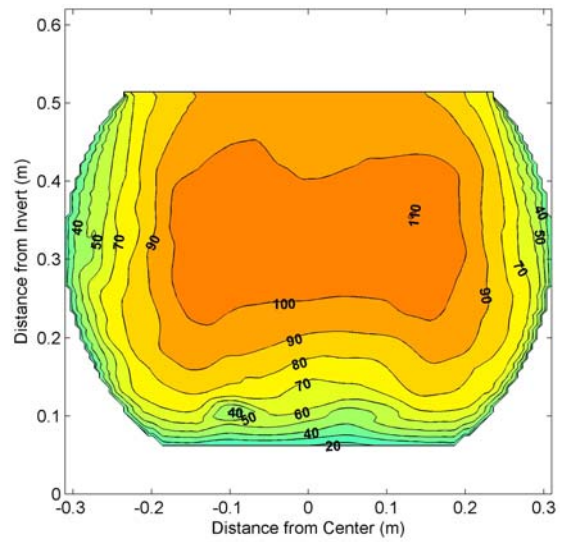


Figure B - 51: $S=0.5\%$, $Q=0.221\text{m}^3/\text{s}$ XS23,
 $y_o=0.449\text{ m}$, $A=0.250\text{ m}^2$, $u_{avg}=88.3\text{ cm/s}$

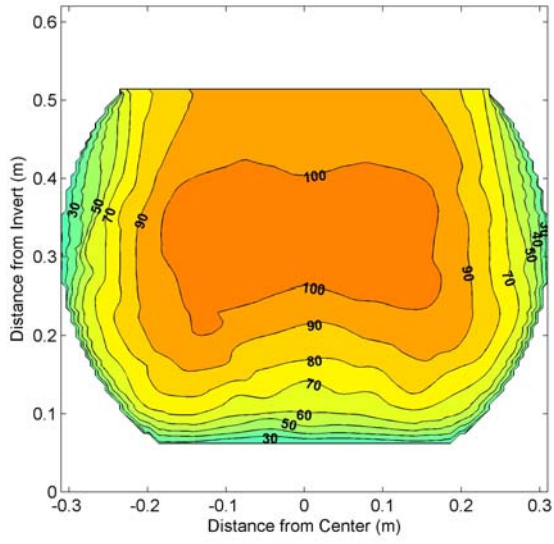


Figure B - 52: $S=0.5\%$, $Q=0.221\text{m}^3/\text{s}$ XS26,
 $y_o=0.449\text{ m}$, $A=0.250\text{ m}^2$, $u_{avg}=88.3\text{ cm/s}$

SIQ150

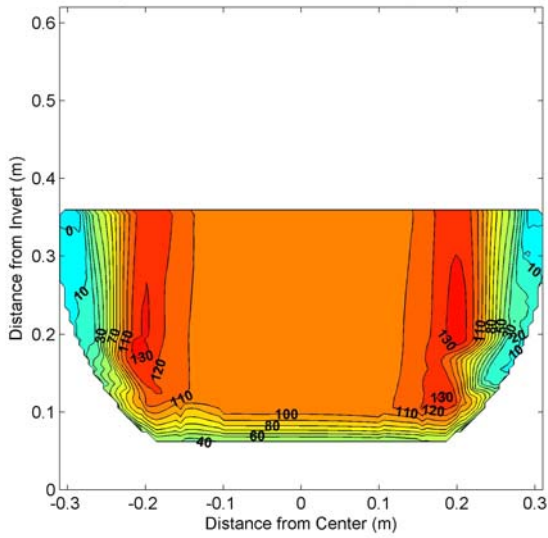


Figure B - 53: $S=1.0\%$, $Q=0.150\text{m}^3/\text{s}$ XS1,
 $y_o=0.294\text{ m}$, $A=0.163\text{ m}^2$, $u_{avg}=91.9\text{ cm/s}$

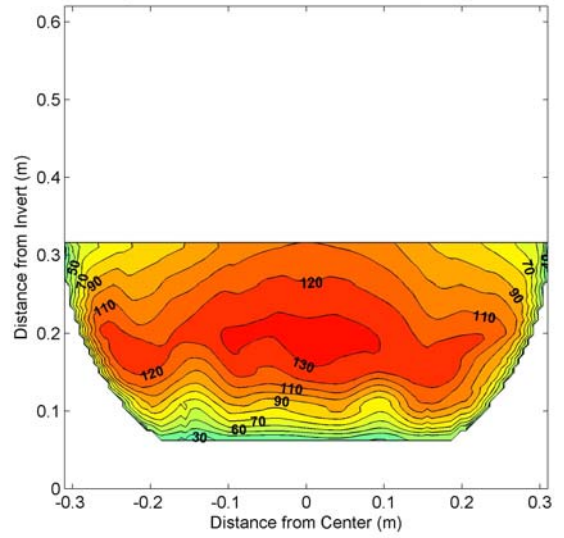


Figure B - 55: $S=1.0\%$, $Q=0.150\text{m}^3/\text{s}$ XS3,
 $y_o=0.252\text{ m}$, $A=0.137\text{ m}^2$, $u_{avg}=109.3\text{ cm/s}$

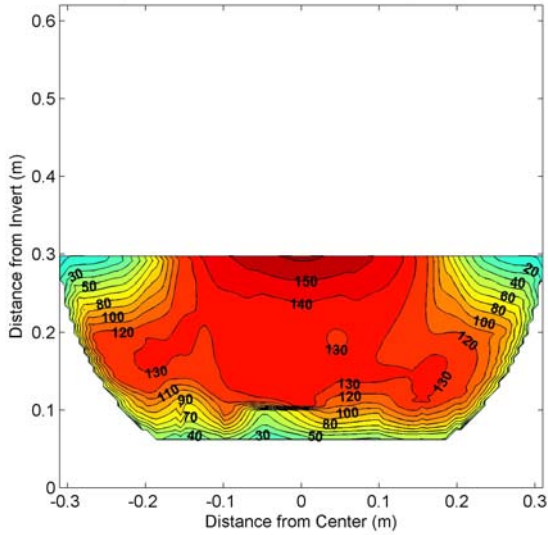


Figure B - 54: $S=1.0\%$, $Q=0.150\text{m}^3/\text{s}$ XS2,
 $y_o=0.232\text{ m}$, $A=0.125\text{ m}^2$, $u_{avg}=120.2\text{ cm/s}$

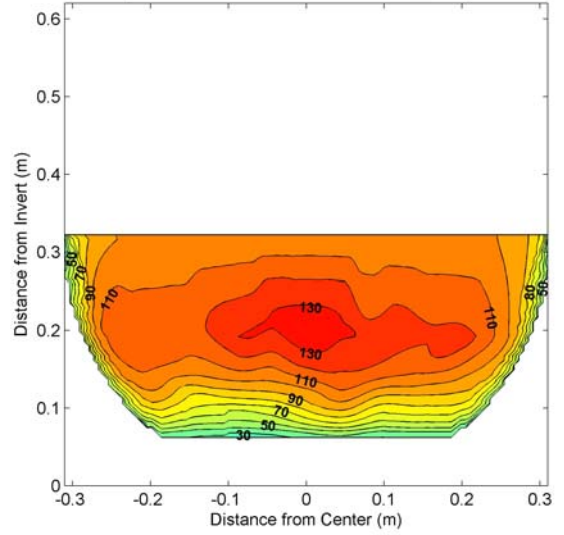


Figure B - 56: $S=1.0\%$, $Q=0.150\text{m}^3/\text{s}$ XS4,
 $y_o=0.259\text{ m}$, $A=0.142\text{ m}^2$, $u_{avg}=106.0\text{ cm/s}$

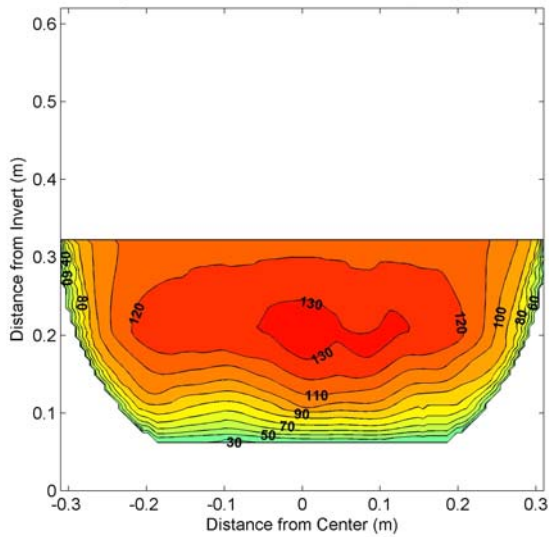


Figure B - 57: $S=1.0\%$, $Q=0.150\text{m}^3/\text{s}$ XS6,
 $y_o=0.262\text{ m}$, $A=0.143\text{ m}^2$, $u_{avg}=104.6\text{ cm/s}$

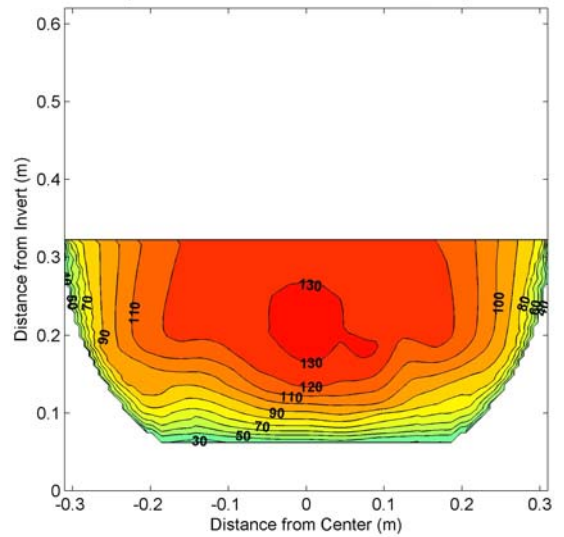


Figure B - 59: $S=1.0\%$, $Q=0.150\text{m}^3/\text{s}$ XS10,
 $y_o=0.259\text{ m}$, $A=0.142\text{ m}^2$, $u_{avg}=106.0\text{ cm/s}$

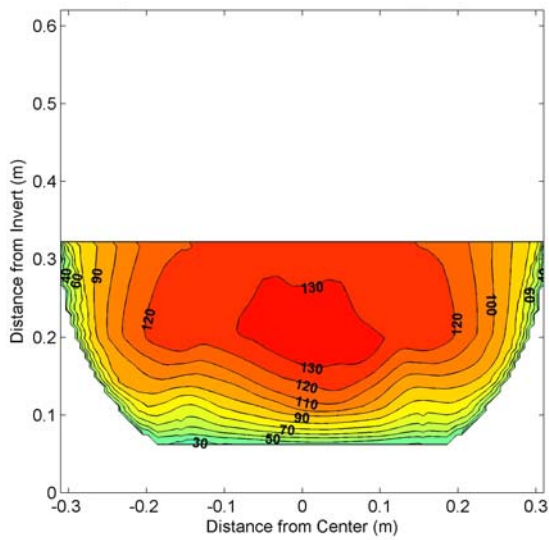


Figure B - 58: $S=1.0\%$, $Q=0.150\text{m}^3/\text{s}$ XS8,
 $y_o=0.261\text{ m}$, $A=0.143\text{ m}^2$, $u_{avg}=105.0\text{ cm/s}$

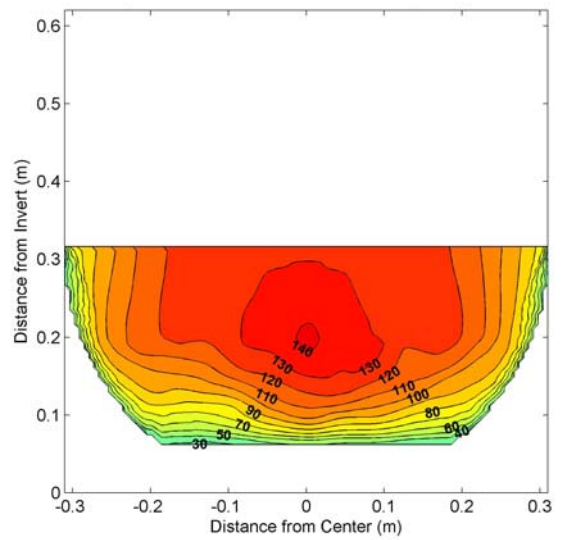


Figure B - 60: $S=1.0\%$, $Q=0.150\text{m}^3/\text{s}$ XS12,
 $y_o=0.255\text{ m}$, $A=0.139\text{ m}^2$, $u_{avg}=107.9\text{ cm/s}$

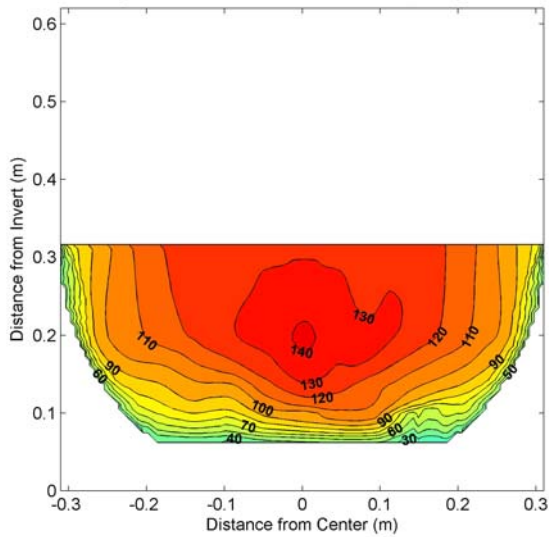


Figure B - 61: $S=1.0\%$, $Q=0.150\text{m}^3/\text{s}$ XS14,
 $y_o=0.255\text{ m}$, $A=0.139\text{ m}^2$, $u_{avg}=107.9\text{ cm/s}$

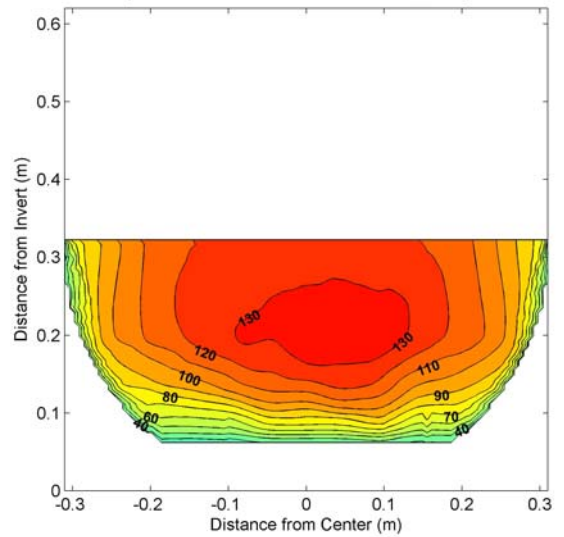


Figure B - 63: $S=1.0\%$, $Q=0.150\text{m}^3/\text{s}$ XS20,
 $y_o=0.261\text{ m}$, $A=0.143\text{ m}^2$, $u_{avg}=105.0\text{ cm/s}$

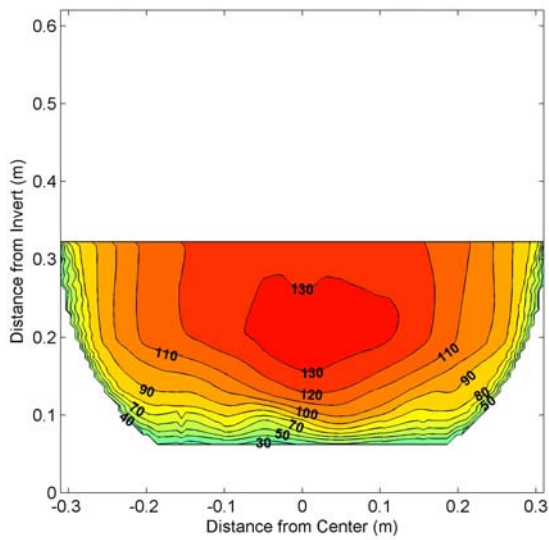


Figure B - 62: $S=1.0\%$, $Q=0.150\text{m}^3/\text{s}$ XS17,
 $y_o=0.260\text{ m}$, $A=0.142\text{ m}^2$, $u_{avg}=105.5\text{ cm/s}$

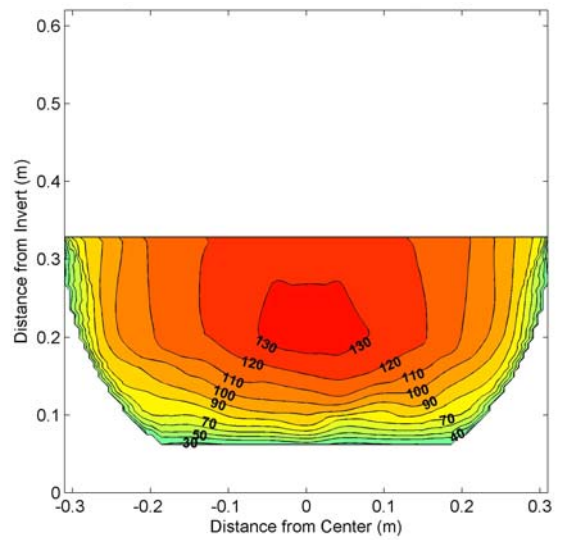


Figure B - 64: $S=1.0\%$, $Q=0.150\text{m}^3/\text{s}$ XS23,
 $y_o=0.263\text{ m}$, $A=0.144\text{ m}^2$, $u_{avg}=104.1\text{ cm/s}$

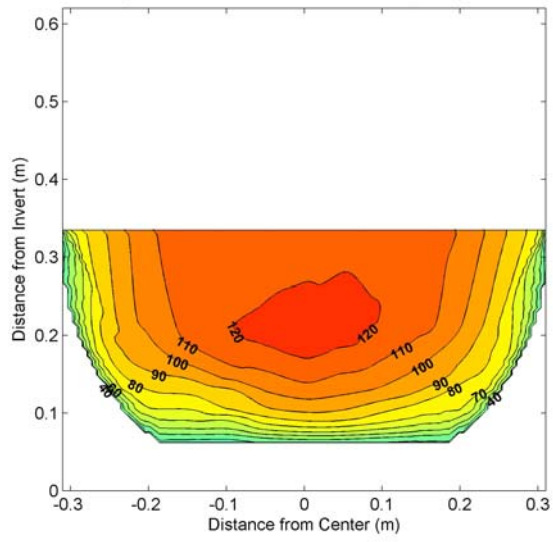


Figure B - 65: $S=1.0\%$, $Q=0.150\text{m}^3/\text{s}$ XS26,
 $y_o=0.271\text{ m}$, $A=0.149\text{ m}^2$, $u_{avg}=100.7\text{ cm/s}$

SIQ254

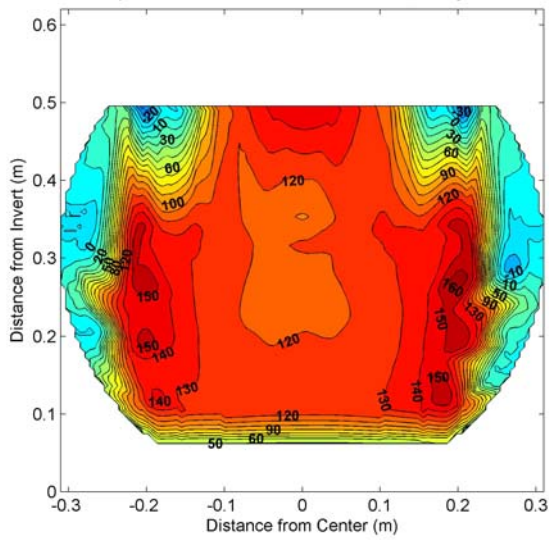


Figure B - 66: $S=1.0\%$, $Q=0.254\text{m}^3/\text{s}$ XS1,
 $y_o=0.431\text{ m}$, $A=0.241\text{ m}^2$, $u_{avg}=105.2\text{ cm/s}$

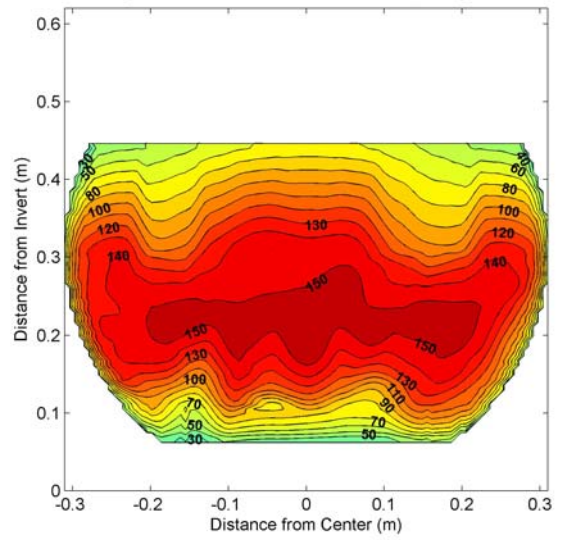


Figure B - 68: $S=1.0\%$, $Q=0.254\text{m}^3/\text{s}$ XS3,
 $y_o=0.384\text{ m}$, $A=0.216\text{ m}^2$, $u_{avg}=117.4\text{ cm/s}$

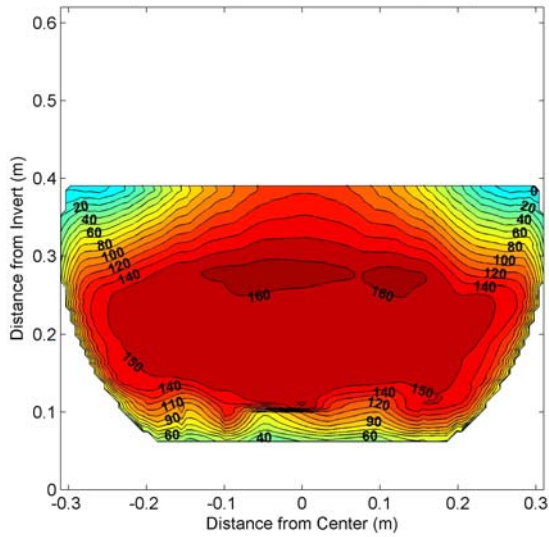


Figure B - 67: $S=1.0\%$, $Q=0.254\text{m}^3/\text{s}$ XS2,
 $y_o=0.342\text{ m}$, $A=0.181\text{ m}^2$, $u_{avg}=140.0\text{ cm/s}$

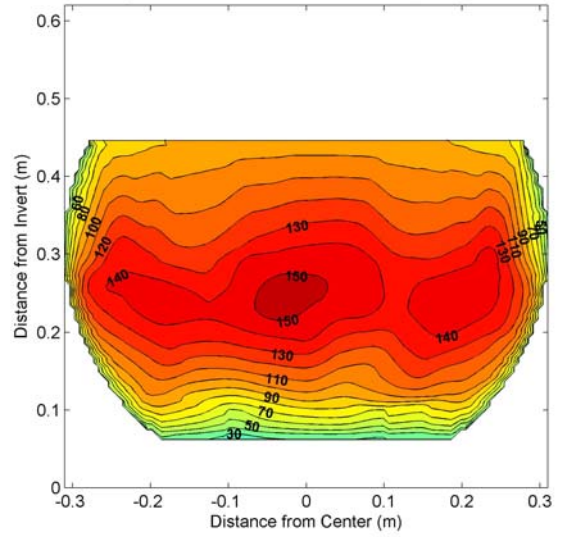


Figure B - 69: $S=1.0\%$, $Q=0.254\text{m}^3/\text{s}$ XS4,
 $y_o=0.384\text{ m}$, $A=0.216\text{ m}^2$, $u_{avg}=117.4\text{ cm/s}$

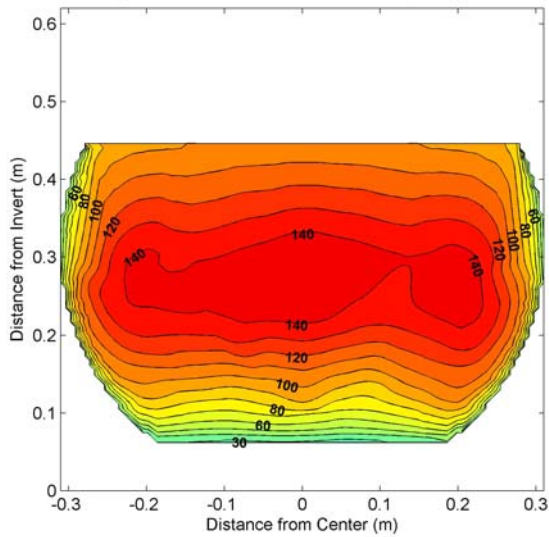


Figure B - 70: $S=1.0\%$, $Q=0.254\text{m}^3/\text{s}$ XS6,
 $y_o=0.384\text{ m}$, $A=0.216\text{ m}^2$, $u_{avg}=117.4\text{ cm/s}$

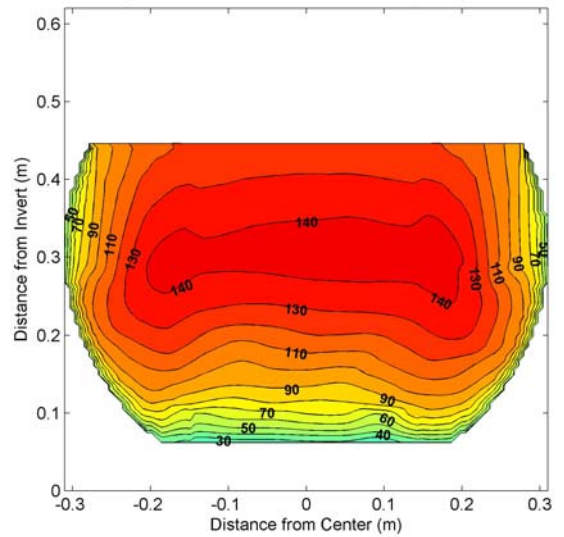


Figure B - 72: $S=1.0\%$, $Q=0.254\text{m}^3/\text{s}$ XS10,
 $y_o=0.384\text{ m}$, $A=0.216\text{ m}^2$, $u_{avg}=117.4\text{ cm/s}$

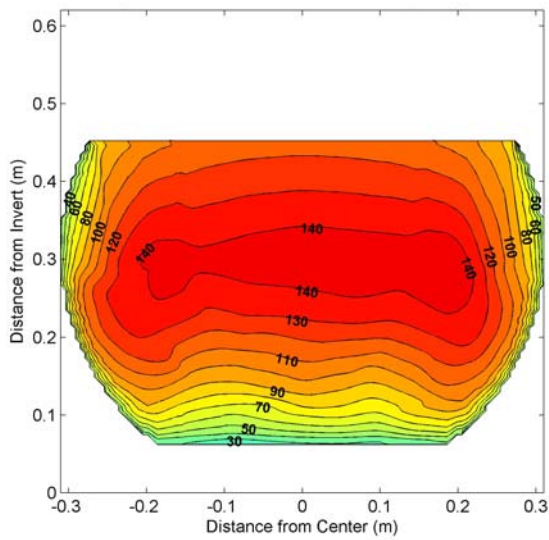


Figure B - 71: $S=1.0\%$, $Q=0.254\text{m}^3/\text{s}$ XS8,
 $y_o=0.387\text{ m}$, $A=0.218\text{ m}^2$, $u_{avg}=116.5\text{ cm/s}$

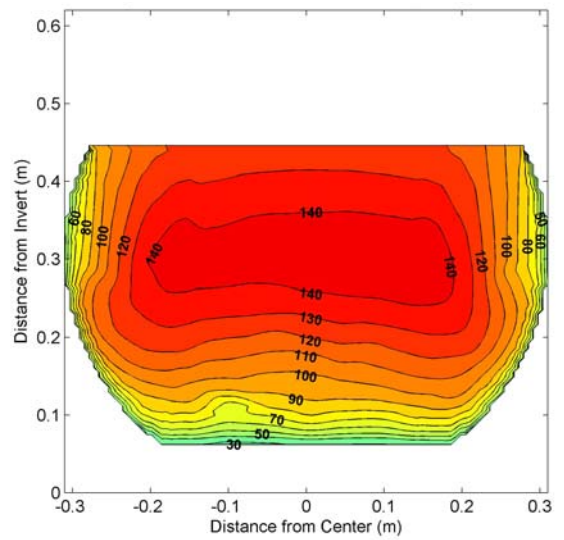


Figure B - 73: $S=1.0\%$, $Q=0.254\text{m}^3/\text{s}$ XS12,
 $y_o=0.381\text{ m}$, $A=0.215\text{ m}^2$, $u_{avg}=118.3\text{ cm/s}$

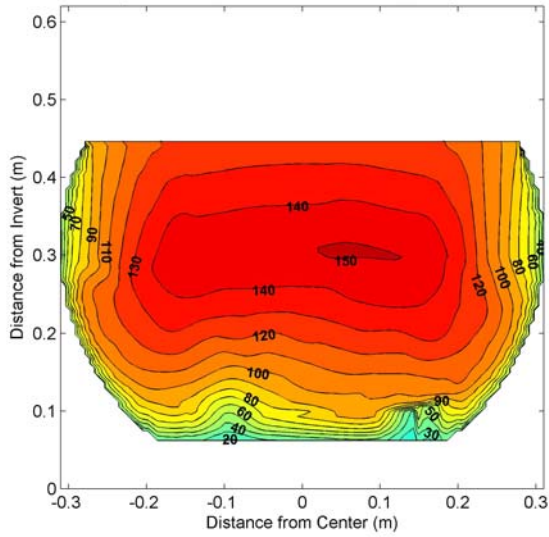


Figure B - 74: $S=1.0\%$, $Q=0.254\text{m}^3/\text{s}$ XS14,
 $y_o=0.380\text{ m}$, $A=0.214\text{ m}^2$, $u_{avg}=118.6\text{ cm/s}$

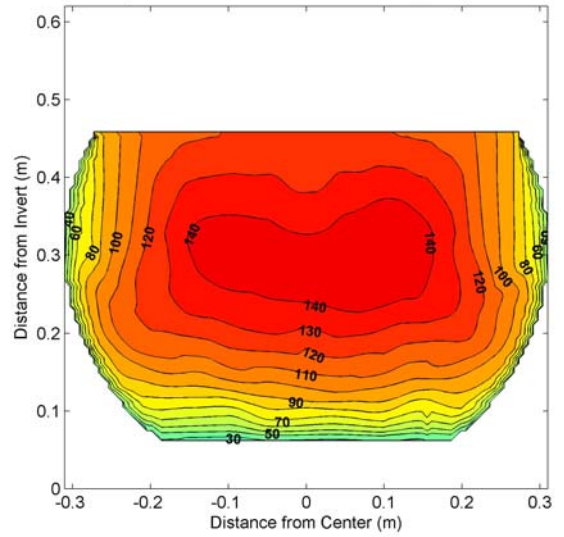


Figure B - 76: $S=1.0\%$, $Q=0.254\text{m}^3/\text{s}$ XS20,
 $y_o=0.392\text{ m}$, $A=0.221\text{ m}^2$, $u_{avg}=115.0\text{ cm/s}$

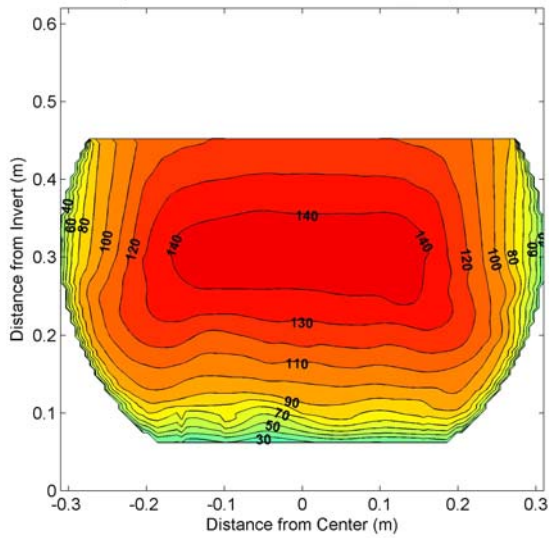


Figure B - 75: $S=1.0\%$, $Q=0.254\text{m}^3/\text{s}$ XS17,
 $y_o=0.391\text{ m}$, $A=0.220\text{ m}^2$, $u_{avg}=115.3\text{ cm/s}$

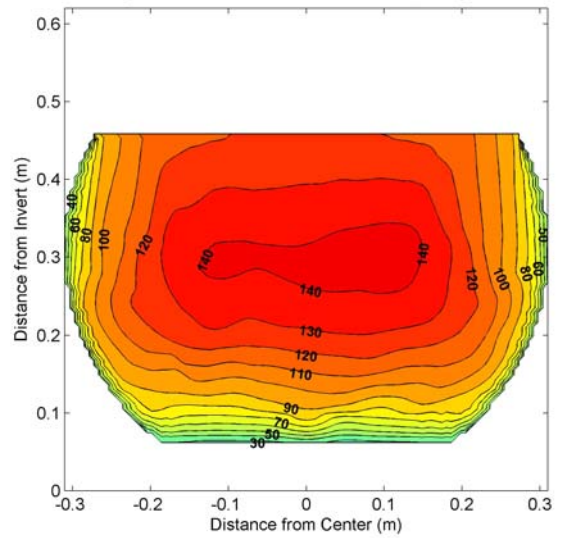


Figure B - 77: $S=1.0\%$, $Q=0.254\text{m}^3/\text{s}$ XS23,
 $y_o=0.393\text{ m}$, $A=0.221\text{ m}^2$, $u_{avg}=114.7\text{ cm/s}$

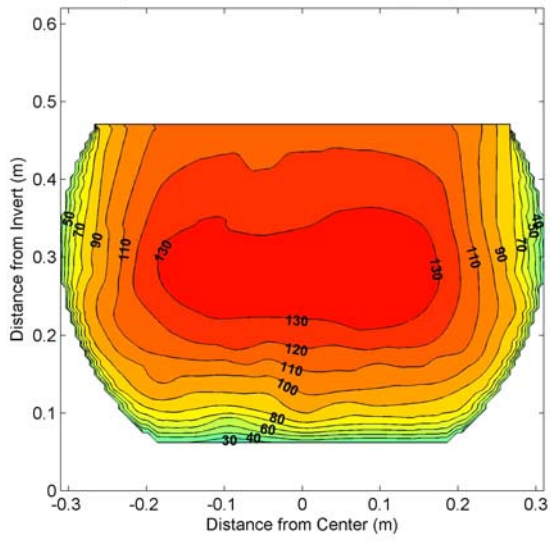


Figure B - 78: $S=1.0\%$, $Q=0.254\text{m}^3/\text{s}$ XS26,
 $y_o=0.408\text{ m}$, $A=0.230\text{ m}^2$, $u_{avg}=110.7\text{ cm/s}$

S5Q145s – Smooth Wall

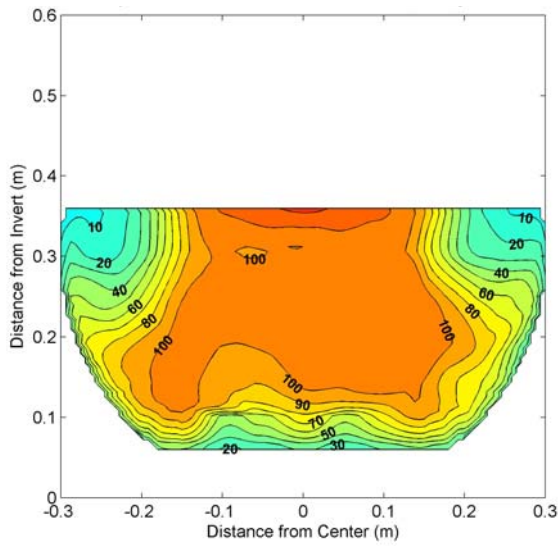


Figure B - 79: $S=0.5\%$, $Q=0.145\text{m}^3/\text{s}$ XS2,
 $y_o=0.297\text{ m}$, $A=0.161\text{ m}^2$, $u_{avg}=90.3\text{ cm/s}$

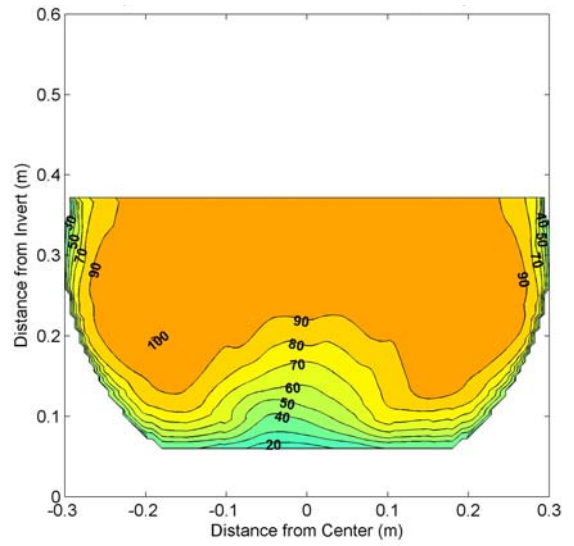


Figure B - 81: $S=0.5\%$, $Q=0.145\text{m}^3/\text{s}$ XS6,
 $y_o=0.306\text{ m}$, $A=0.166\text{ m}^2$, $u_{avg}=87.4\text{ cm/s}$

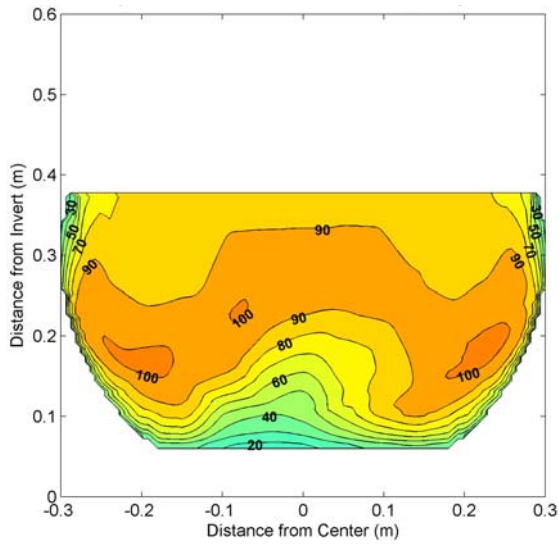


Figure B - 80: $S=0.5\%$, $Q=0.145\text{m}^3/\text{s}$ XS4,
 $y_o=0.312\text{ m}$, $A=0.169\text{ m}^2$, $u_{avg}=85.6\text{ cm/s}$

S5Q221s – Smooth Wall

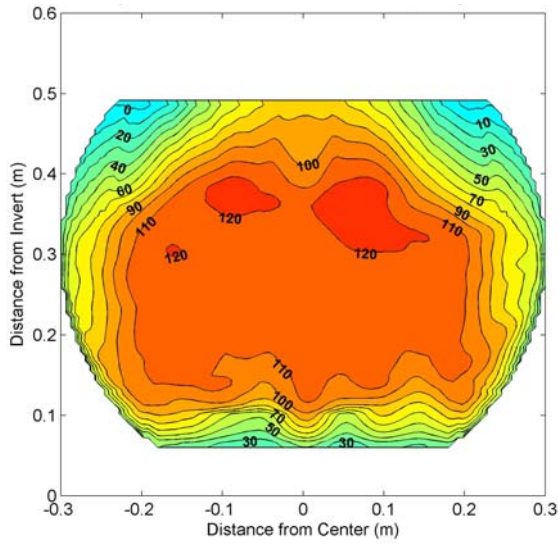


Figure B - 82: $S=0.5\%$, $Q=0.221\text{m}^3/\text{s}$ XS2,
 $y_o=0.426\text{ m}$, $A=0.231\text{ m}^2$, $u_{avg}=95.9\text{ cm/s}$

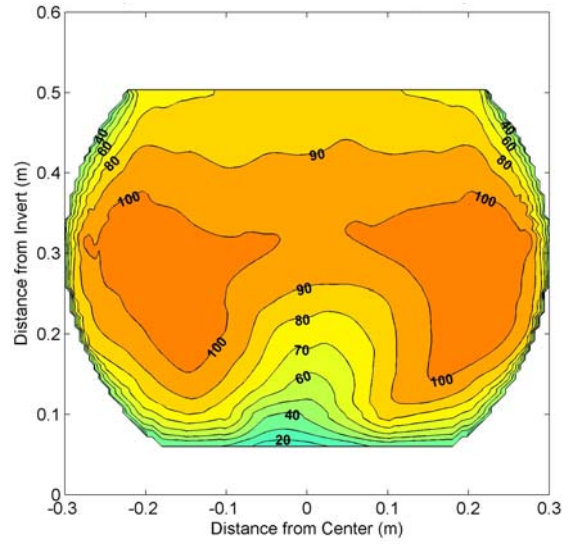


Figure B - 84: $S=0.5\%$, $Q=0.221\text{m}^3/\text{s}$ XS6,
 $y_o=0.437\text{ m}$, $A=0.236\text{ m}^2$, $u_{avg}=93.8\text{ cm/s}$

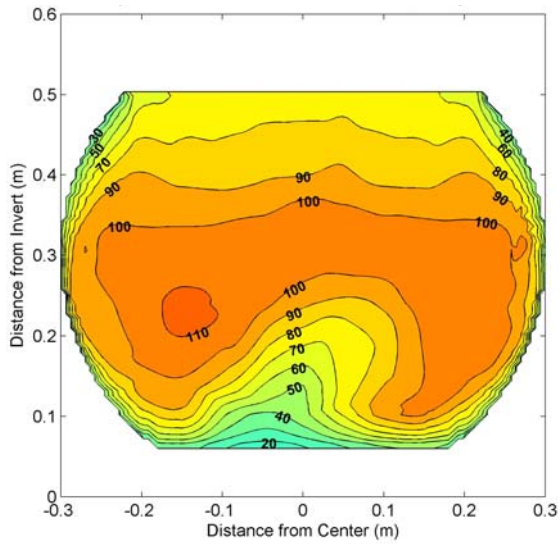


Figure B - 83: $S=0.5\%$, $Q=0.221\text{m}^3/\text{s}$ XS4,
 $y_o=0.437\text{ m}$, $A=0.236\text{ m}^2$, $u_{avg}=93.8\text{ cm/s}$

Appendix C– Vertical Velocity Profiles

S0Q64

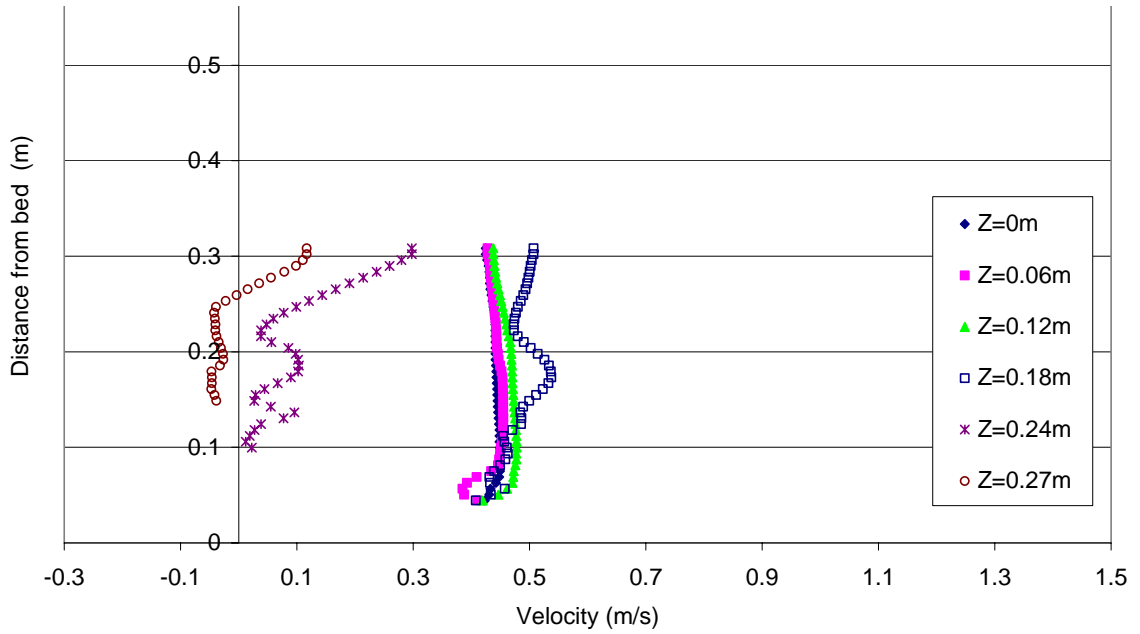


Figure C - 1: Velocity profiles for S0Q64, XS1

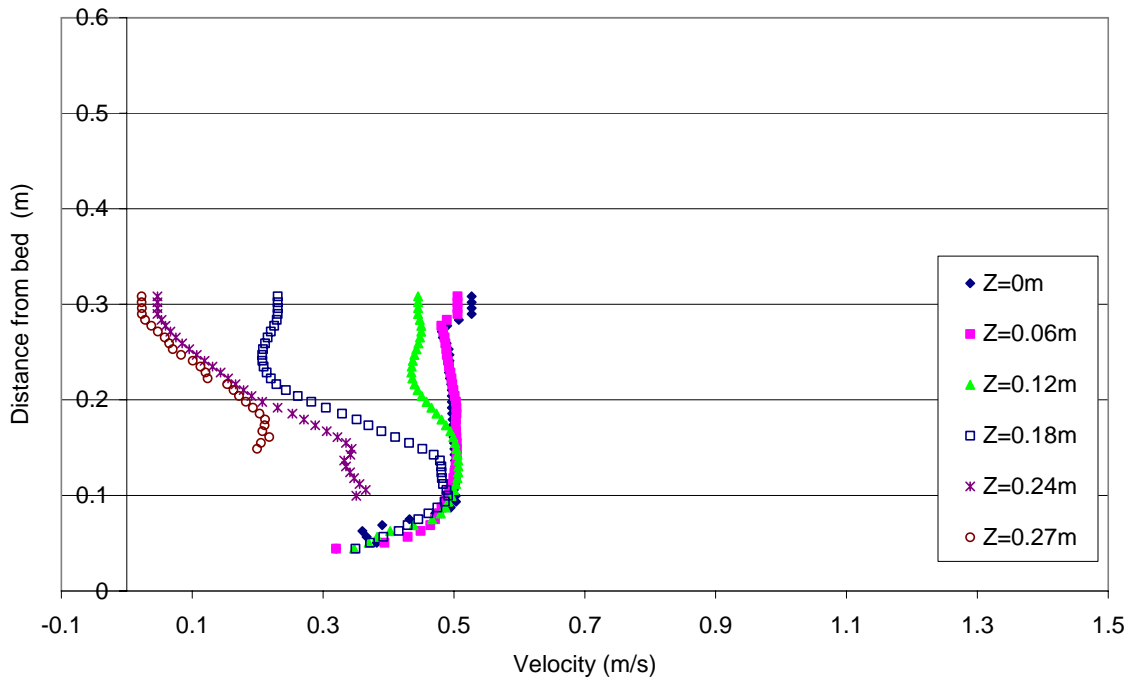


Figure C - 2: Velocity profiles for S0Q64, XS2

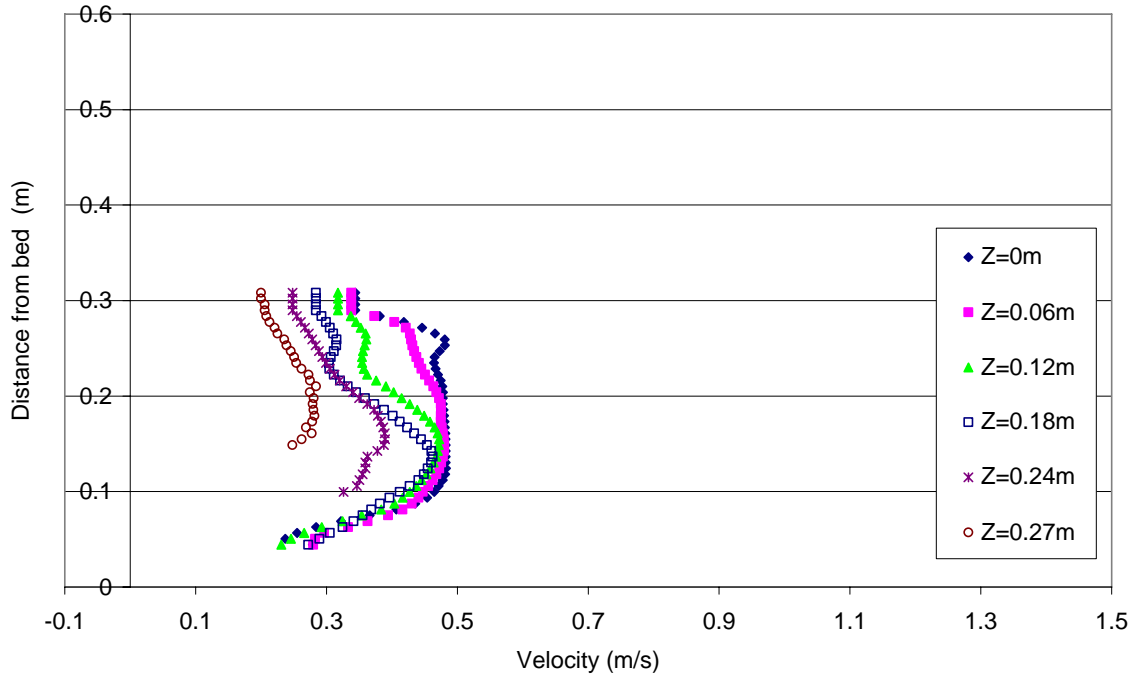


Figure C - 3: Velocity profiles for S0Q64, XS3

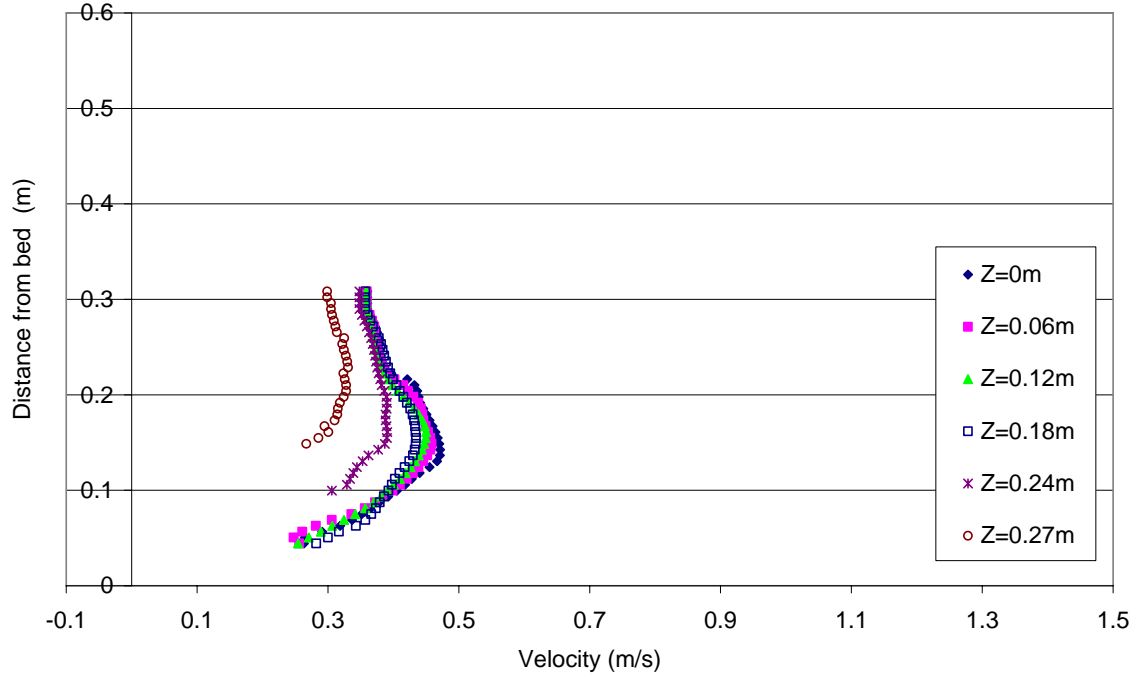


Figure C - 4: Velocity profiles for S0Q64, XS4

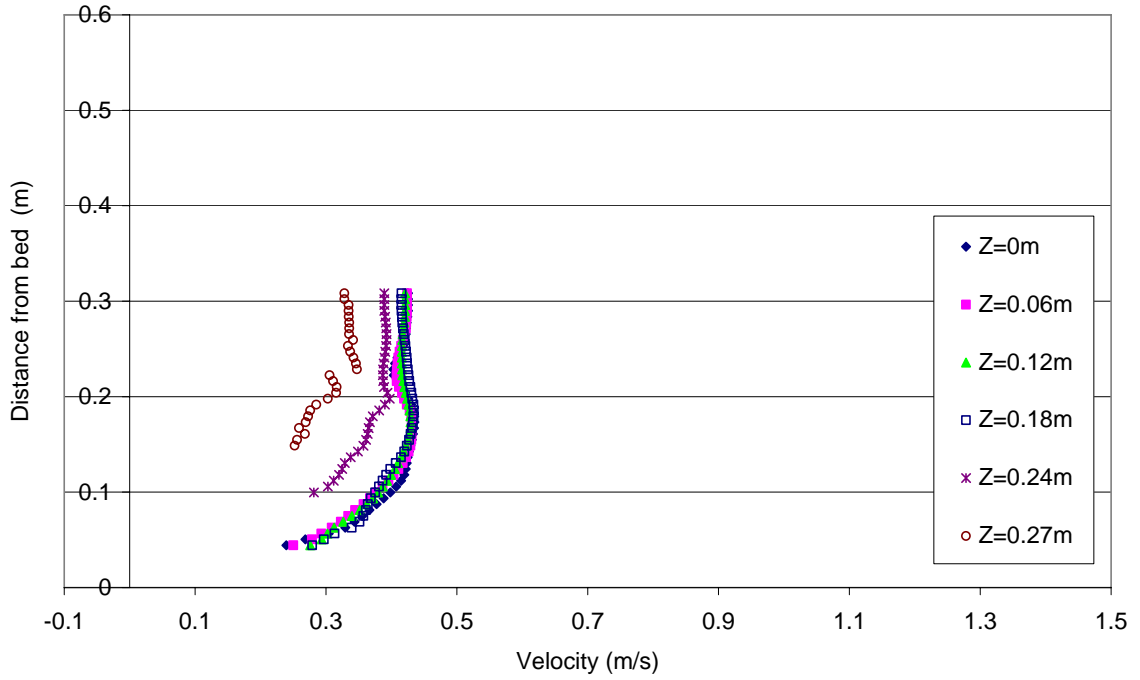


Figure C - 5: Velocity profiles for S0Q64, XS6

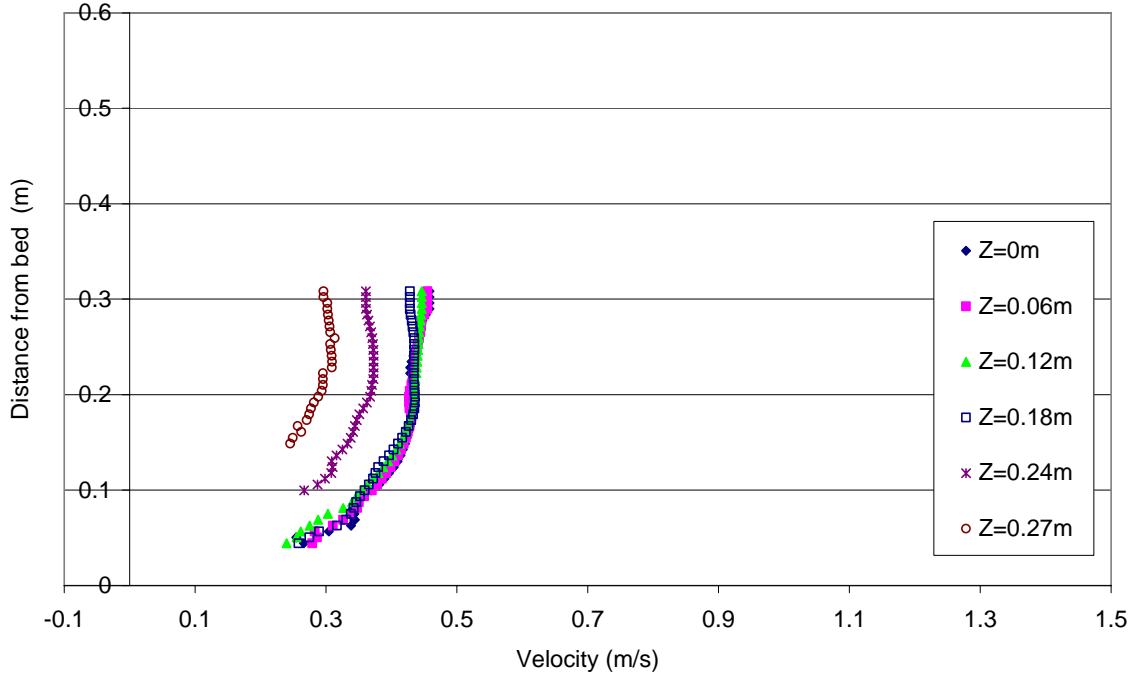


Figure C - 6: Velocity profiles for S0Q64, XS8

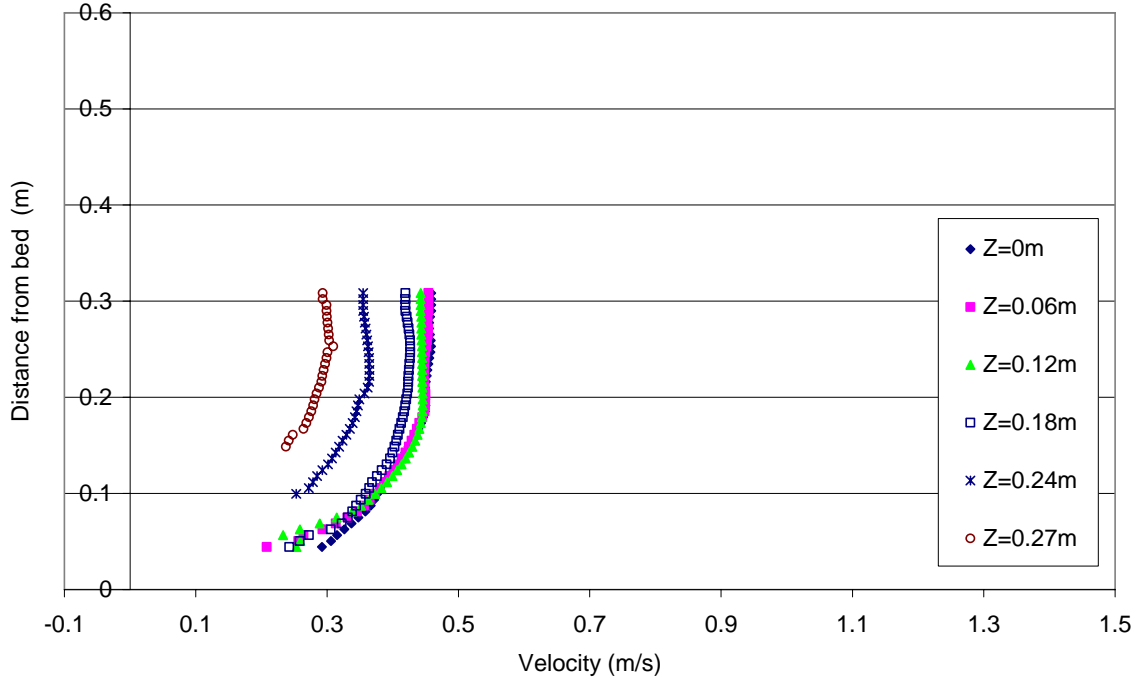


Figure C - 7: Velocity profiles for S0Q64, XS10

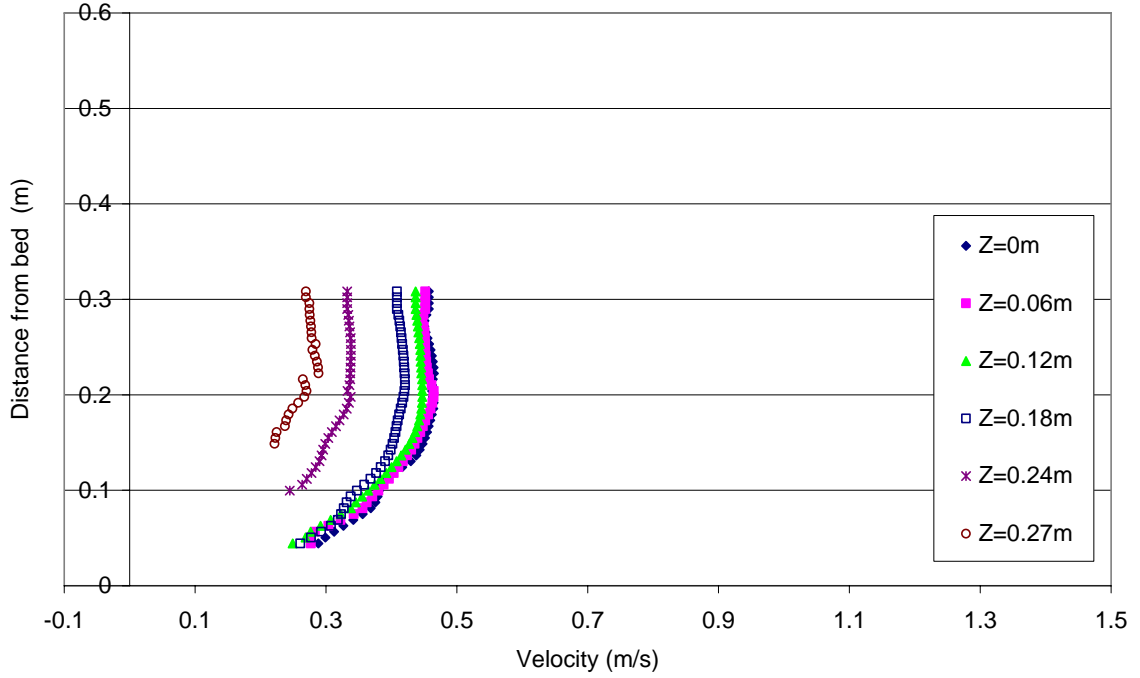


Figure C - 8: Velocity profiles for S0Q64, XS12

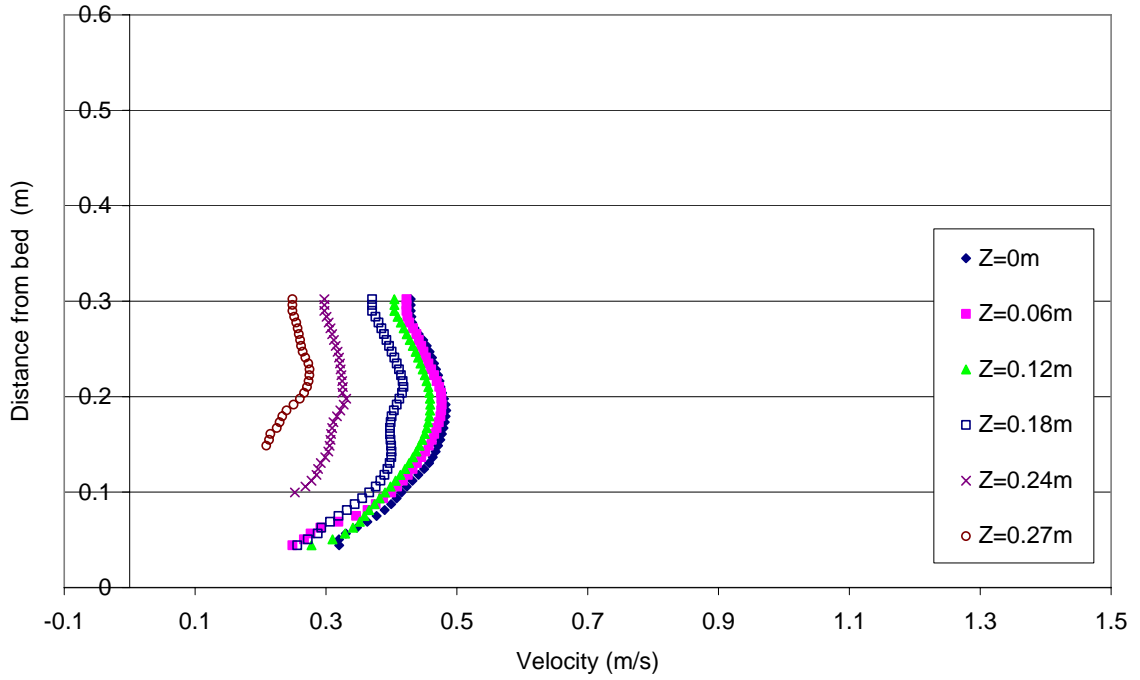


Figure C - 9: Velocity profiles for S0Q64, XS14

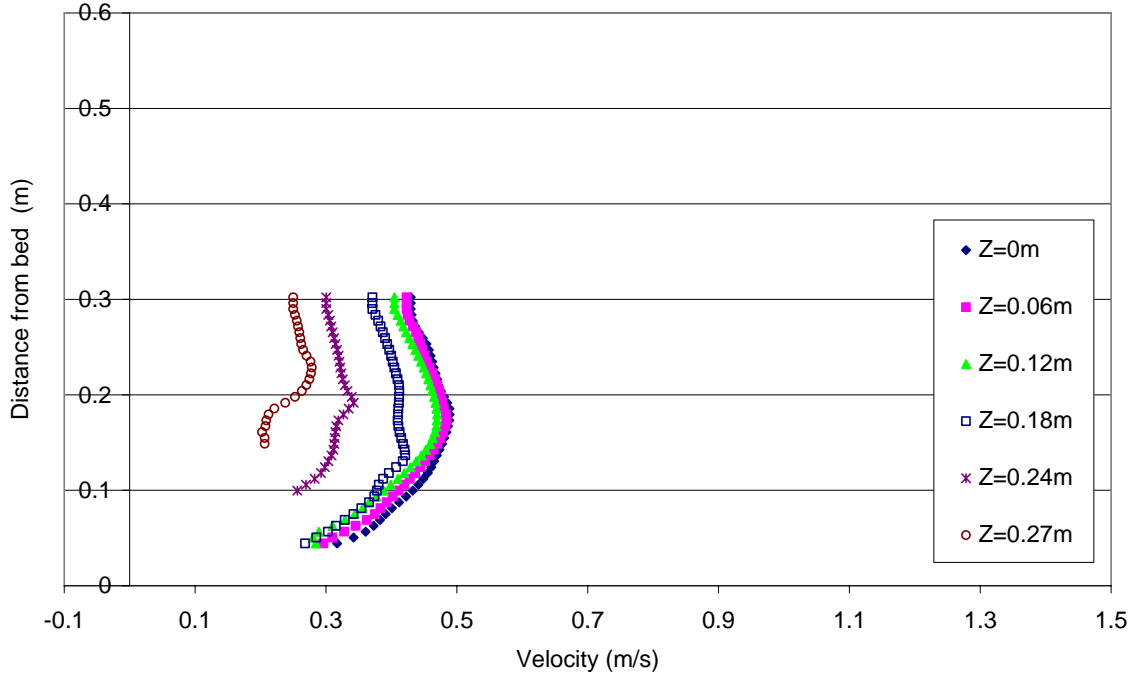


Figure C - 10: Velocity profiles for S0Q64, XS17

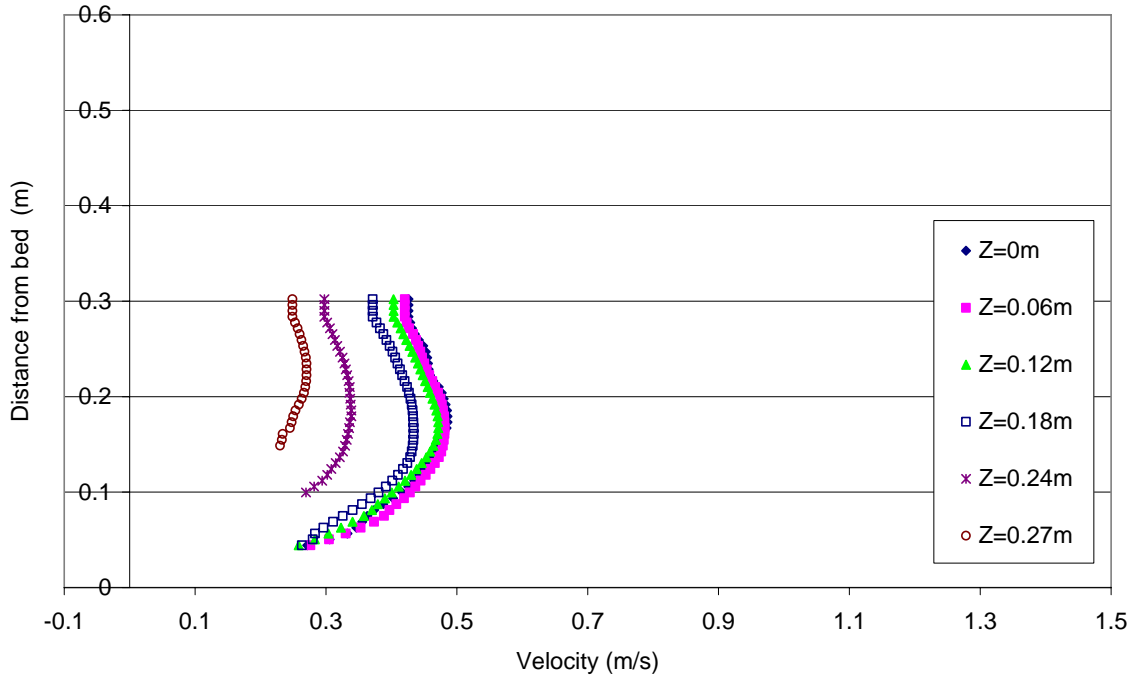


Figure C - 11: Velocity profiles for S0Q64, XS20

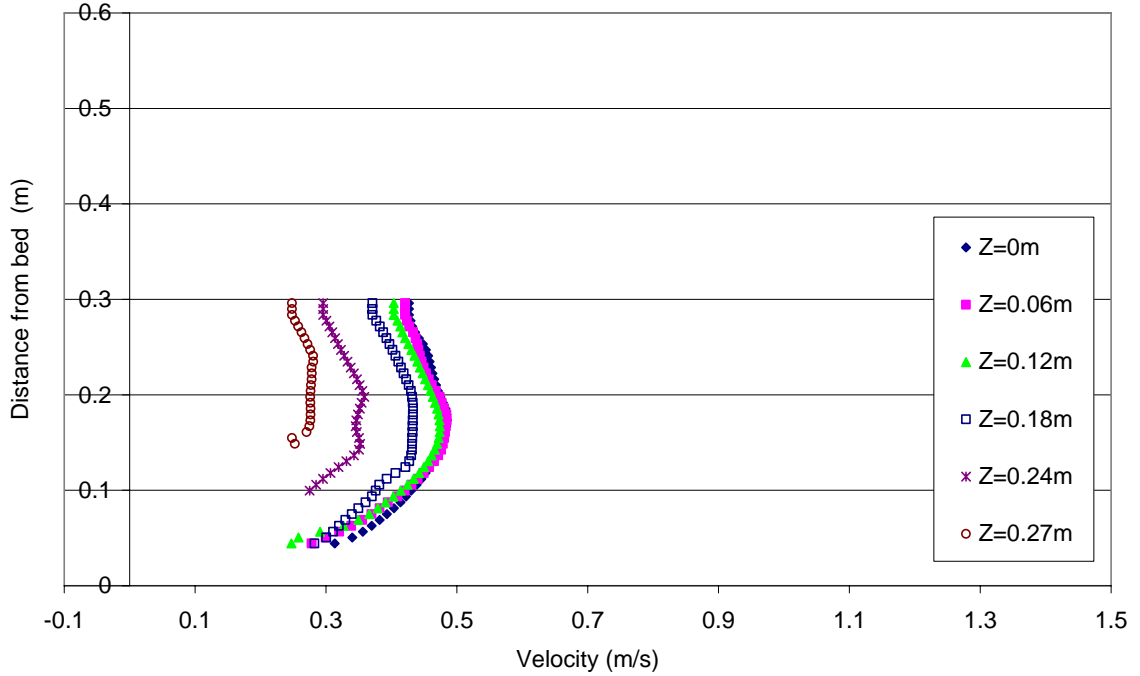


Figure C - 12: Velocity profiles for S0Q64, XS23

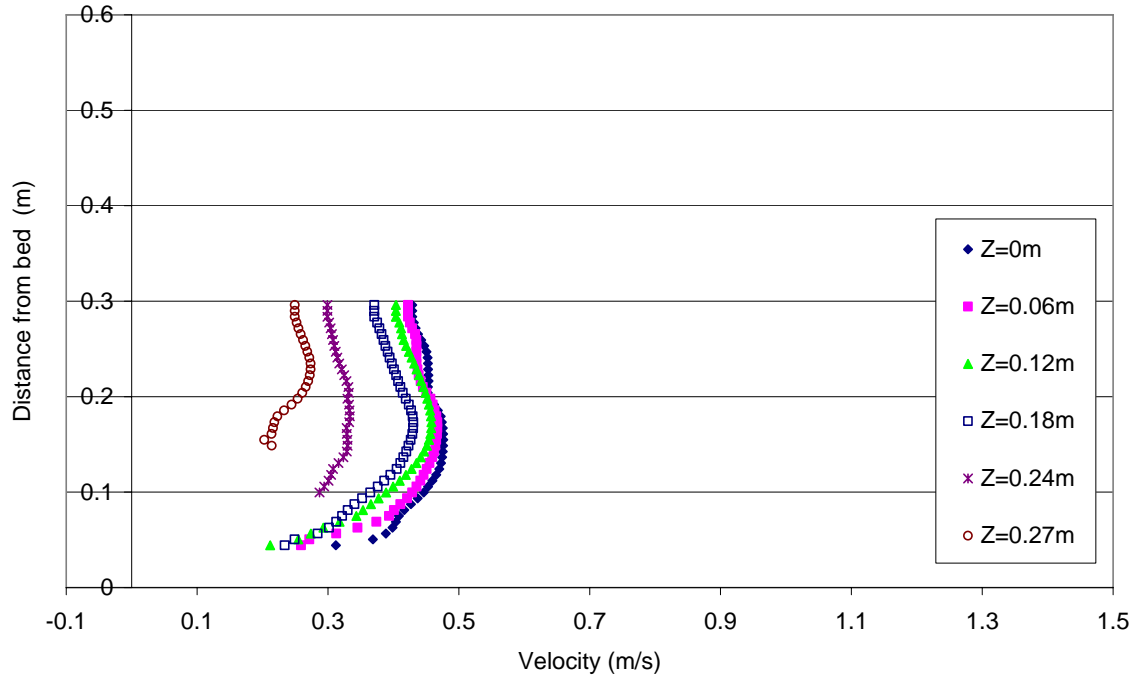


Figure C - 13: Velocity profiles for S0Q64, XS26

S0Q186

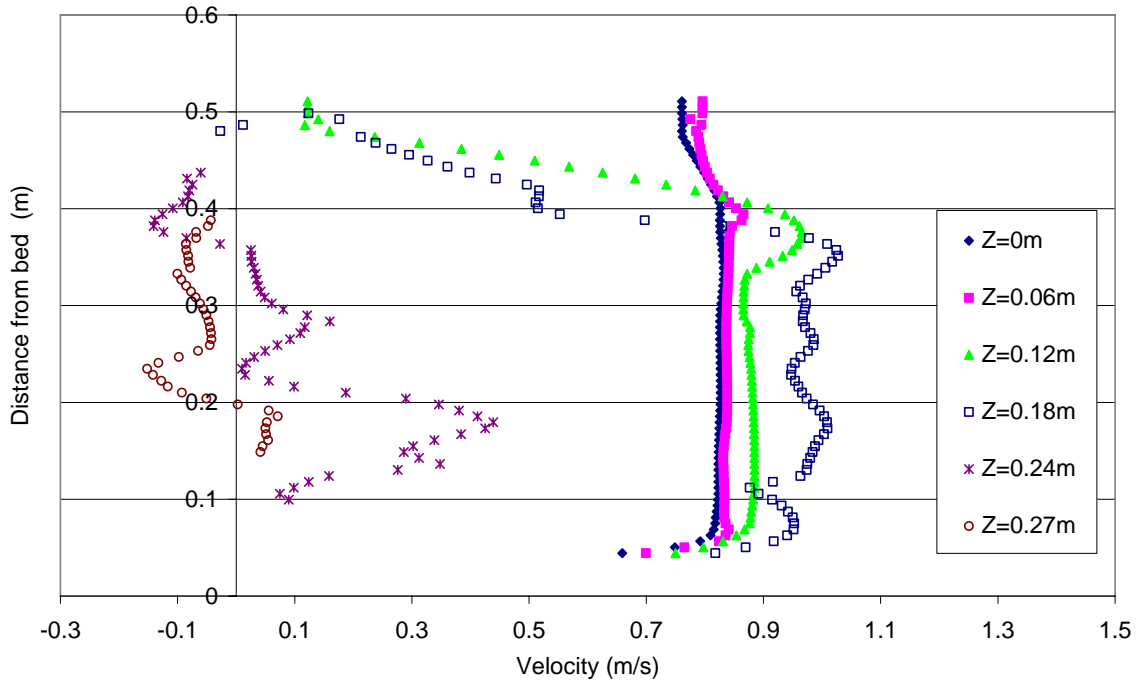


Figure C - 14: Velocity profiles for S0Q186, XS1

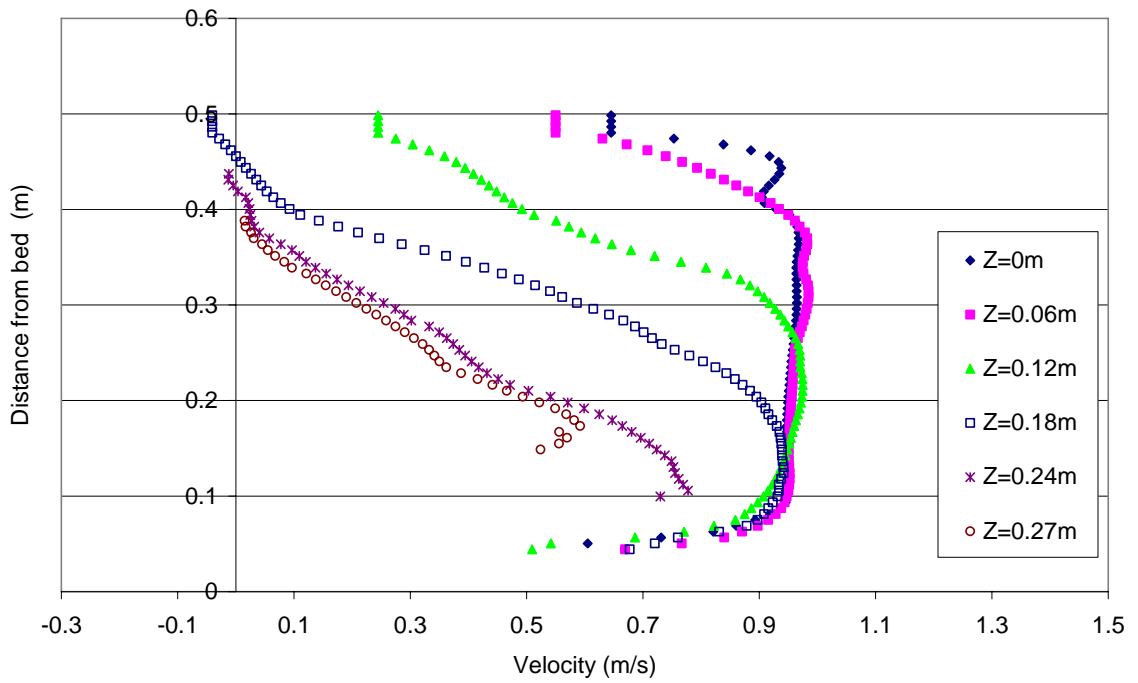


Figure C - 15: Velocity profiles for S0Q186, XS2

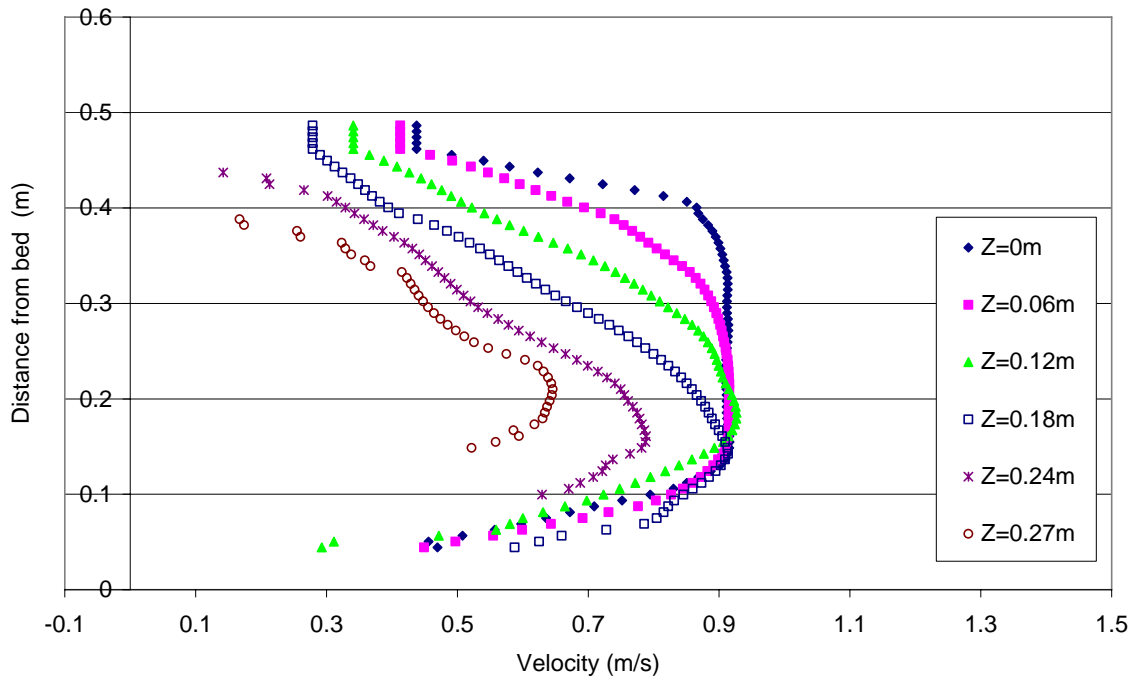


Figure C - 16: Velocity profiles for S0Q186, XS3

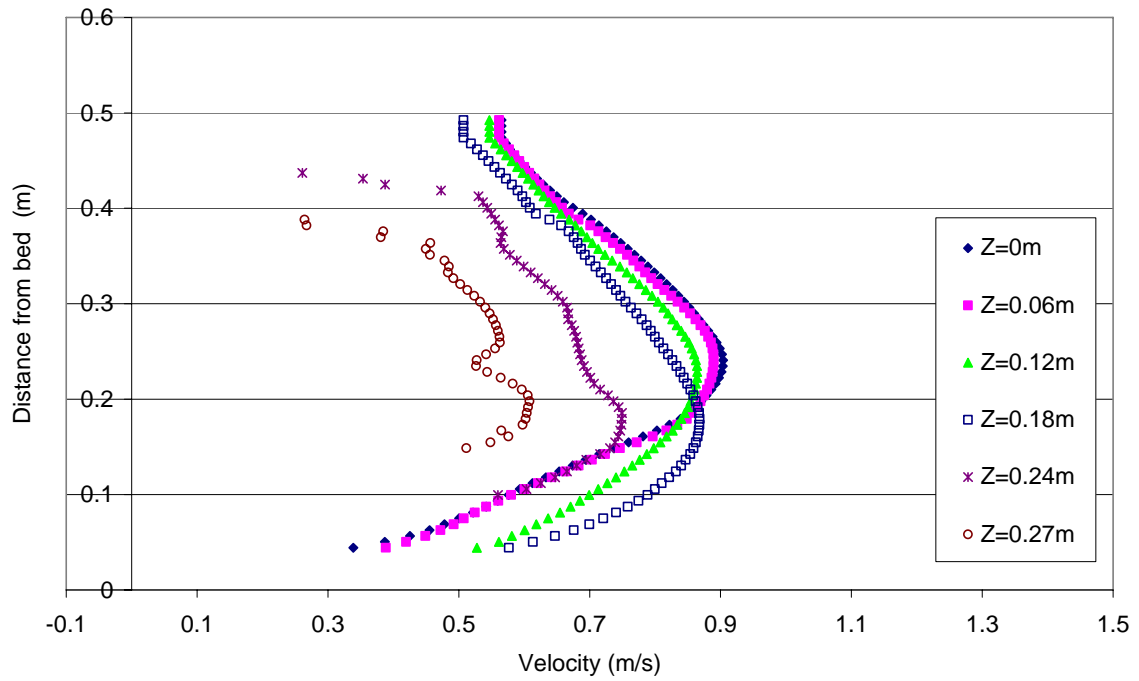


Figure C - 17: Velocity profiles for S0Q186, XS4

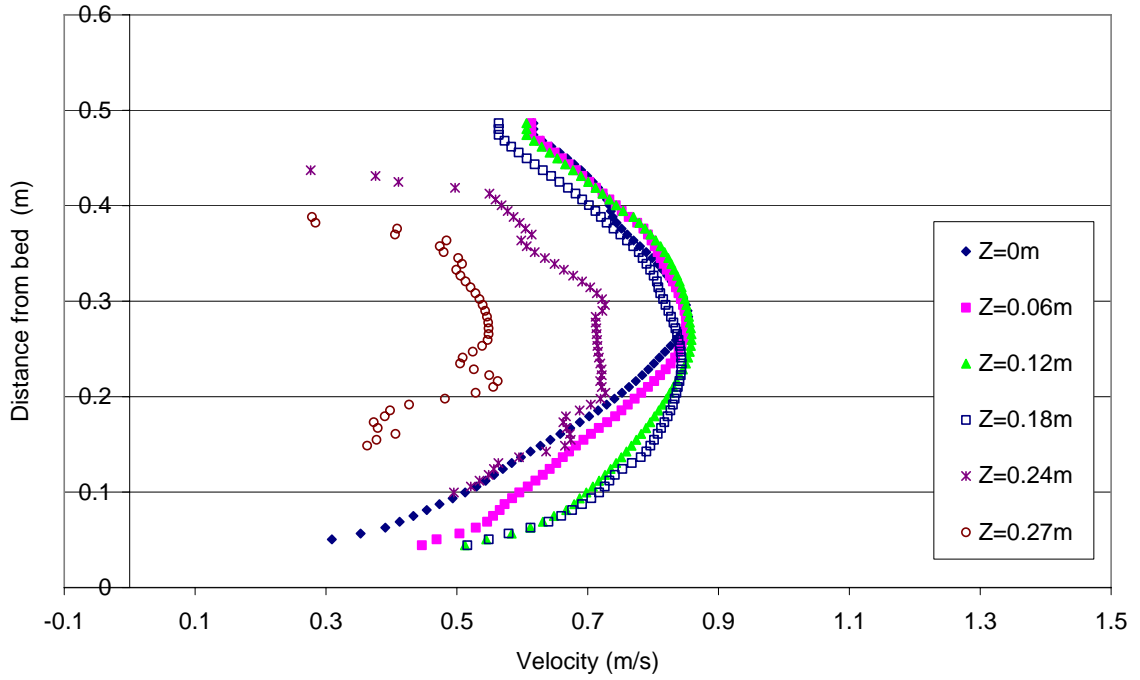


Figure C - 18: Velocity profiles for S0Q186, XS6

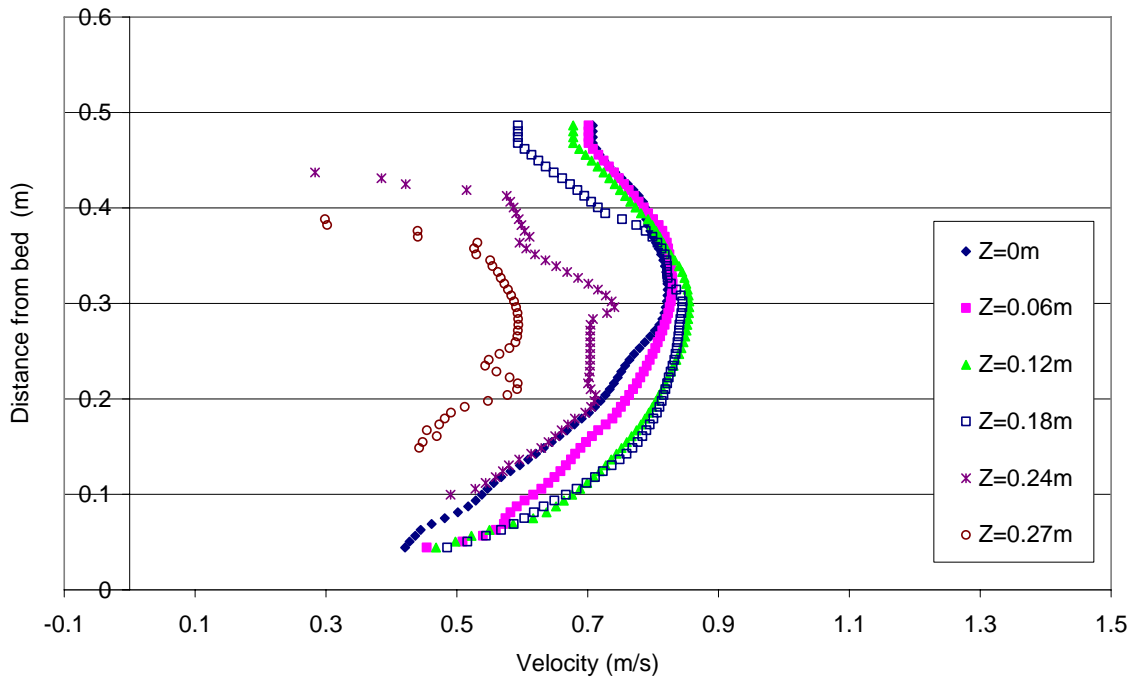


Figure C - 19: Velocity profiles for S0Q186, XS8

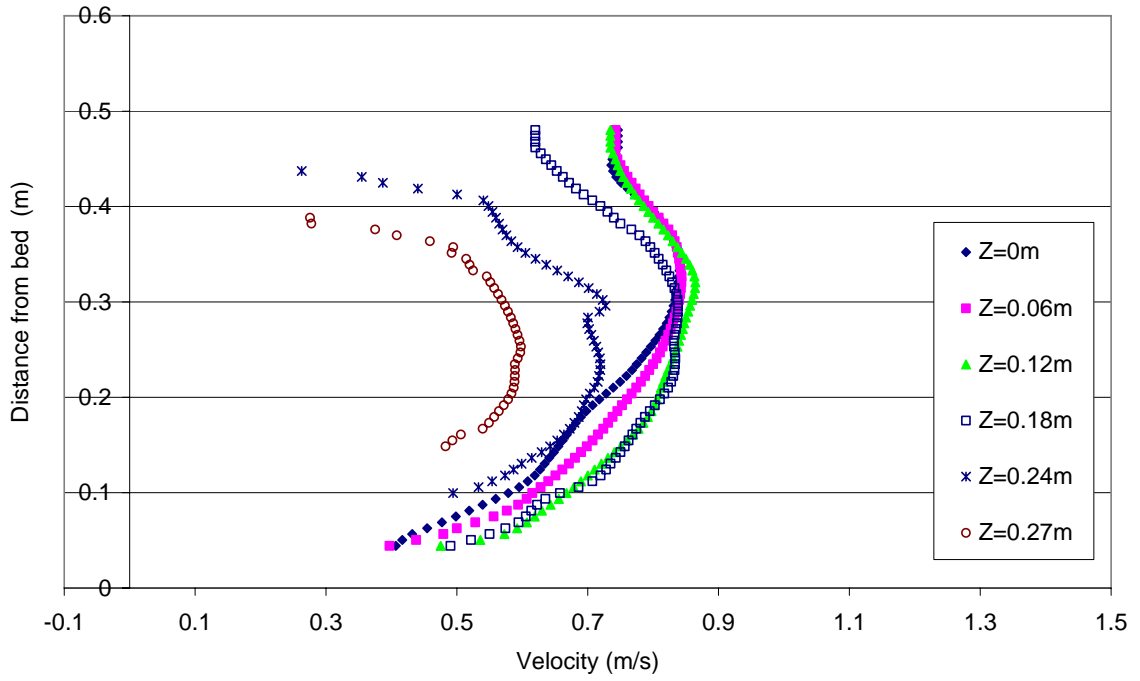


Figure C - 20: Velocity profiles for S0Q186, XS10

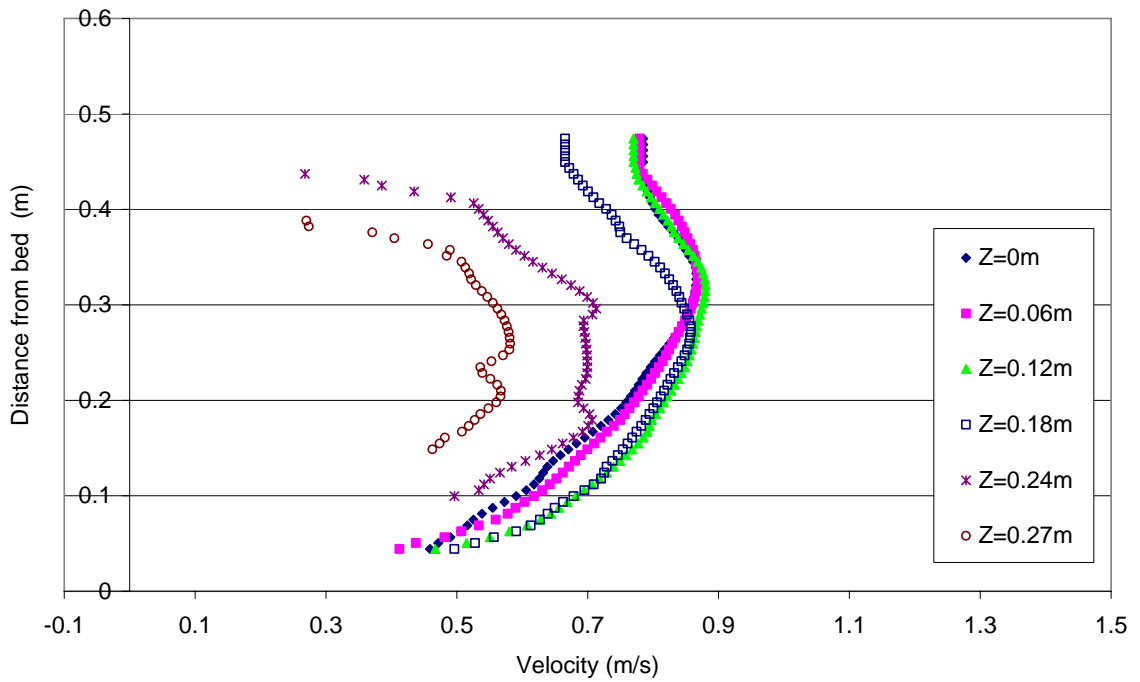


Figure C - 21: Velocity profiles for S0Q186, XS12

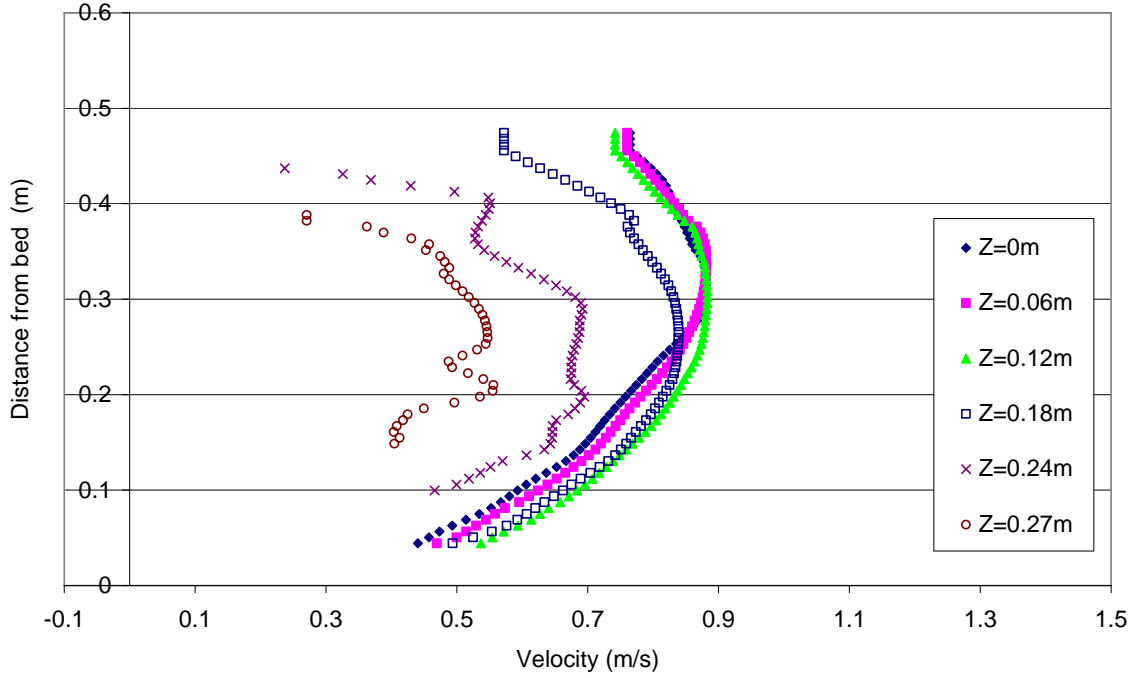


Figure C - 22: Velocity profiles for S0Q186, XS14

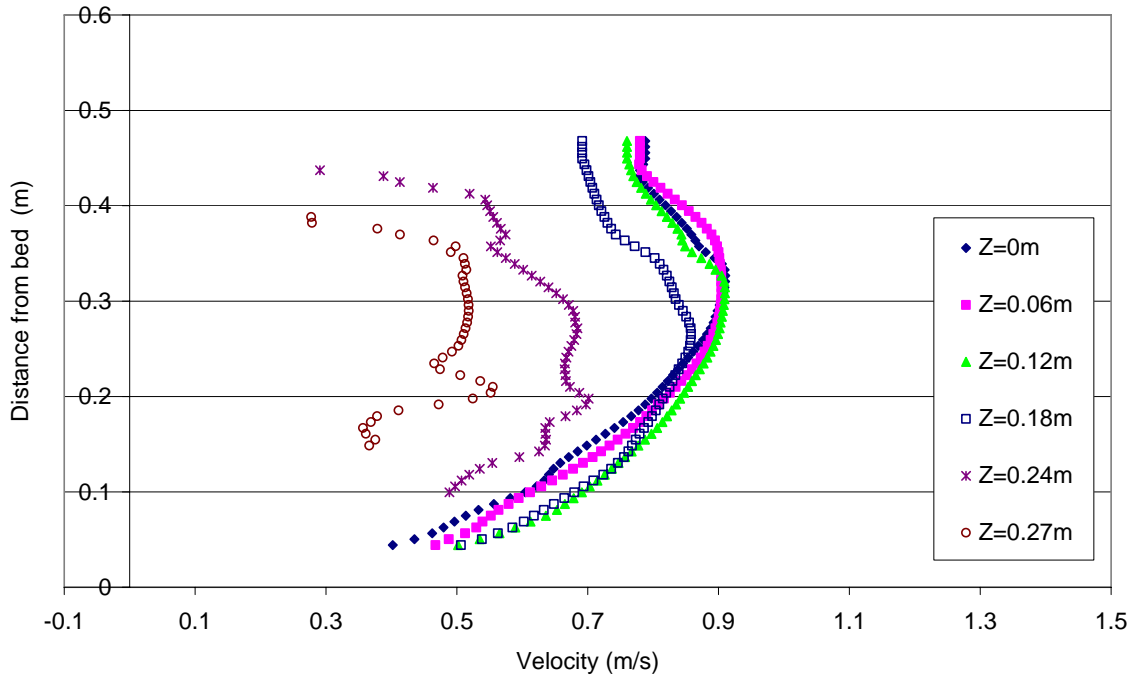


Figure C - 23: Velocity profiles for S0Q186, XS17

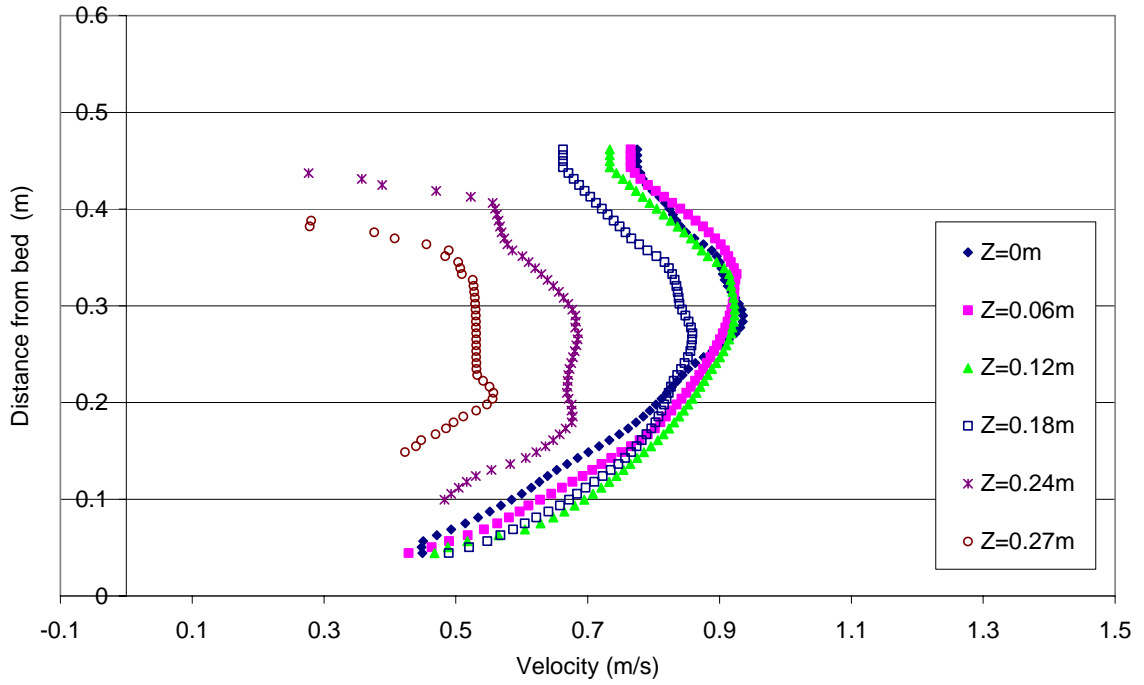


Figure C - 24: Velocity profiles for S0Q186, XS20

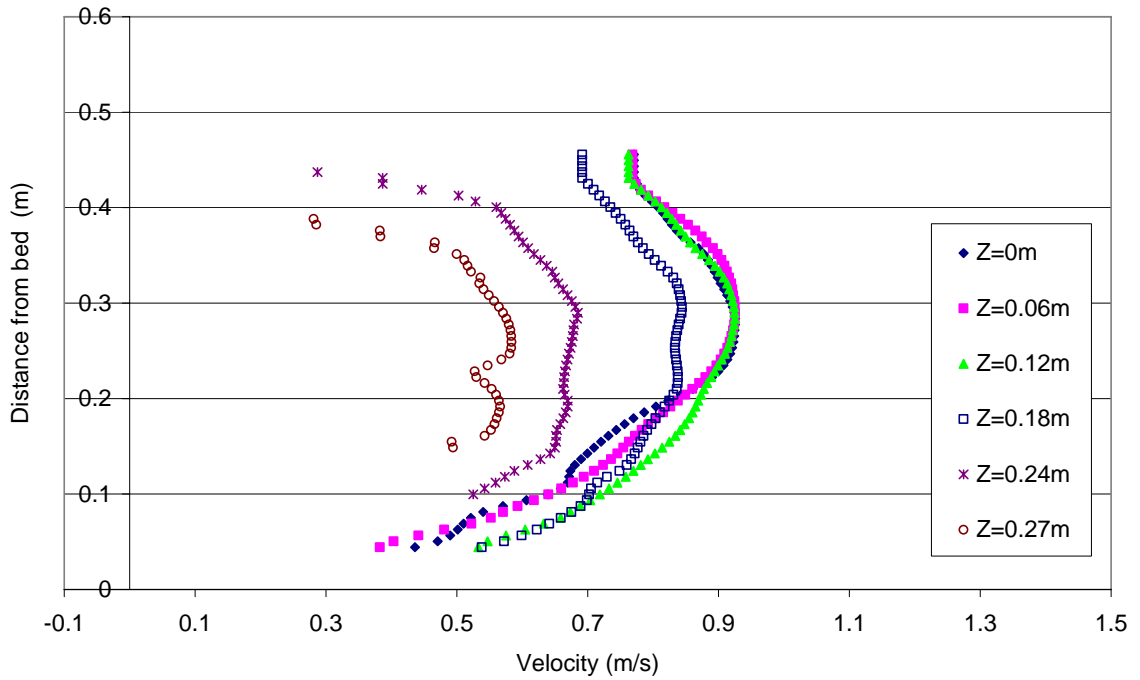


Figure C - 25: Velocity profiles for S0Q186, XS23

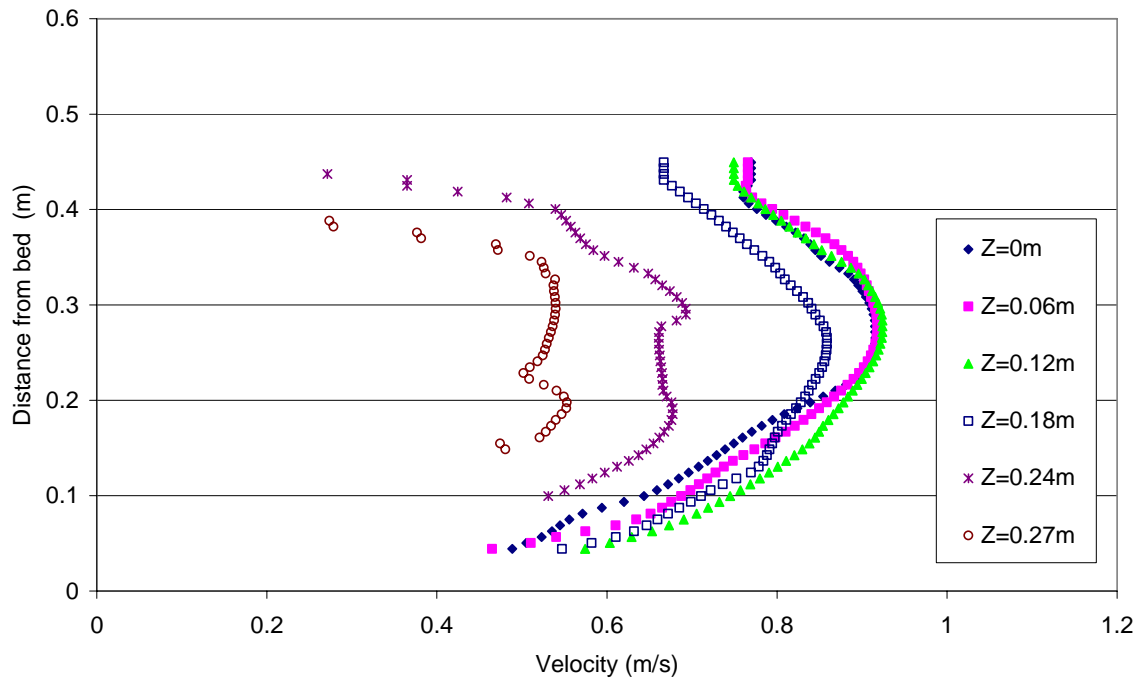


Figure C - 26: Velocity profiles for S0Q186, XS26

S5Q145

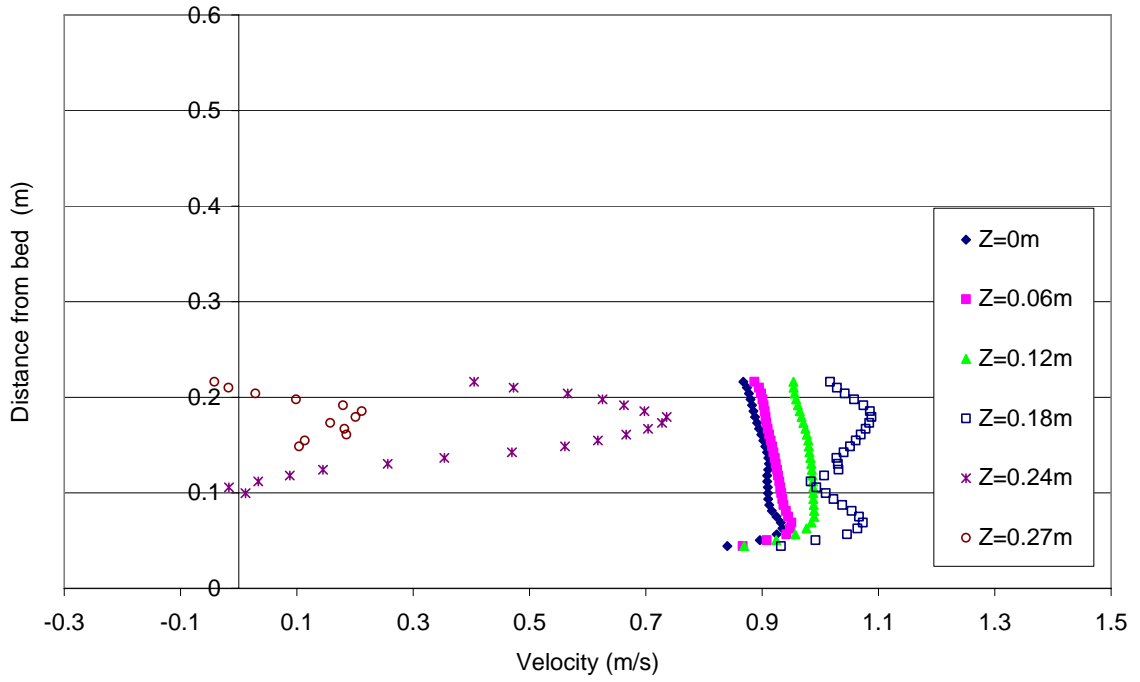


Figure C - 27: Velocity profiles for S5Q145, XS1

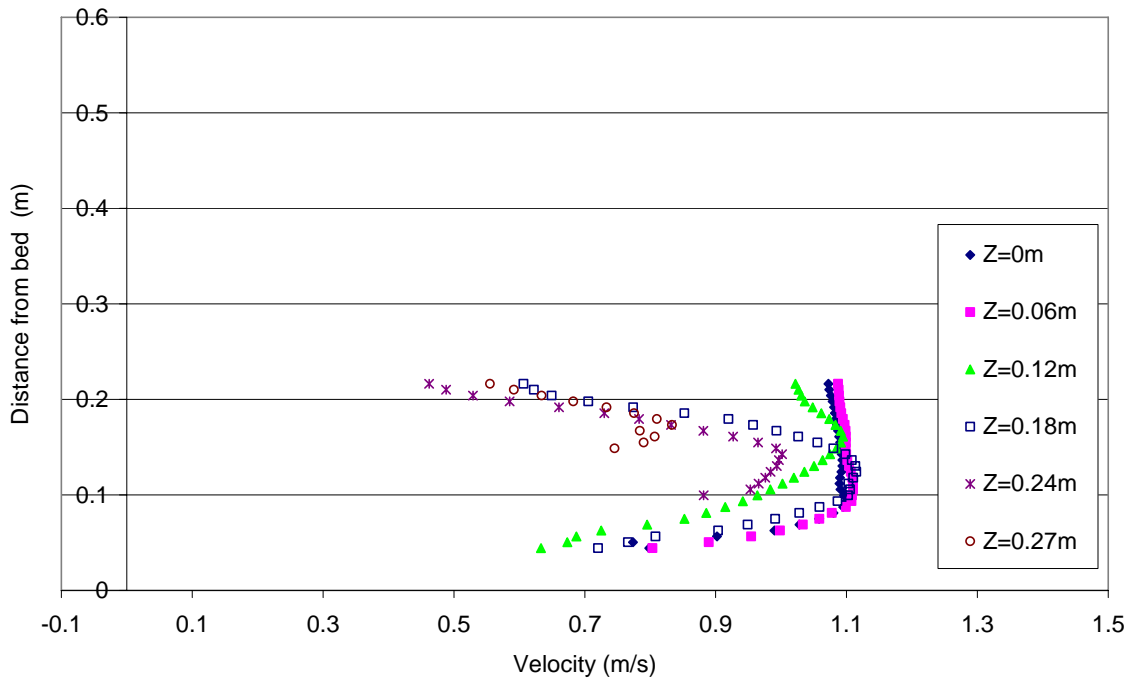


Figure C - 28: Velocity profiles for S5Q145, XS2

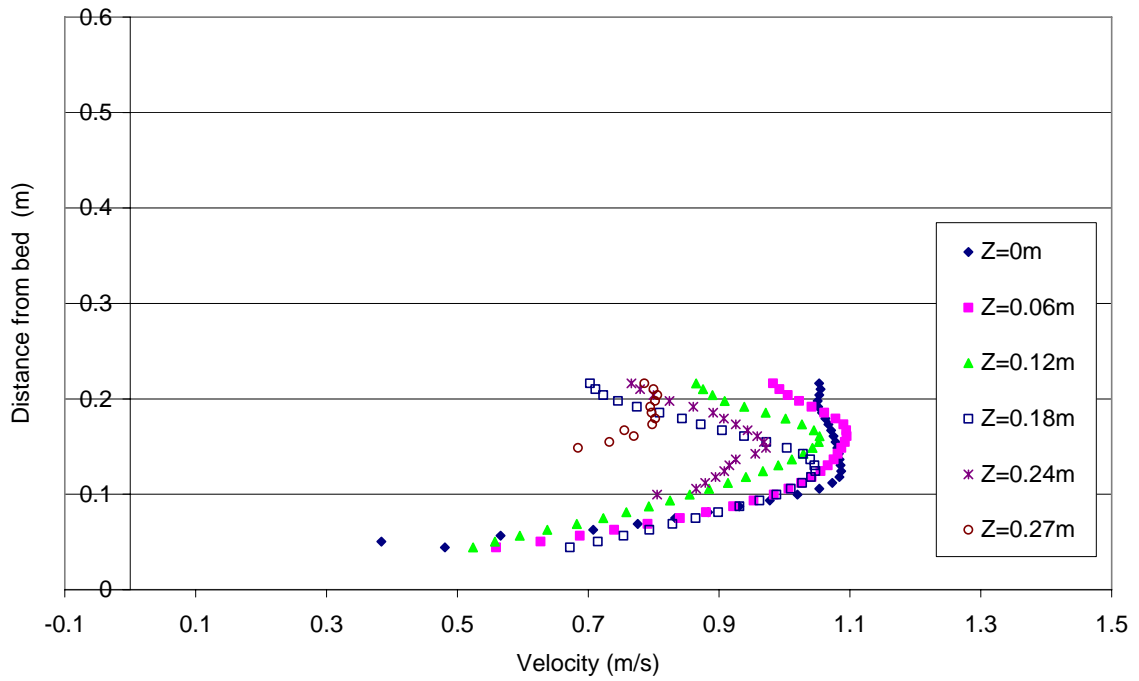


Figure C - 29: Velocity profiles for S5Q145, XS3

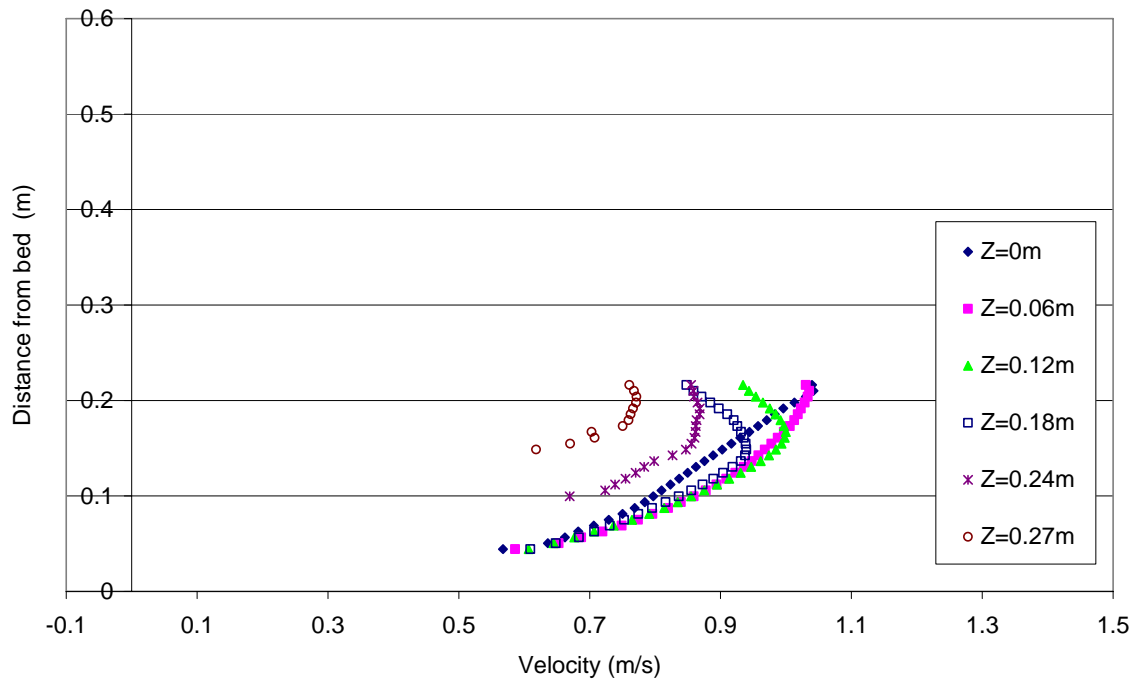


Figure C - 30: Velocity profiles for S5Q145, XS4

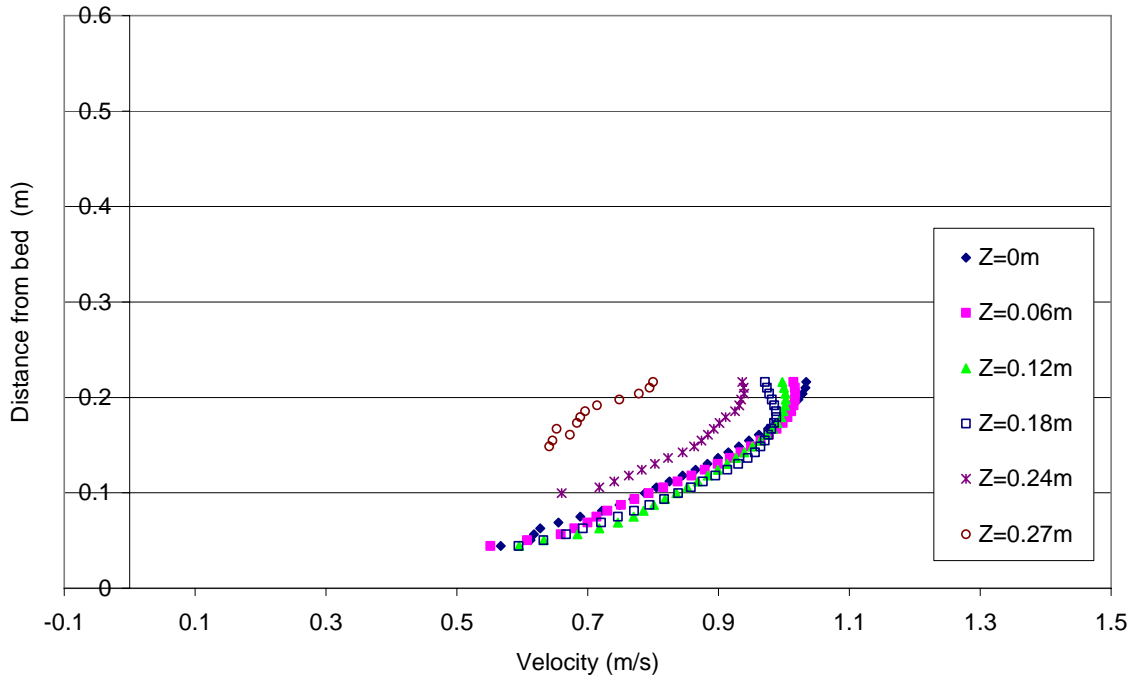


Figure C - 31: Velocity profiles for S5Q145, XS6

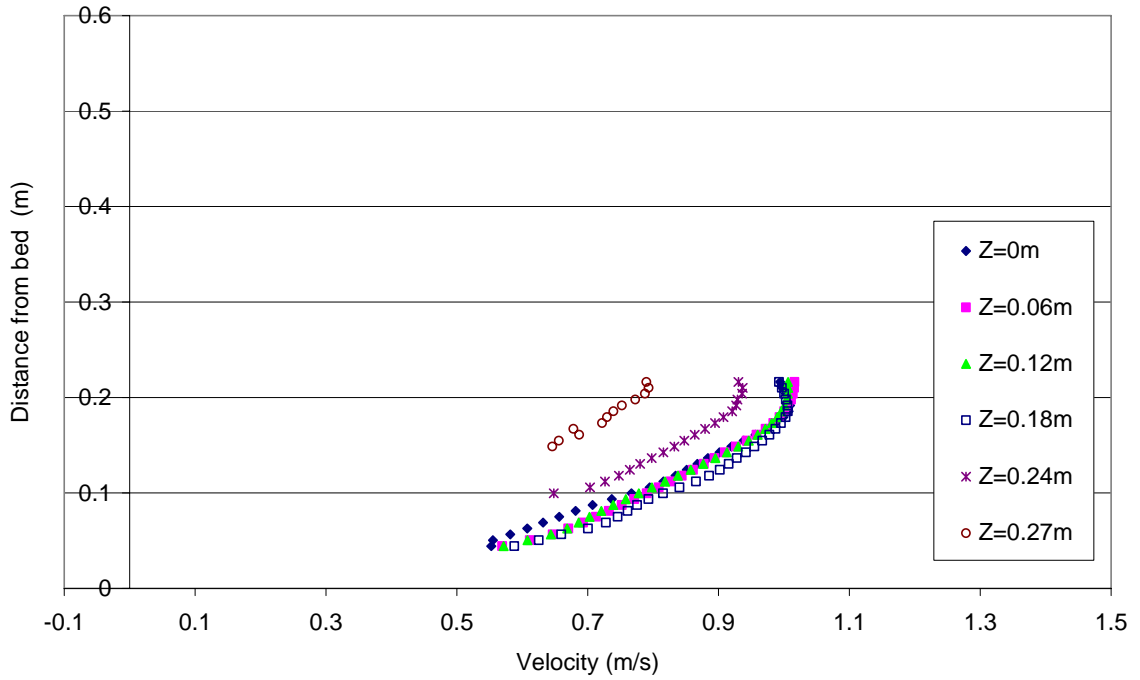


Figure C - 32: Velocity profiles for S5Q145, XS8

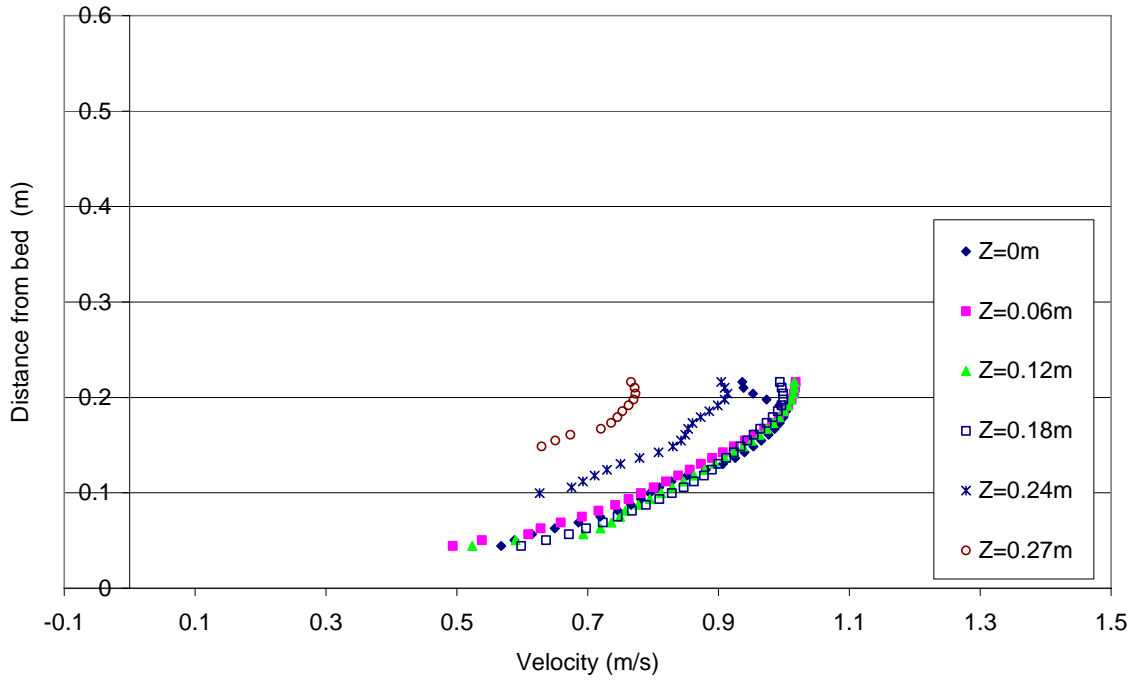


Figure C - 33: Velocity profiles for S5Q145, XS10

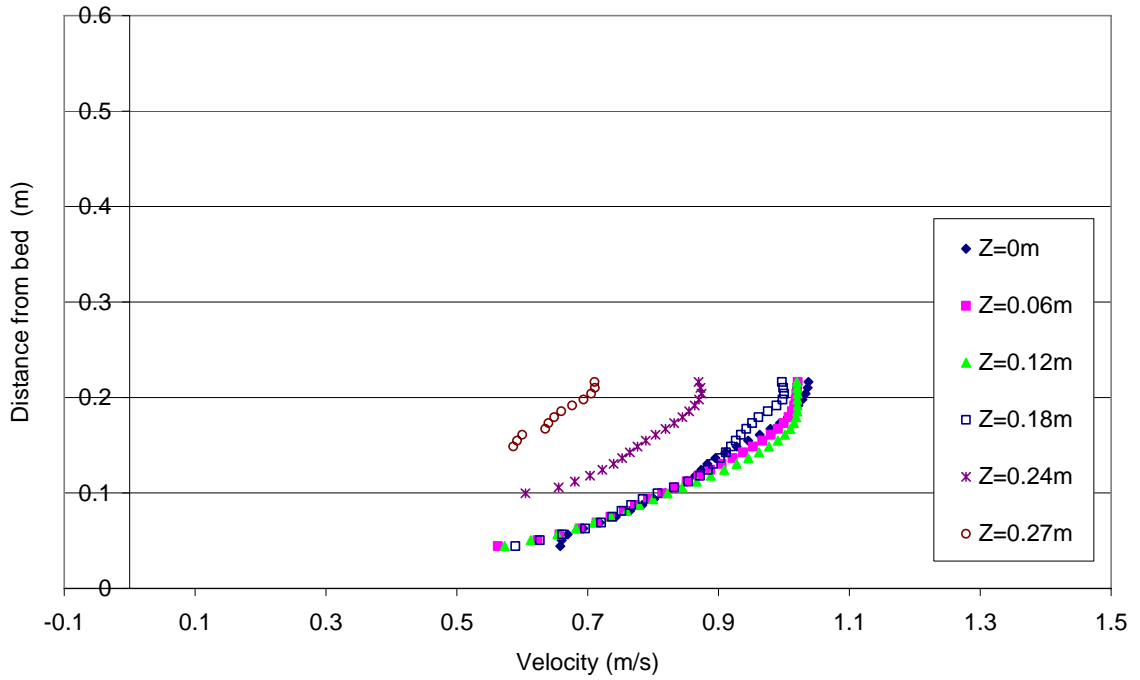


Figure C - 34: Velocity profiles for S5Q145, XS12

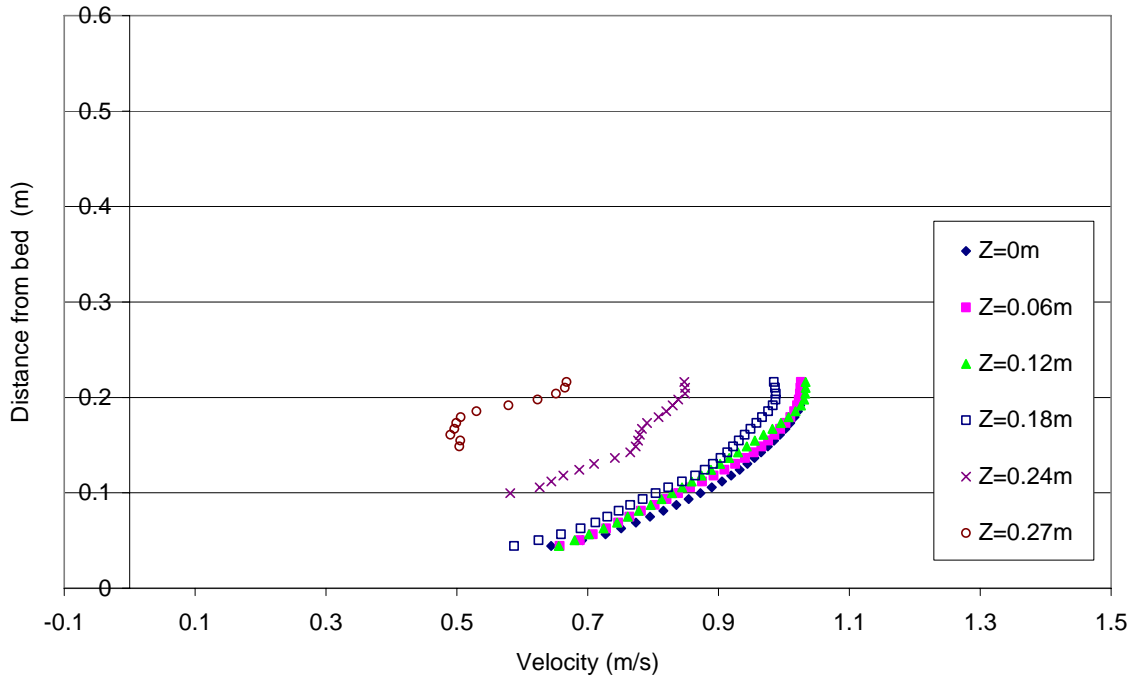


Figure C - 35: Velocity profiles for S5Q145, XS14

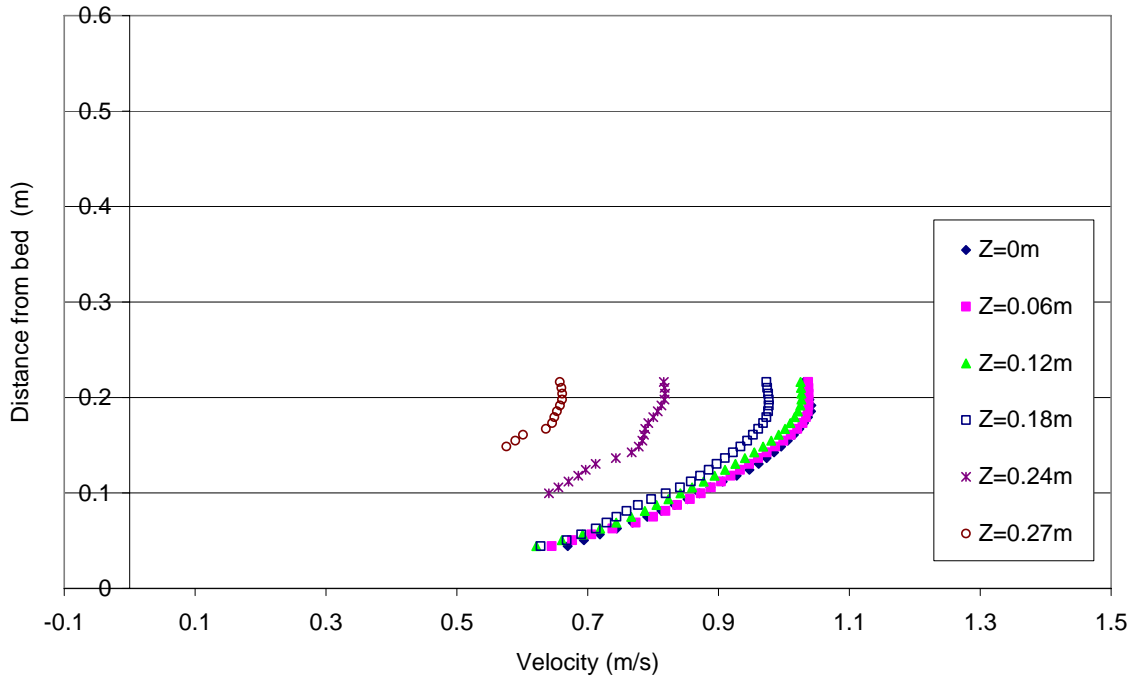


Figure C - 36: Velocity profiles for S5Q145, XS17

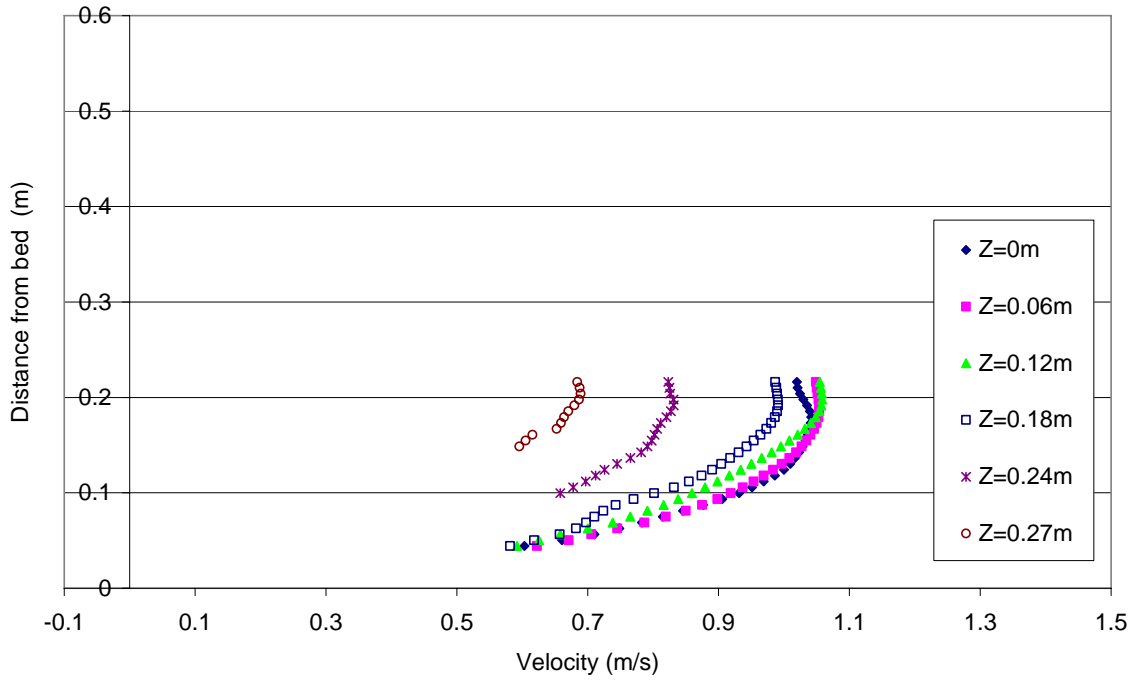


Figure C - 37: Velocity profiles for S5Q145, XS20

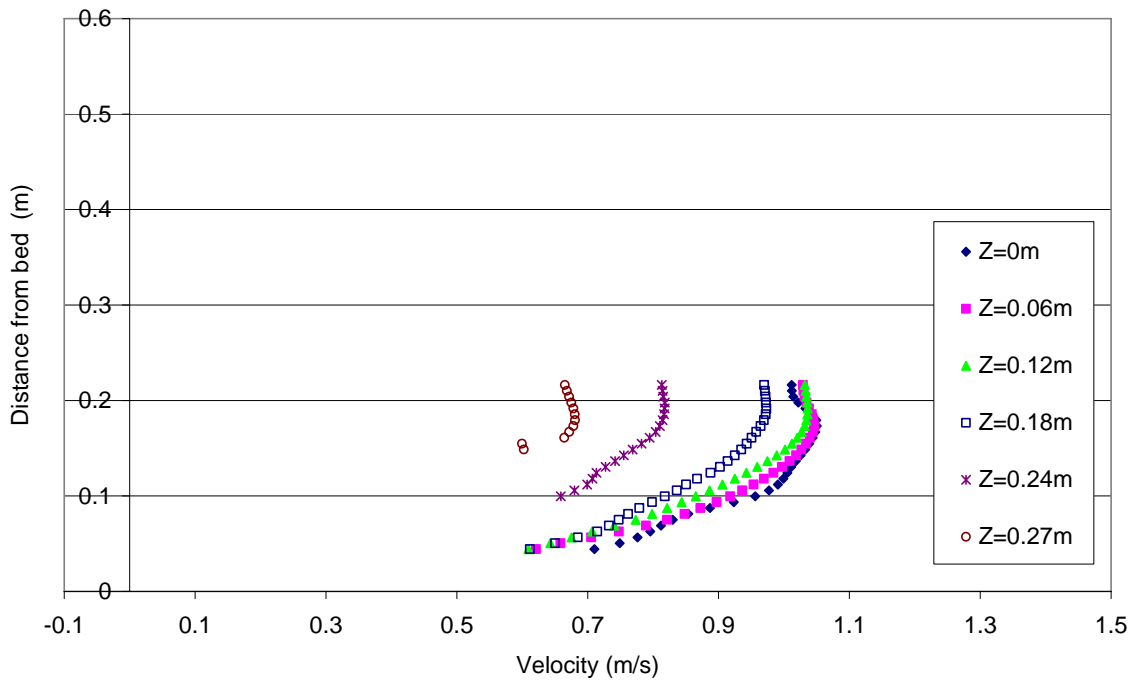


Figure C - 38: Velocity profiles for S5Q145, XS23

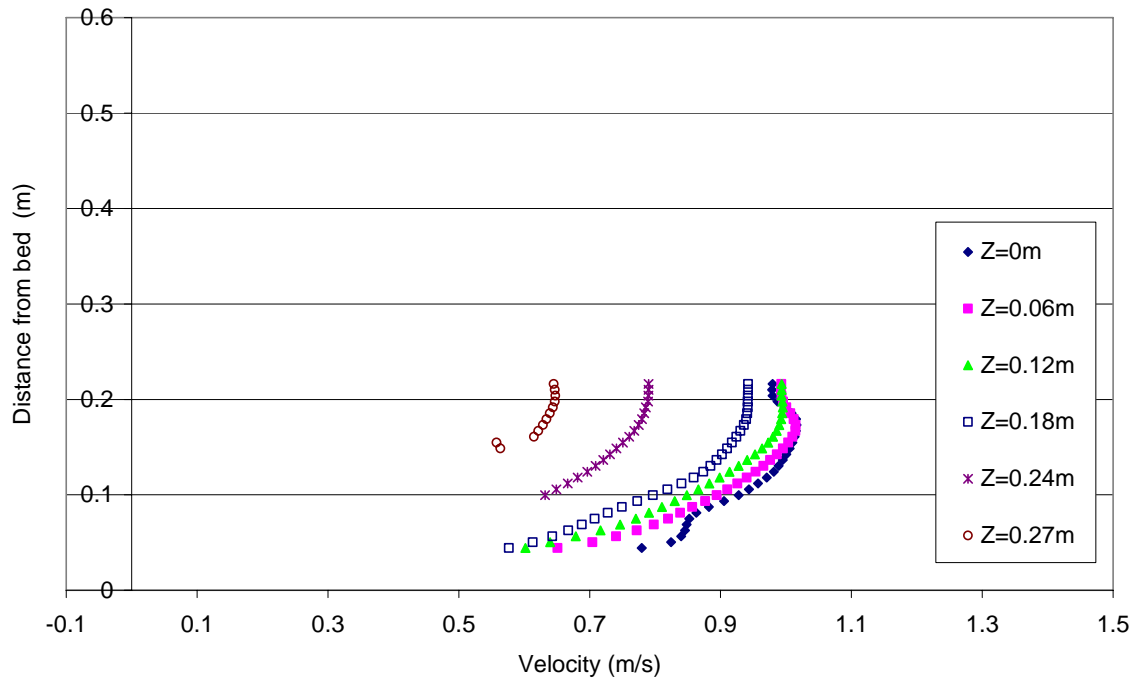


Figure C - 39: Velocity profiles for S5Q145, XS26

S5Q221

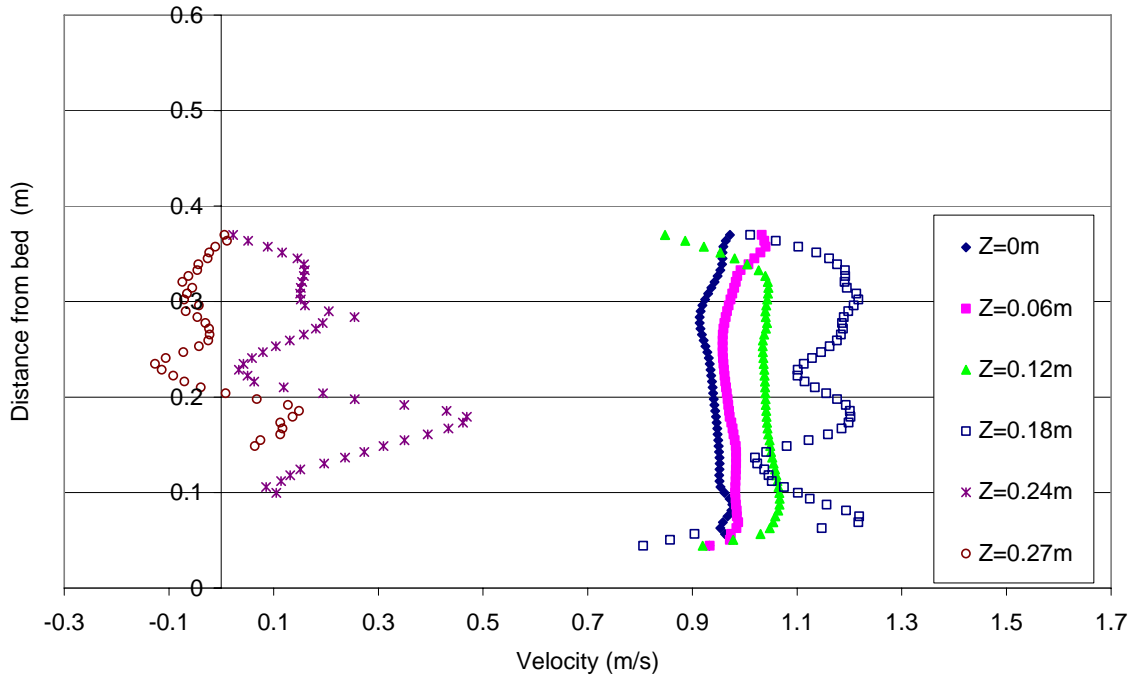


Figure C - 40: Velocity profiles for S5Q221, XS1

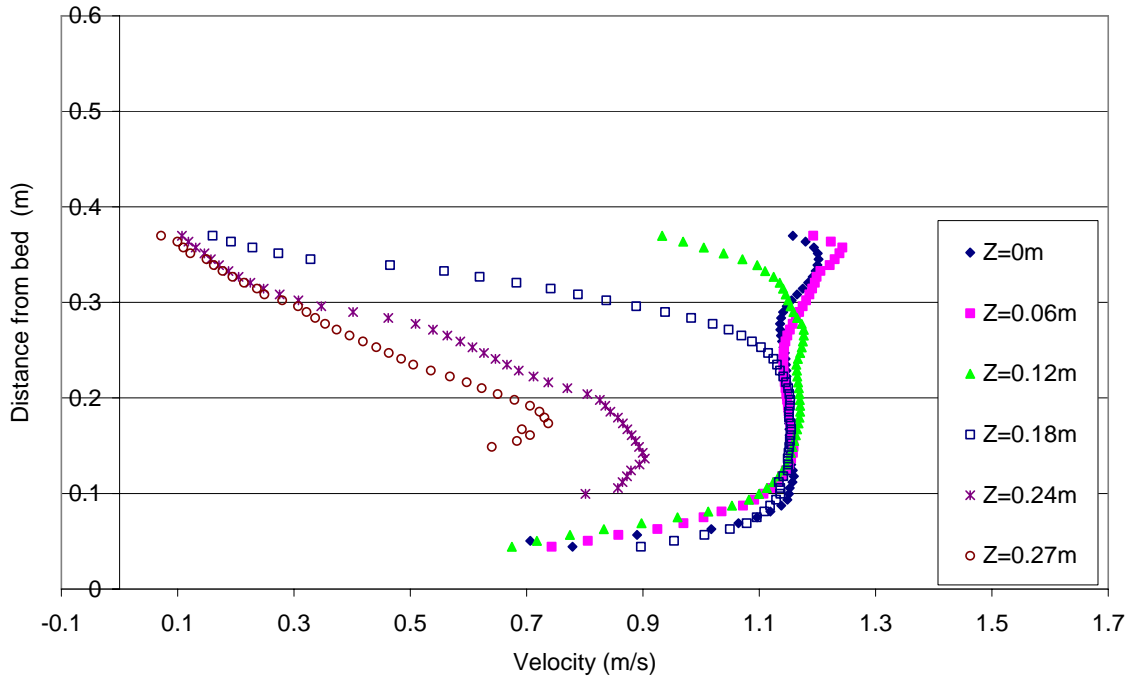


Figure C - 41: Velocity profiles for S5Q221, XS2

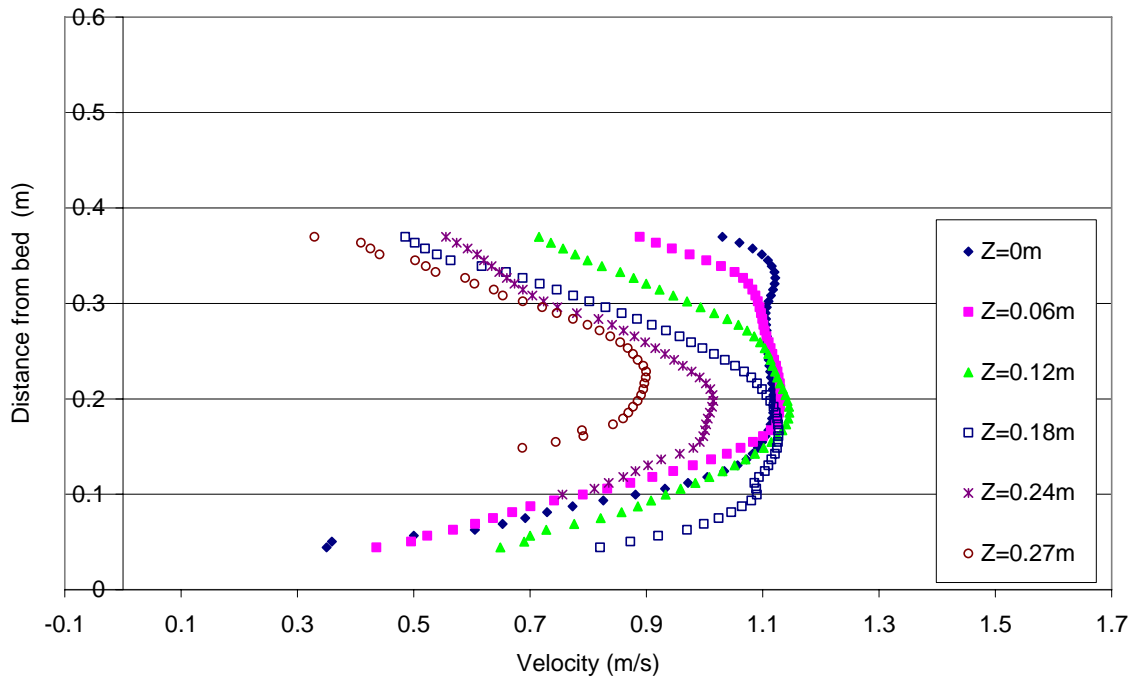


Figure C - 42: Velocity profiles for S5Q221, XS3

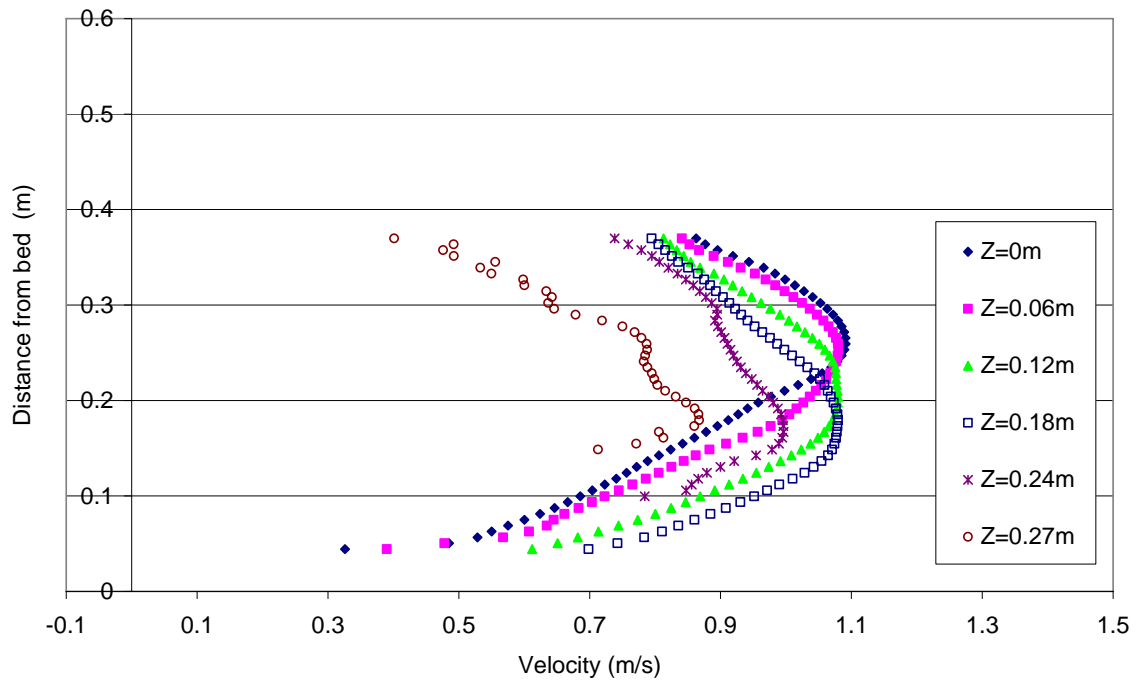


Figure C - 43: Velocity profiles for S5Q221, XS4

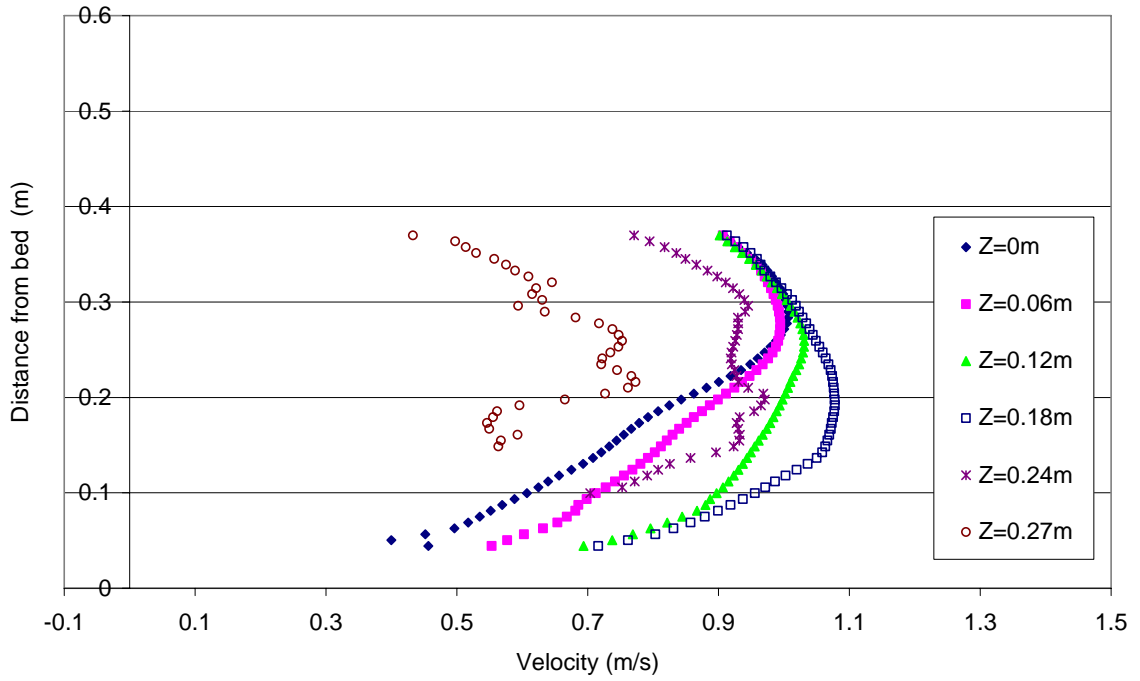


Figure C - 44: Velocity profiles for S5Q221, XS6

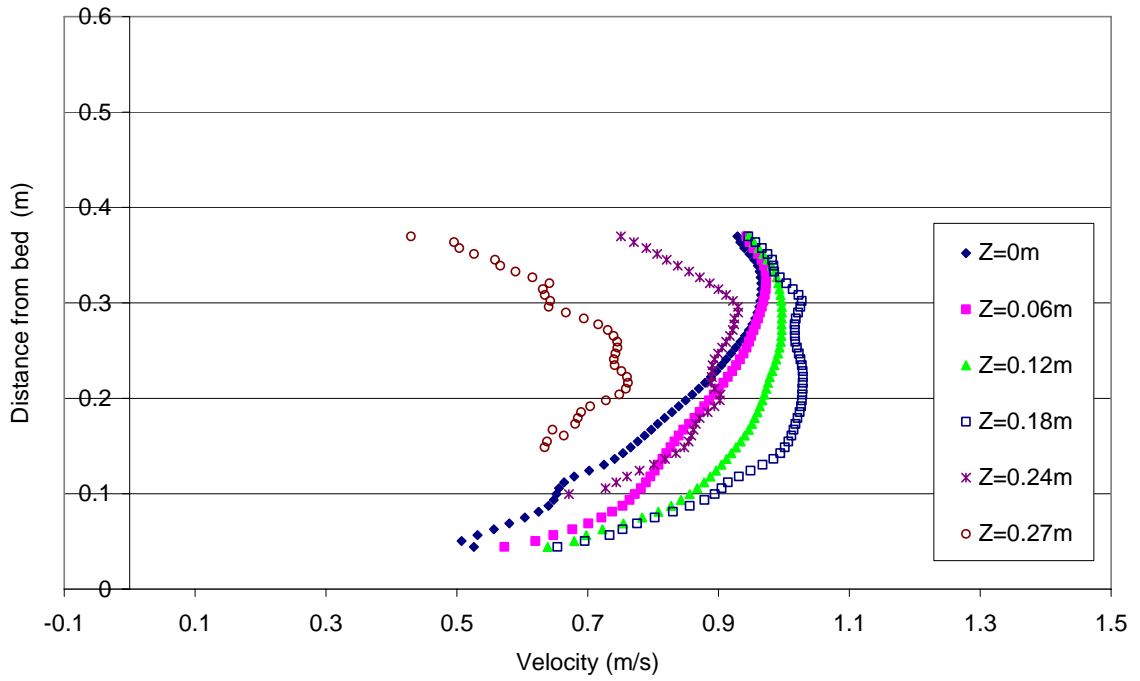


Figure C - 45: Velocity profiles for S5Q221, XS8

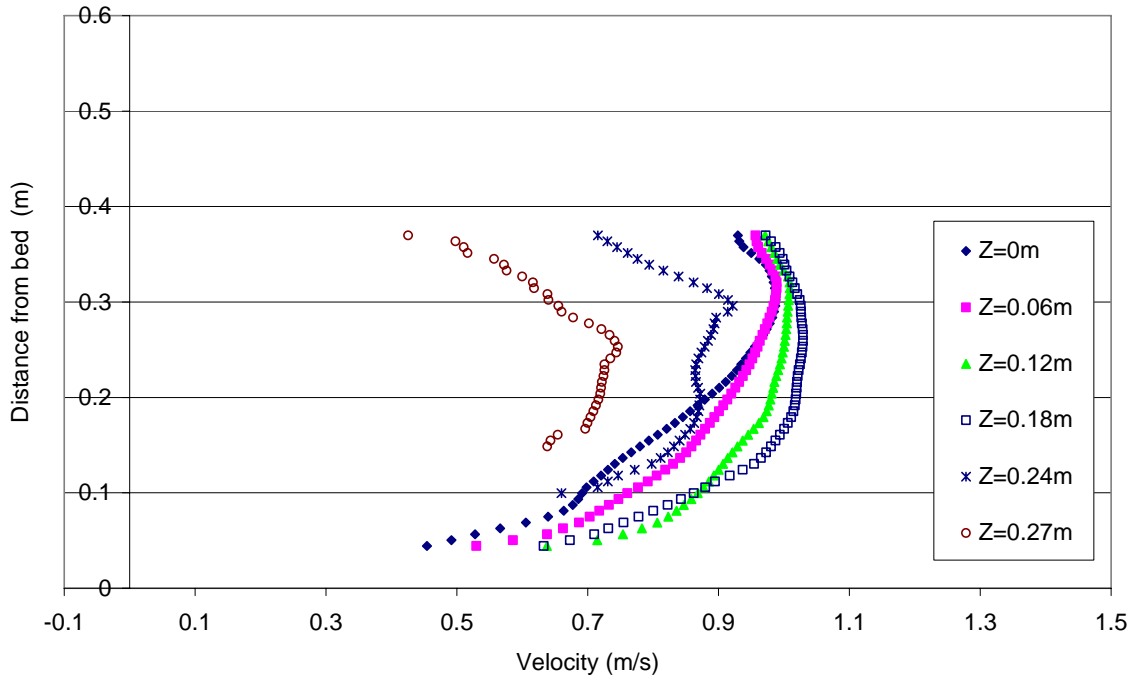


Figure C - 46: Velocity profiles for S5Q221, XS10

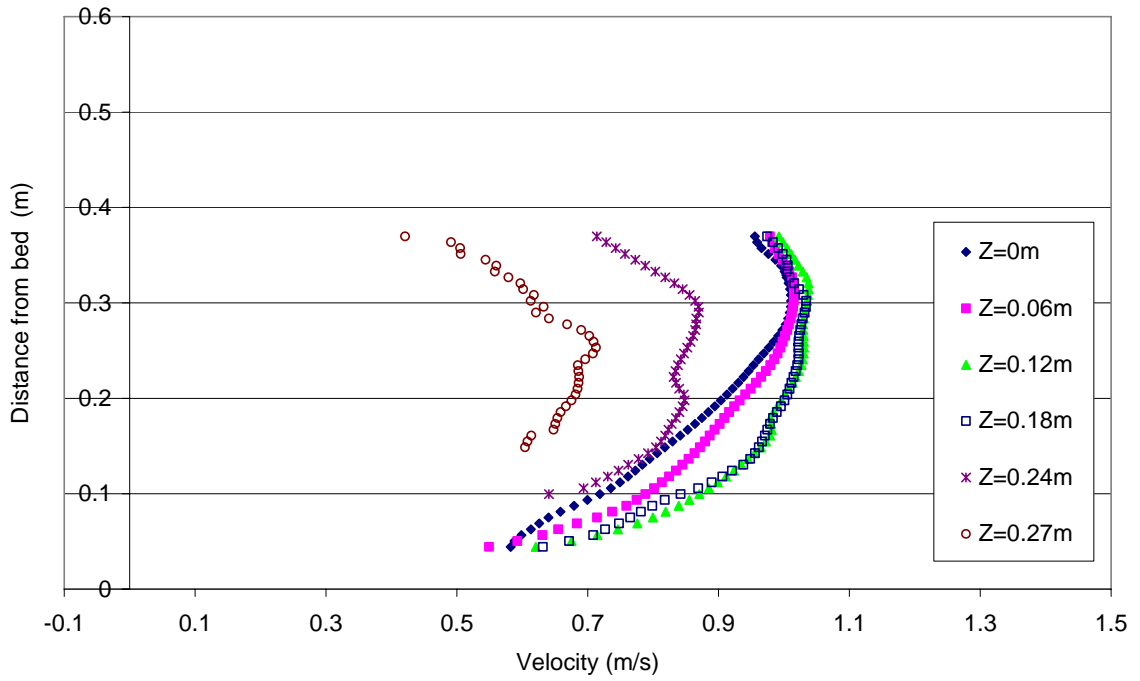


Figure C - 47: Velocity profiles for S5Q221, XS12

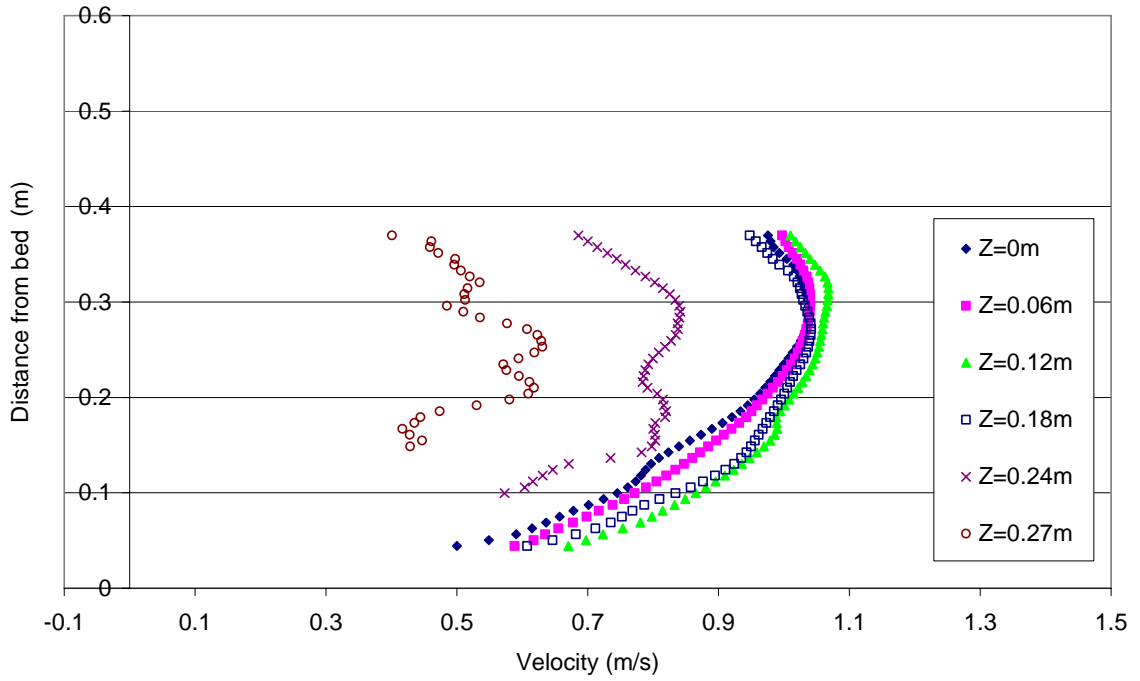


Figure C - 48: Velocity profiles for S5Q221, XS14

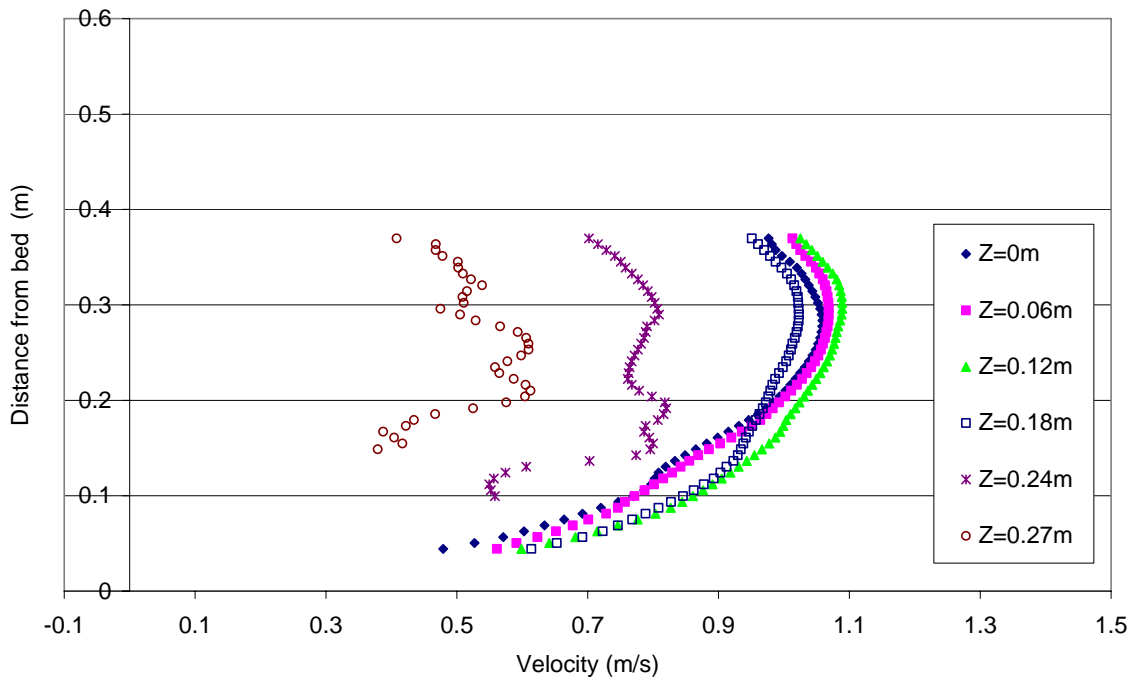


Figure C - 49: Velocity profiles for S5Q221, XS17

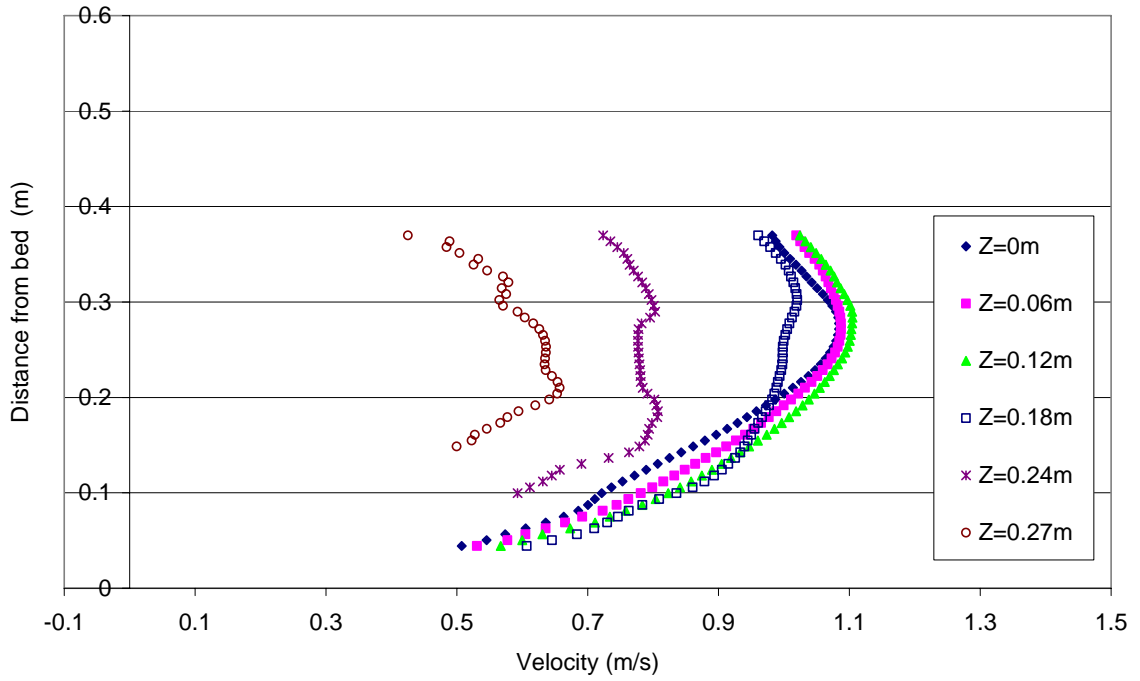


Figure C - 50: Velocity profiles for S5Q221, XS20

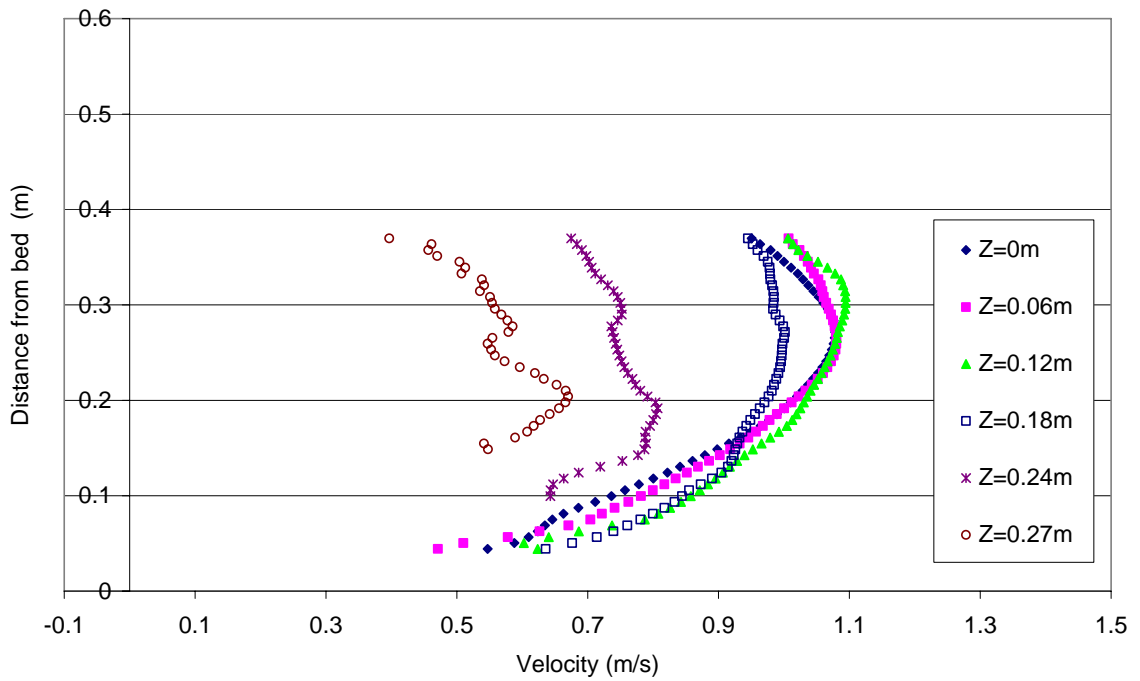


Figure C - 51: Velocity profiles for S5Q221, XS23

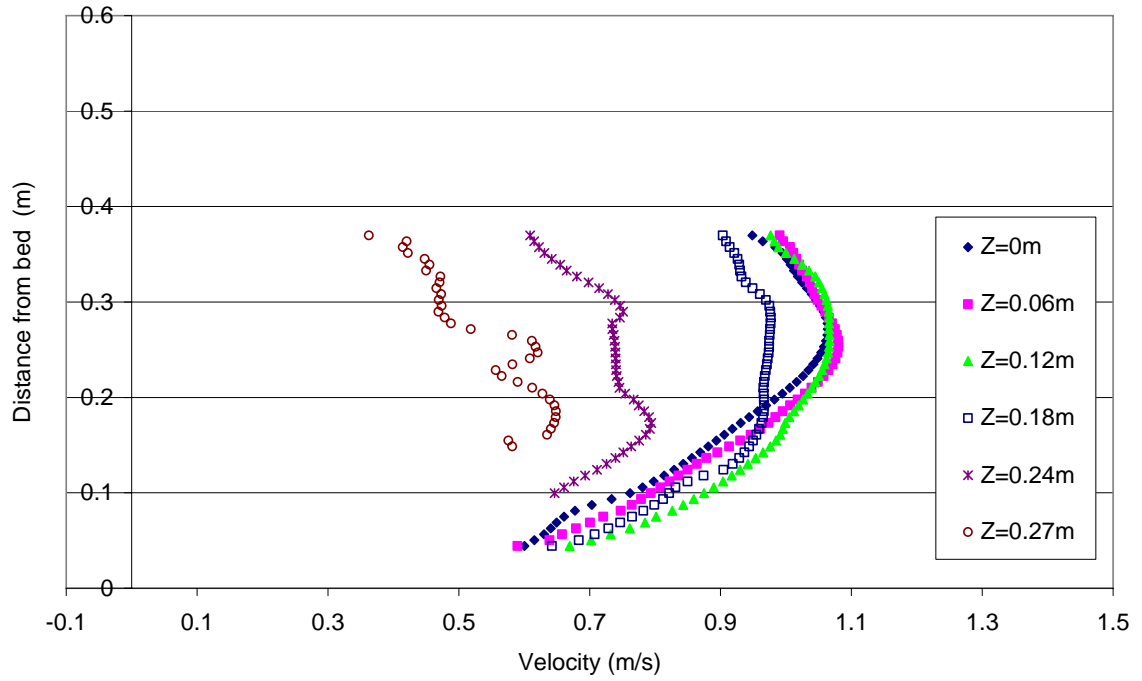


Figure C - 52: Velocity profiles for S5Q221, XS26

S1Q150

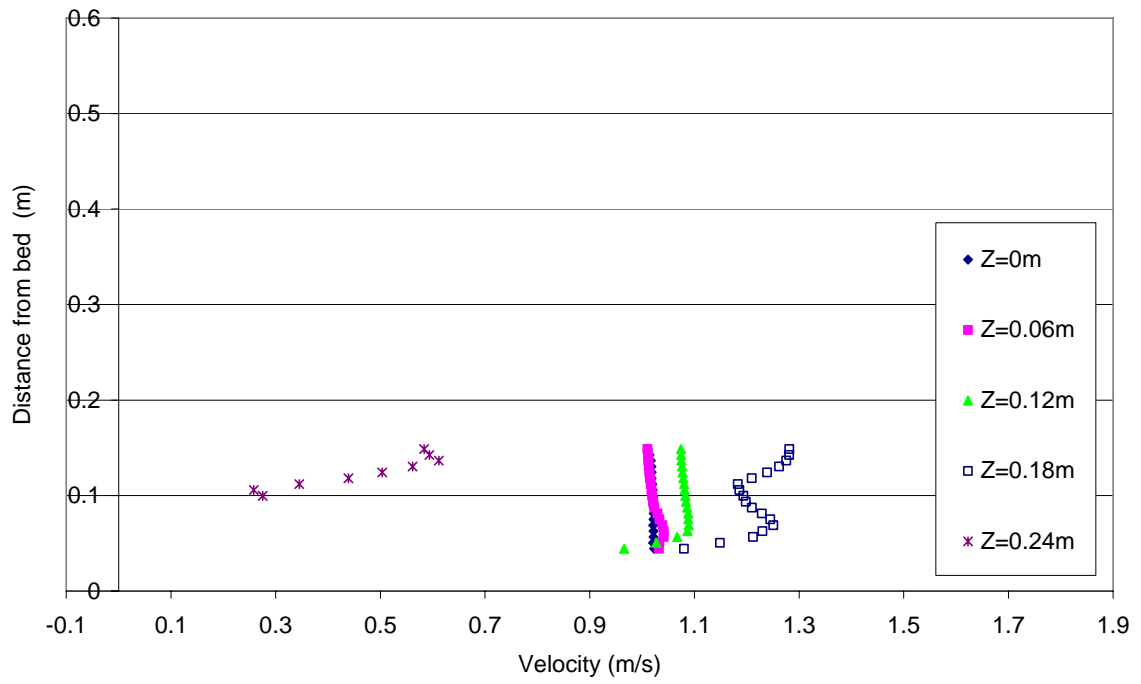


Figure C - 53: Velocity profiles for S1Q150, XS1

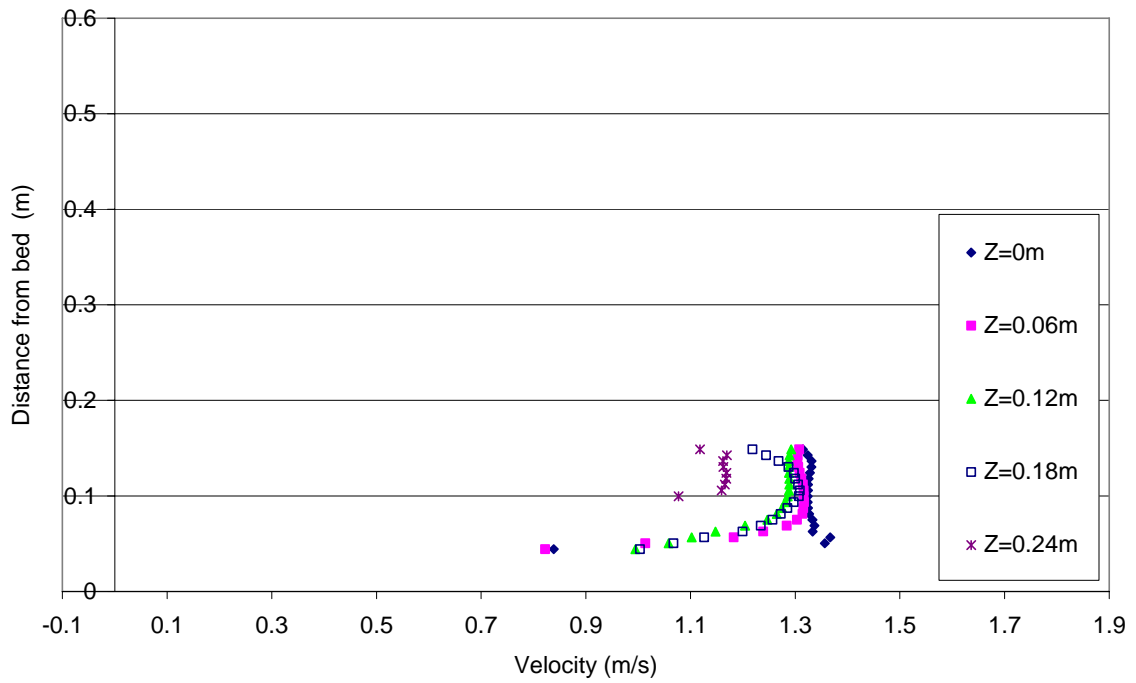


Figure C - 54: Velocity profiles for S1Q150, XS2

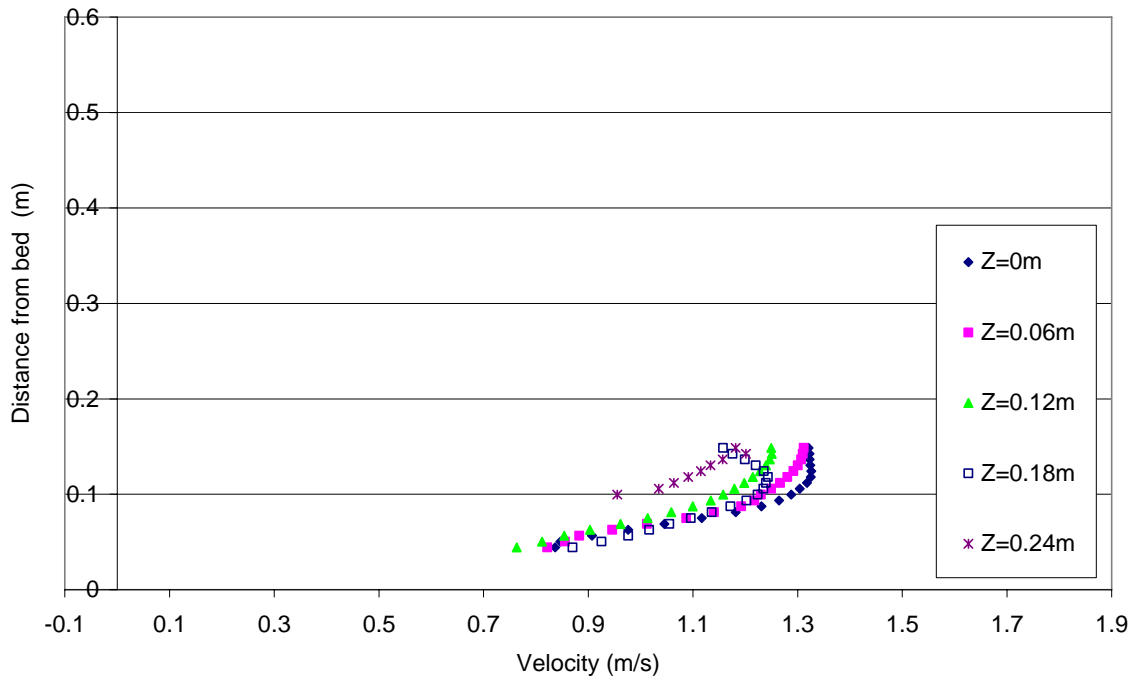


Figure C - 55: Velocity profiles for S1Q150, XS3

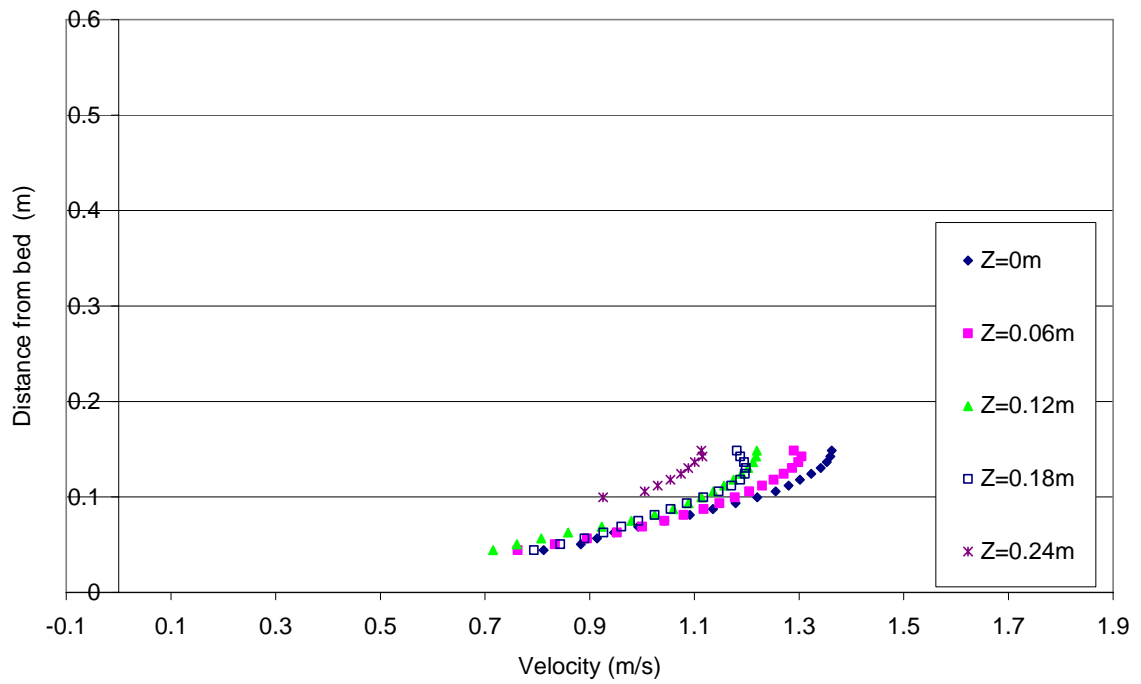


Figure C - 56: Velocity profiles for S1Q150, XS4

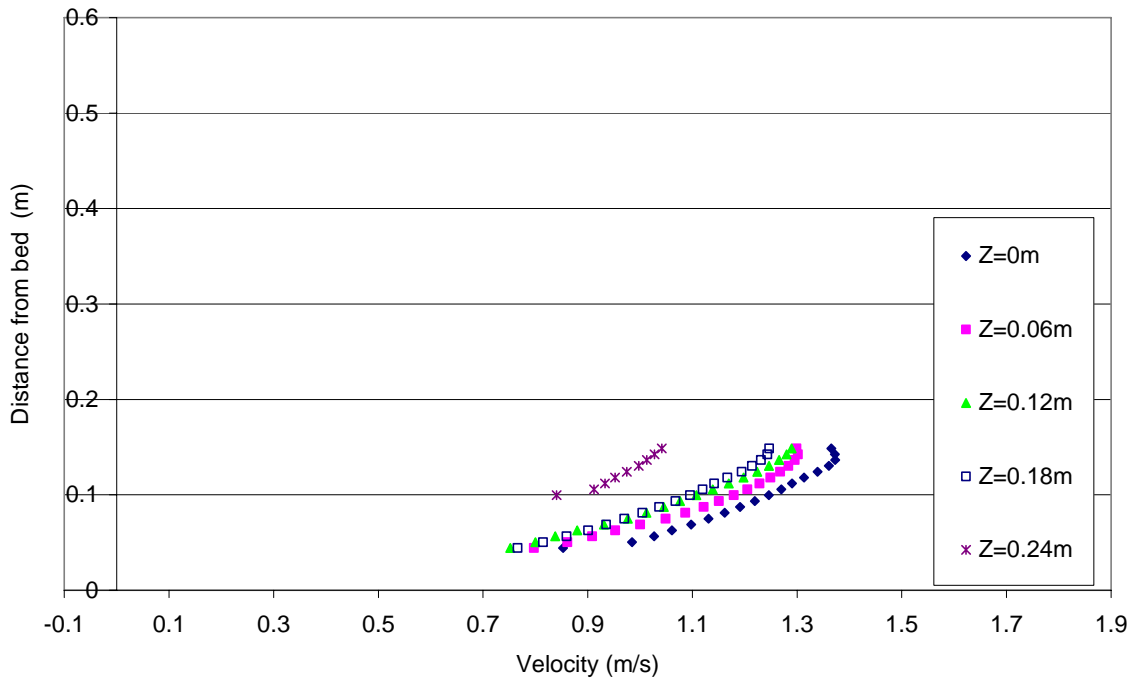


Figure C - 57: Velocity profiles for S1Q150, XS6

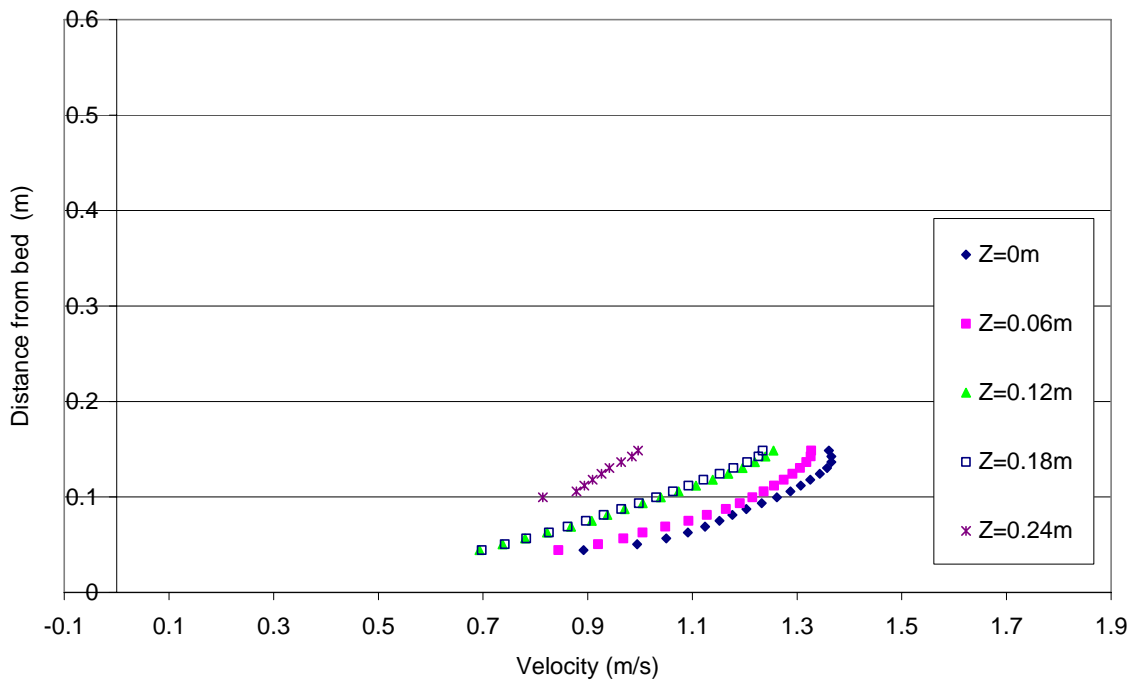


Figure C - 58: Velocity profiles for S1Q150, XS8

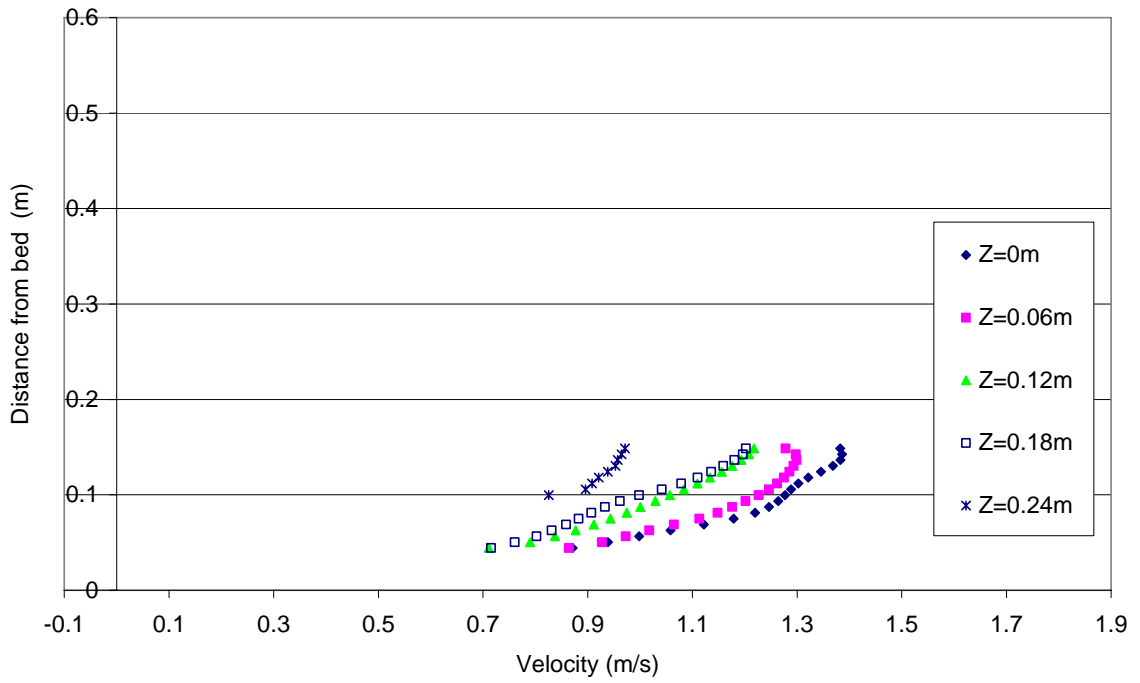


Figure C - 59: Velocity profiles for S1Q150, XS10

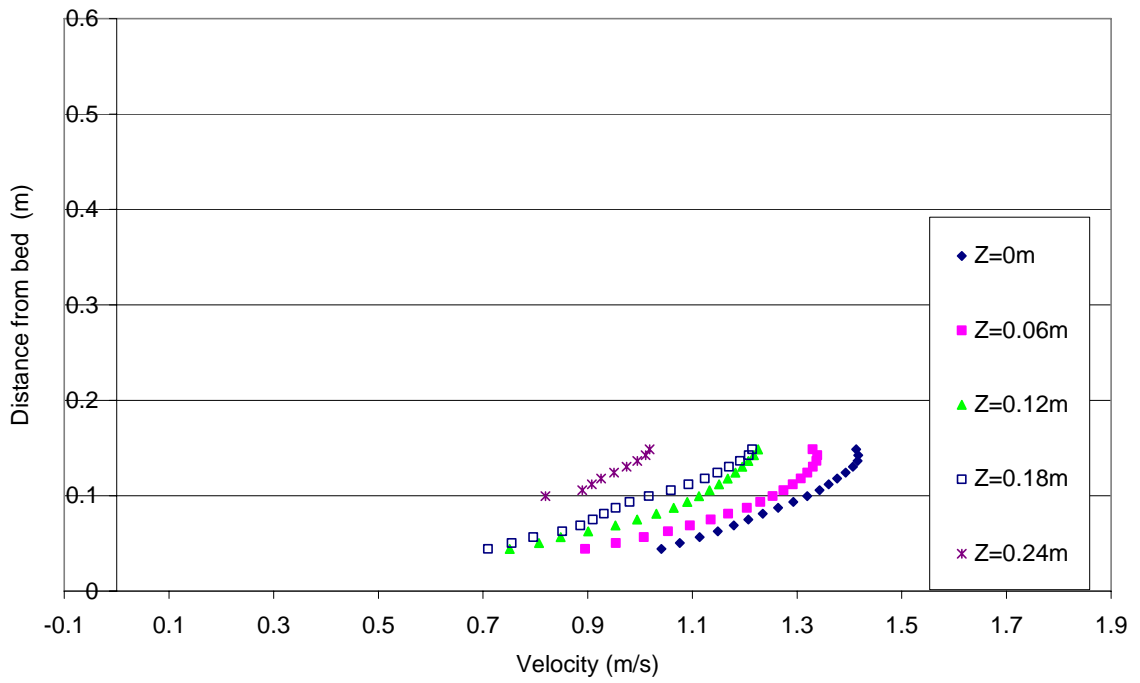


Figure C - 60: Velocity profiles for S1Q150, XS12

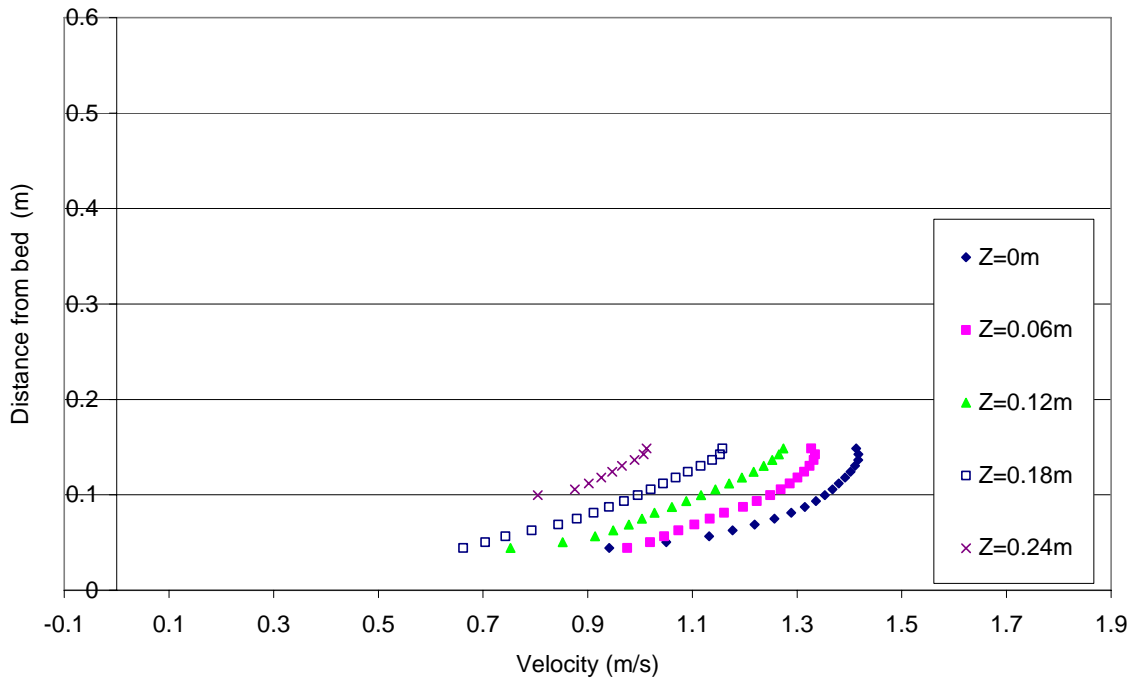


Figure C - 61: Velocity profiles for S1Q150, XS14

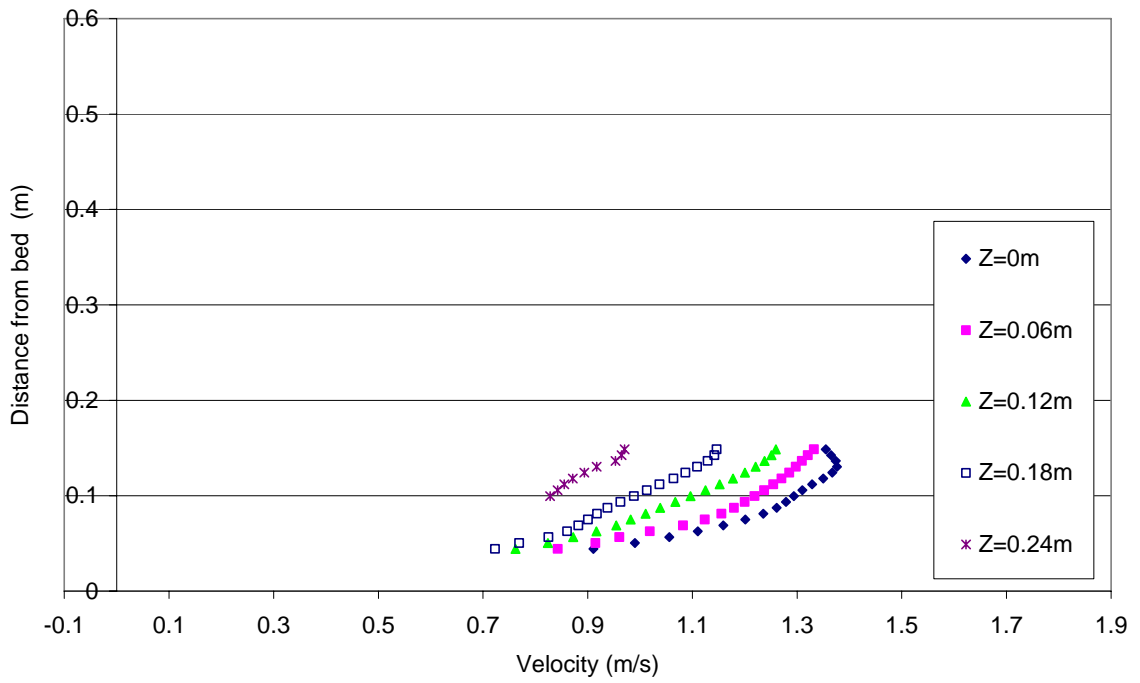


Figure C - 62: Velocity profiles for S1Q150, XS17

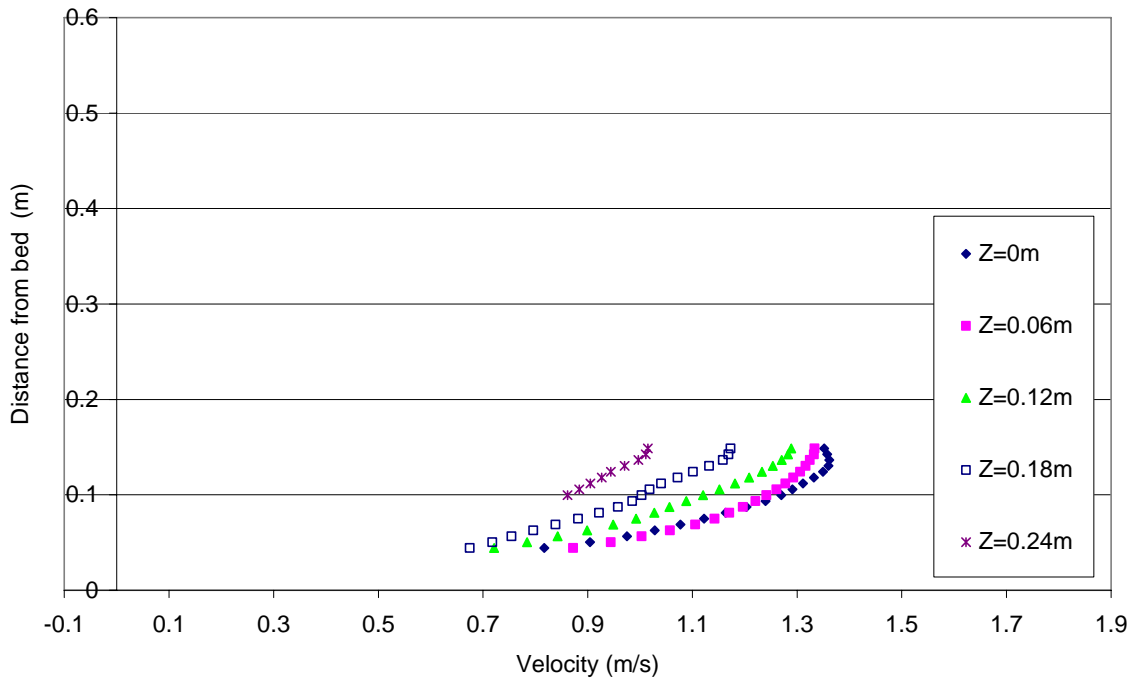


Figure C - 63: Velocity profiles for S1Q150, XS20

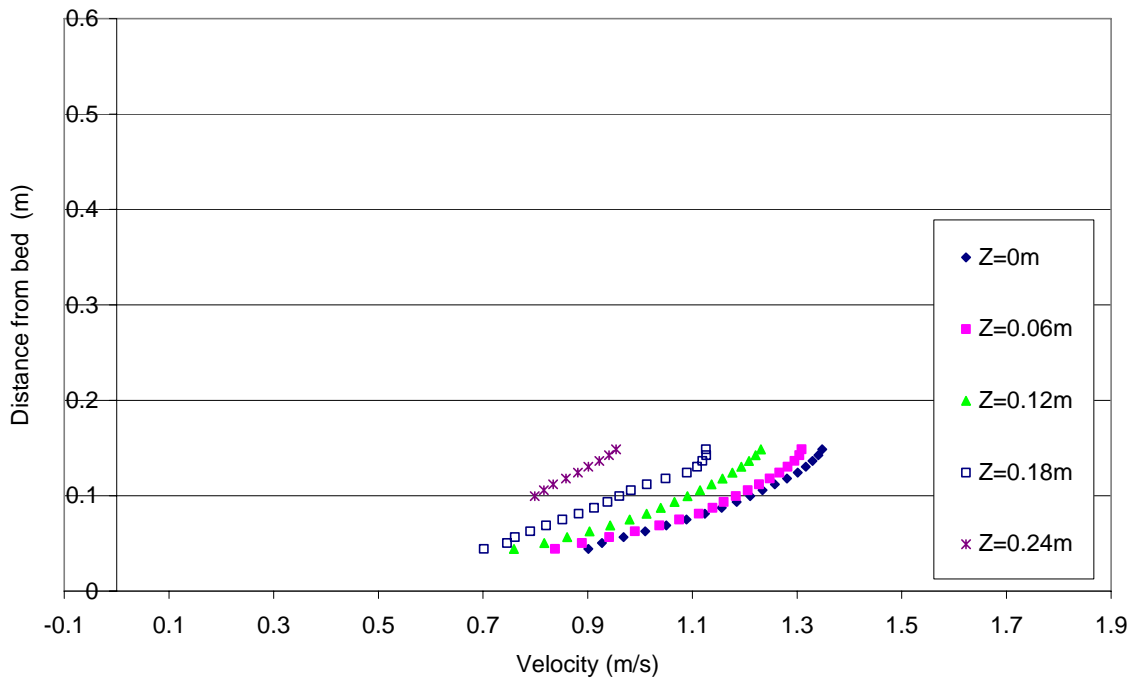


Figure C - 64: Velocity profiles for S1Q150, XS23

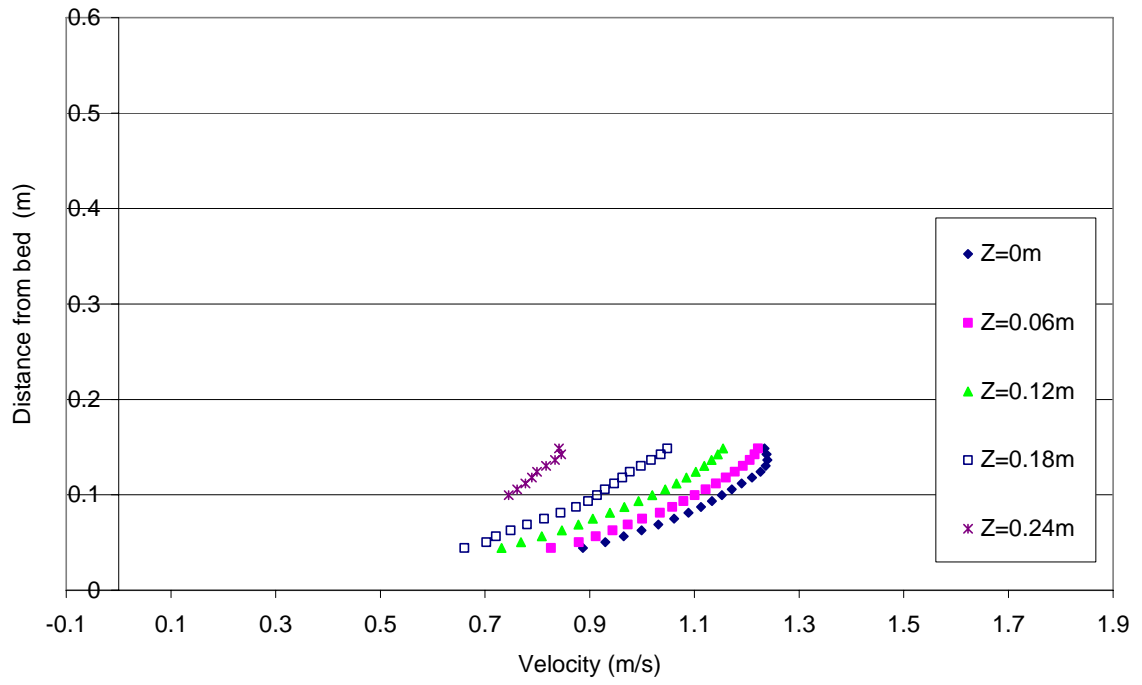


Figure C - 65: Velocity profiles for S1Q150, XS26

S1Q254

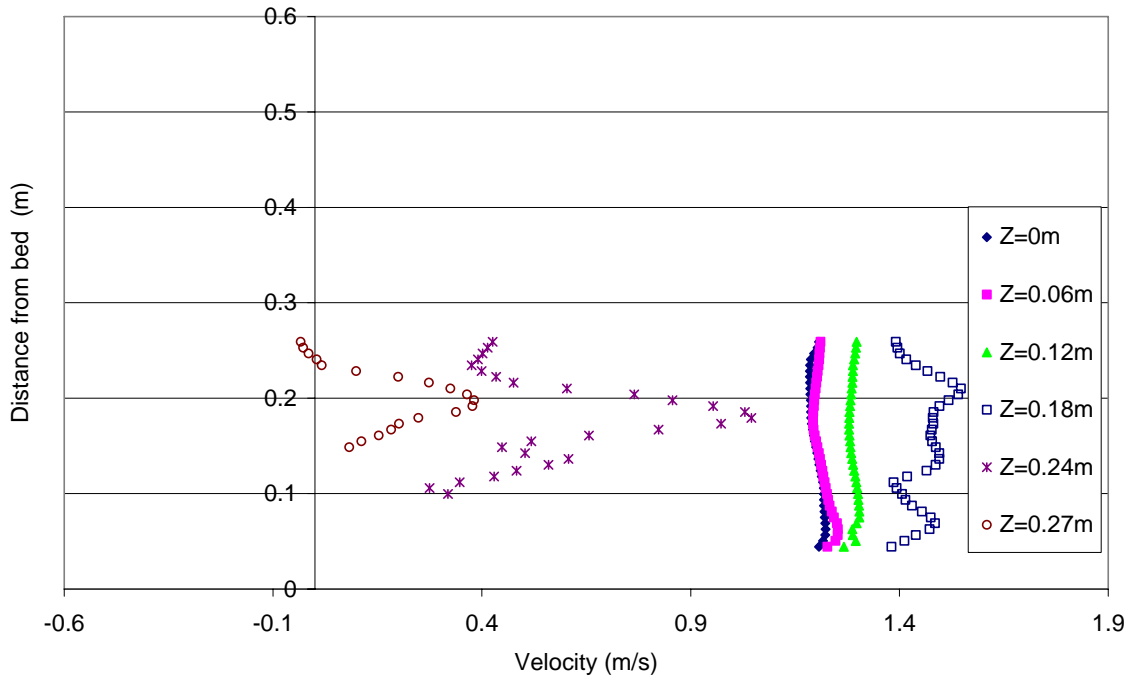


Figure C - 66: Velocity profiles for S1Q254, XS1

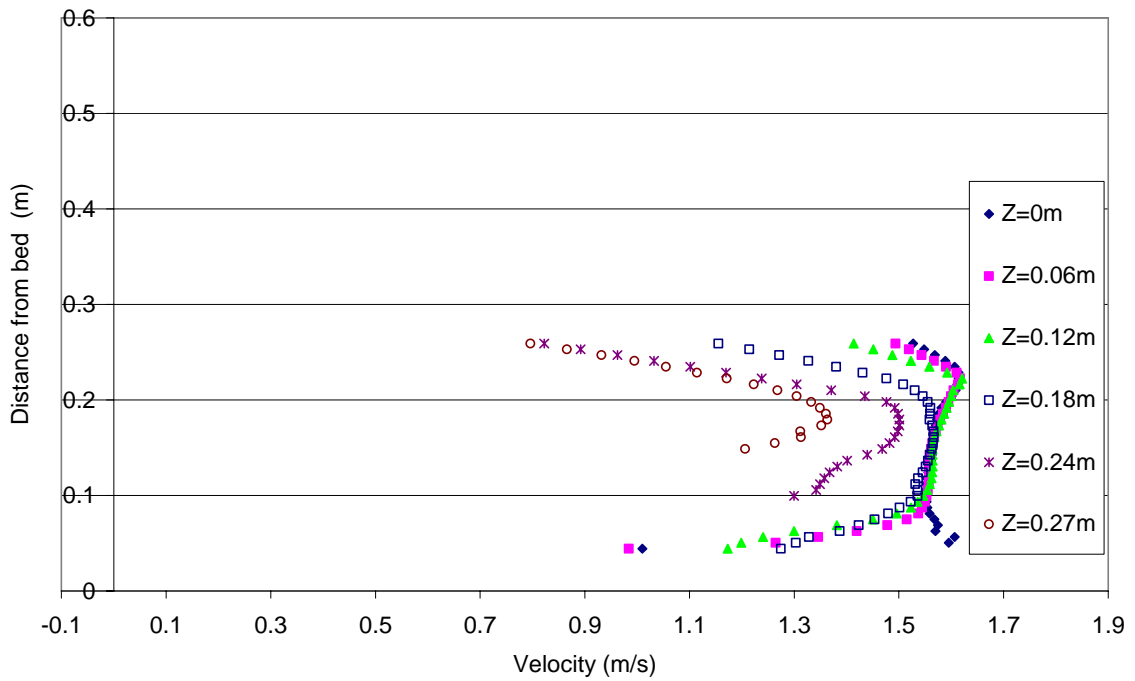


Figure C - 67: Velocity profiles for S1Q254, XS2

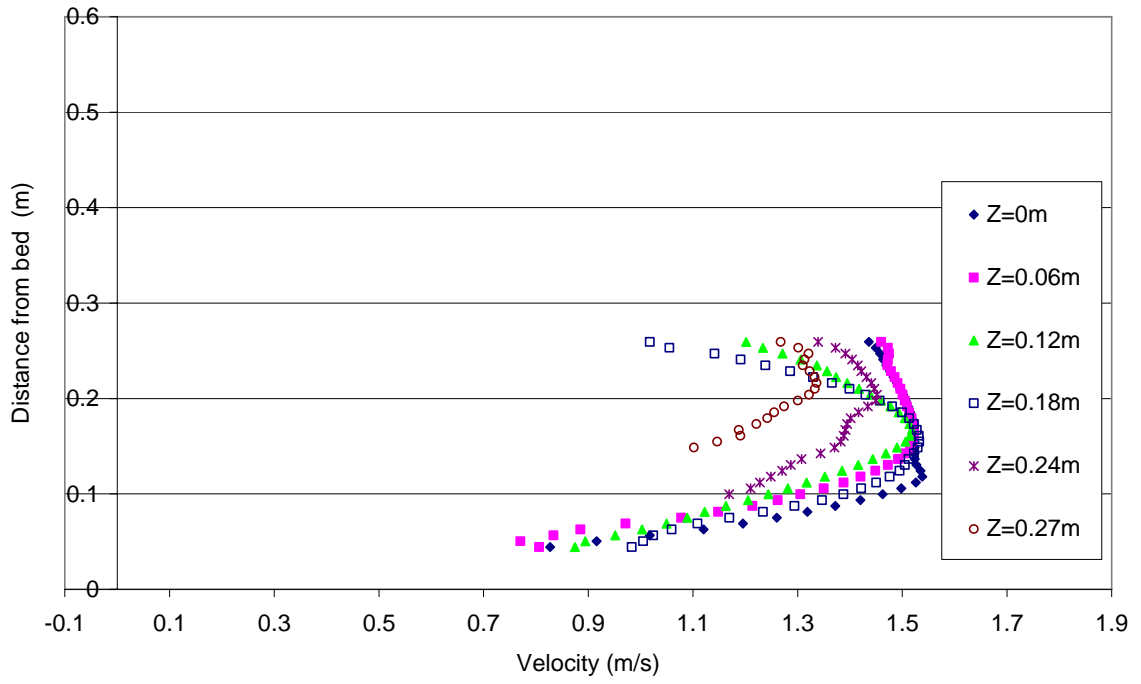


Figure C - 68: Velocity profiles for S1Q254, XS3

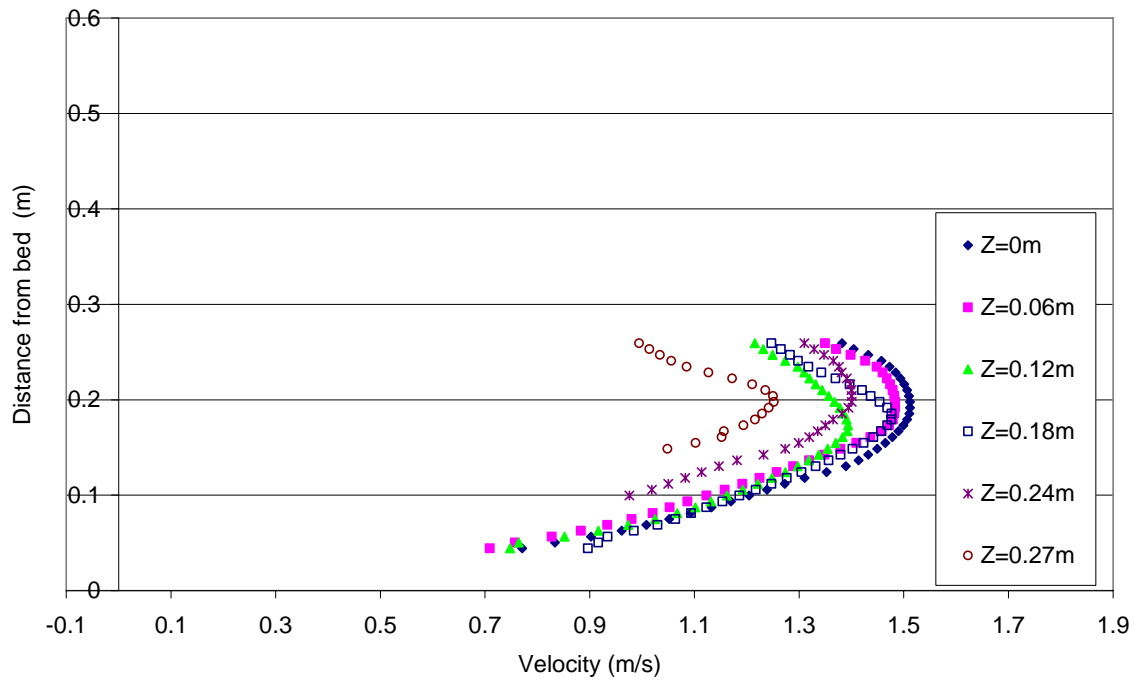


Figure C - 69: Velocity profiles for S1Q254, XS4

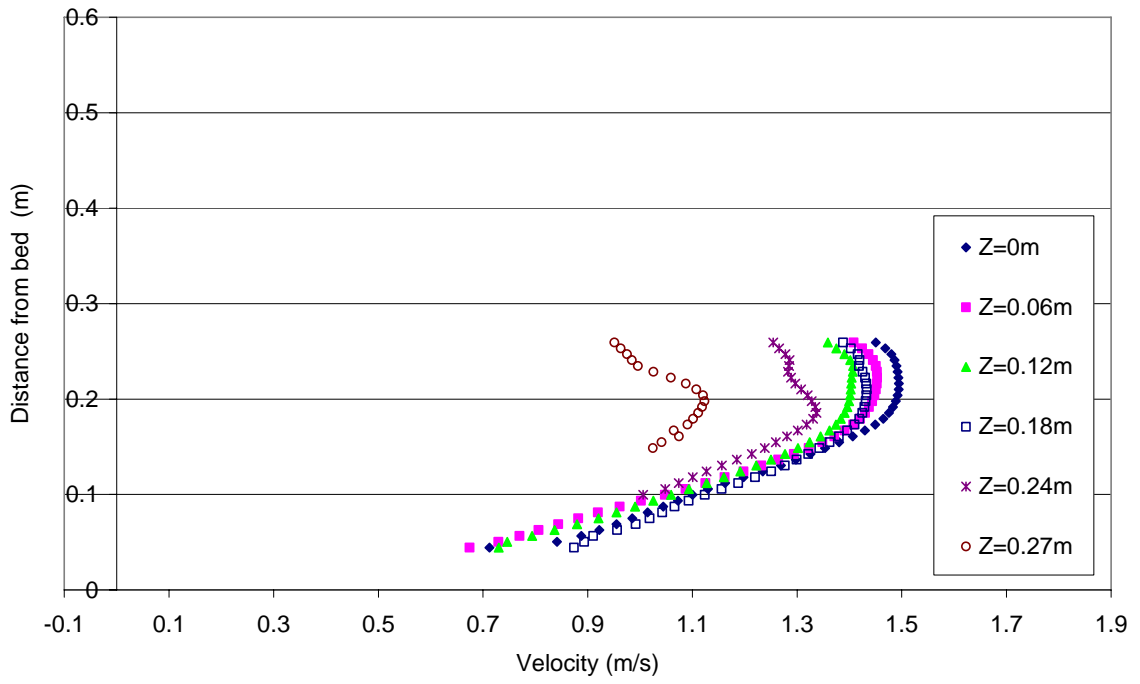


Figure C - 70: Velocity profiles for S1Q254, XS6

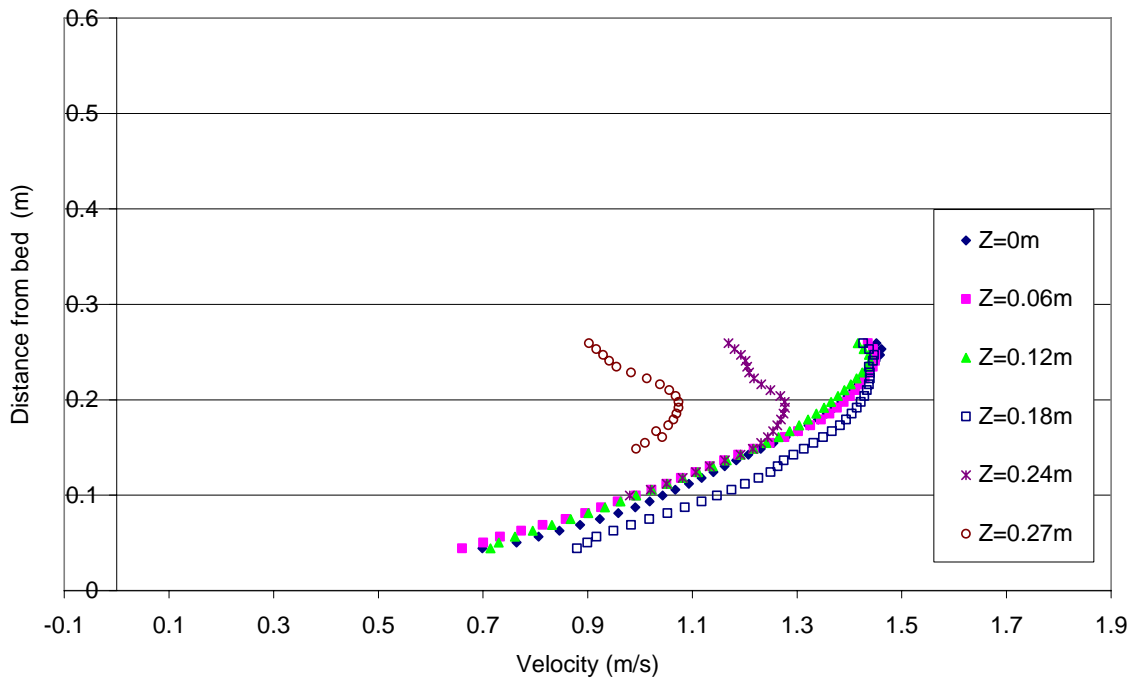


Figure C - 71: Velocity profiles for S1Q254, XS8

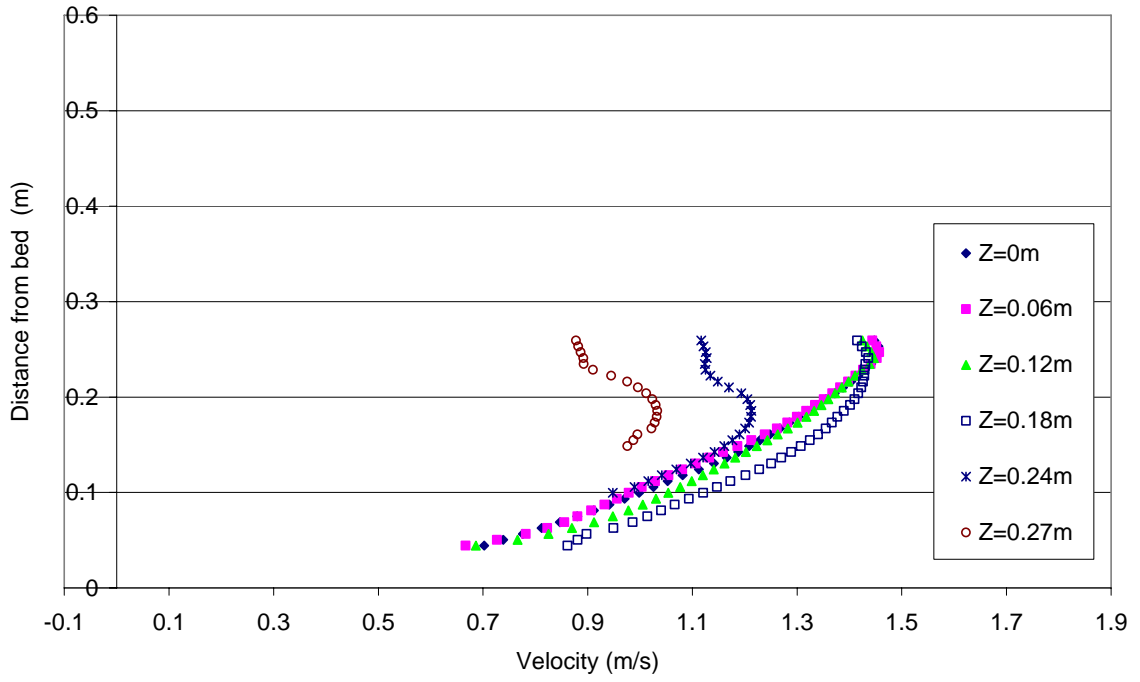


Figure C - 72: Velocity profiles for S1Q254, XS10

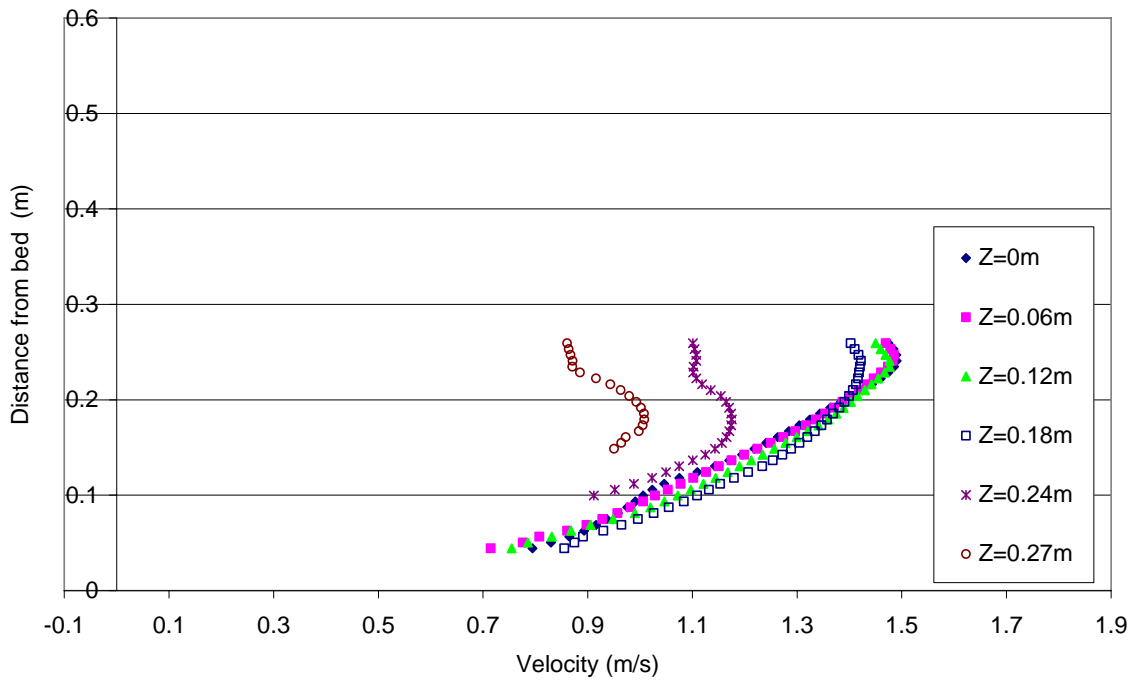


Figure C - 73: Velocity profiles for S1Q254, XS12

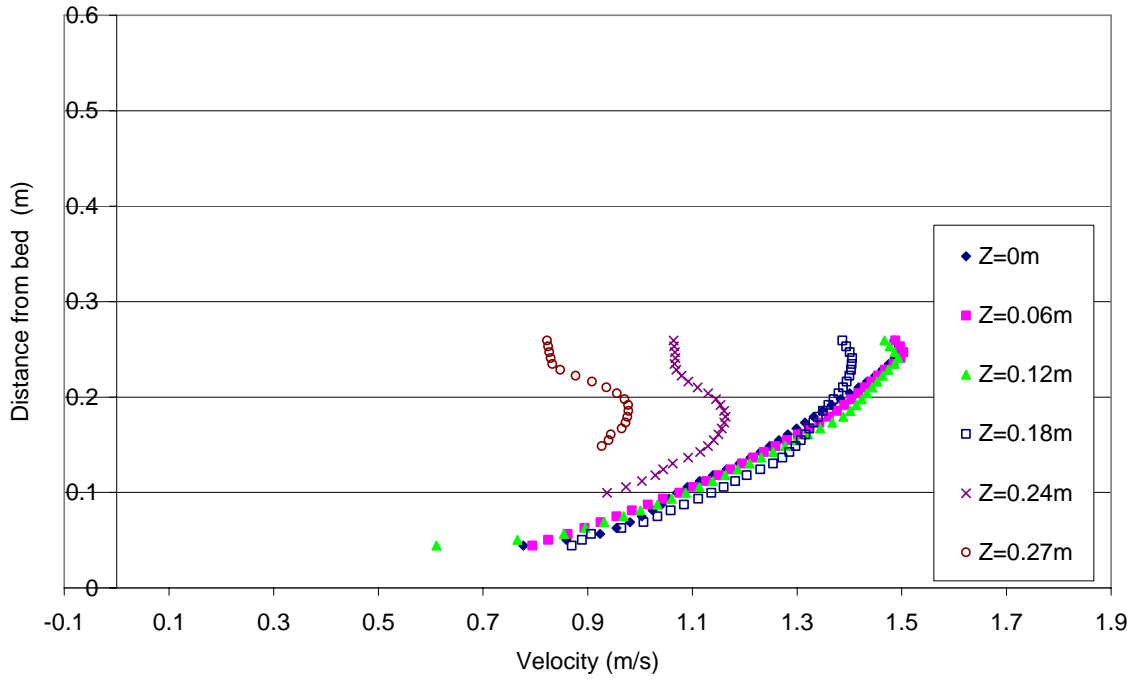


Figure C - 74: Velocity profiles for S1Q254, XS14

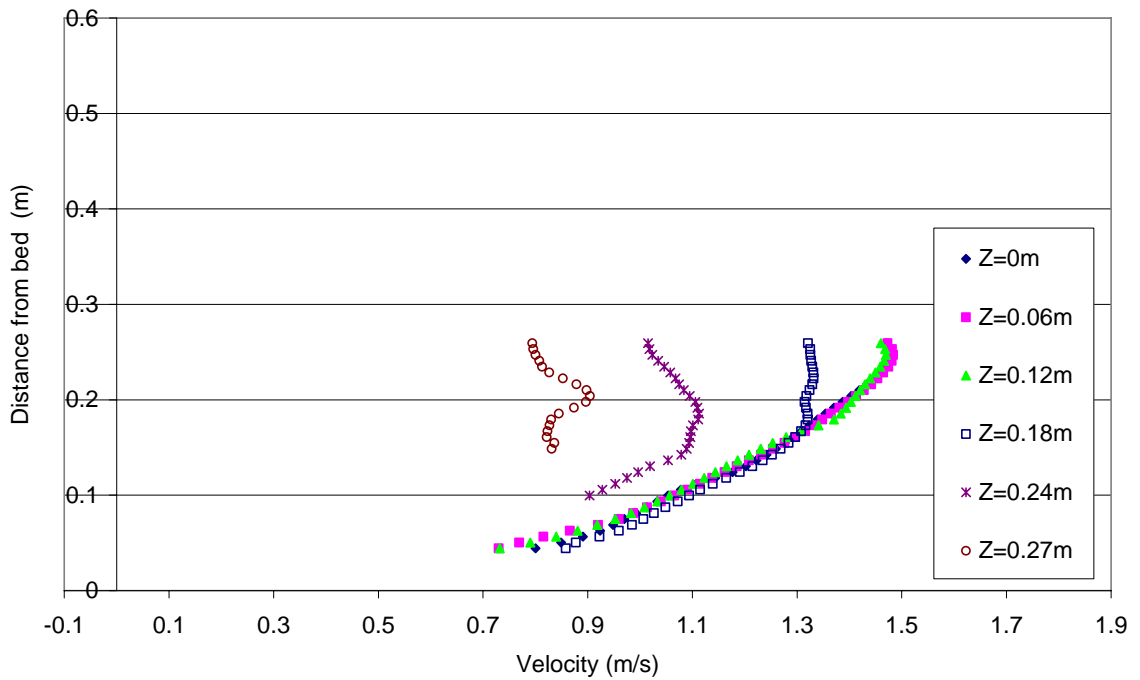


Figure C - 75: Velocity profiles for S1Q254, XS17

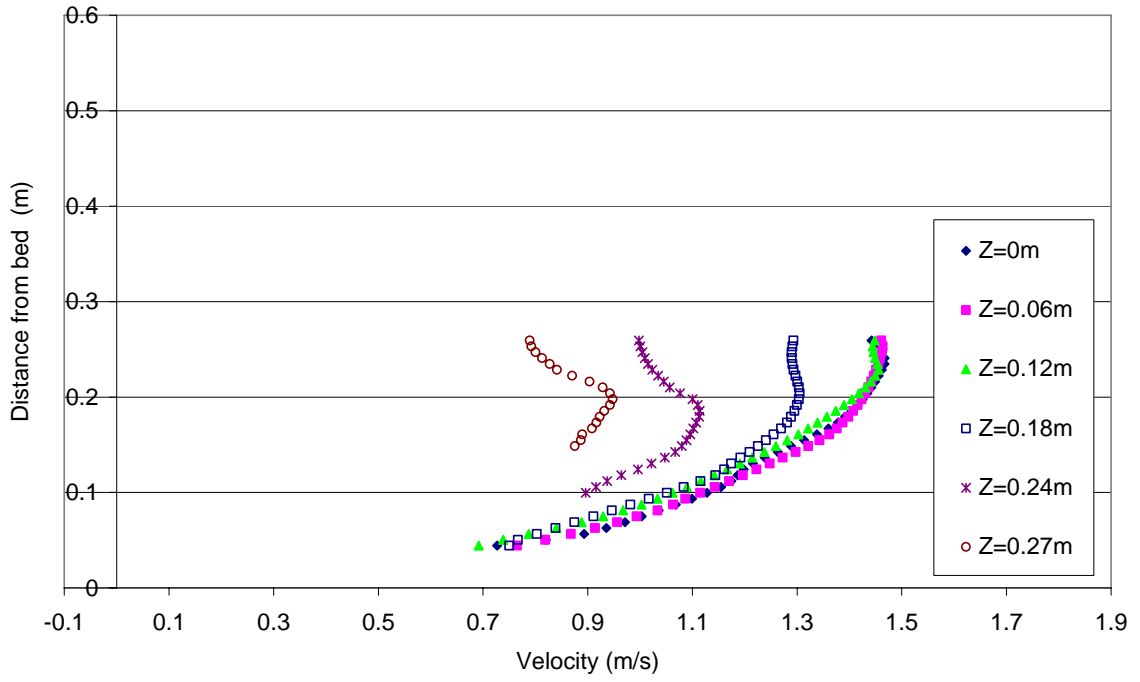


Figure C - 76: Velocity profiles for S1Q254, XS20

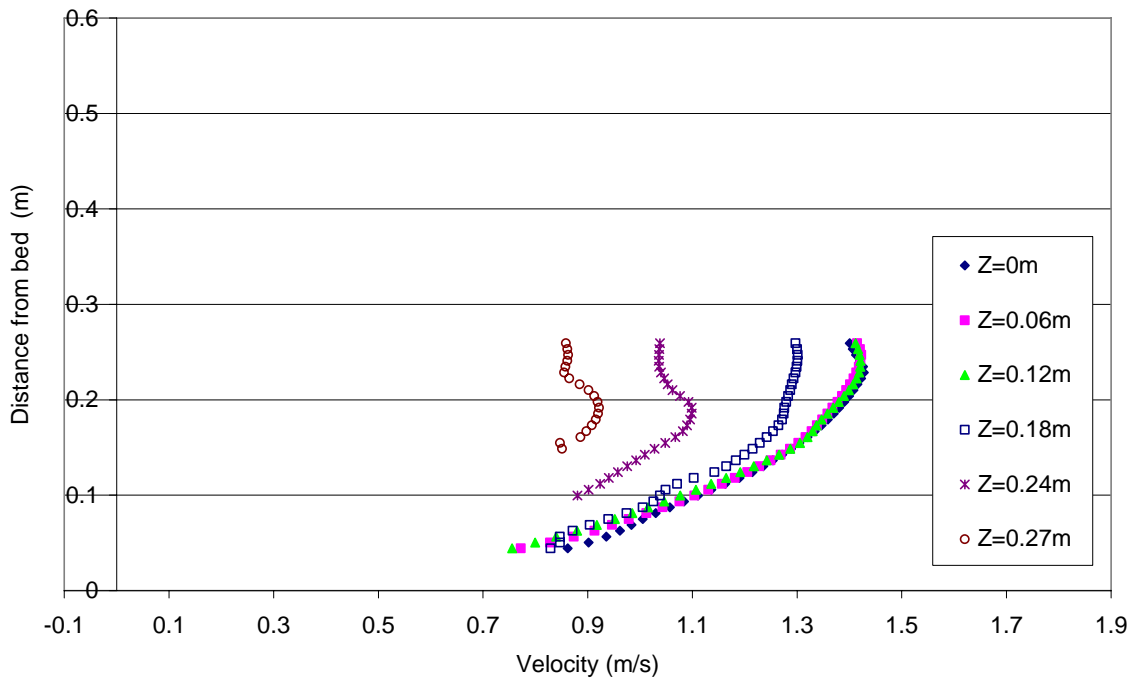


Figure C - 77: Velocity profiles for S1Q254, XS23

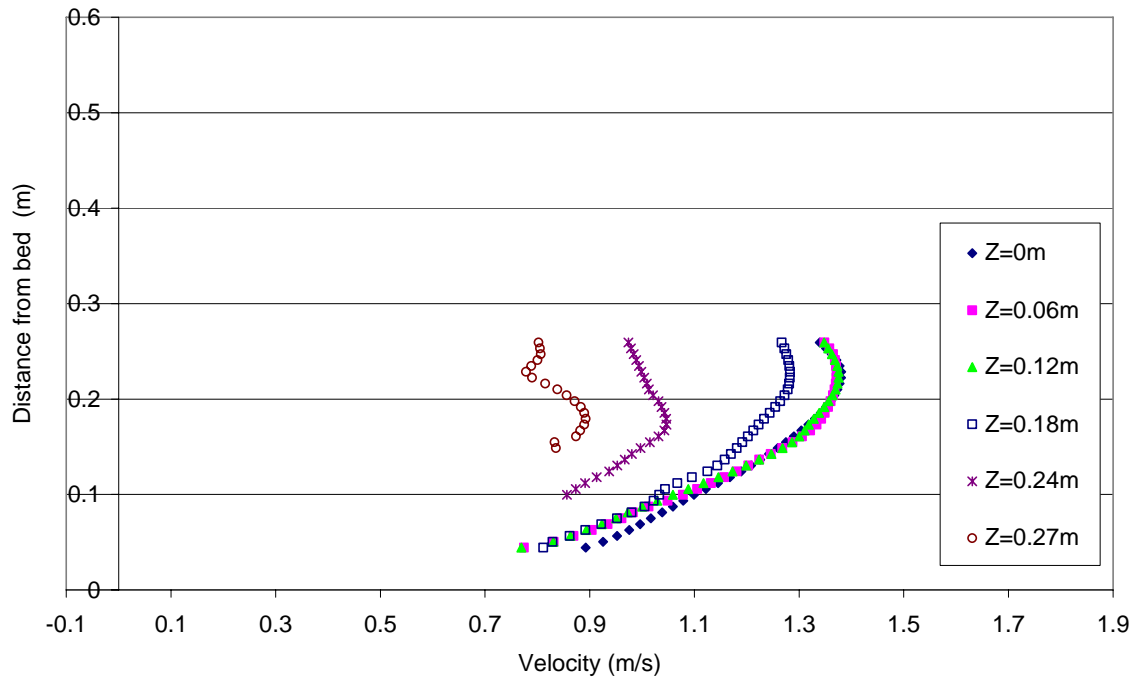


Figure C - 78: Velocity profiles for S1Q254, XS26

Smooth wall runs

S0Q145s

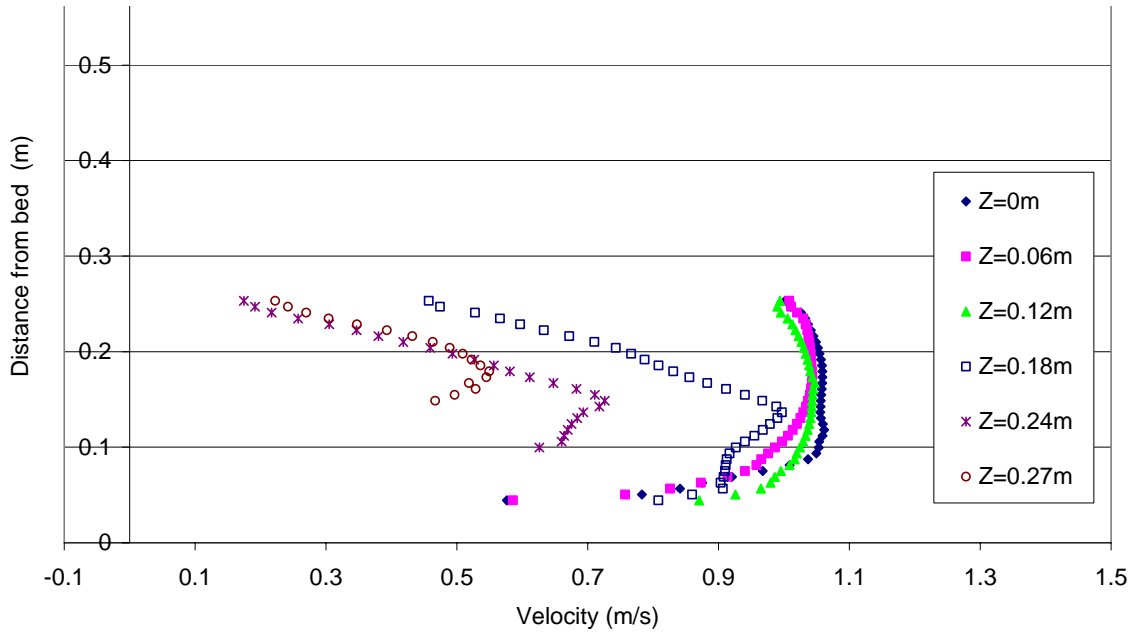


Figure C - 79: Velocity profiles for S0Q145s, XS2

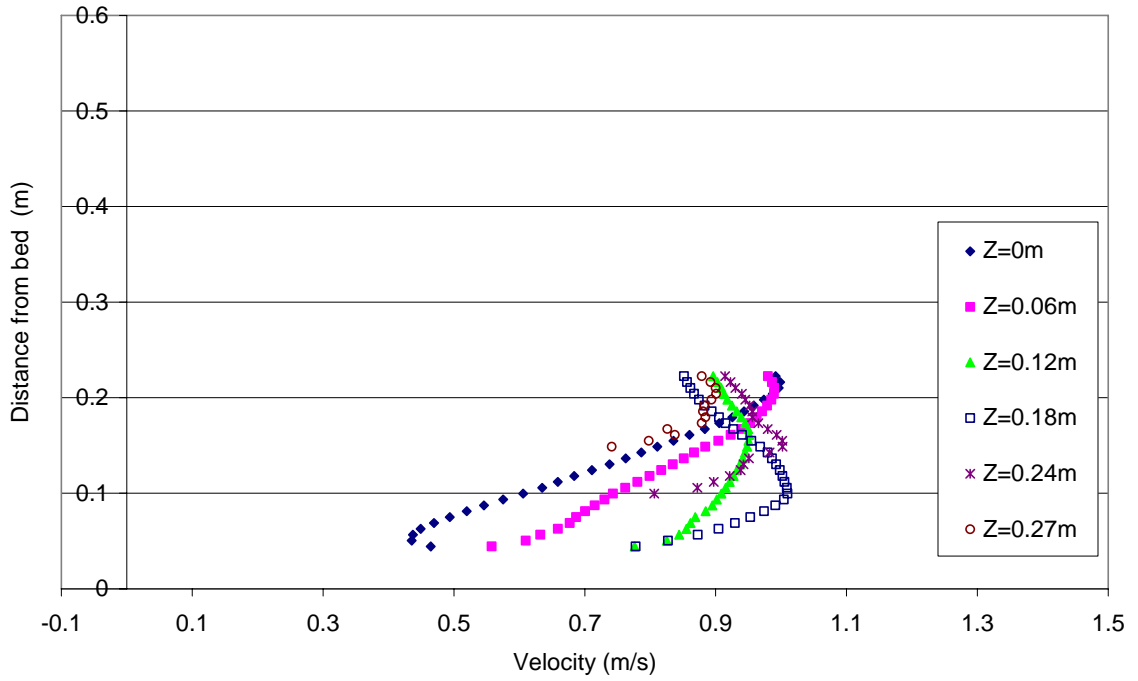


Figure C - 80: Velocity profiles for S0Q145s, XS4

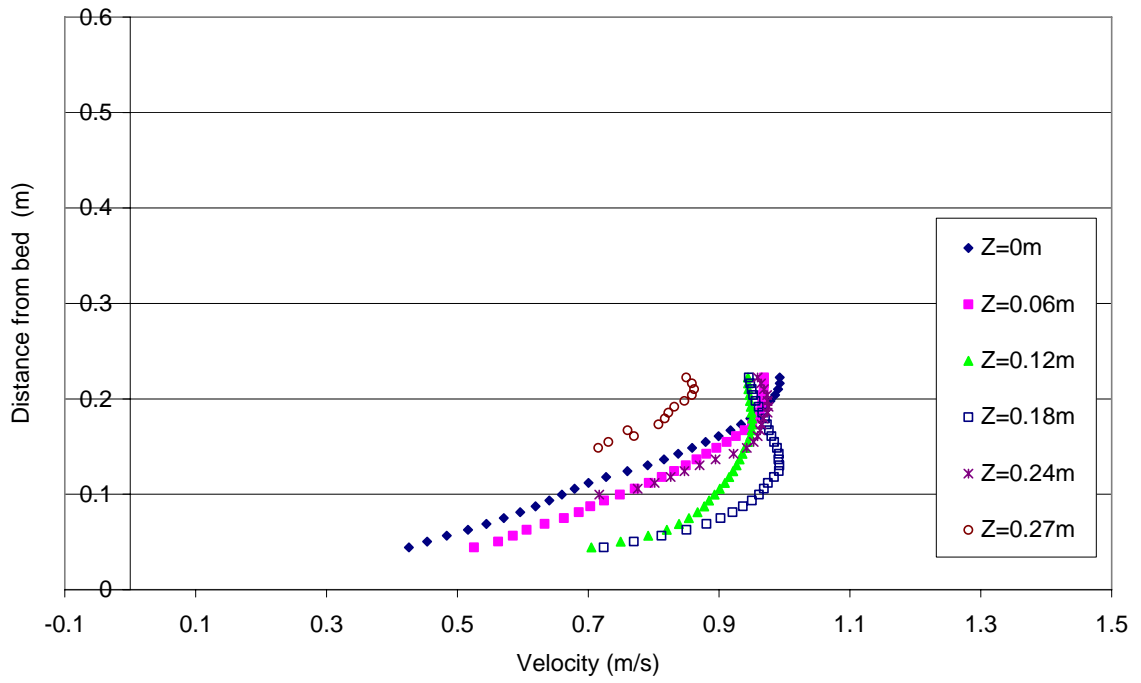


Figure C - 81: Velocity profiles for S0Q145s, XS6

S0Q221s

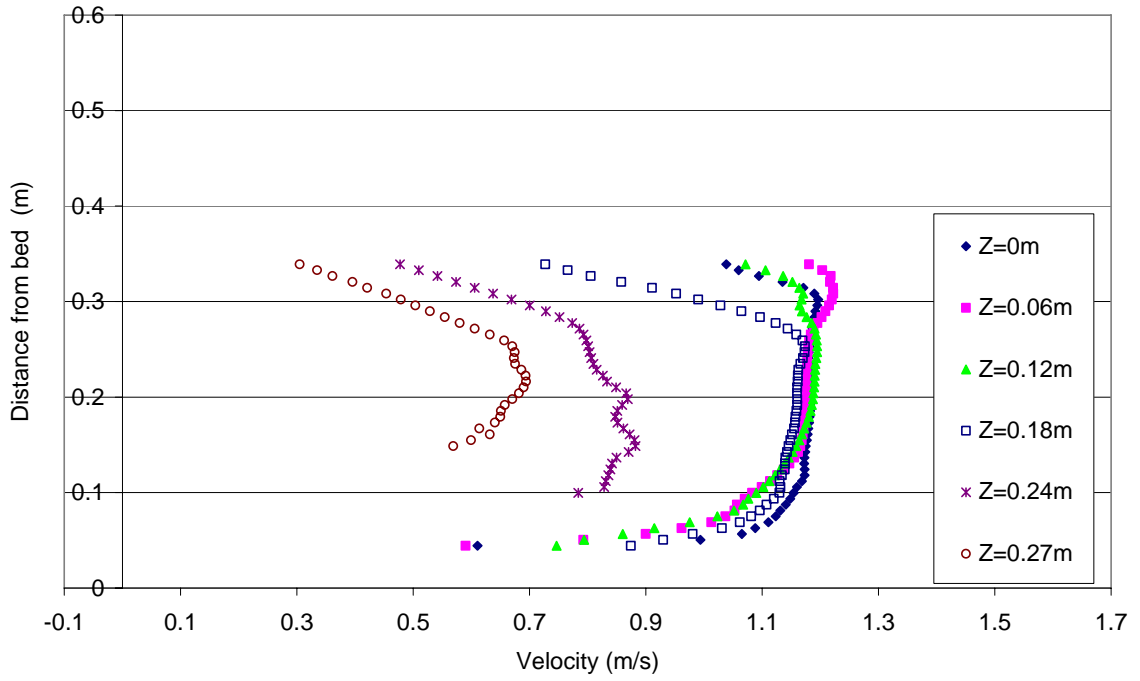


Figure C - 82: Velocity profiles for S0Q221s, XS2

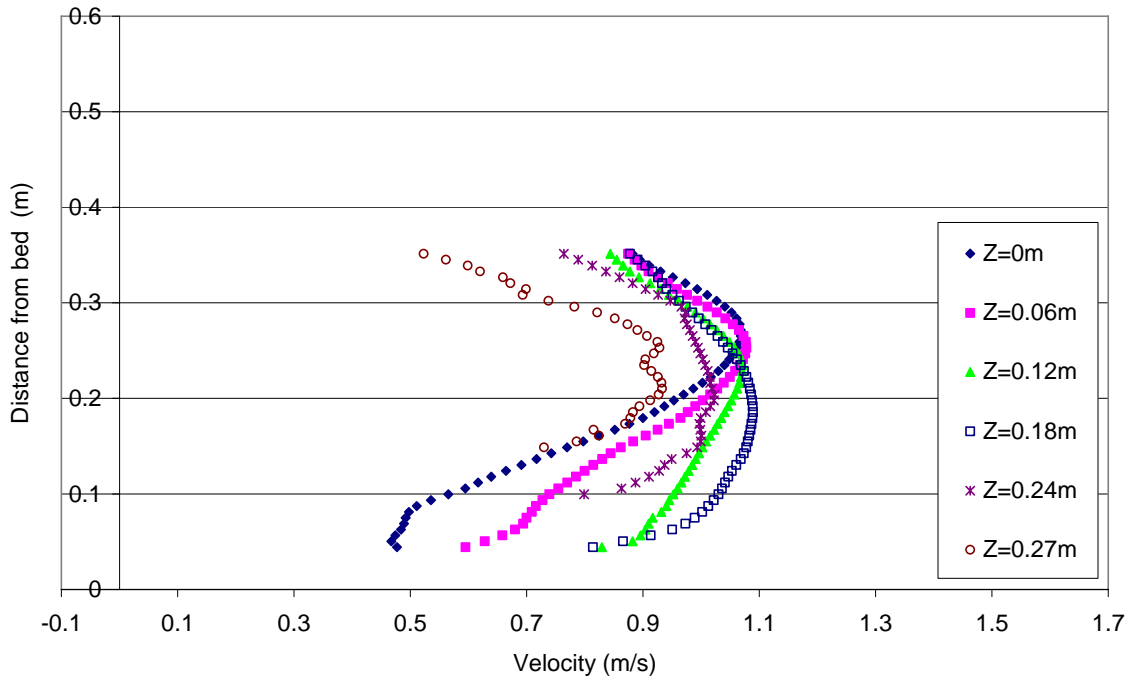


Figure C - 83: Velocity profiles for S0Q221s, XS4

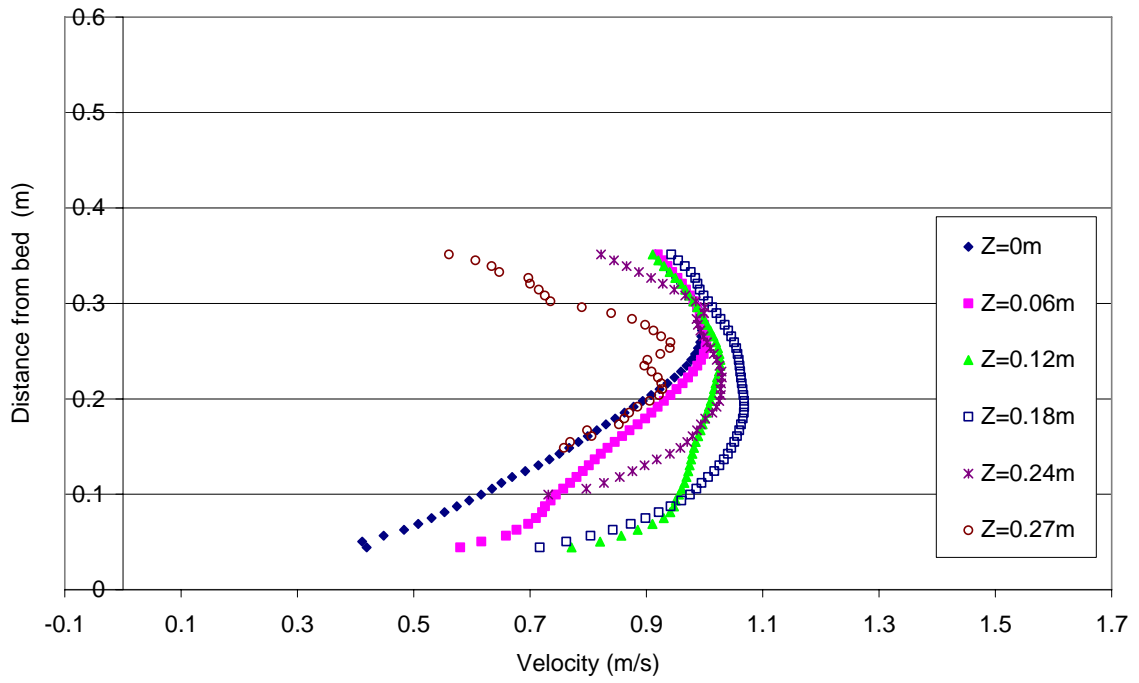


Figure C - 84: Velocity profiles for S0Q221s, XS6

Appendix D – Shear Velocity Determination

S0Q64

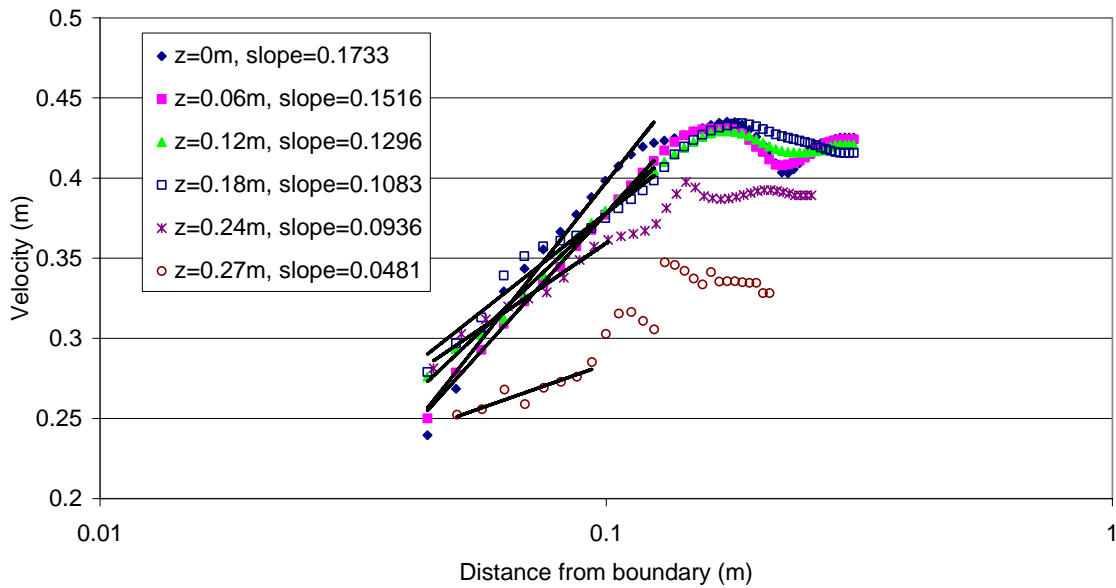


Figure D - 1: Logarithmic variation of velocity profiles for S0Q64, XS6

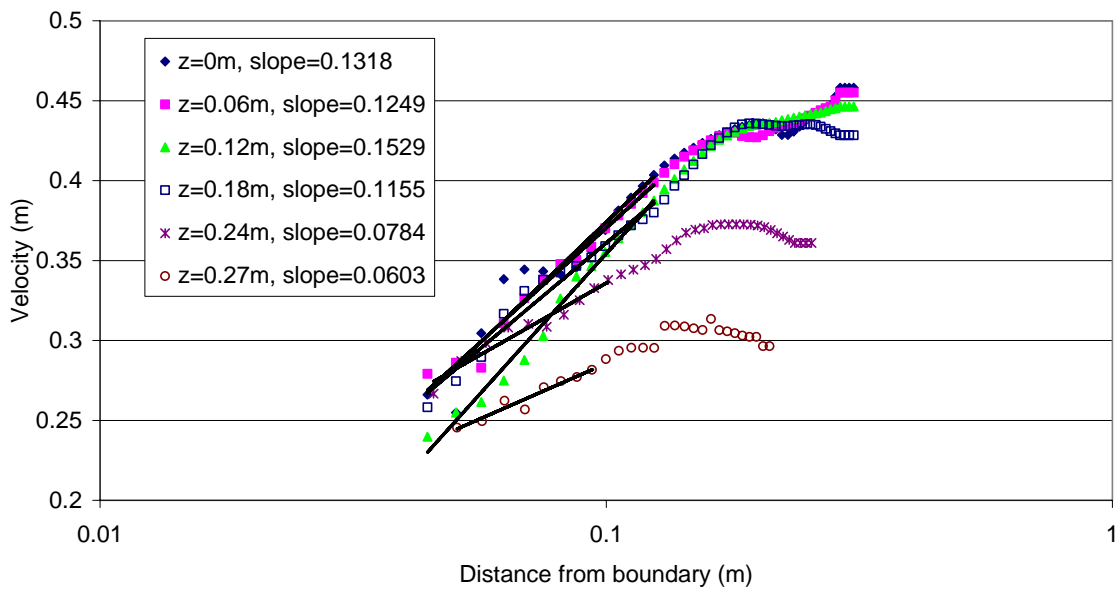


Figure D - 2: Logarithmic variation of velocity profiles for S0Q64, XS8

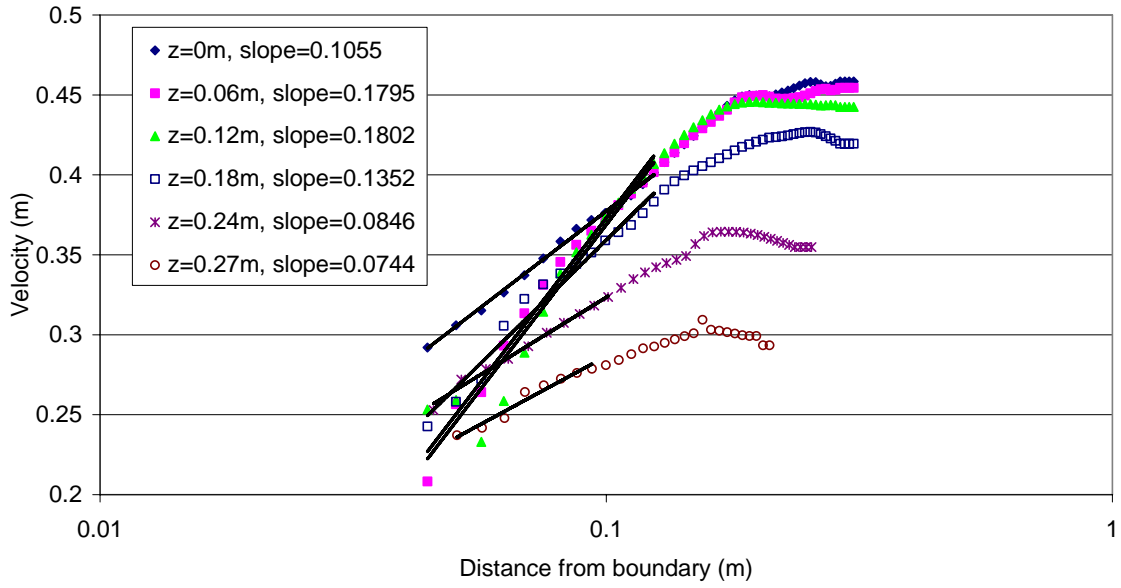


Figure D - 3: Logarithmic variation of velocity profiles for S0Q64, XS10

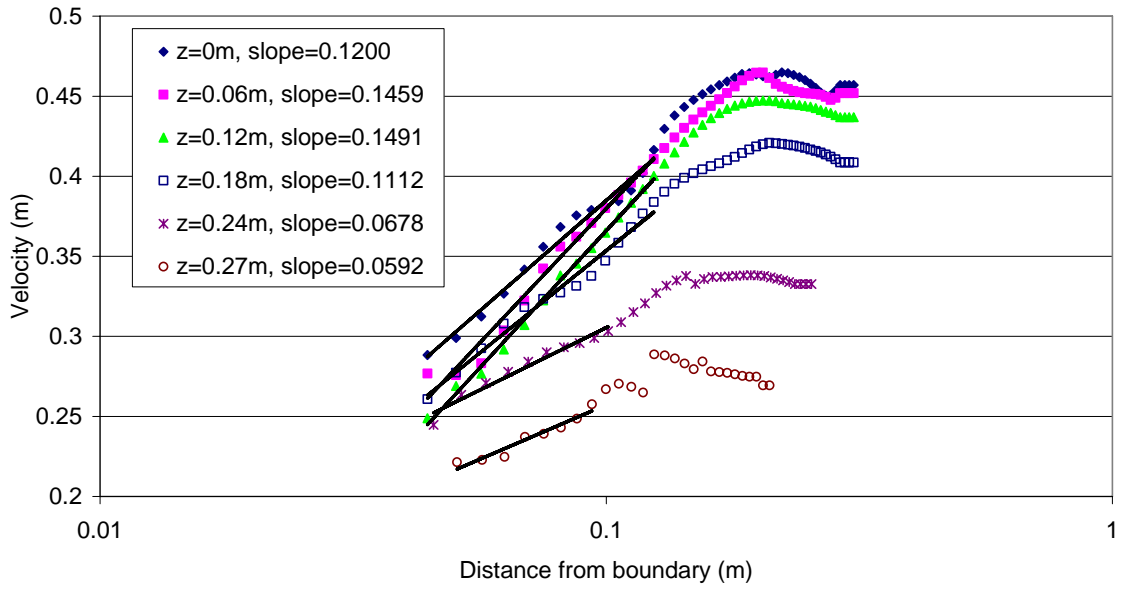


Figure D - 4: Logarithmic variation of velocity profiles for S0Q64, XS12

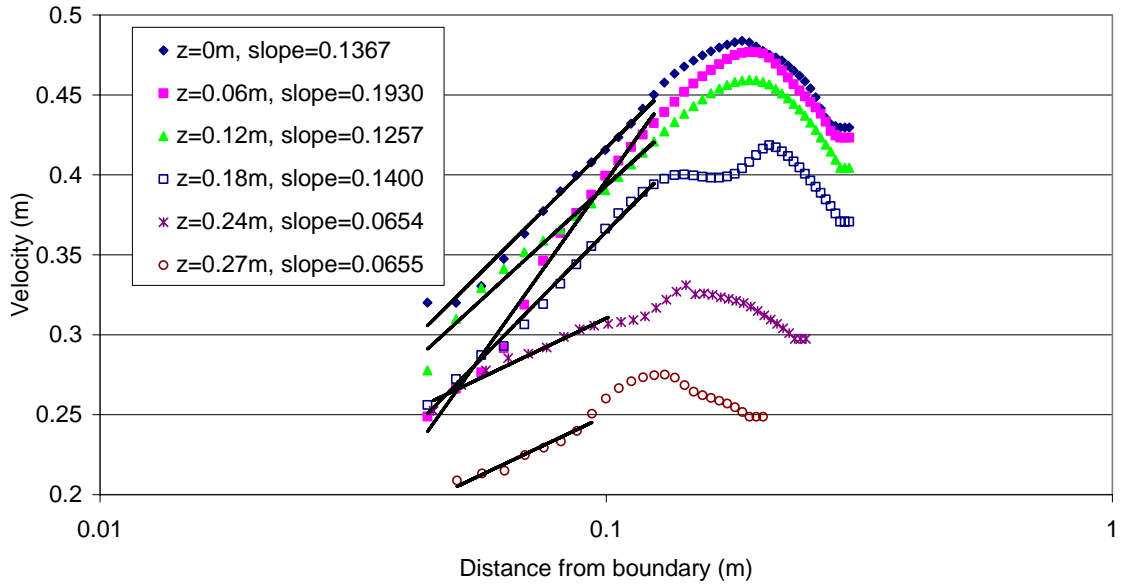


Figure D - 5: Logarithmic variation of velocity profiles for S0Q64, XS14

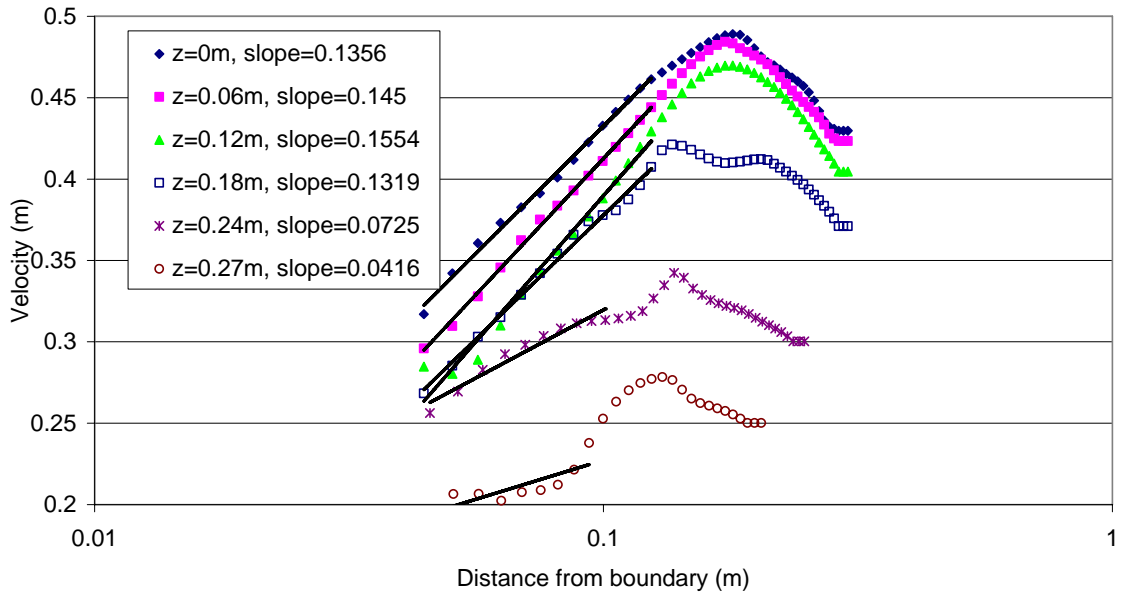


Figure D - 6: Logarithmic variation of velocity profiles for S0Q64, XS17

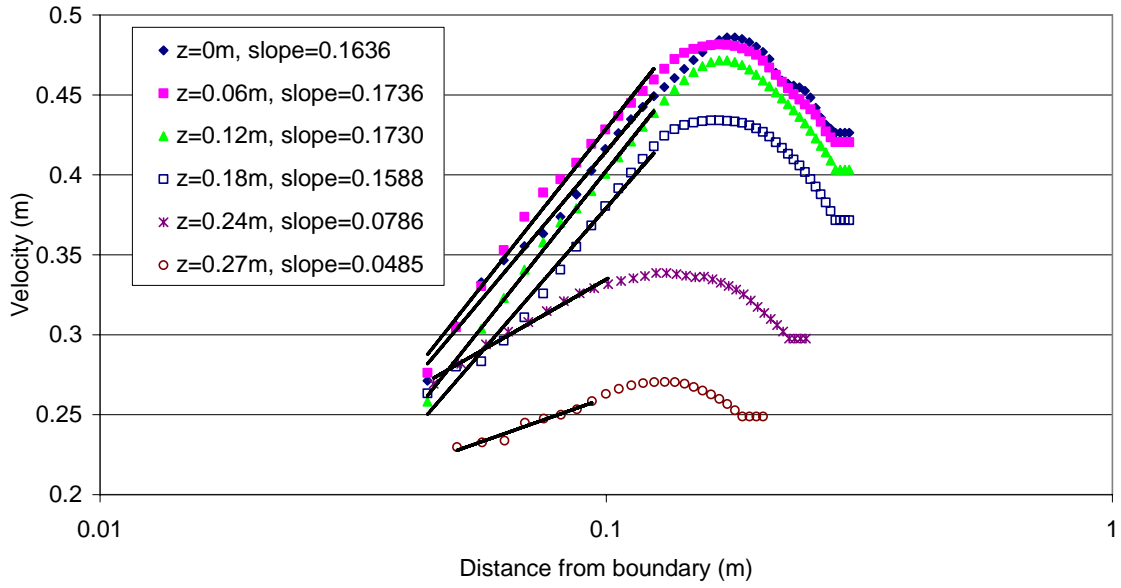


Figure D - 7: Logarithmic variation of velocity profiles for S0Q64, XS20

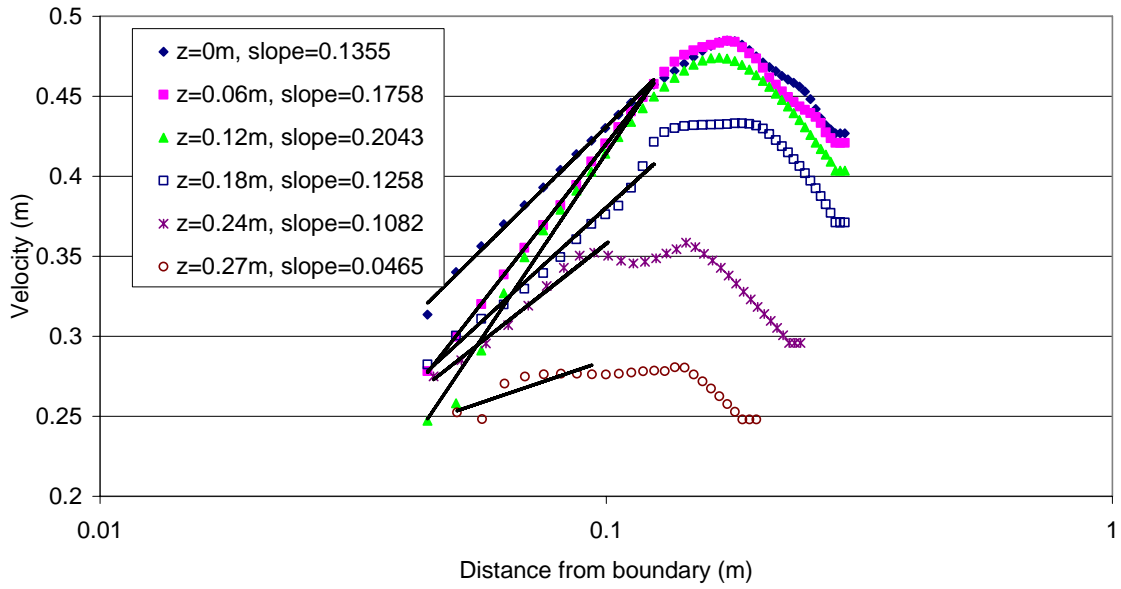


Figure D - 8: Logarithmic variation of velocity profiles for S0Q64, XS23

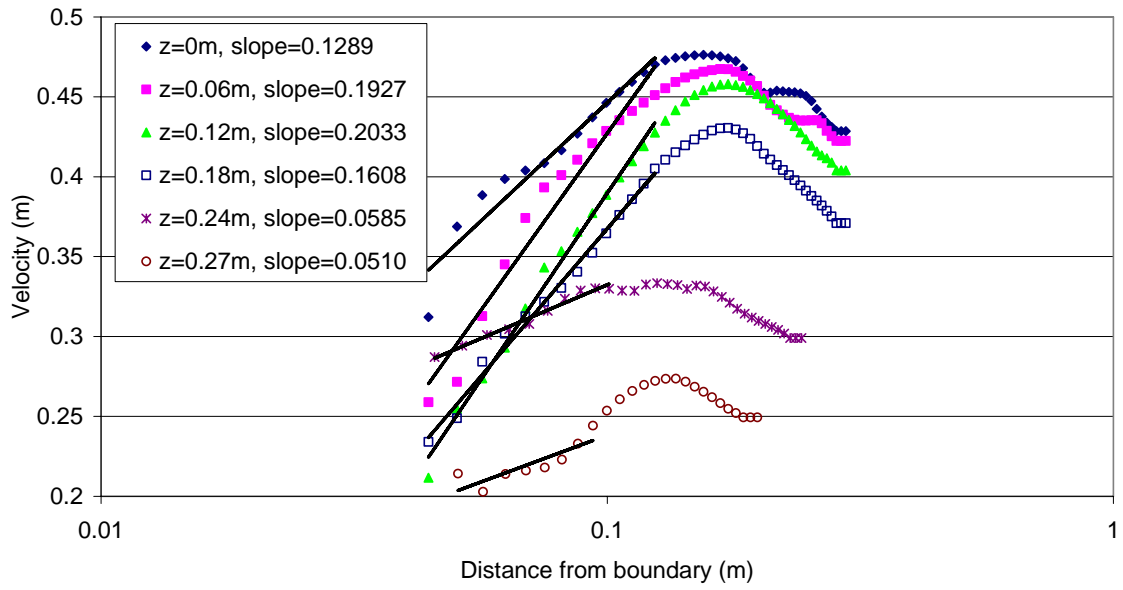


Figure D - 9: Logarithmic variation of velocity profiles for S0Q64, XS26

S0Q186

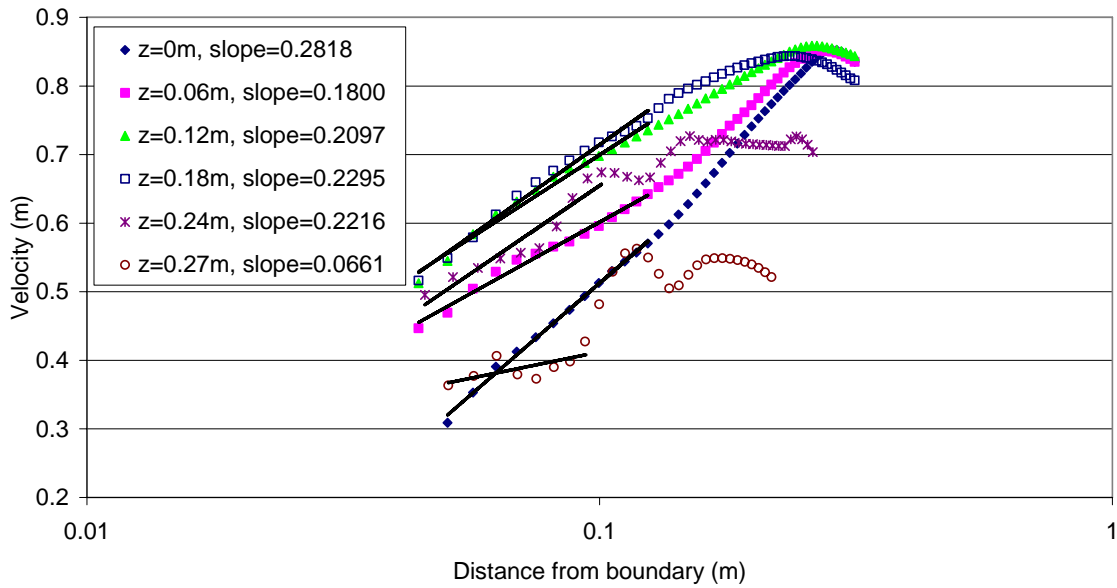


Figure D - 10: Logarithmic variation of velocity profiles for S0Q186, XS6

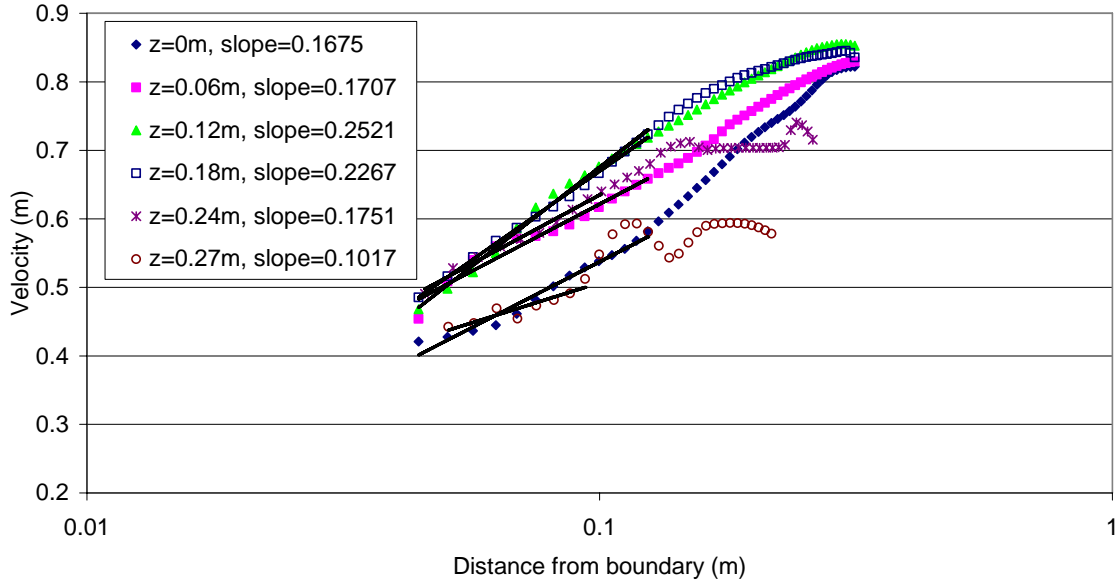


Figure D - 11: Logarithmic variation of velocity profiles for S0Q186, XS8

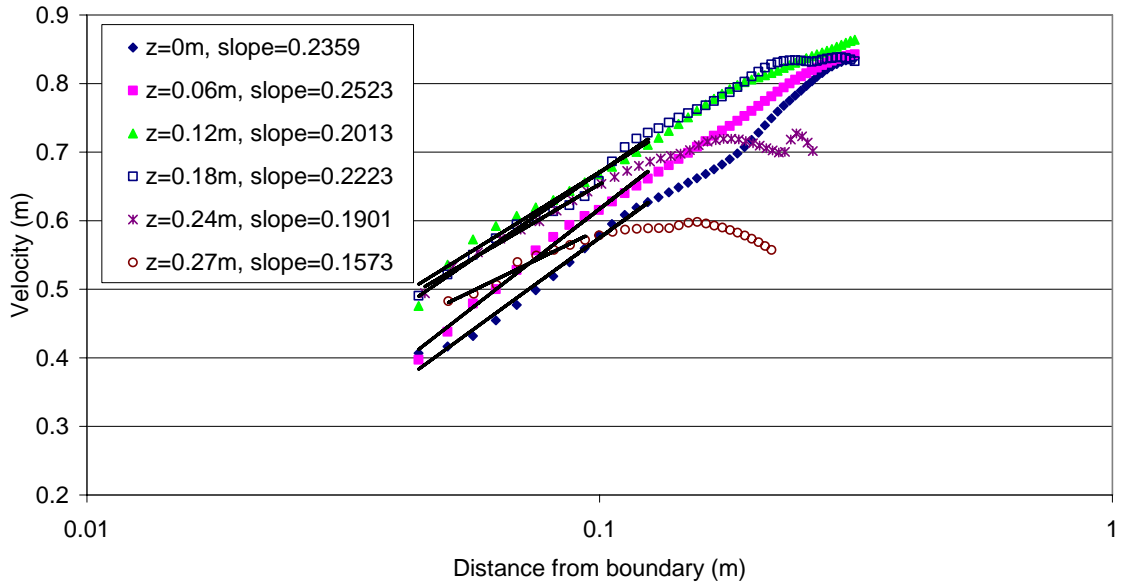


Figure D - 12: Logarithmic variation of velocity profiles for S0Q186, XS10

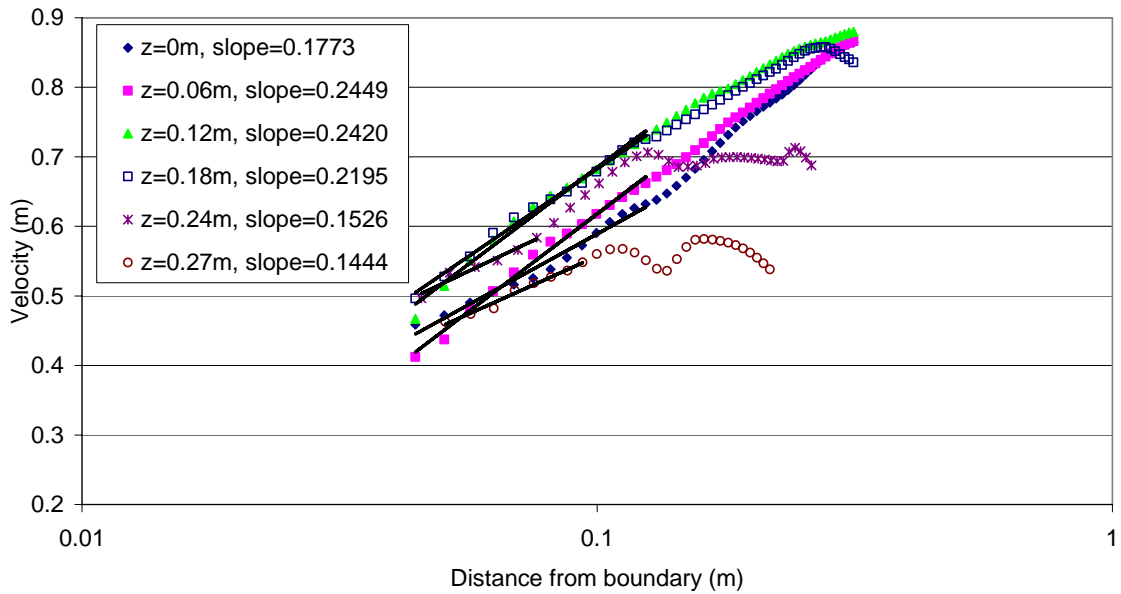


Figure D - 13: Logarithmic variation of velocity profiles for S0Q186, XS12

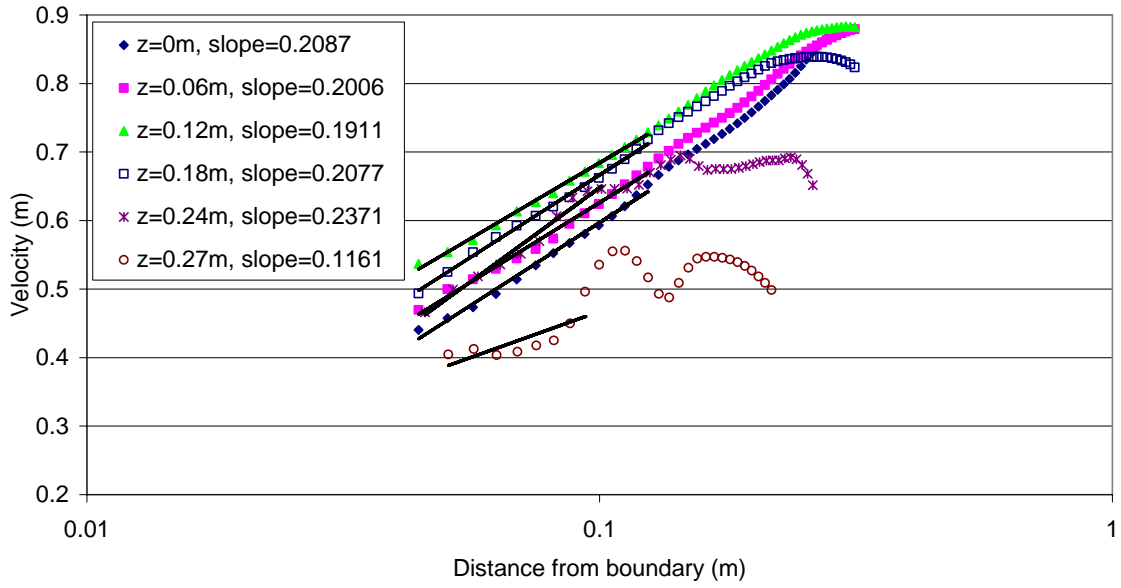


Figure D - 14: Logarithmic variation of velocity profiles for S0Q186, XS14

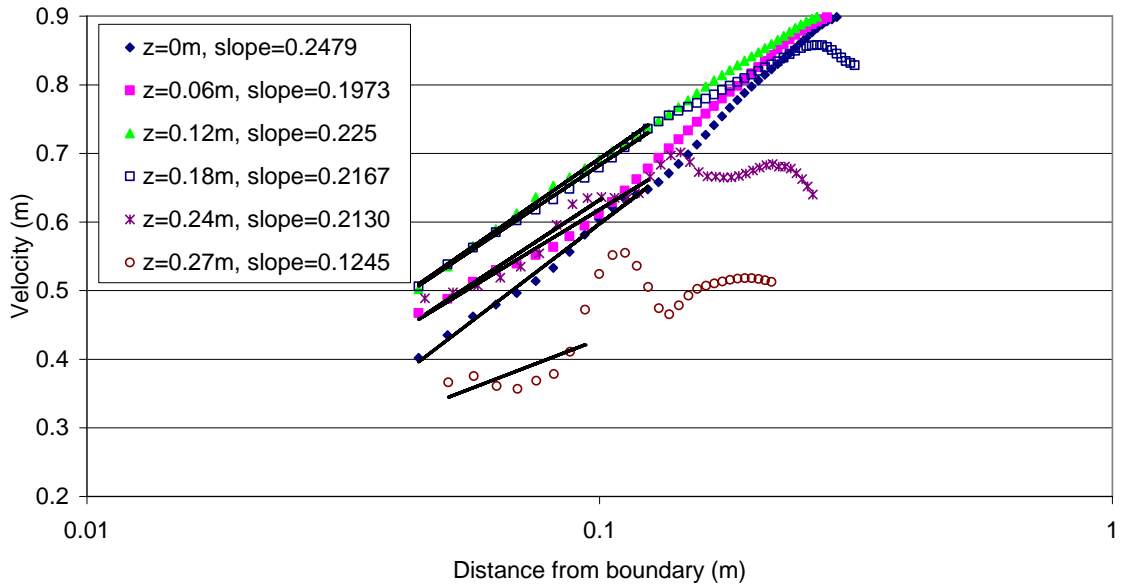


Figure D - 15: Logarithmic variation of velocity profiles for S0Q186, XS17

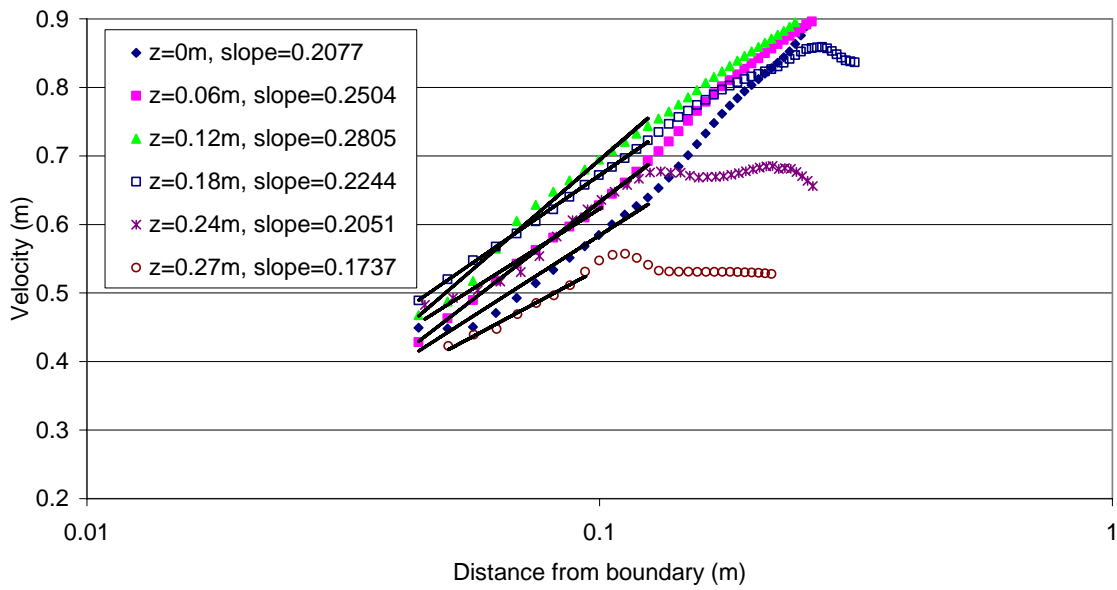


Figure D - 16: Logarithmic variation of velocity profiles for S0Q186, XS20

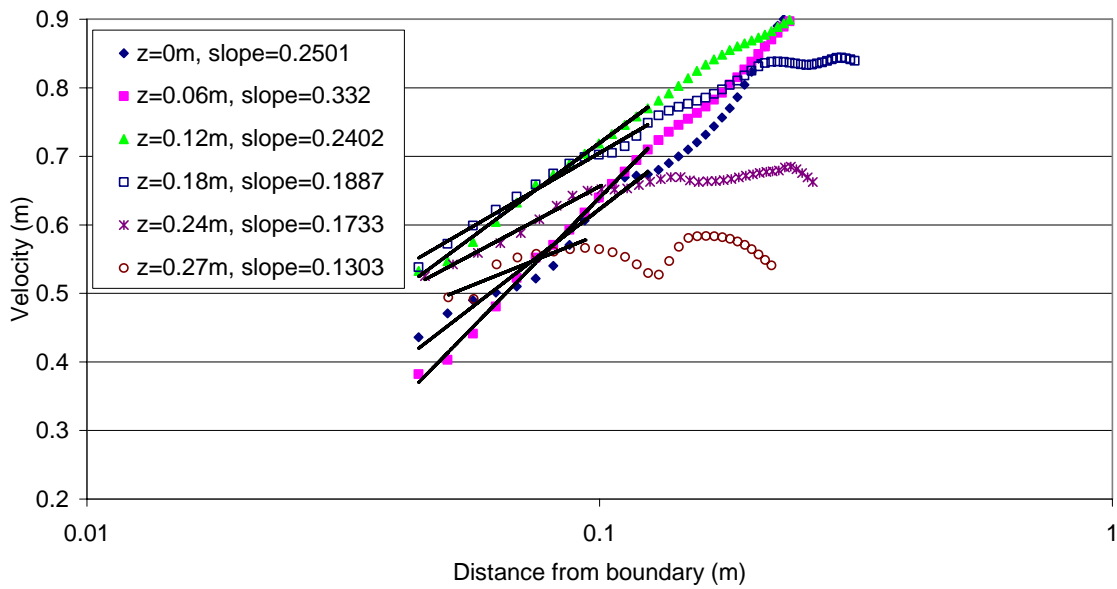


Figure D - 17: Logarithmic variation of velocity profiles for S0Q186, XS23

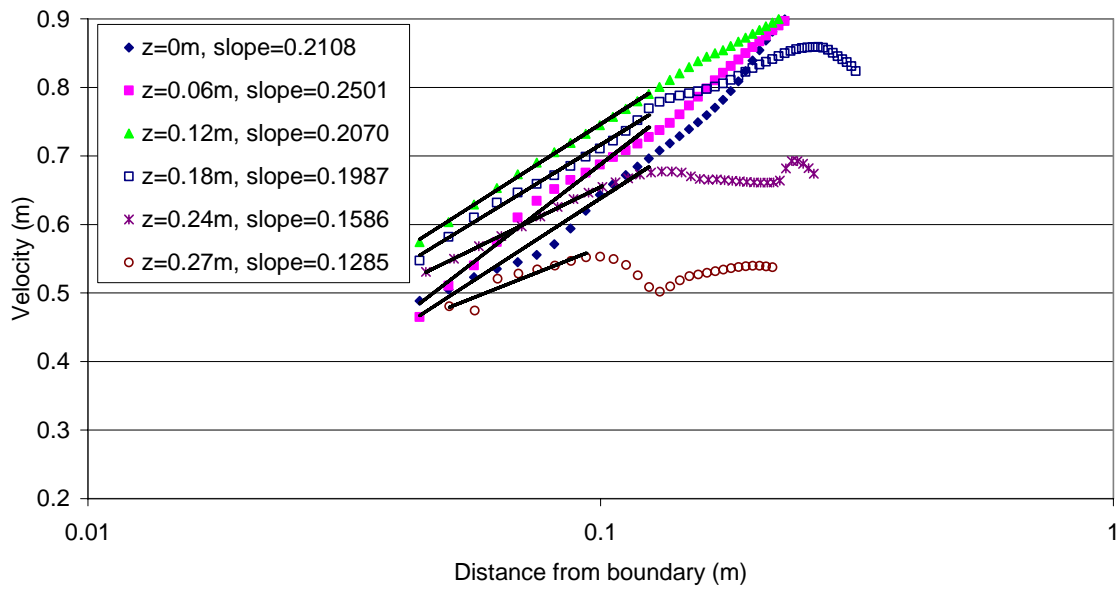


Figure D - 18: Logarithmic variation of velocity profiles for S0Q186, XS26

S5Q145

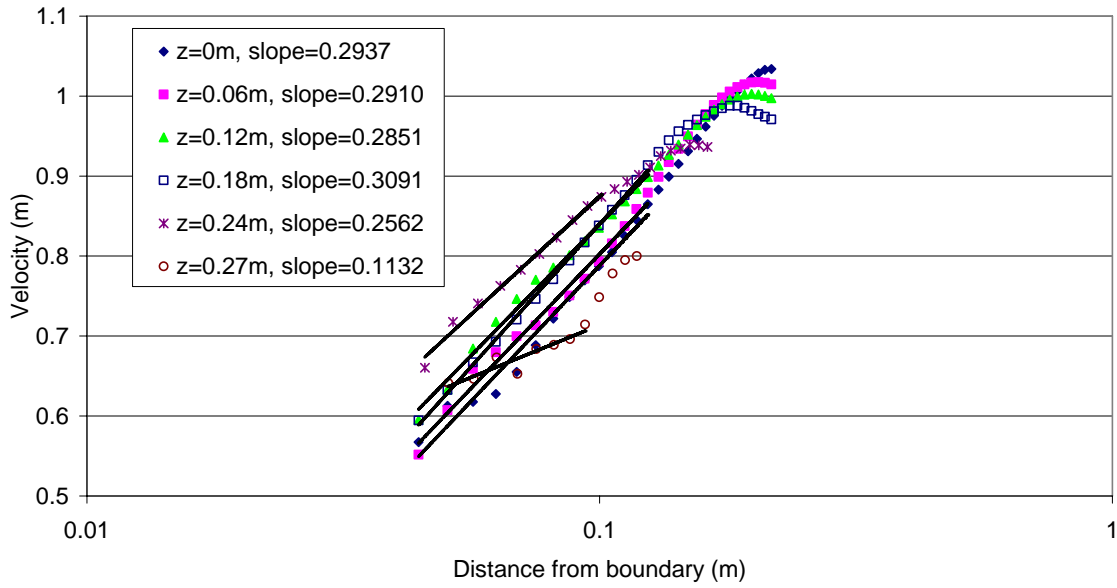


Figure D - 19: Logarithmic variation of velocity profiles for S5Q145, XS6

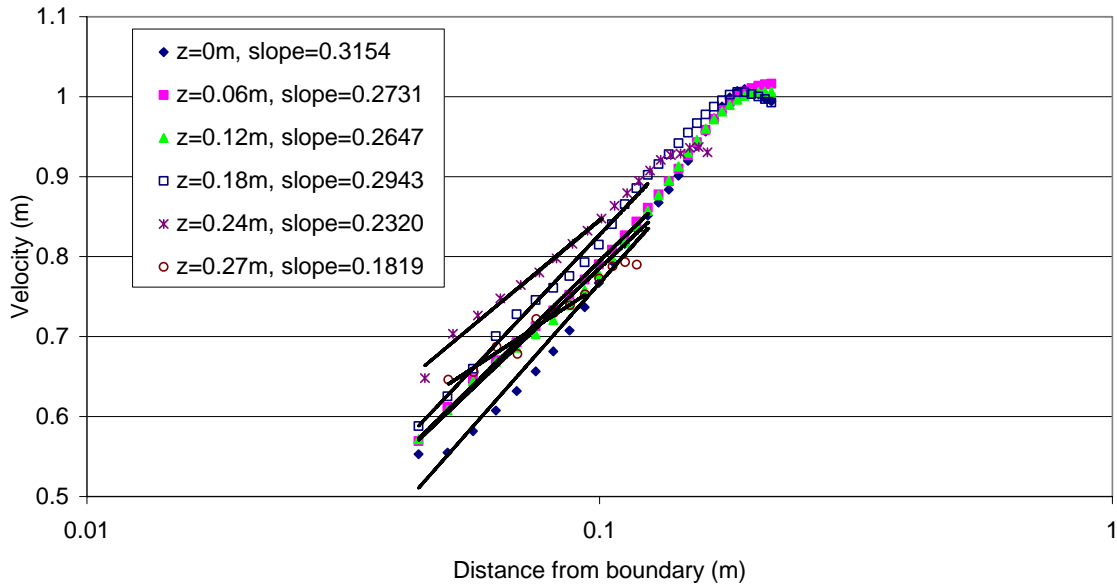


Figure D - 20: Logarithmic variation of velocity profiles for S5Q145, XS8

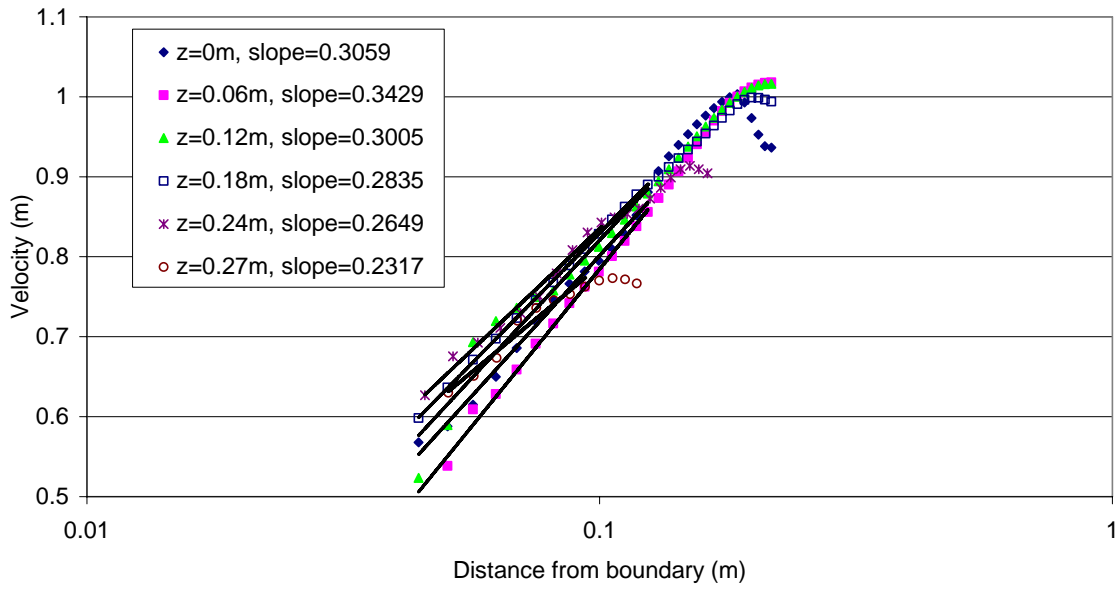


Figure D - 21: Logarithmic variation of velocity profiles for S5Q145, XS10

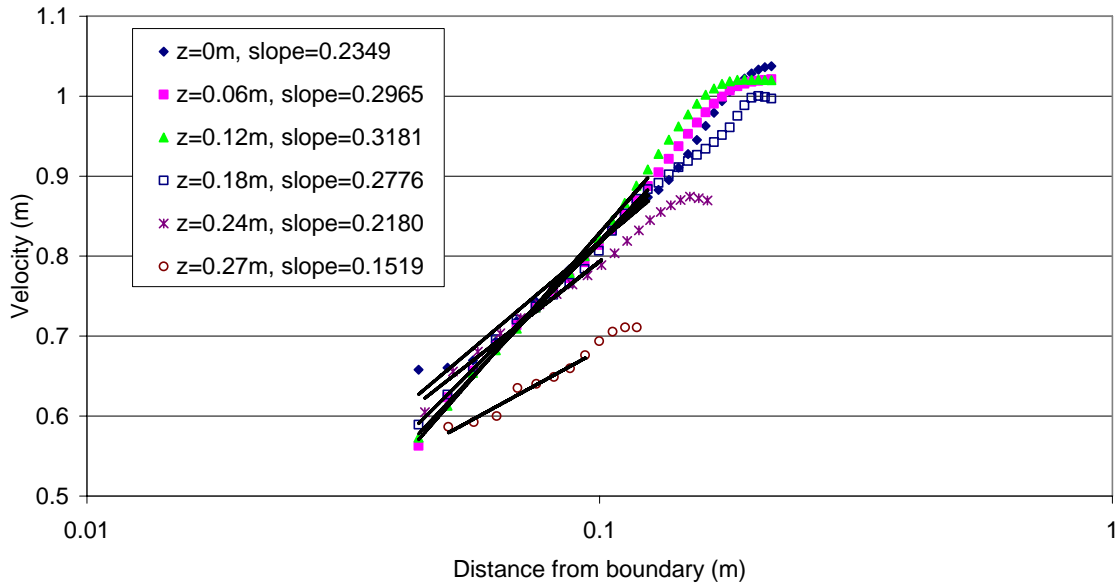


Figure D - 22: Logarithmic variation of velocity profiles for S5Q145, XS12

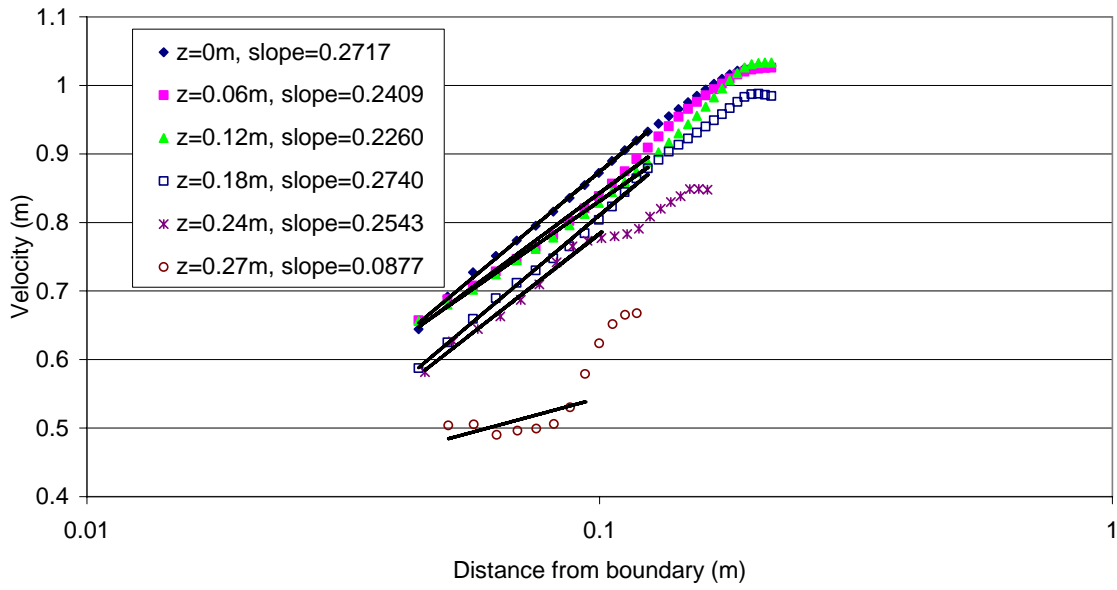


Figure D - 23: Logarithmic variation of velocity profiles for S5Q145, XS14

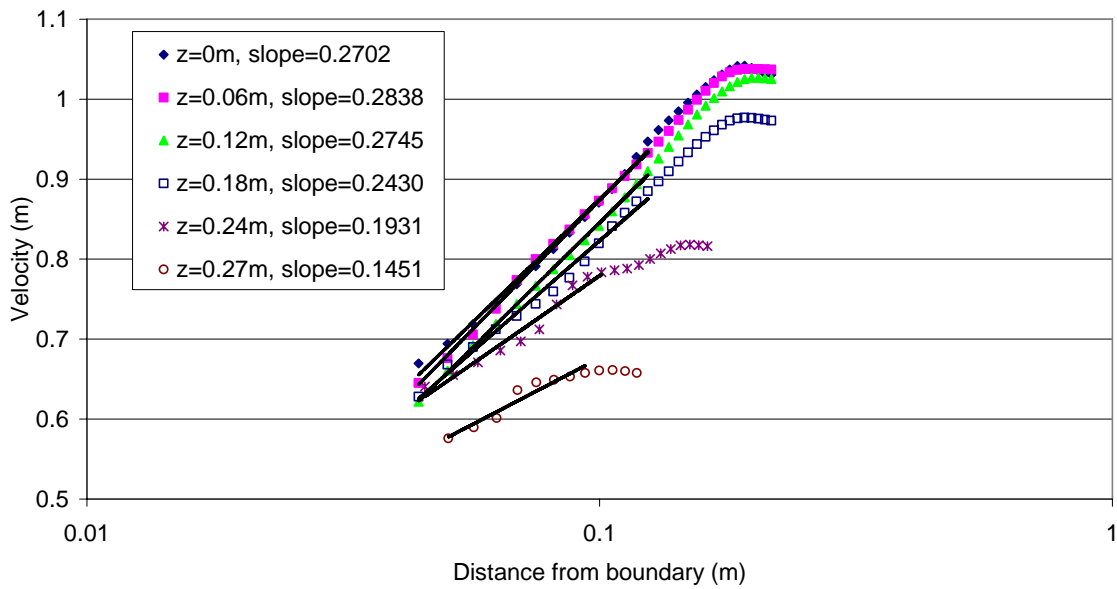


Figure D - 24: Logarithmic variation of velocity profiles for S5Q145, XS17

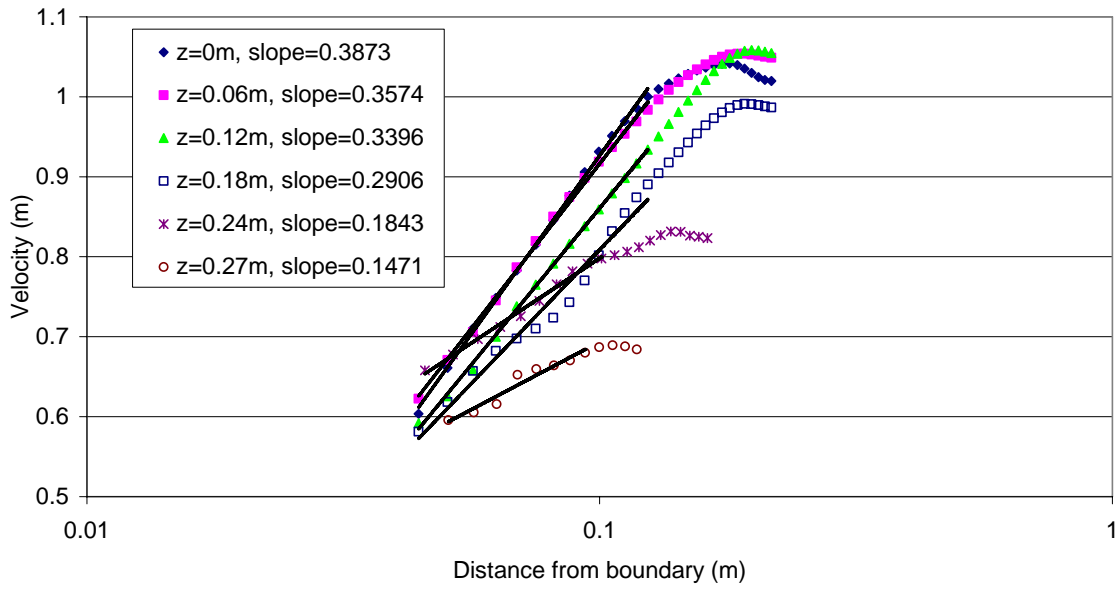


Figure D - 25: Logarithmic variation of velocity profiles for S5Q145, XS20

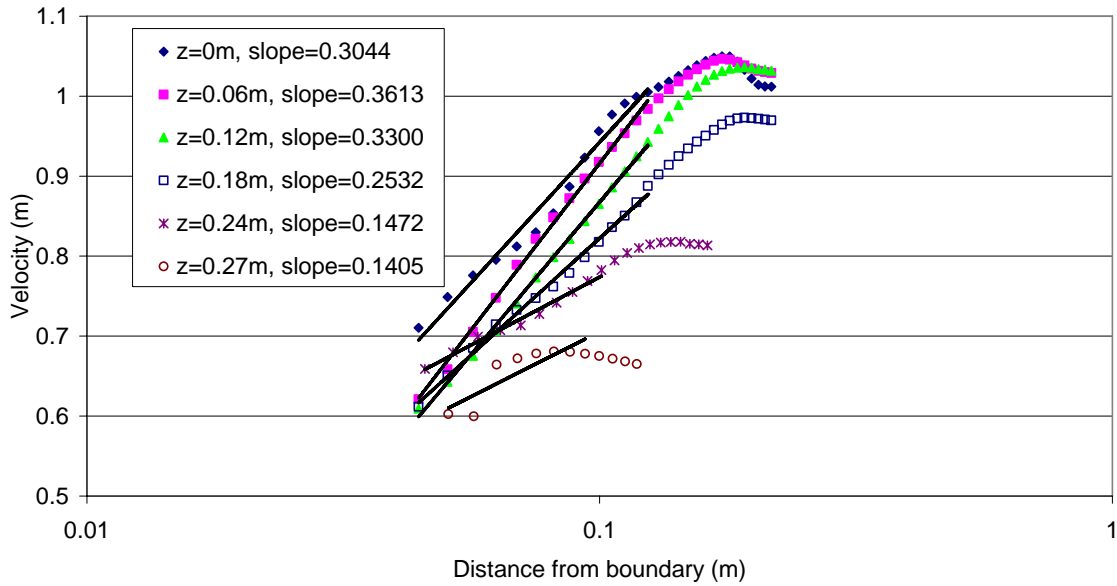


Figure D - 26: Logarithmic variation of velocity profiles for S5Q145, XS23

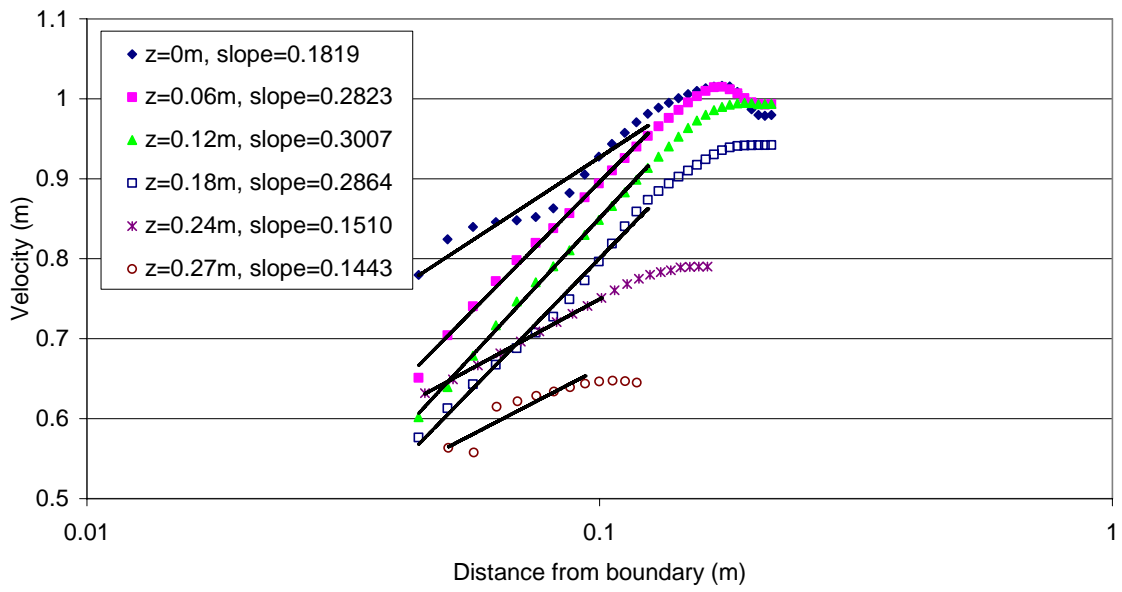


Figure D - 27: Logarithmic variation of velocity profiles for S5Q145, XS26

S5Q221

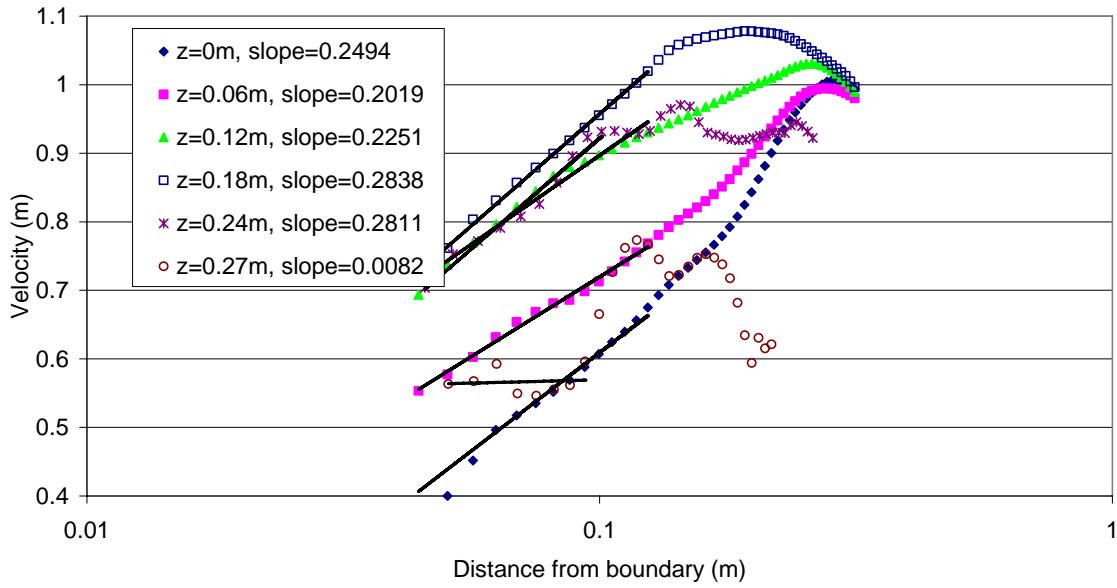


Figure D - 28: Logarithmic variation of velocity profiles for S5Q221, XS6

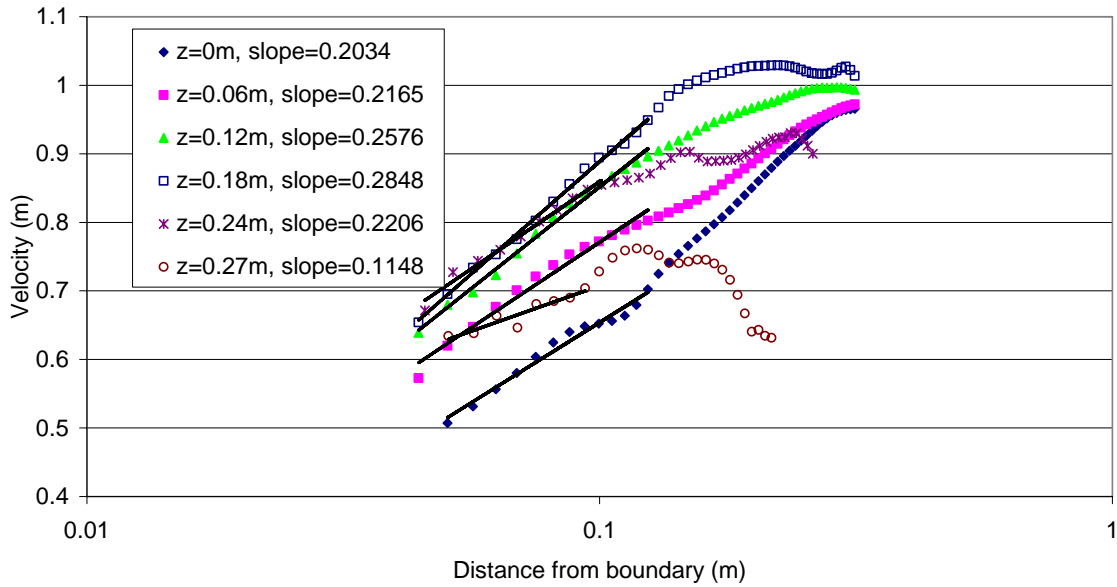


Figure D - 29: Logarithmic variation of velocity profiles for S5Q221, XS8

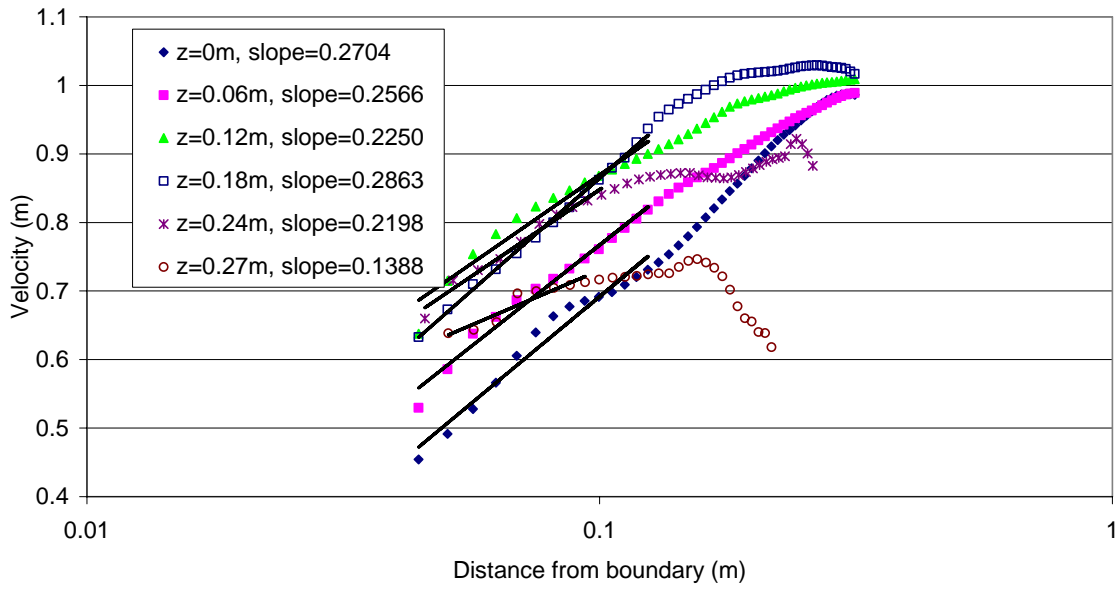


Figure D - 30: Logarithmic variation of velocity profiles for S5Q221, XS10

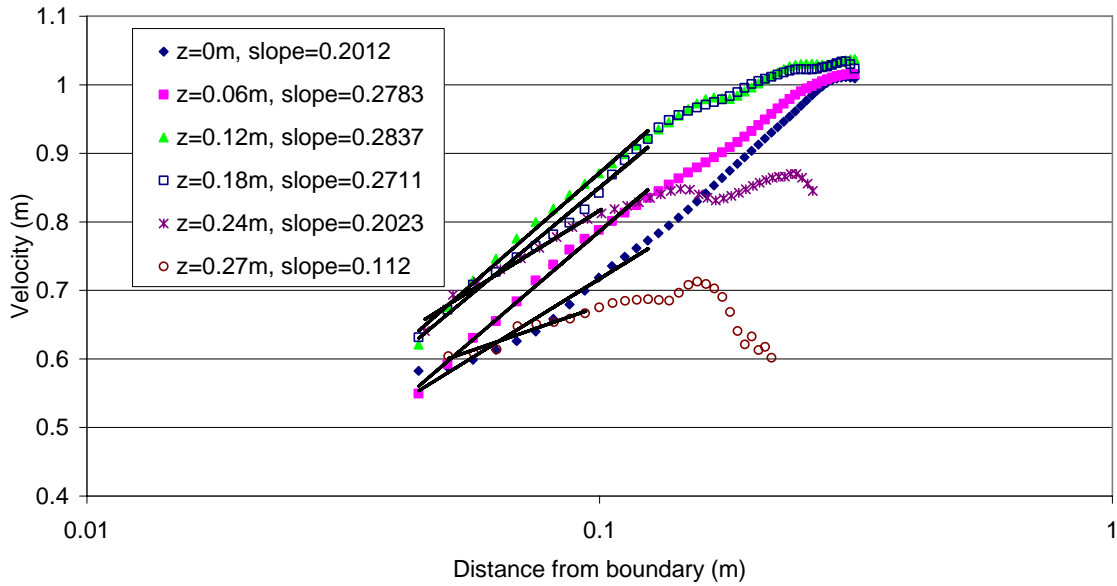


Figure D - 31: Logarithmic variation of velocity profiles for S5Q221, XS12

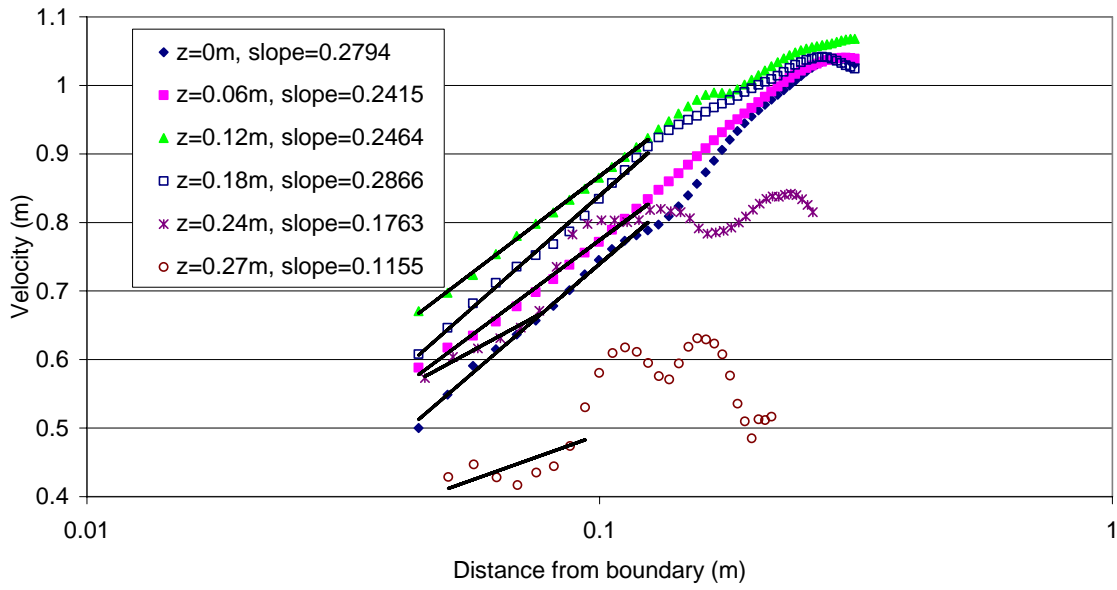


Figure D - 32: Logarithmic variation of velocity profiles for S5Q221, XS14

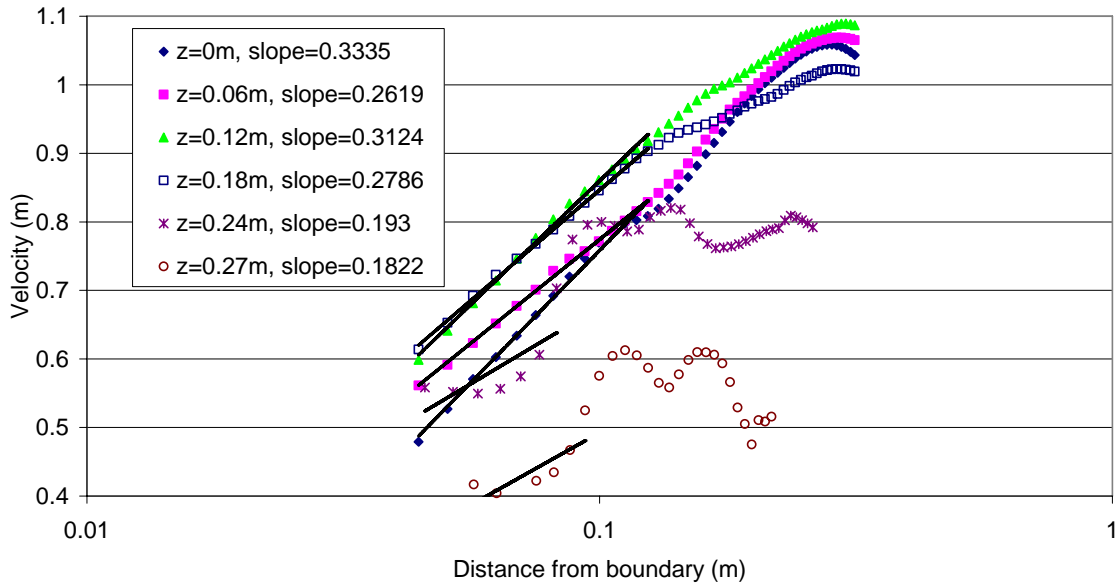


Figure D - 33: Logarithmic variation of velocity profiles for S5Q221, XS17

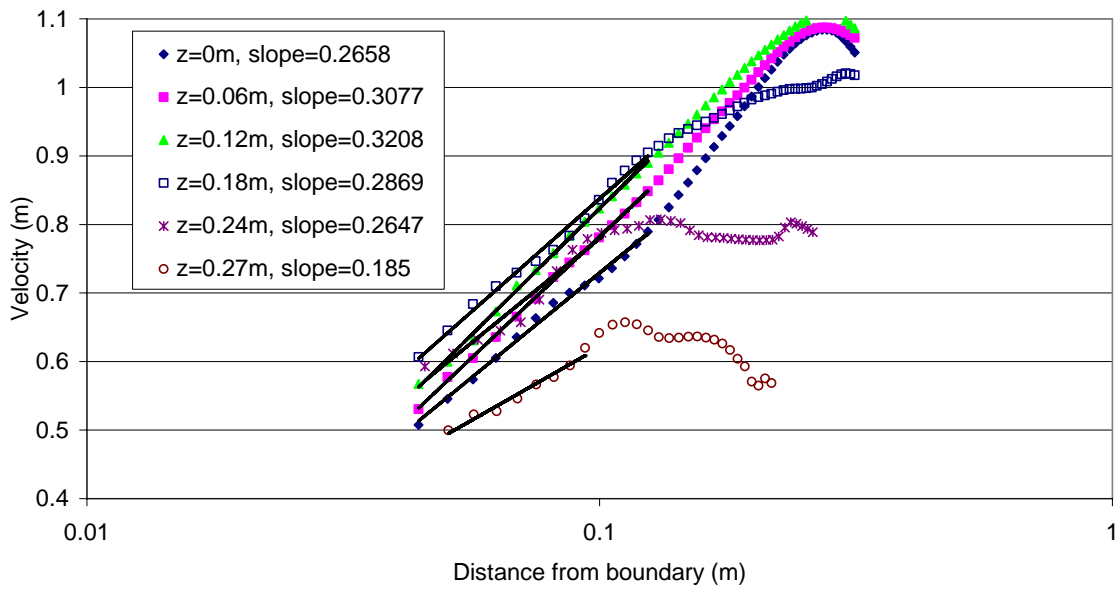


Figure D - 34: Logarithmic variation of velocity profiles for S5Q221, XS20

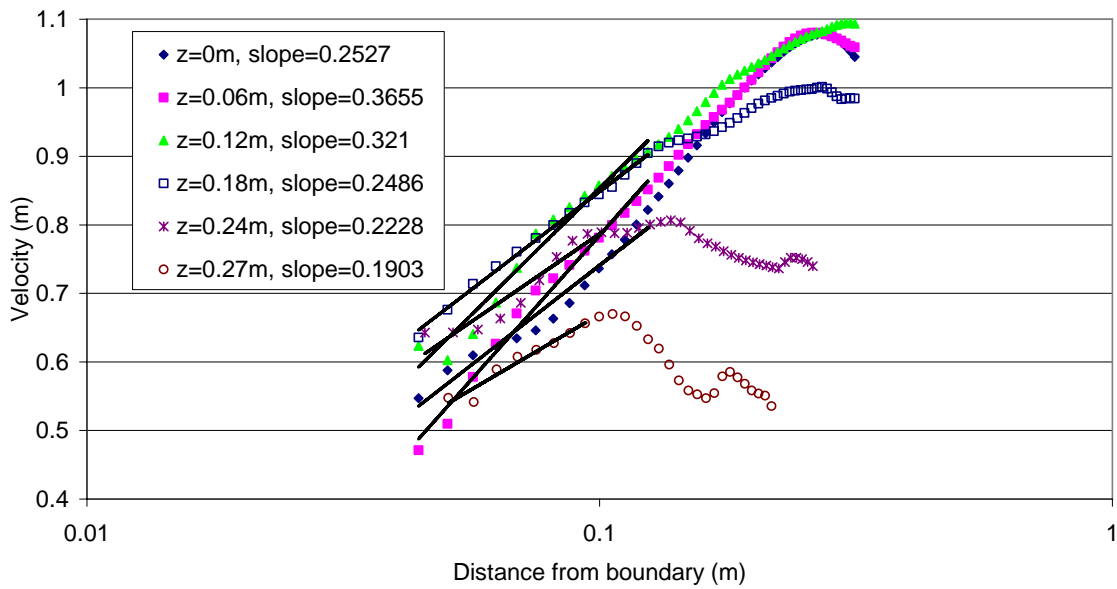


Figure D - 35: Logarithmic variation of velocity profiles for S5Q221, XS23

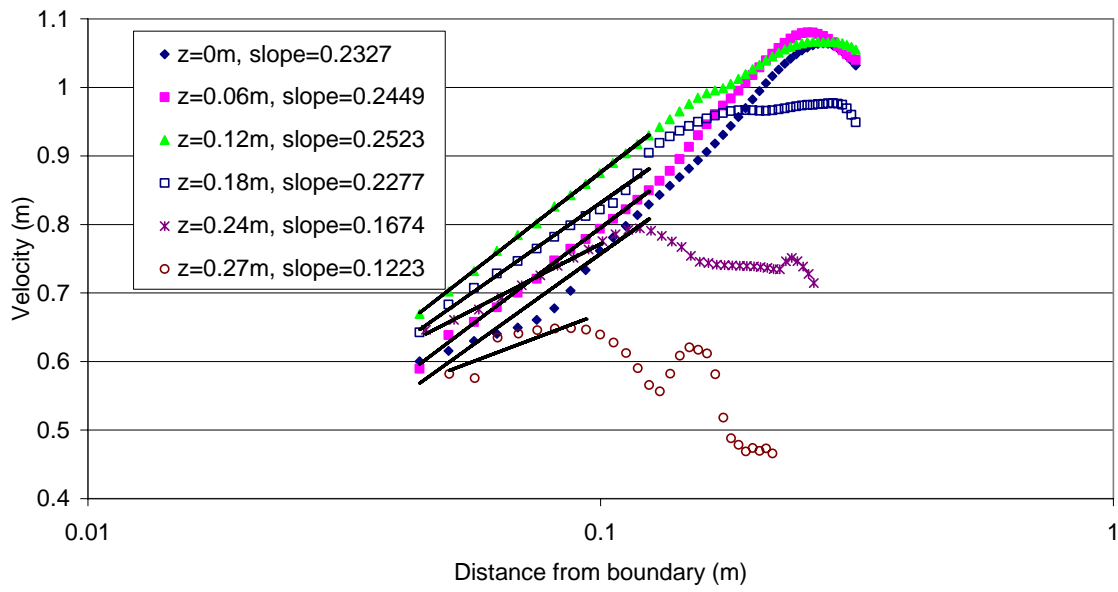


Figure D - 36: Logarithmic variation of velocity profiles for S5Q221, XS26

S1Q150

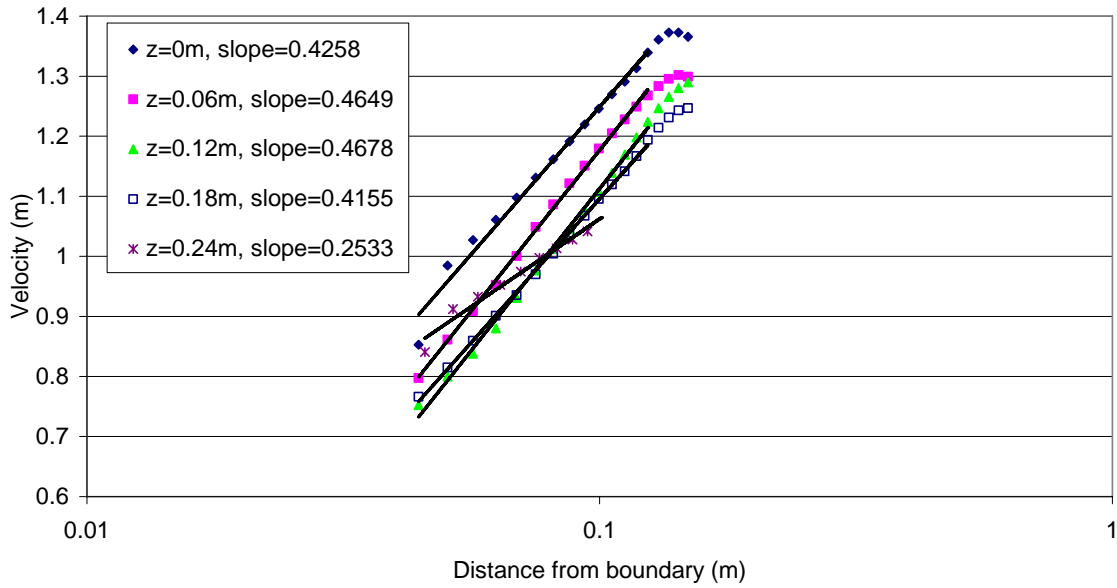


Figure D - 37: Logarithmic variation of velocity profiles for S1Q150, XS6

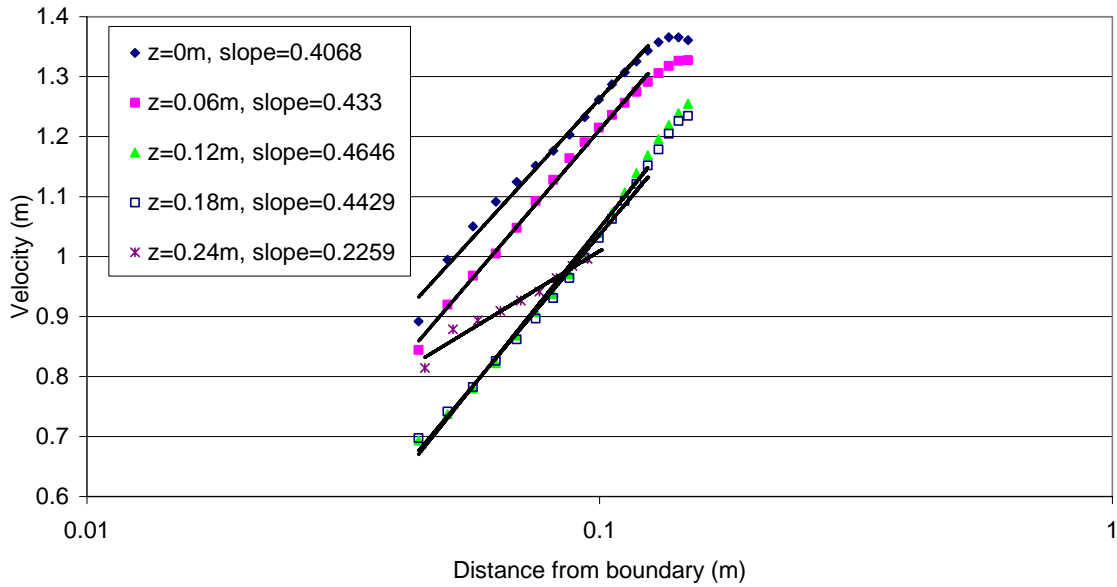


Figure D - 38: Logarithmic variation of velocity profiles for S1Q150, XS8

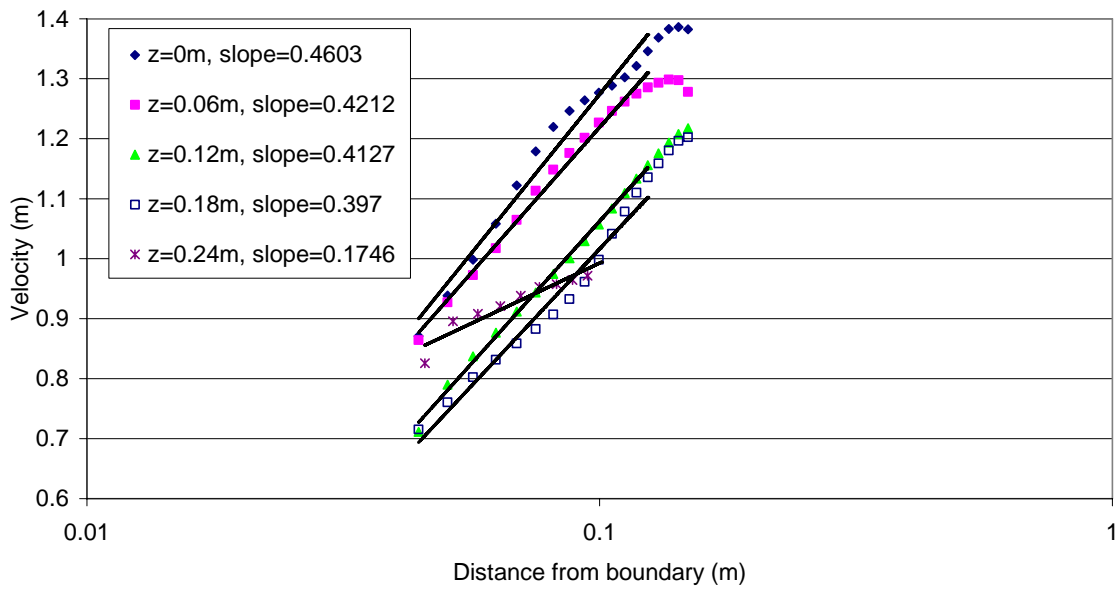


Figure D - 39: Logarithmic variation of velocity profiles for S1Q150, XS10

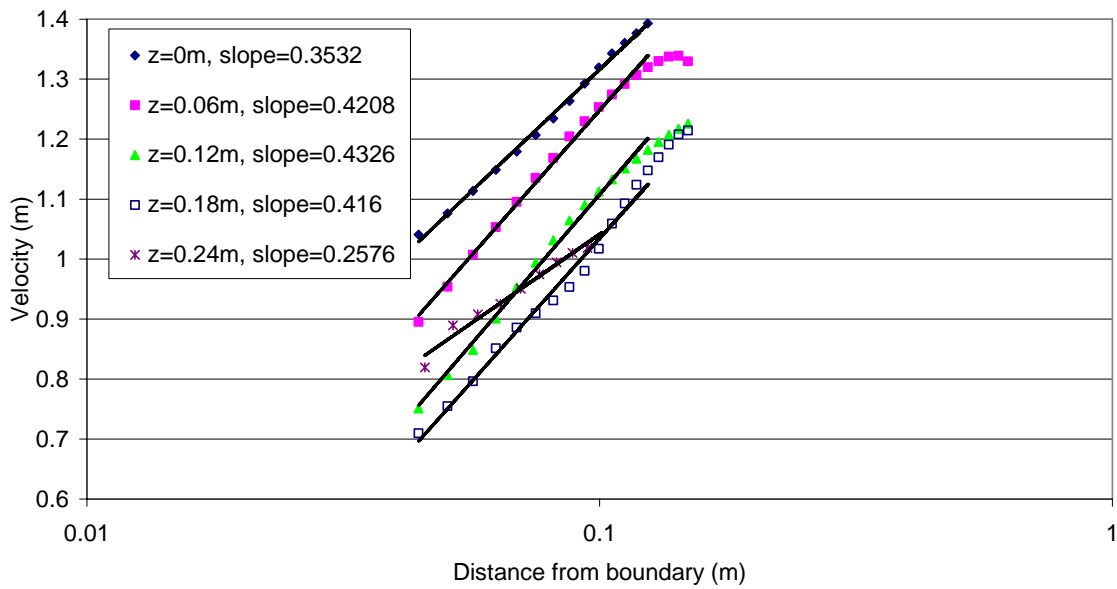


Figure D - 40: Logarithmic variation of velocity profiles for S1Q150, XS12

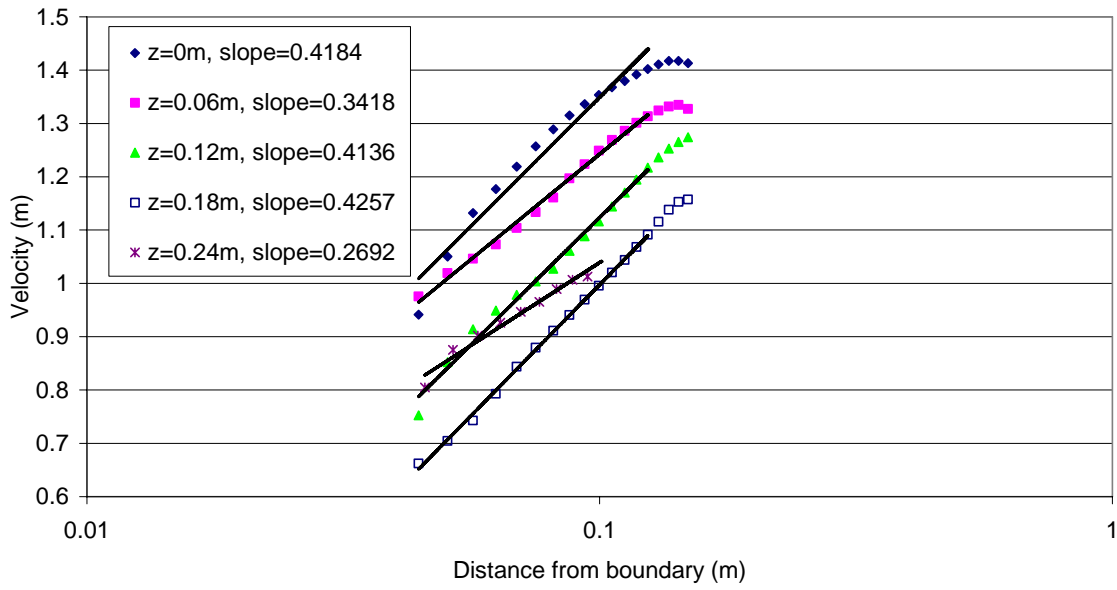


Figure D - 41: Logarithmic variation of velocity profiles for S1Q150, XS14

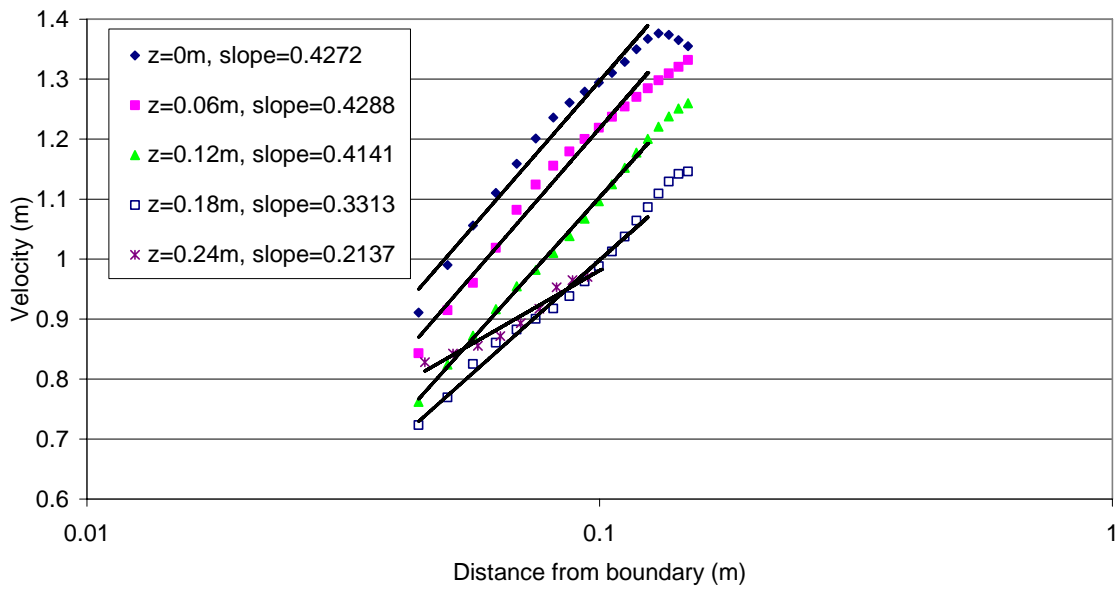


Figure D - 42: Logarithmic variation of velocity profiles for S1Q150, XS17

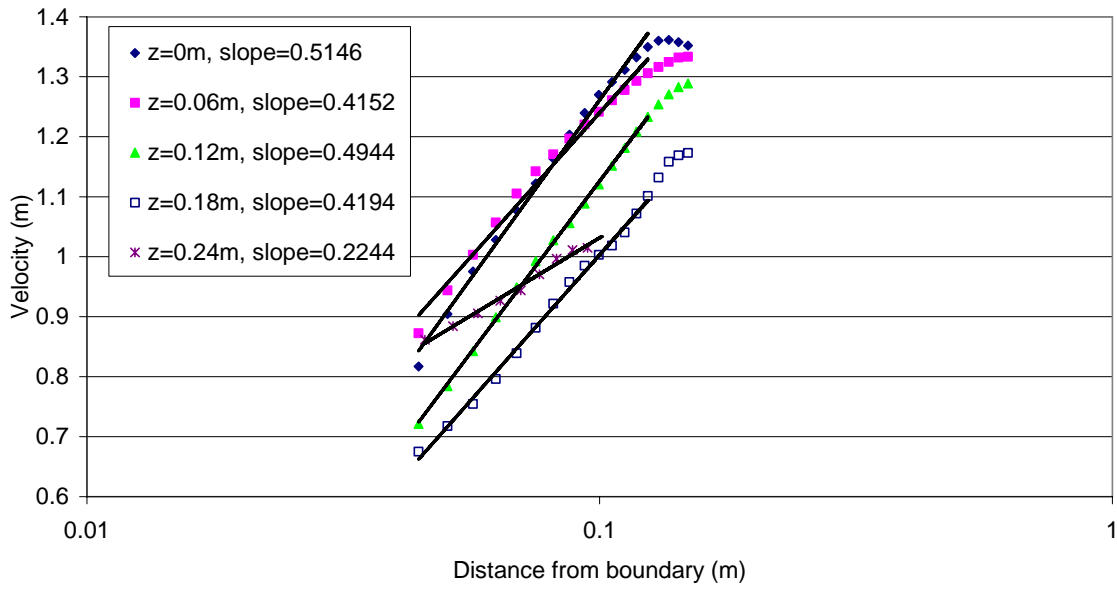


Figure D - 43: Logarithmic variation of velocity profiles for S1Q150, XS20

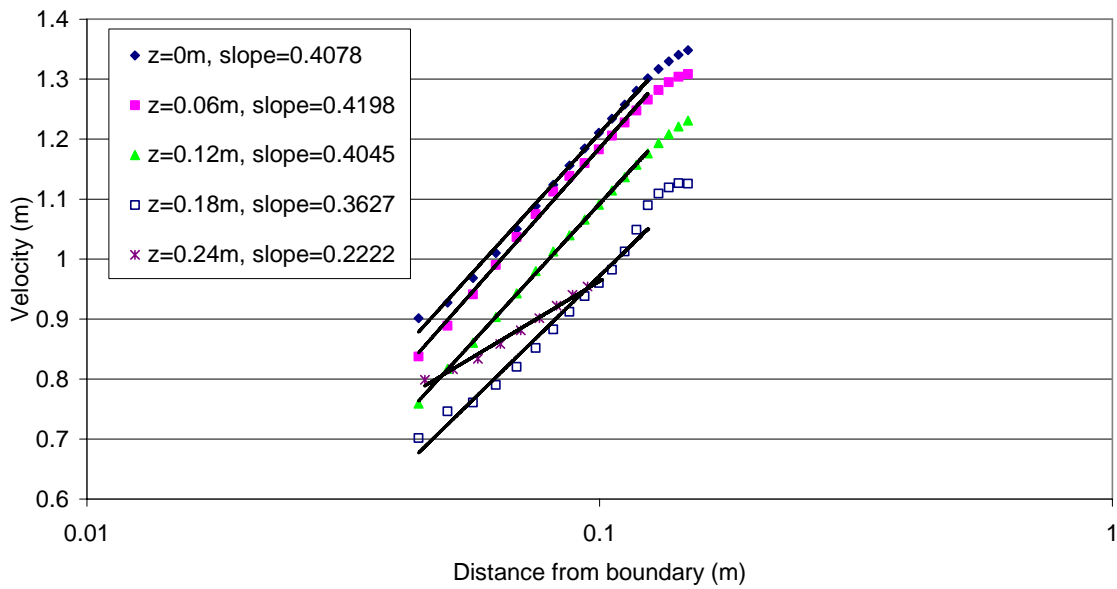


Figure D - 44: Logarithmic variation of velocity profiles for S1Q150, XS23

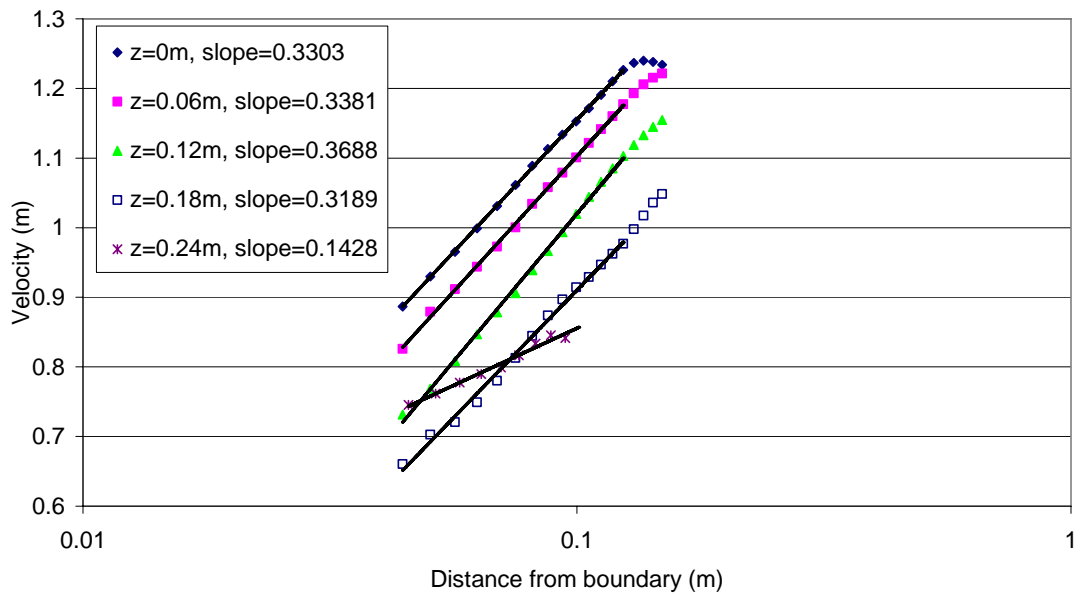


Figure D - 45: Logarithmic variation of velocity profiles for S1Q150, XS26

SIQ254

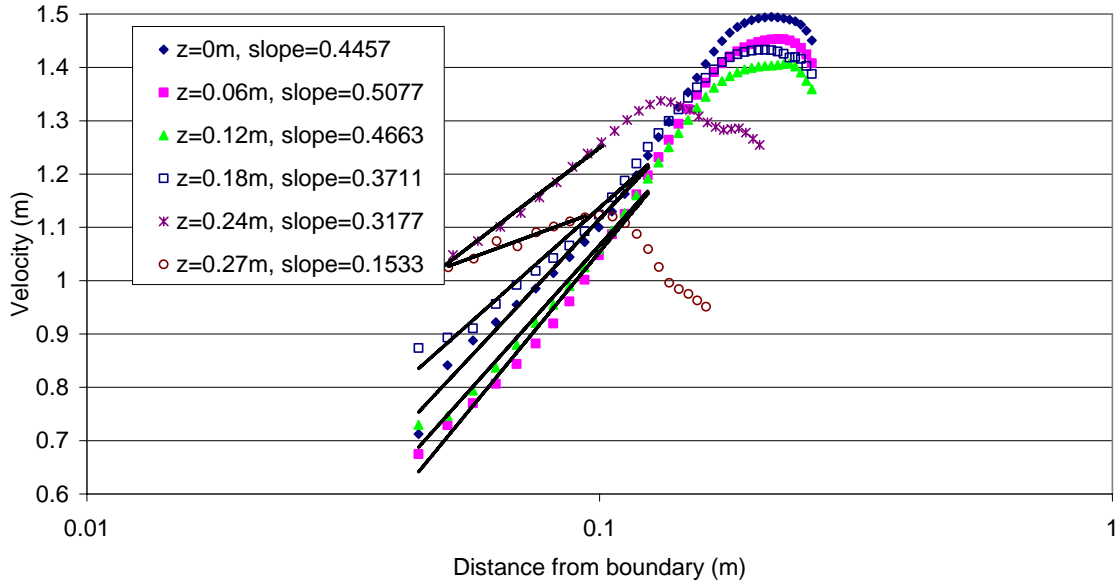


Figure D - 46: Logarithmic variation of velocity profiles for S1Q254, XS6

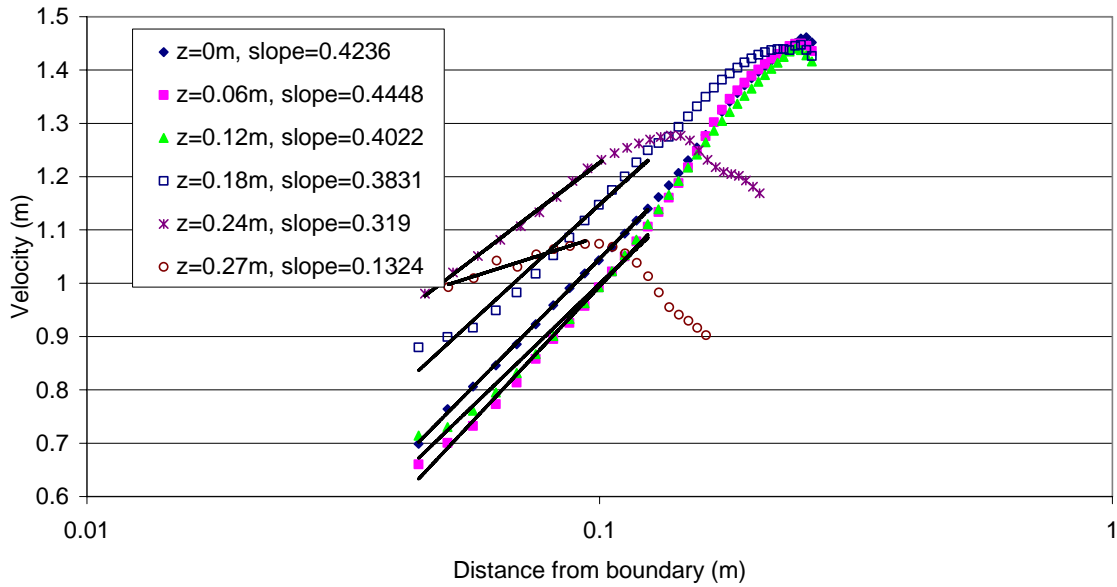


Figure D - 47: Logarithmic variation of velocity profiles for S1Q254, XS8

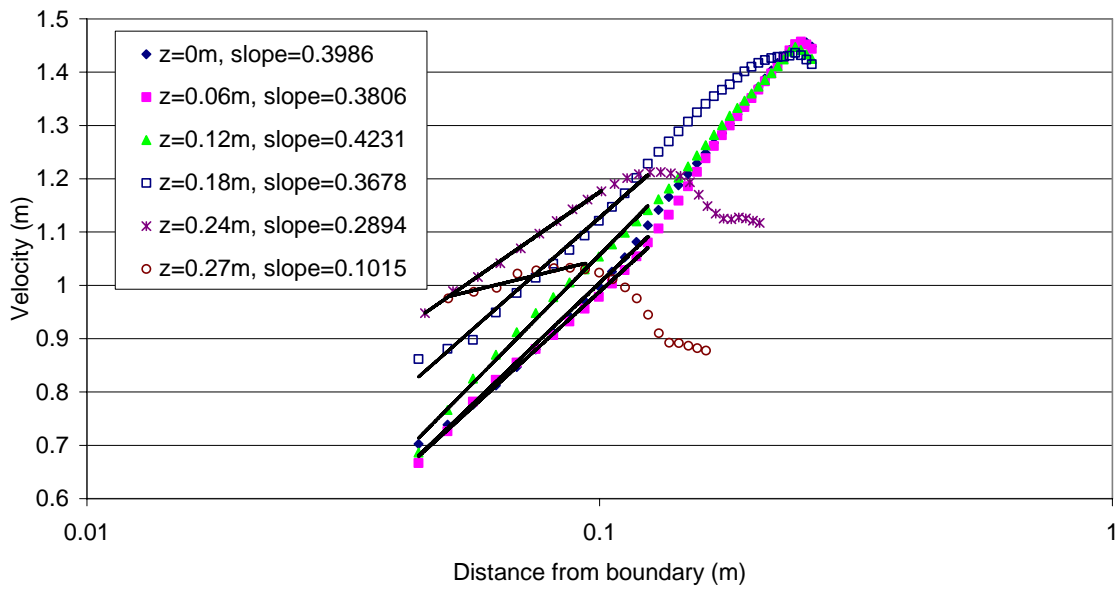


Figure D - 48: Logarithmic variation of velocity profiles for S1Q254, XS10

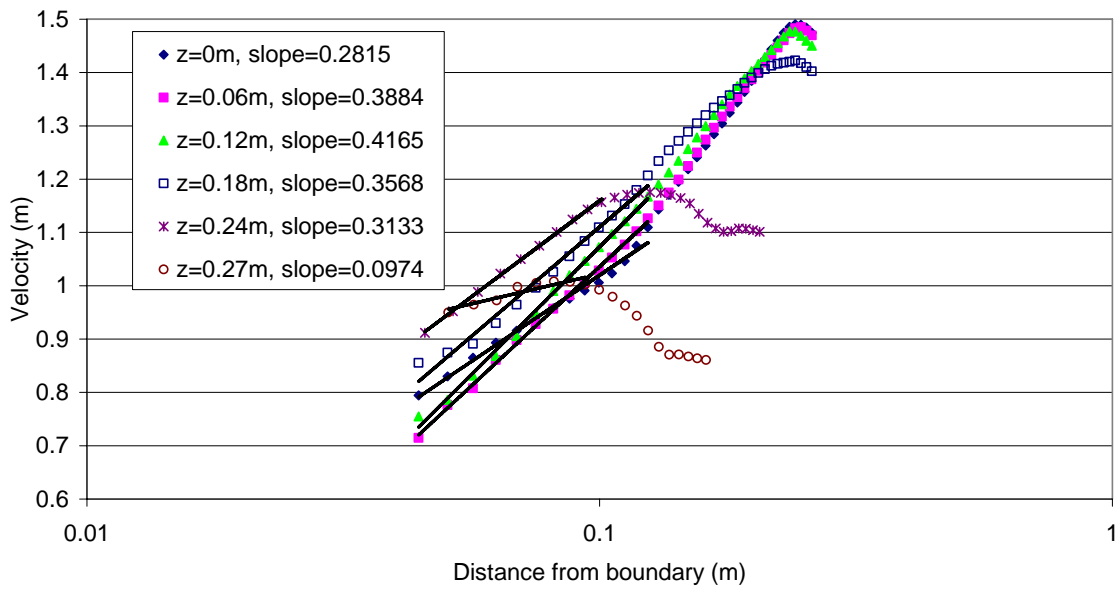


Figure D - 49: Logarithmic variation of velocity profiles for S1Q254, XS12

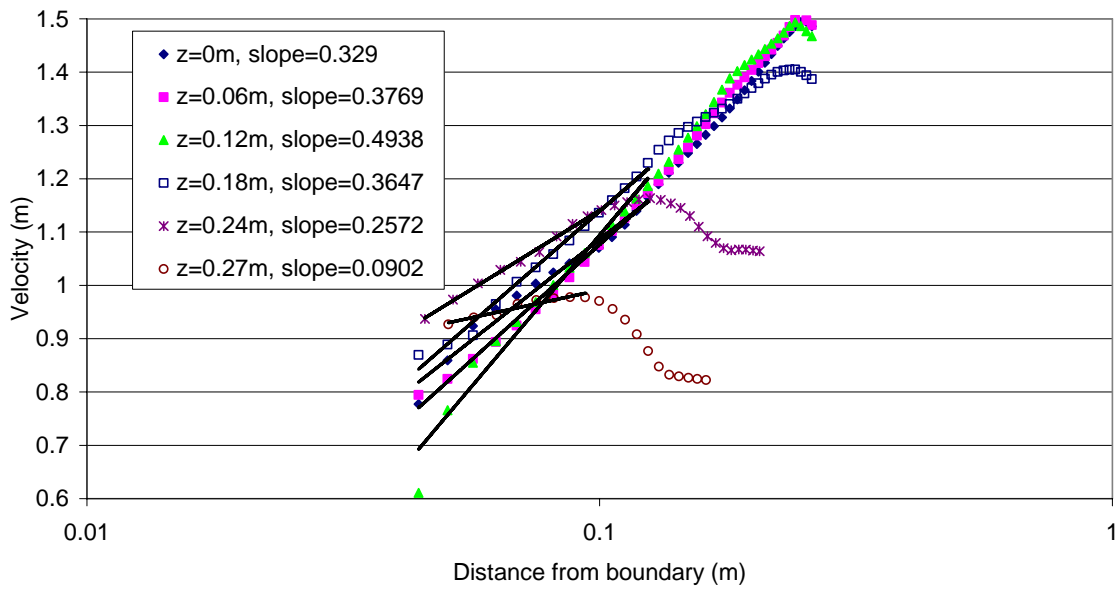


Figure D - 50: Logarithmic variation of velocity profiles for S1Q254, XS14

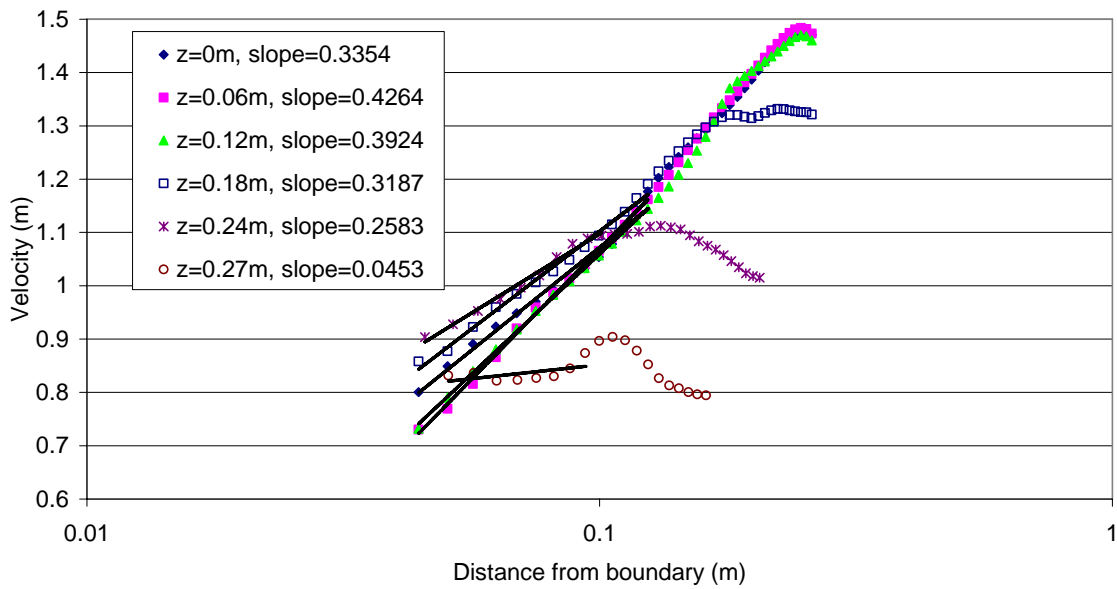


Figure D - 51: Logarithmic variation of velocity profiles for S1Q254, XS17

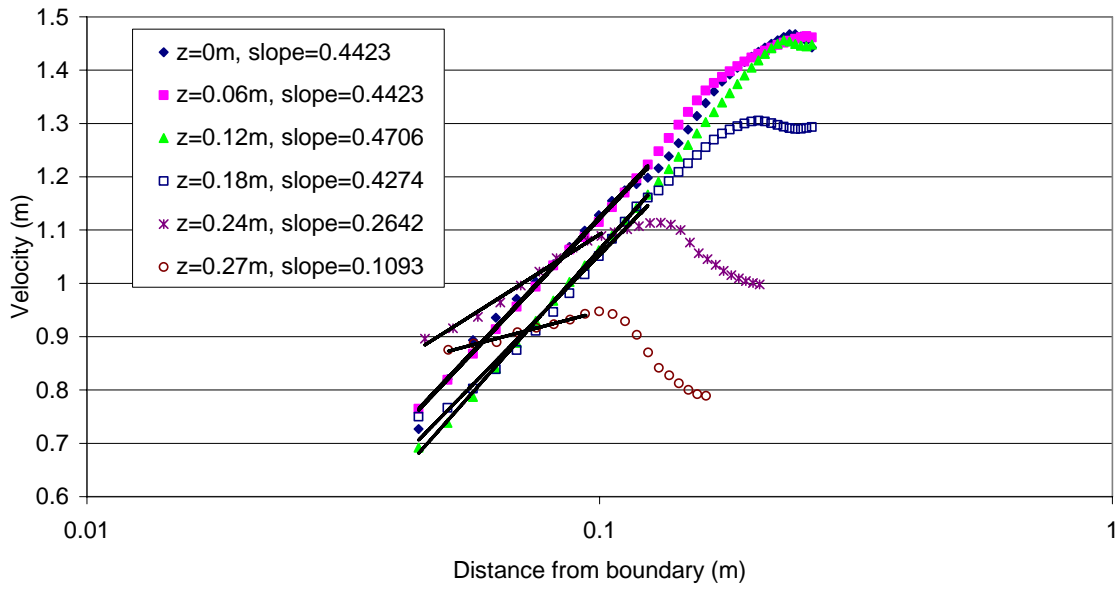


Figure D - 52: Logarithmic variation of velocity profiles for S1Q254, XS20

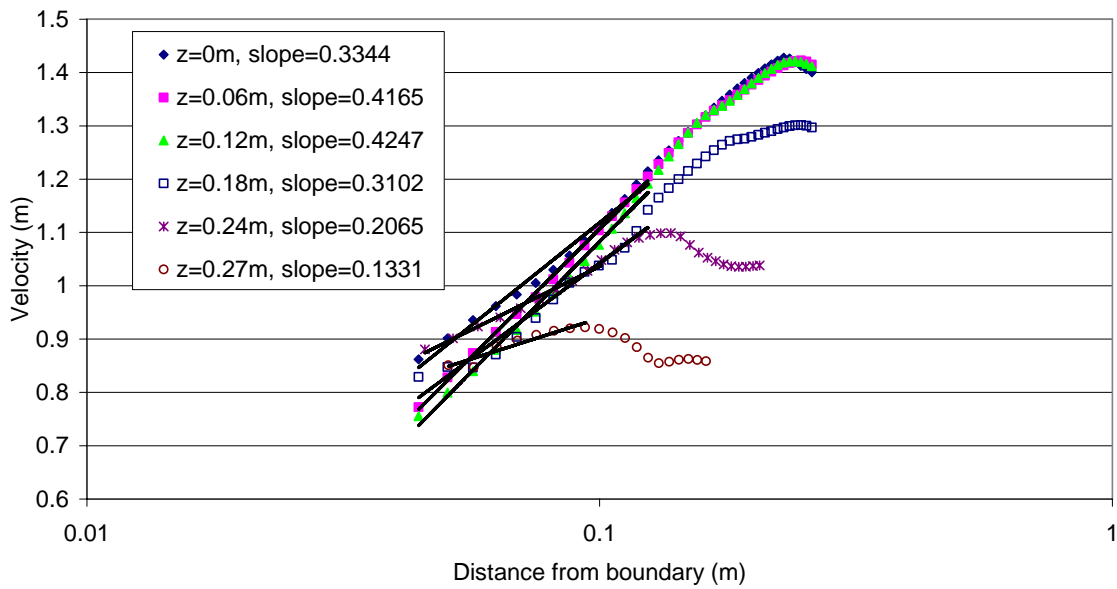


Figure D - 53: Logarithmic variation of velocity profiles for S1Q254, XS23

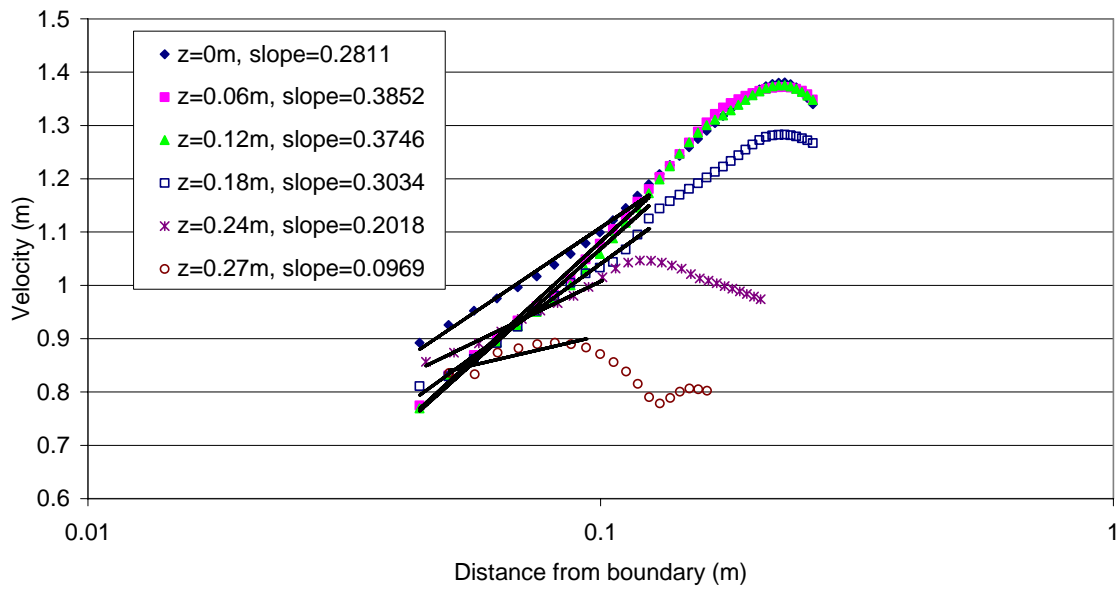


Figure D - 54: Logarithmic variation of velocity profiles for S1Q254, XS26

Appendix E – Log Law Plots for k_s Determination

S0Q64

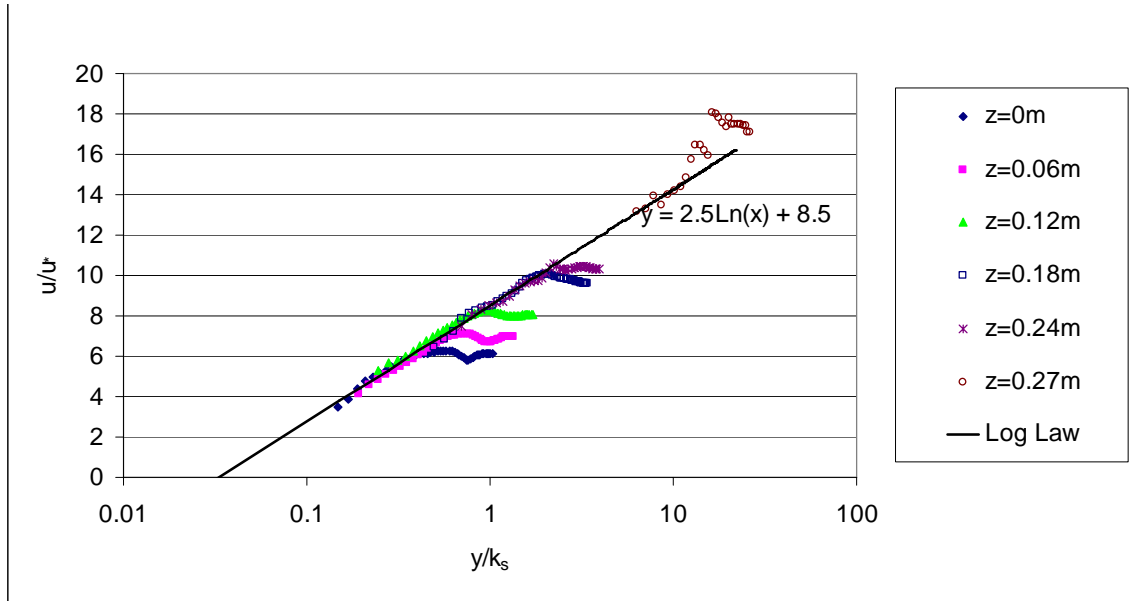


Figure E - 1: Log Law plot for S0Q64, XS6

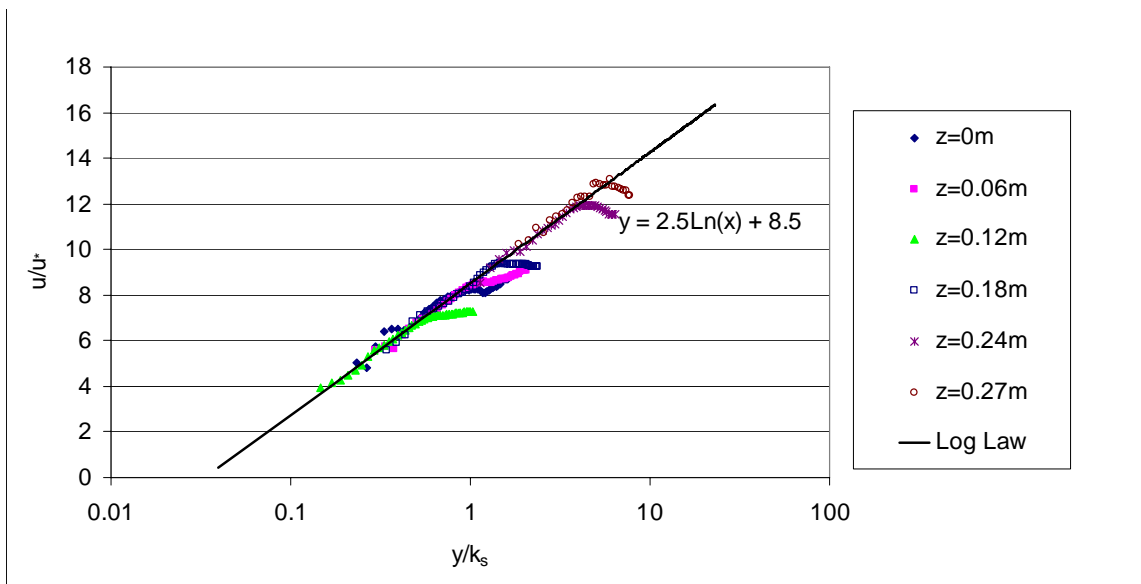


Figure E - 2: Log Law plot for S0Q64, XS8

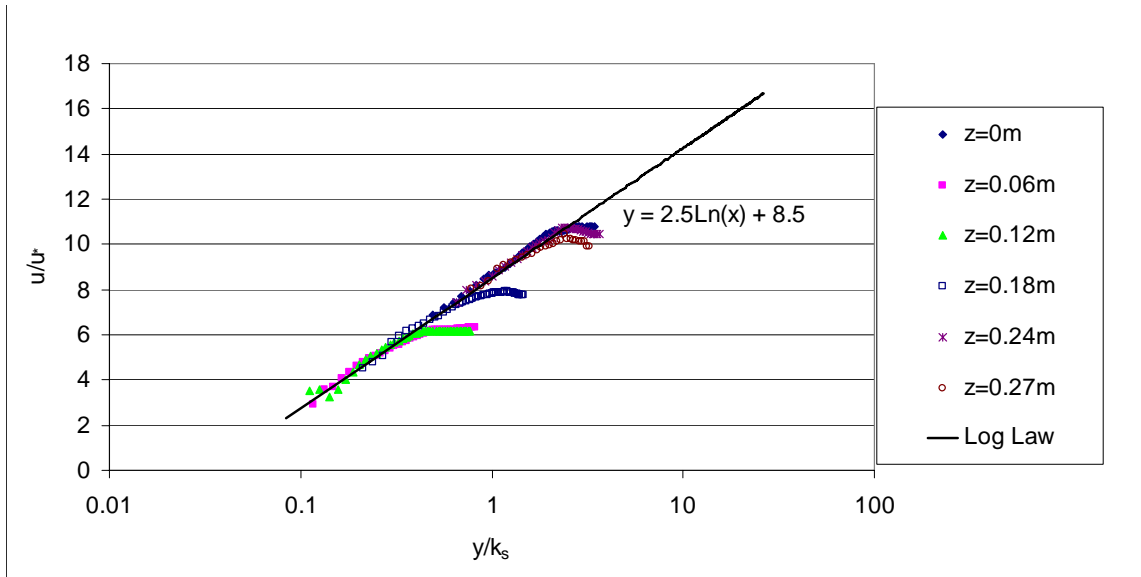


Figure E - 3: Log Law plot for S0Q64, XS10

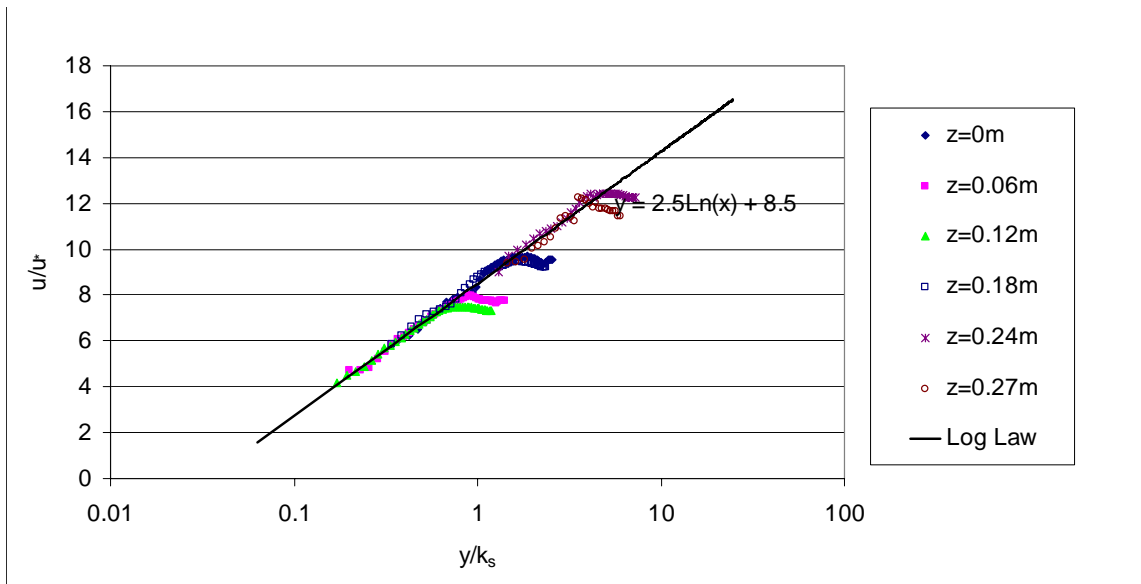


Figure E - 4: Log Law plot for S0Q64, XS12

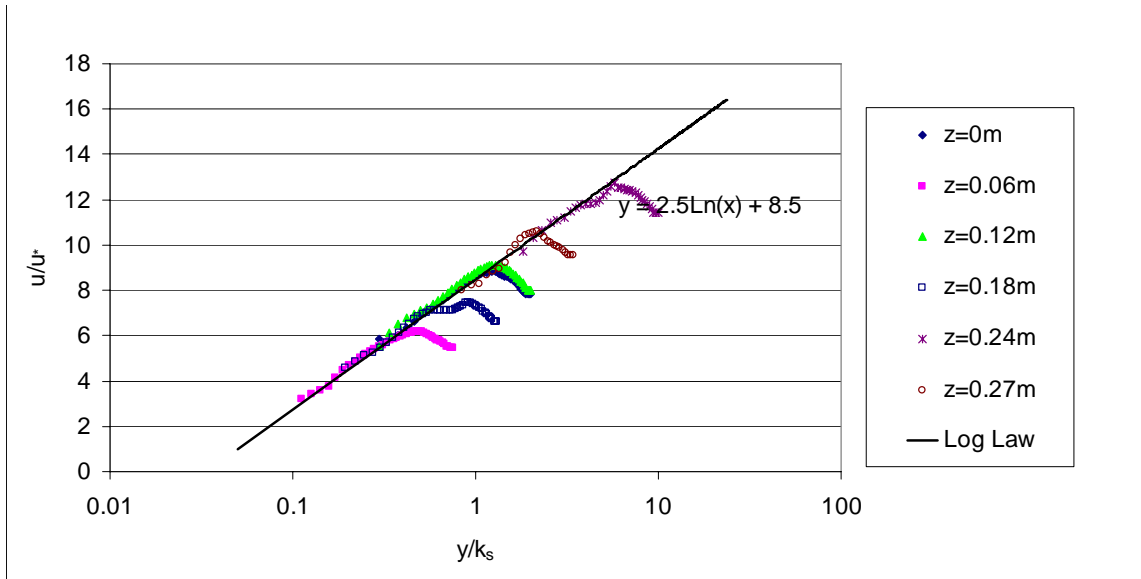


Figure E - 5: Log Law plot for S0Q64, XS14

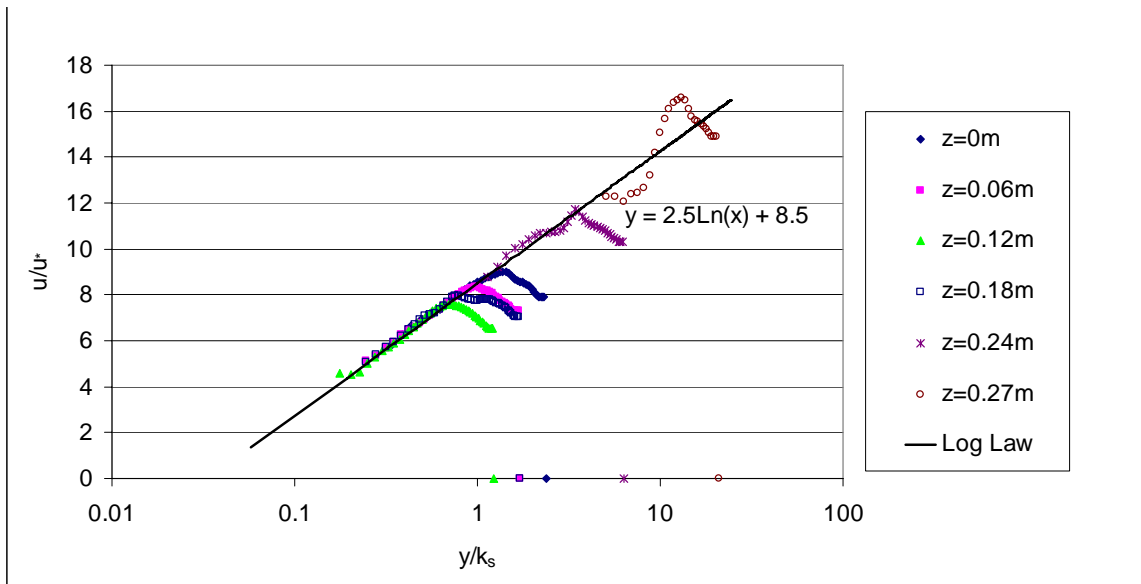


Figure E - 6: Log Law plot for S0Q64, XS17

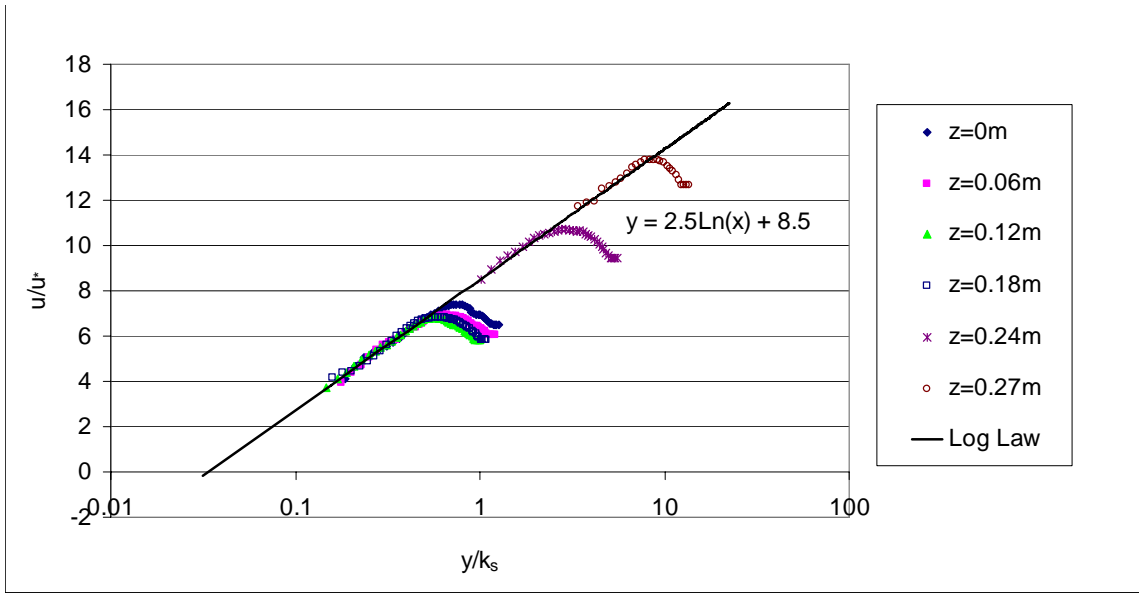


Figure E - 7: Log Law plot for S0Q64, XS20

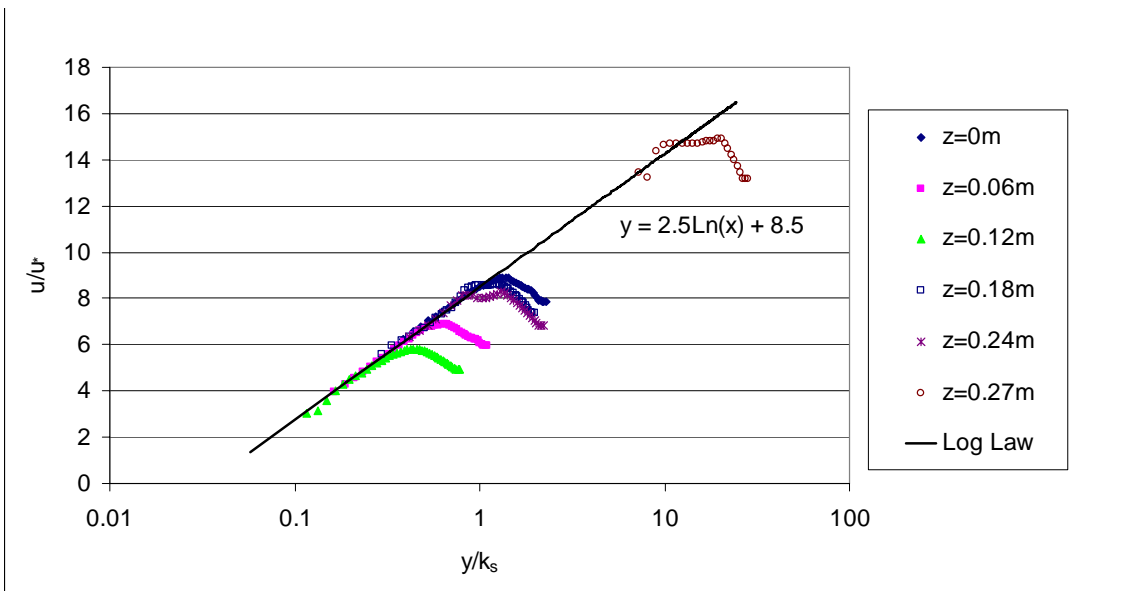


Figure E - 8: Log Law plot for S0Q64, XS23

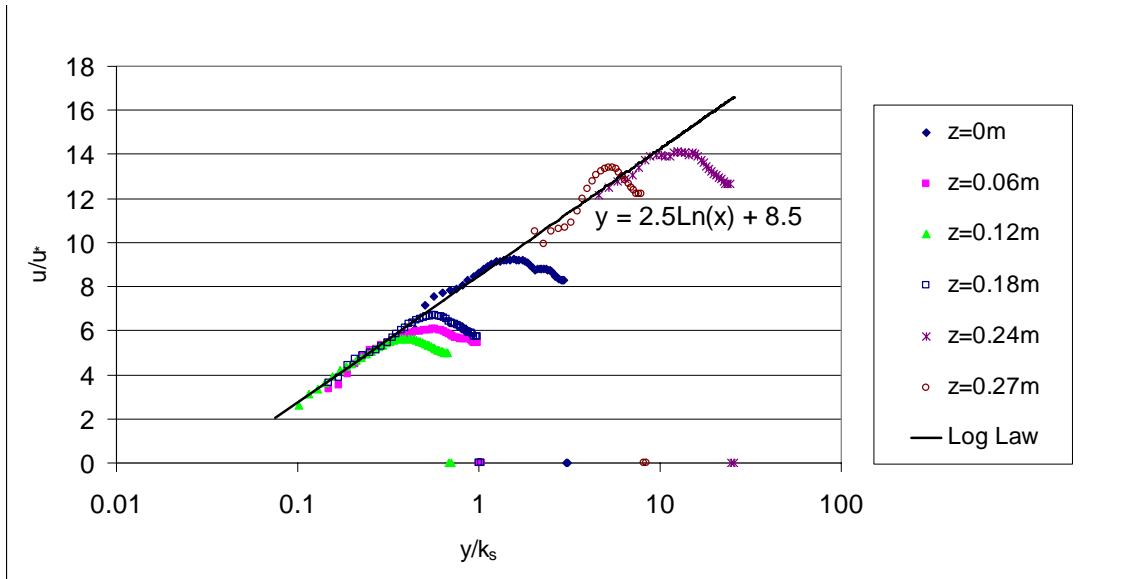


Figure E - 9: Log Law plot for S0Q64, XS26

S0Q186

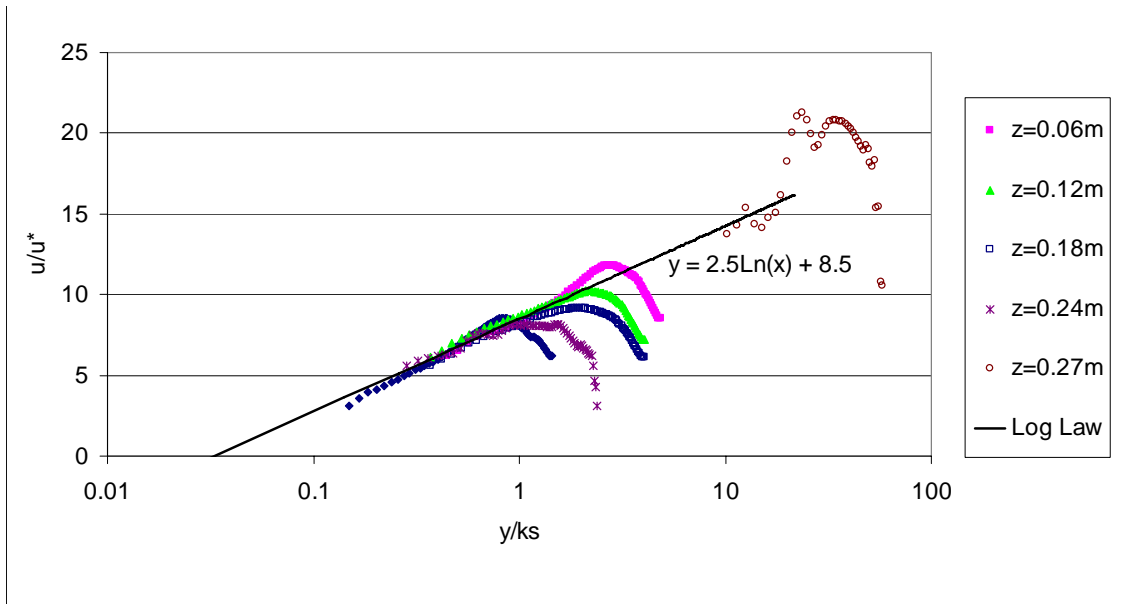


Figure E - 10: Log Law plot for S0Q186, XS6

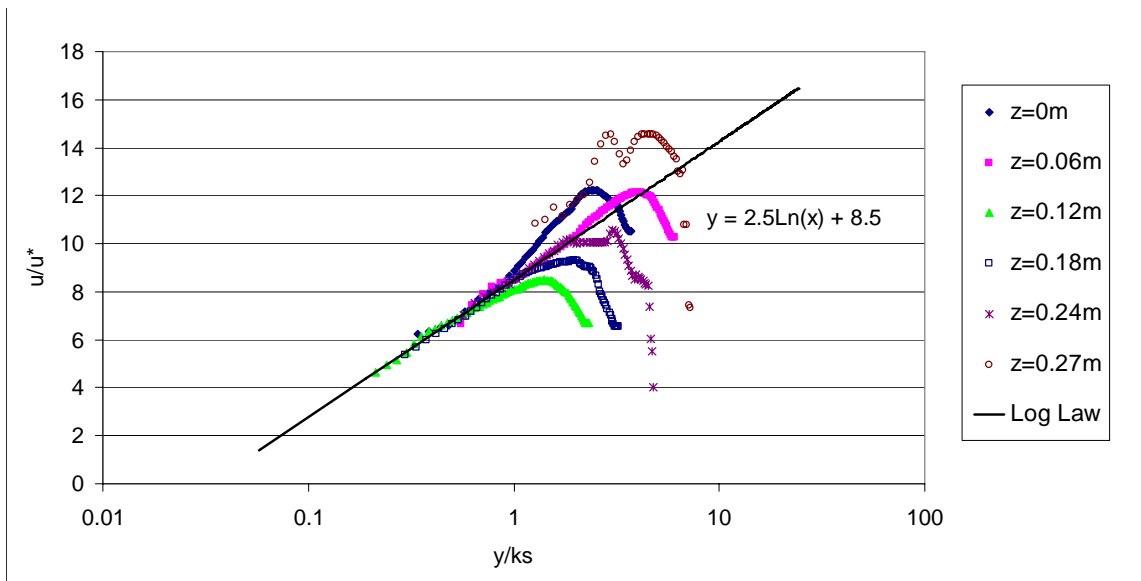


Figure E - 11: Log Law plot for S0Q186, XS8

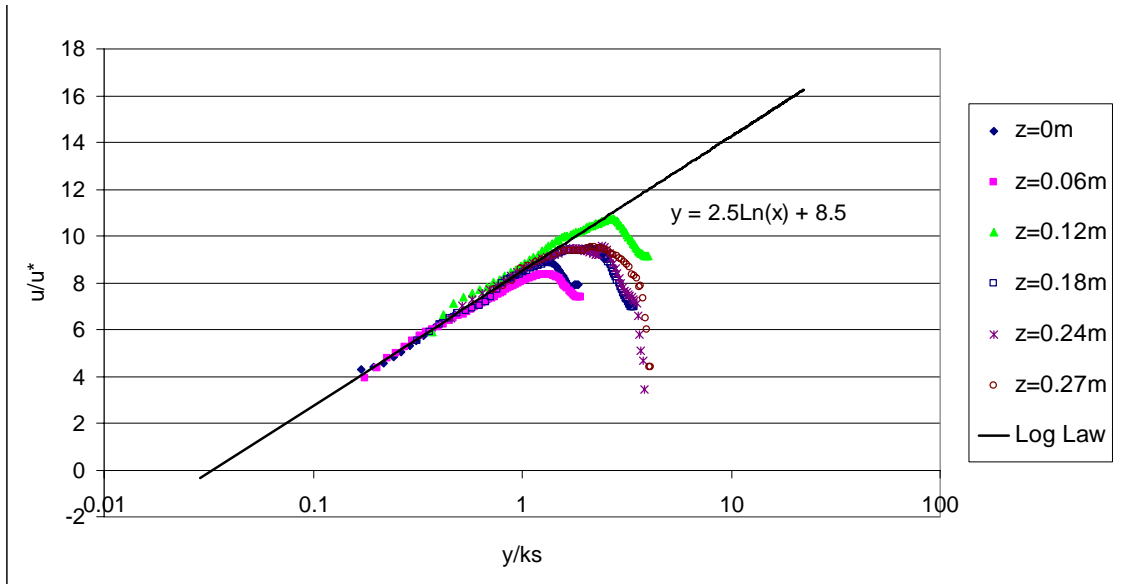


Figure E - 12: Log Law plot for S0Q186, XS10

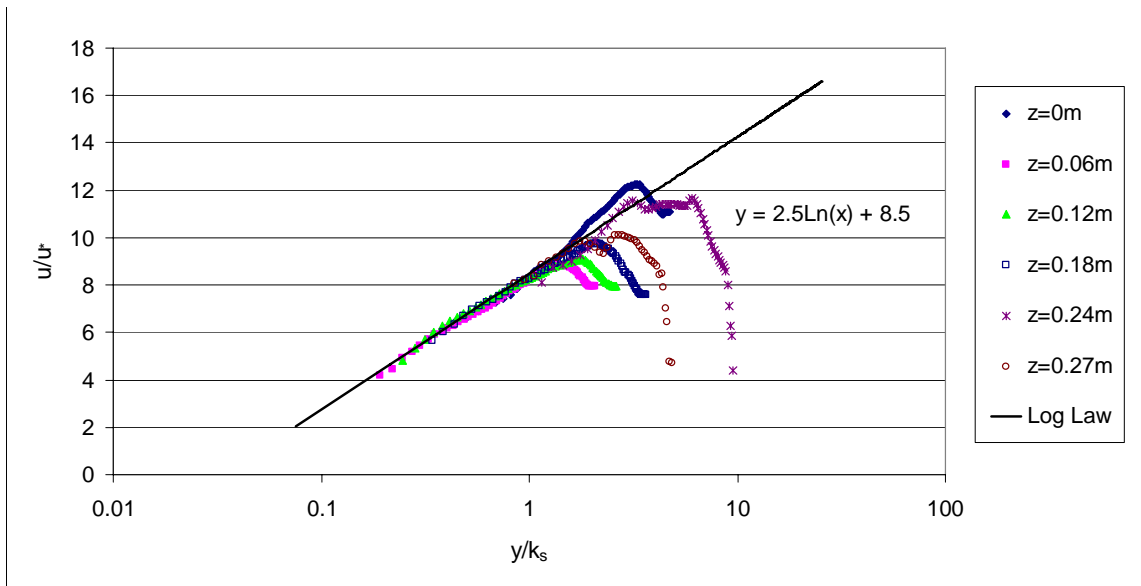


Figure E - 13: Log Law plot for S0Q186, XS12

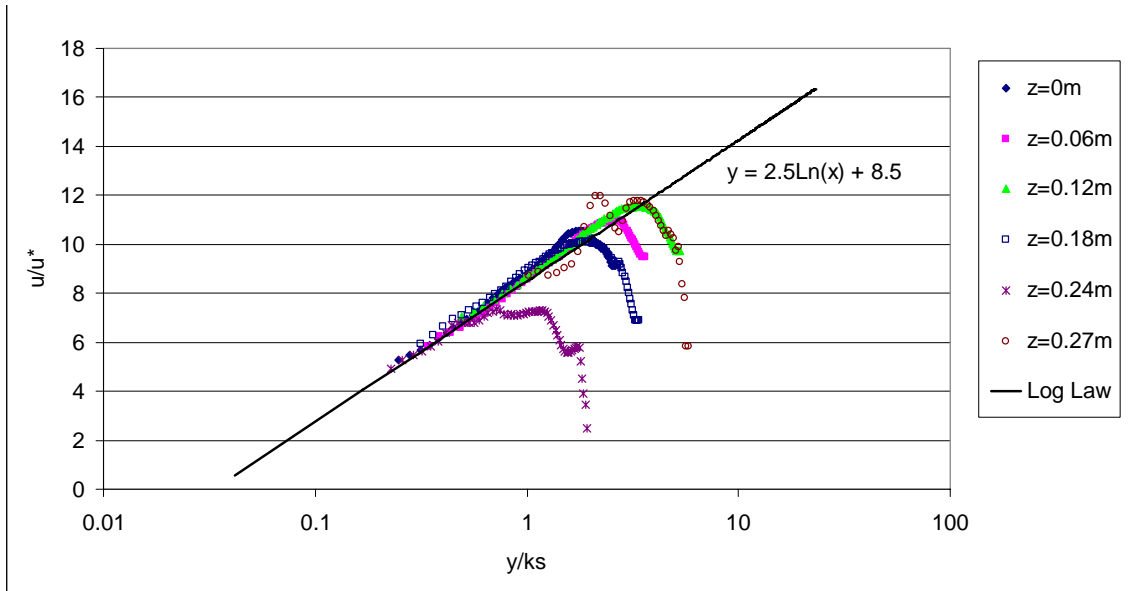


Figure E - 14: Log Law plot for S0Q186, XS14

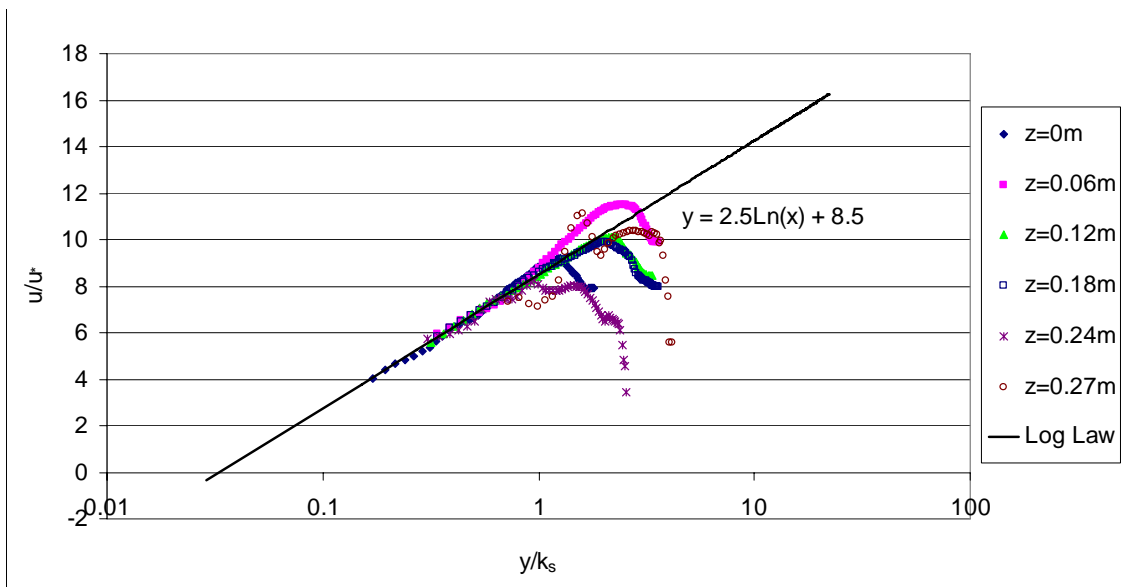


Figure E - 15: Log Law plot for S0Q186, XS17

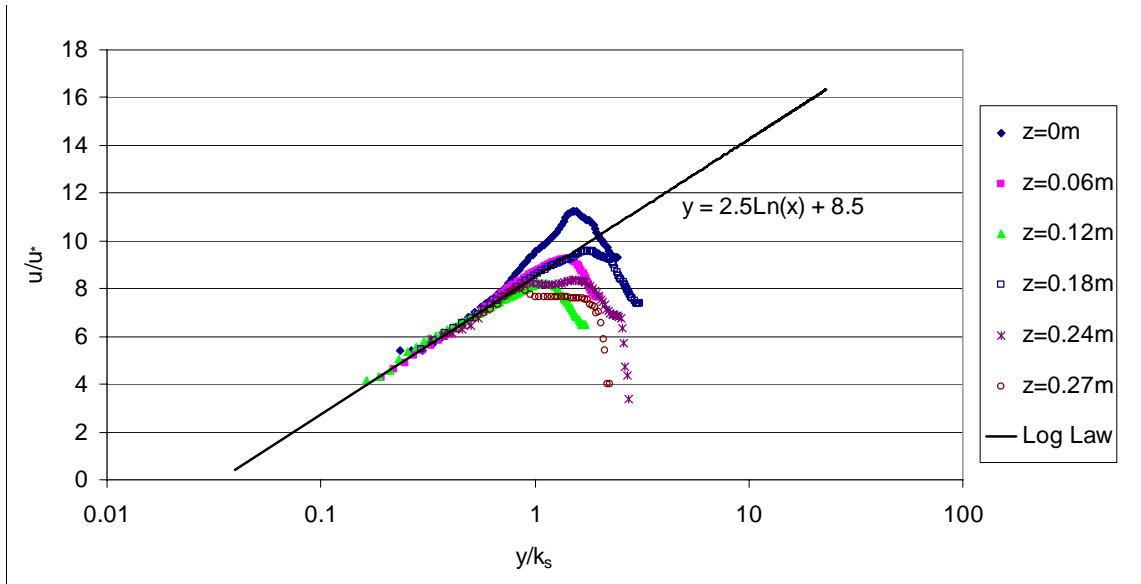


Figure E - 16: Log Law plot for S0Q186, XS20

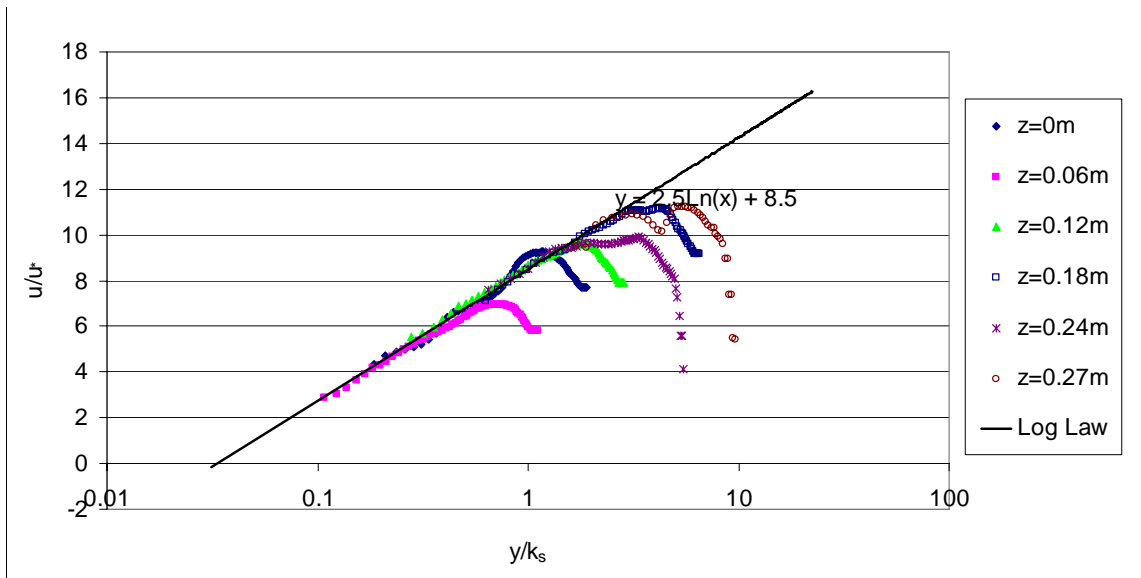


Figure E - 17: Log Law plot for S0Q186, XS23

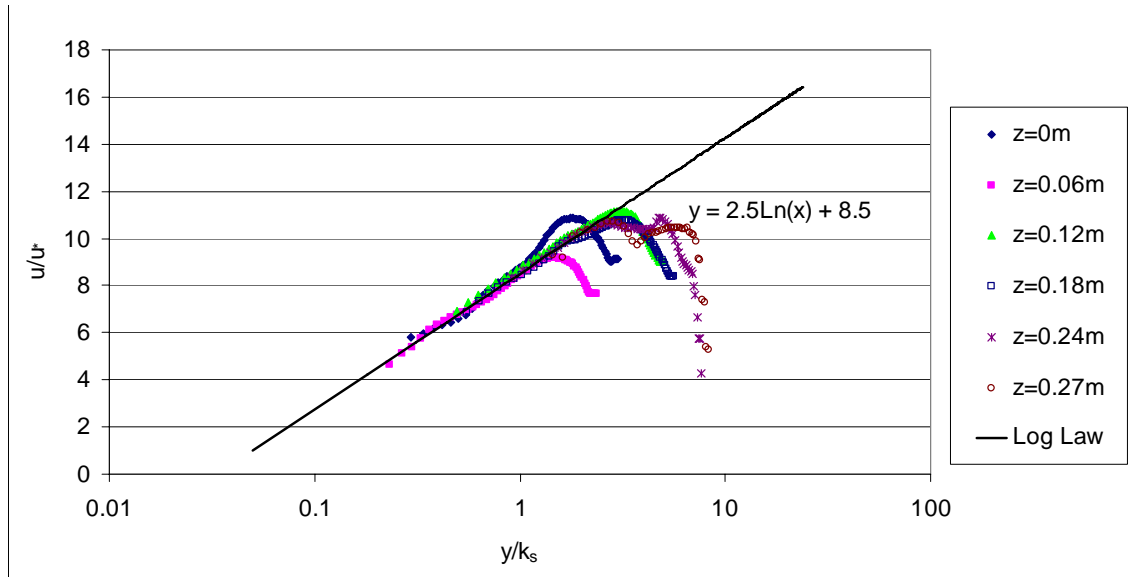


Figure E - 18: Log Law plot for S0Q186, XS26

S5Q145

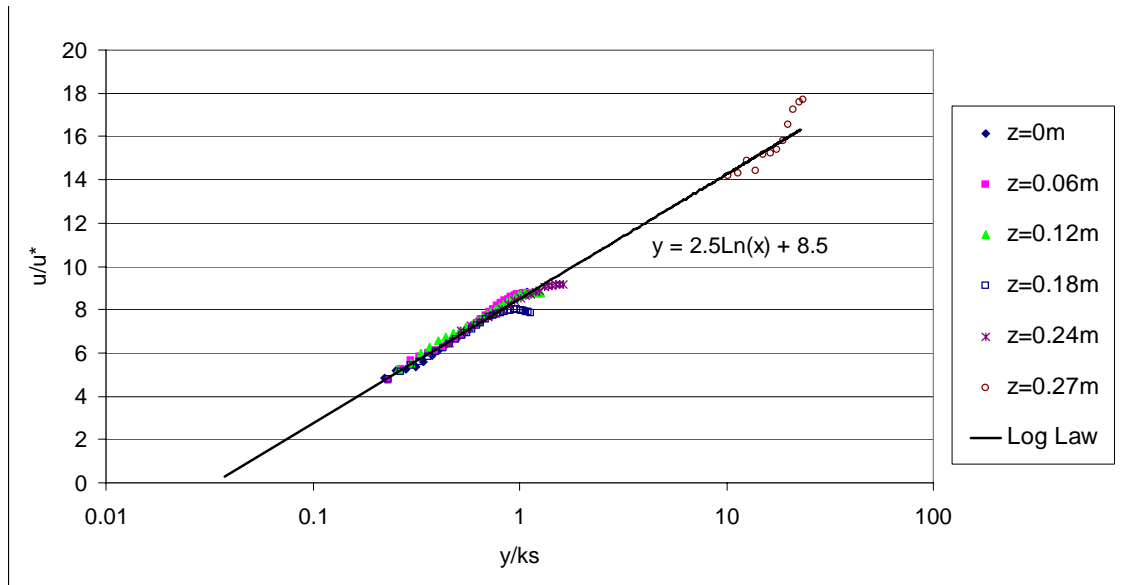


Figure E - 19: Log Law plot for S5Q145, XS6

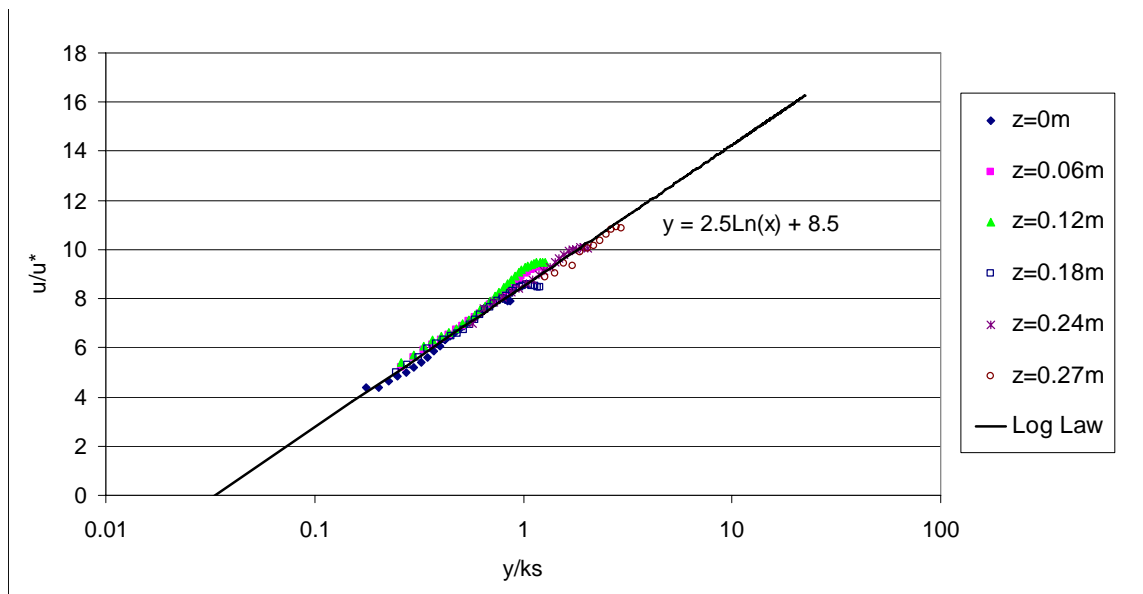


Figure E - 20: Log Law plot for S5Q145, XS8

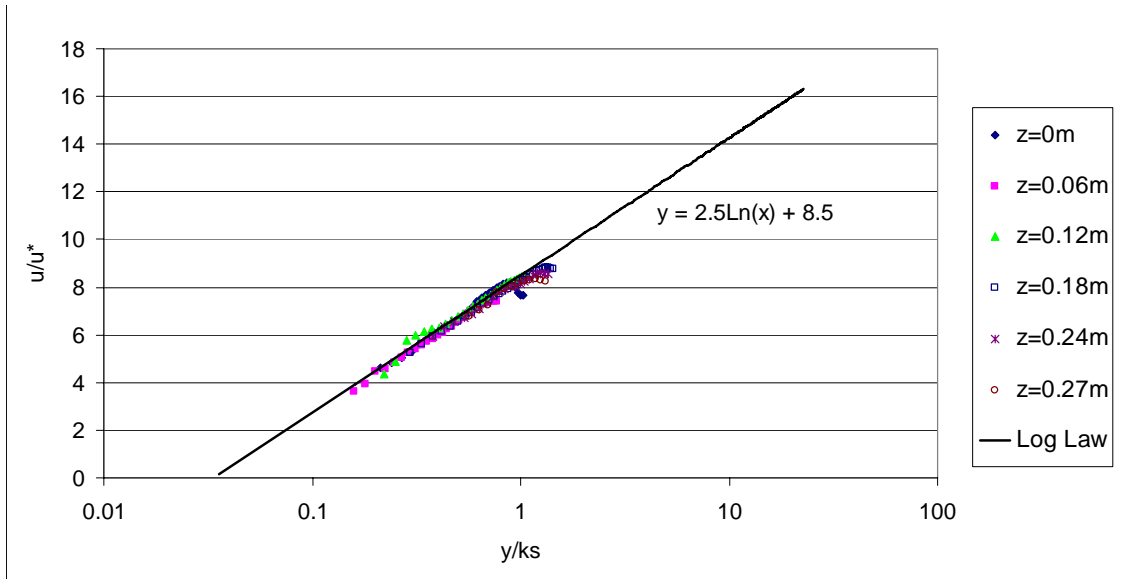


Figure E - 21: Log Law plot for S5Q145, XS10

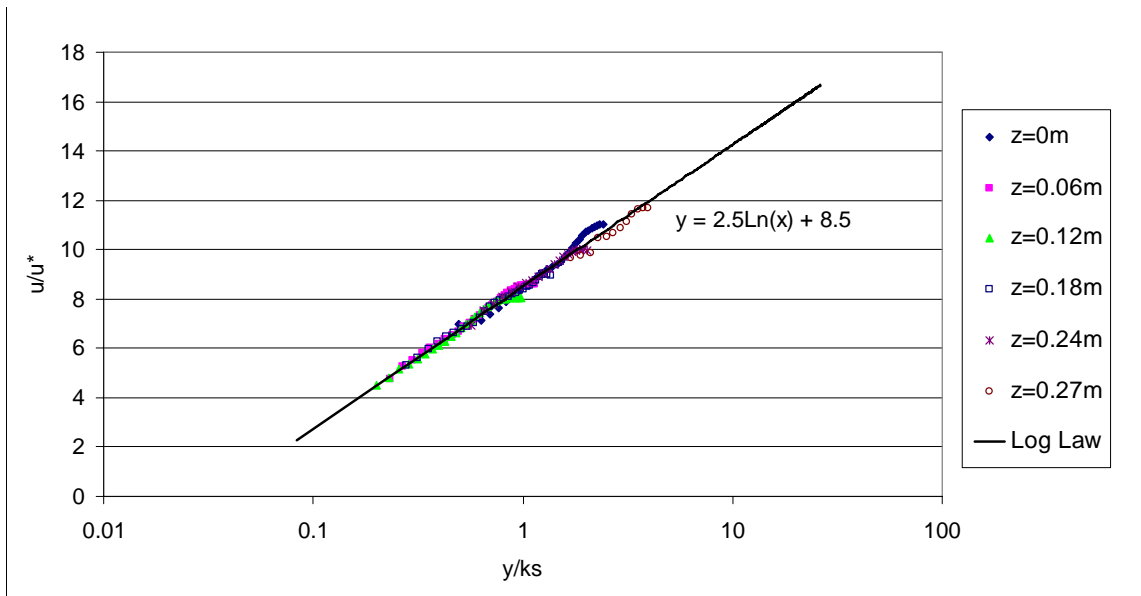


Figure E - 22: Log Law plot for S5Q145, XS12

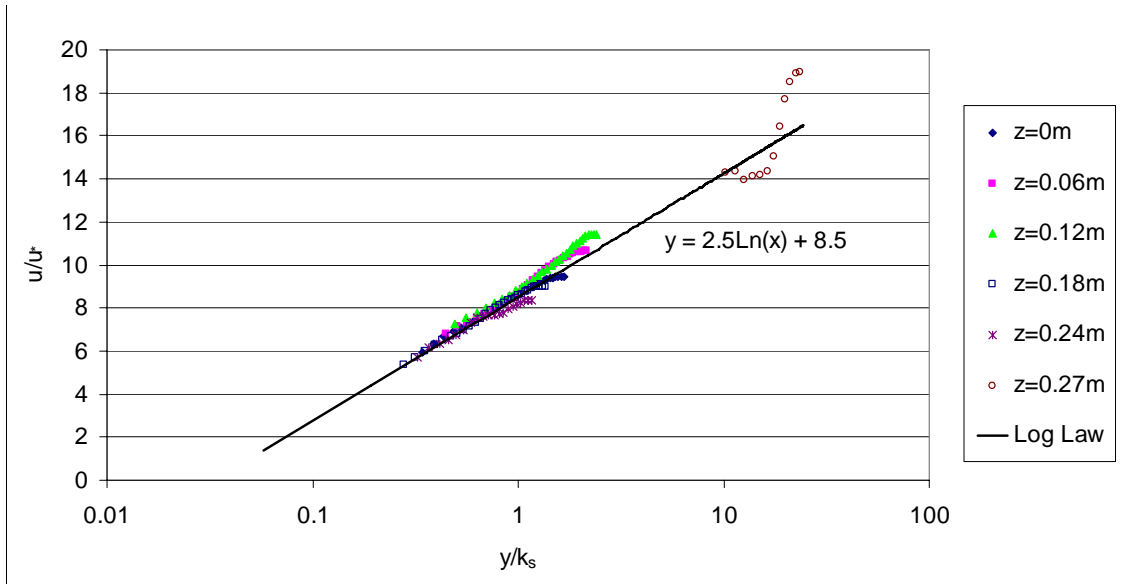


Figure E - 23: Log Law plot for S5Q145, XS14

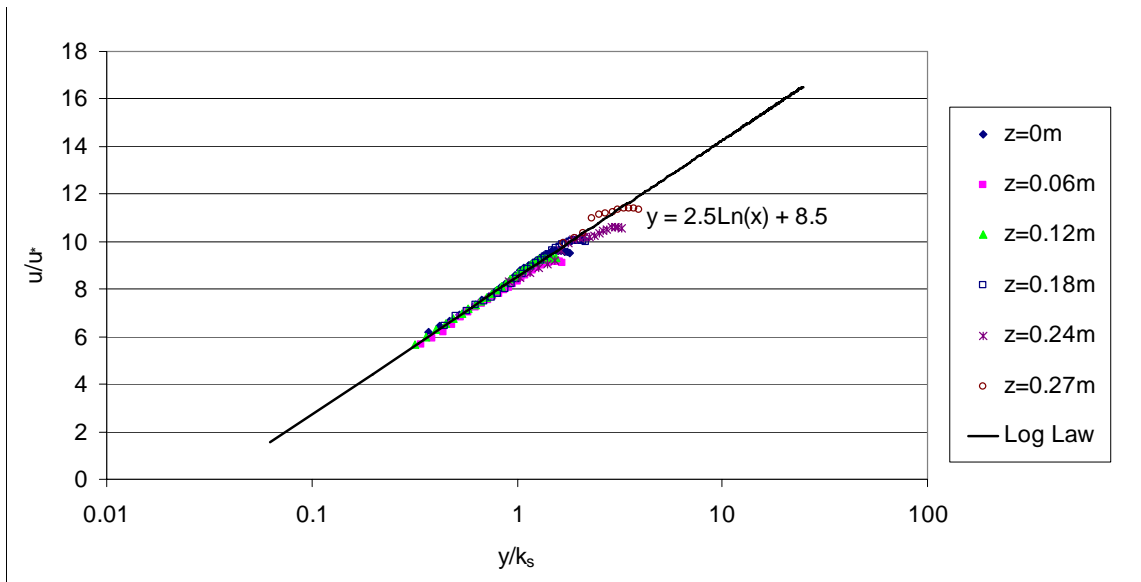


Figure E - 24: Log Law plot for S5Q145, XS17

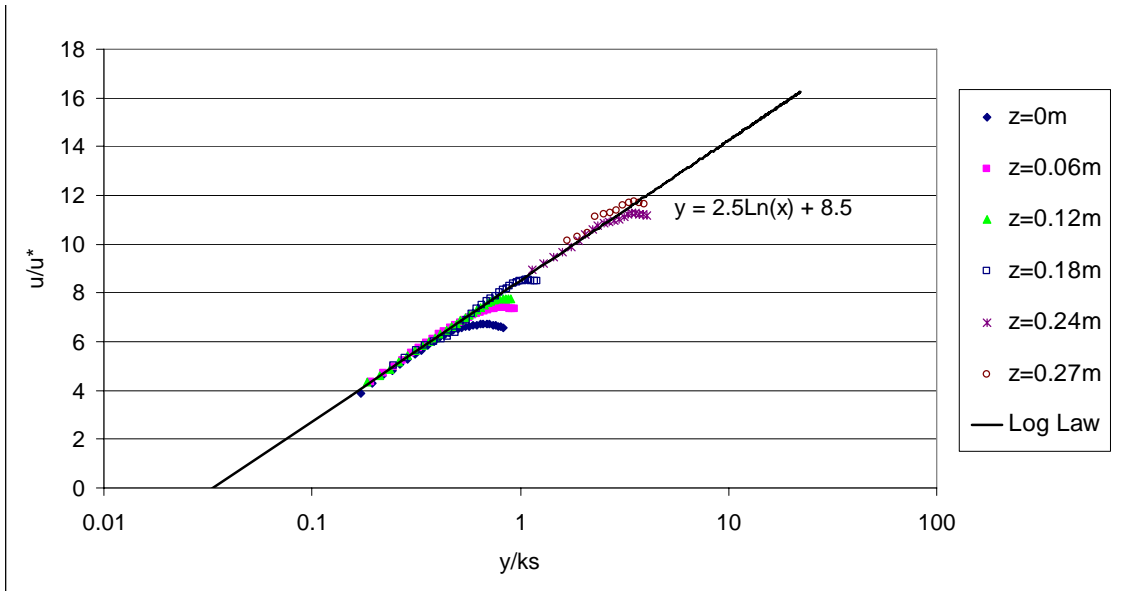


Figure E - 25: Log Law plot for S5Q145, XS20

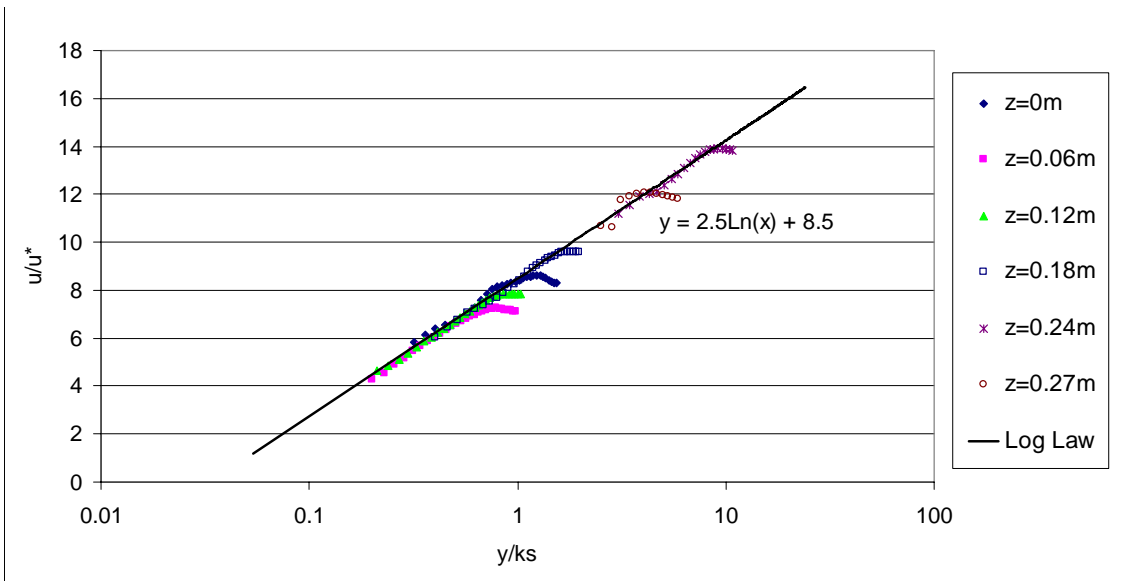


Figure E - 26: Log Law plot for S5Q145, XS23

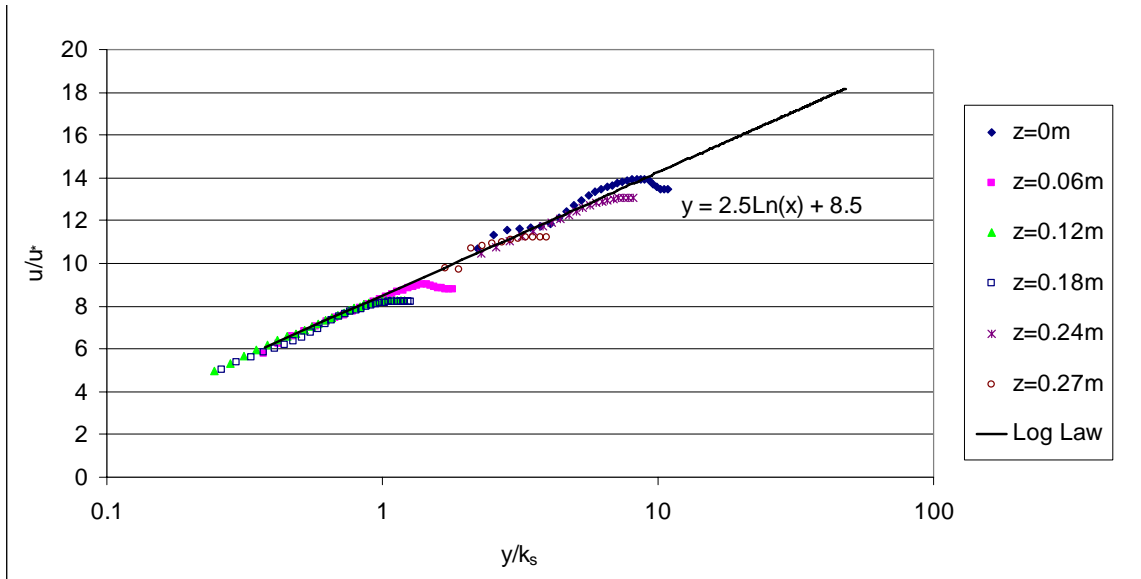


Figure E - 27: Log Law plot for S5Q145, XS26

S5Q221

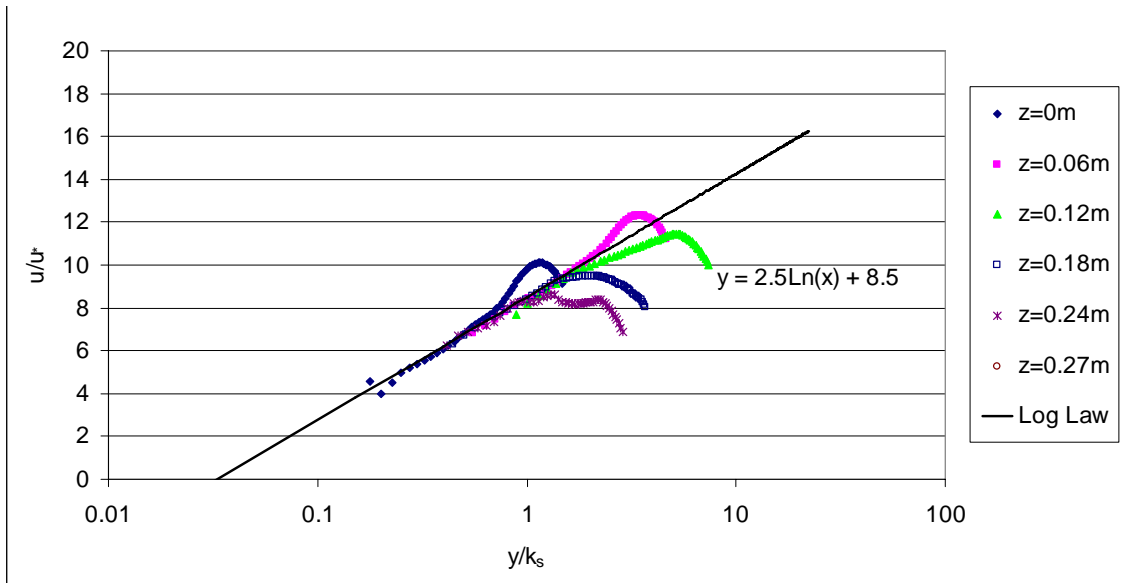


Figure E - 28: Log Law plot for S5Q221, XS6

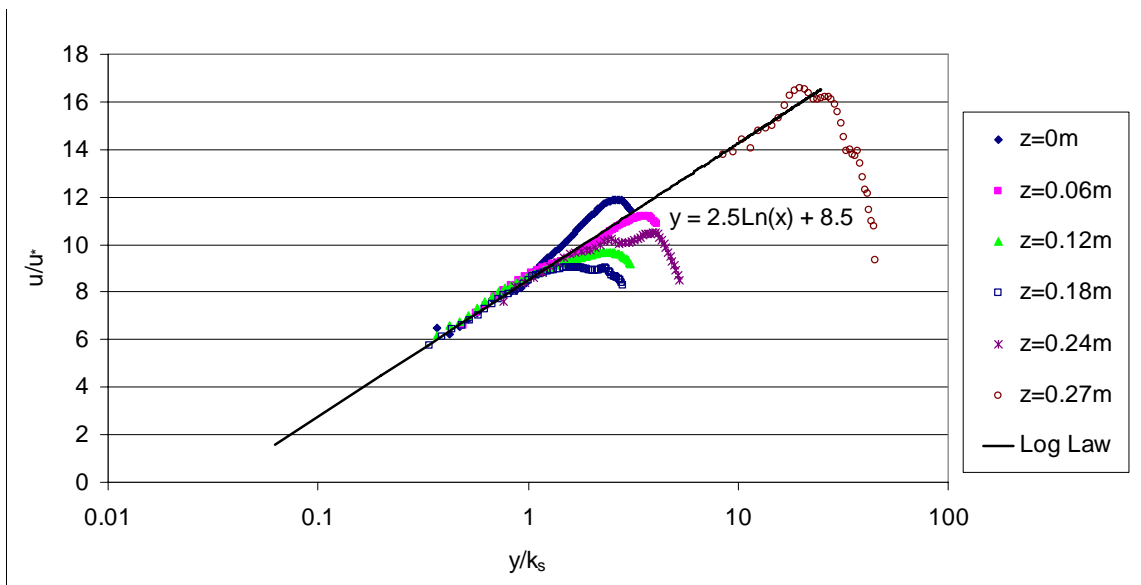


Figure E - 29: Log Law plot for S5Q221, XS8

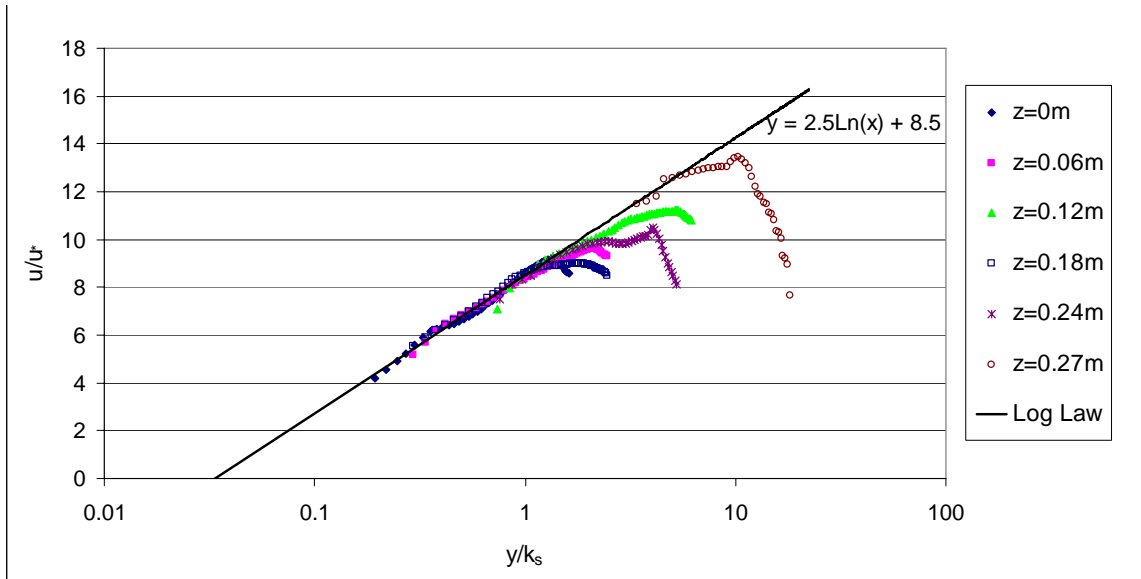


Figure E - 30: Log Law plot for S5Q221, XS10

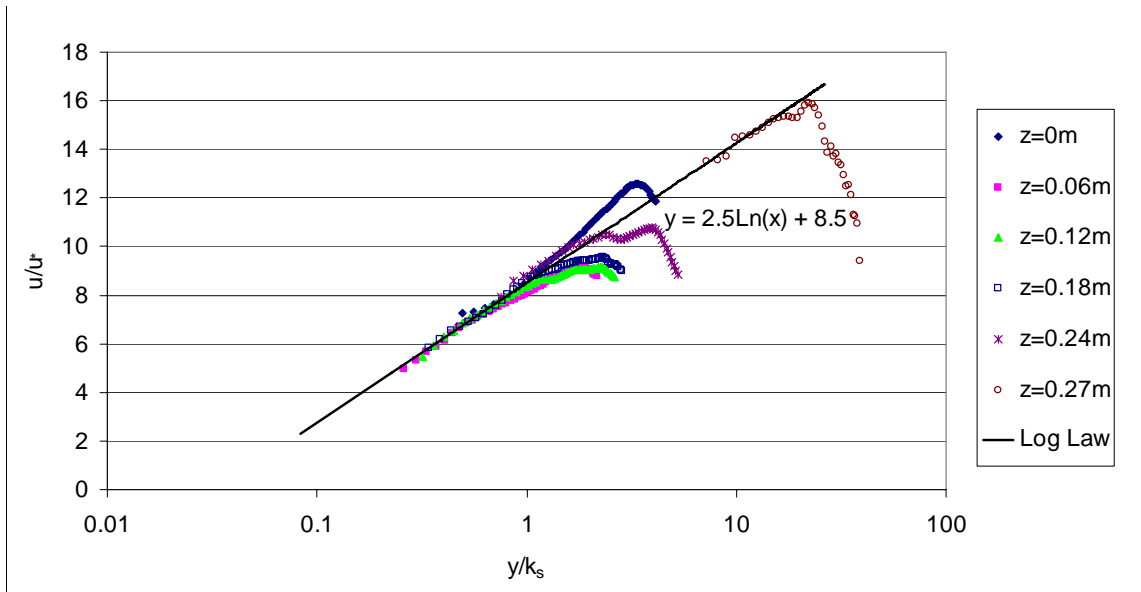


Figure E - 31: Log Law plot for S5Q221, XS12

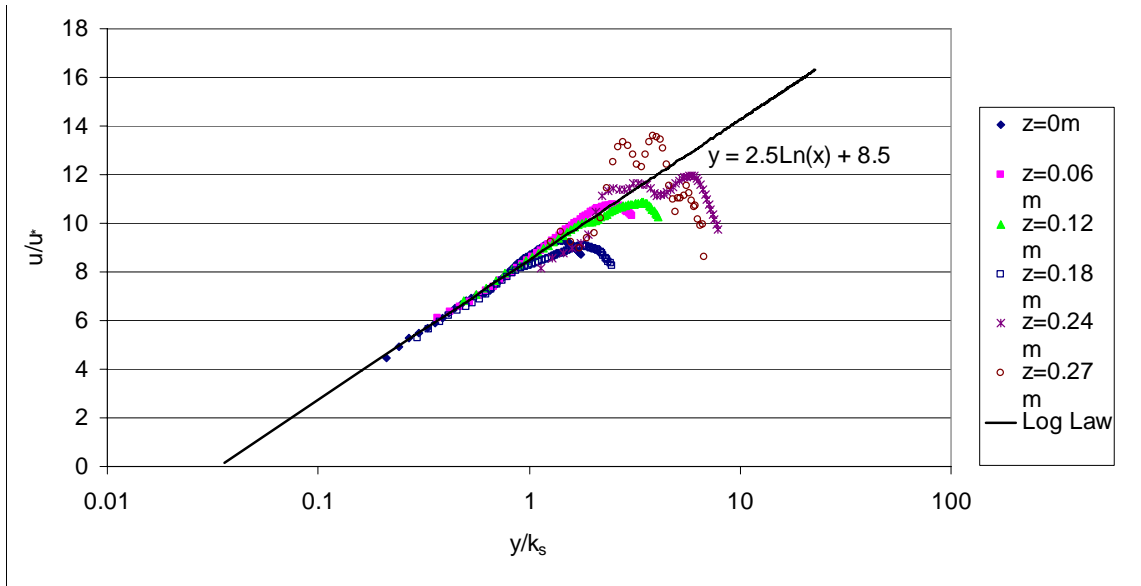


Figure E - 32: Log Law plot for S5Q221, XS14

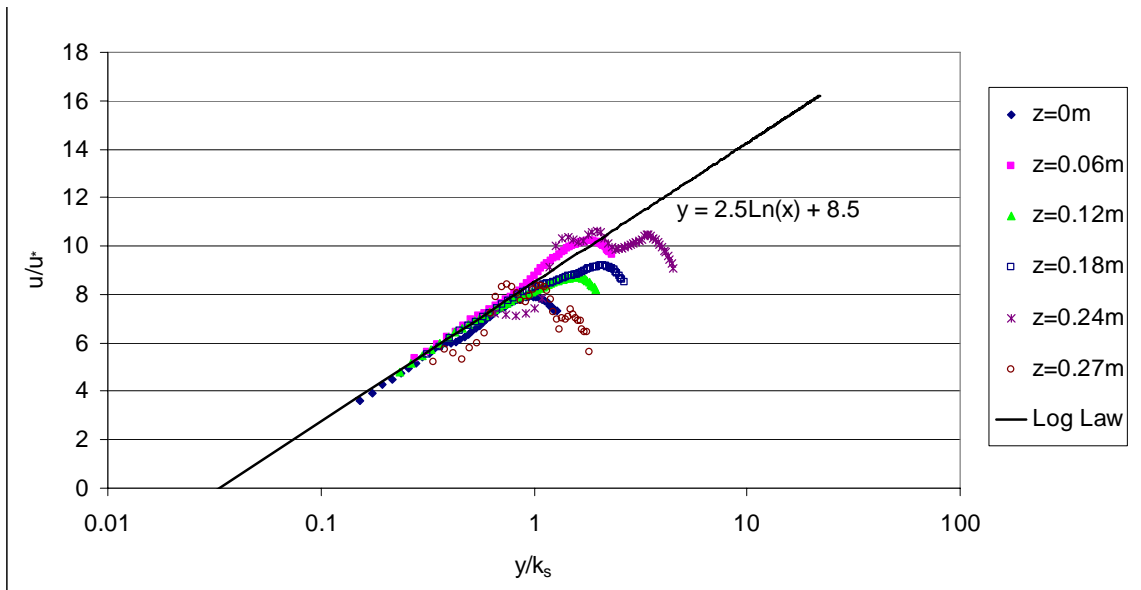


Figure E - 33: Log Law plot for S5Q221, XS17

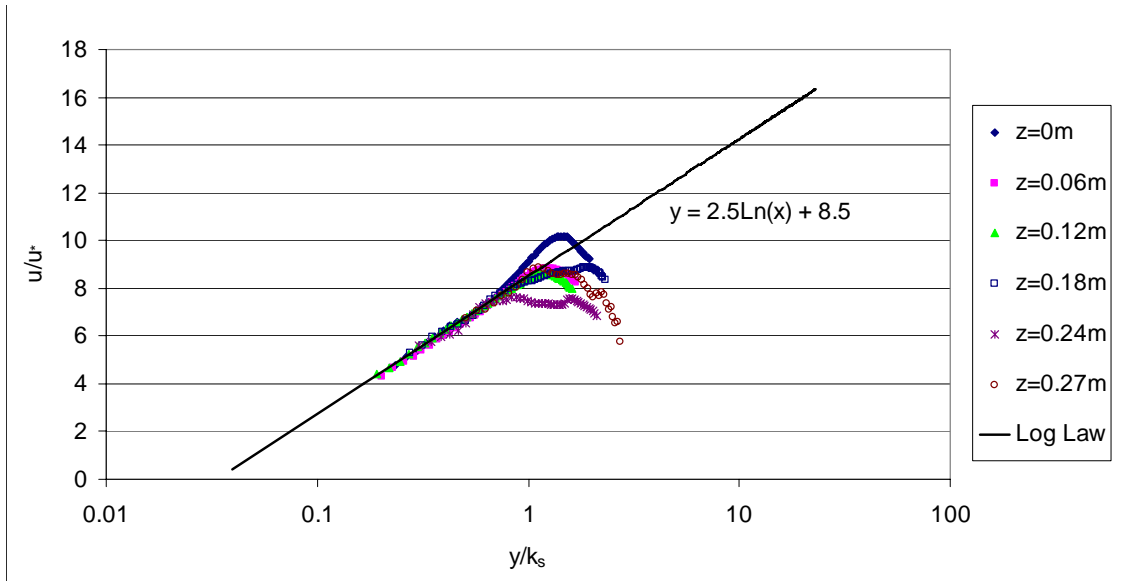


Figure E - 34: Log Law plot for S5Q221, XS20

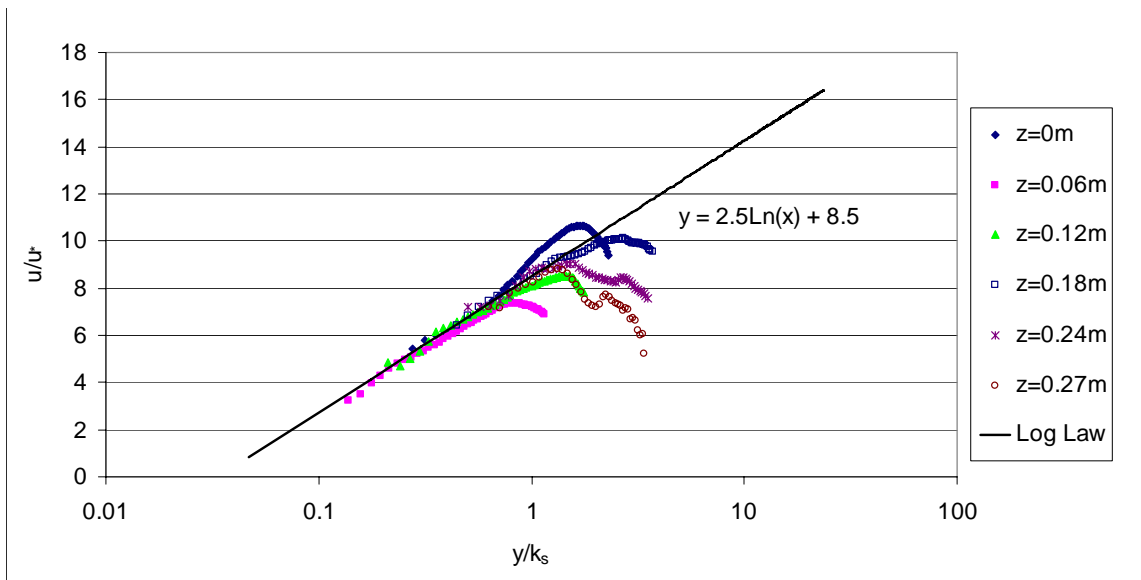


Figure E - 35: Log Law plot for S5Q221, XS23

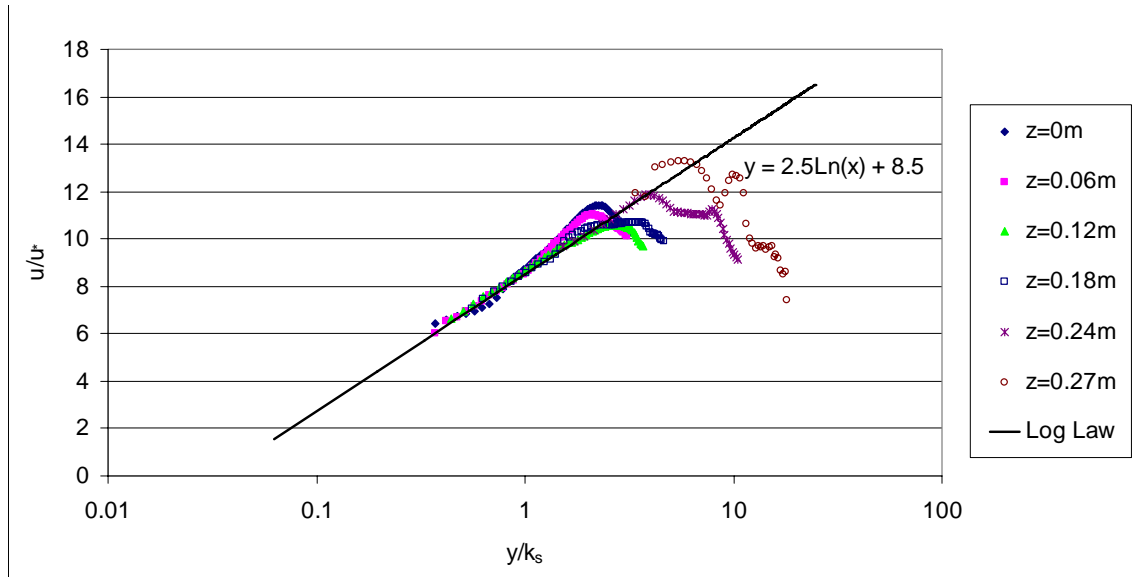


Figure E - 36: Log Law plot for S5Q221, XS26

S1Q150

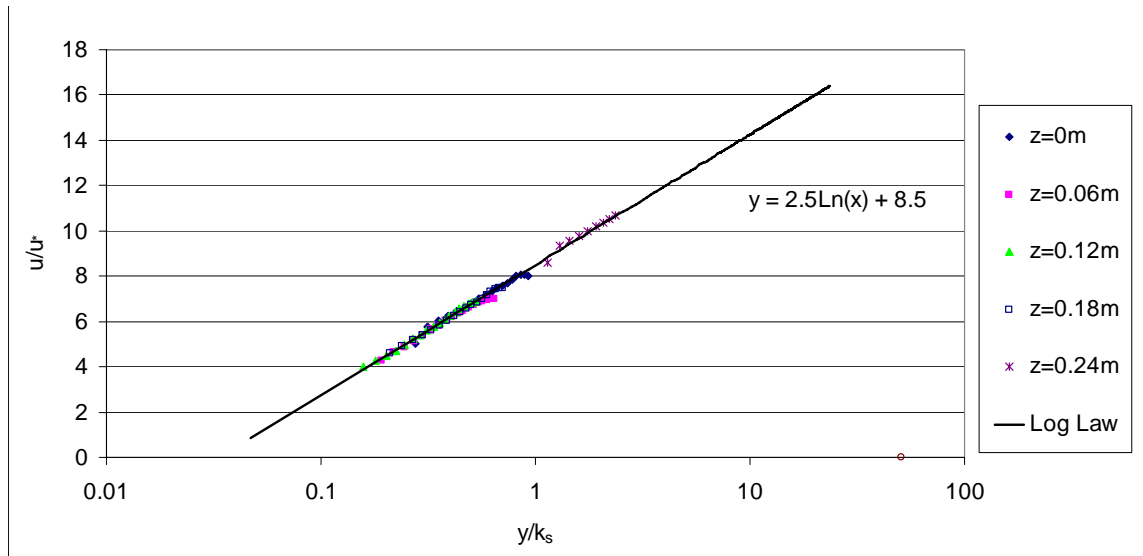


Figure E - 37: Log Law plot for S1Q150, XS6

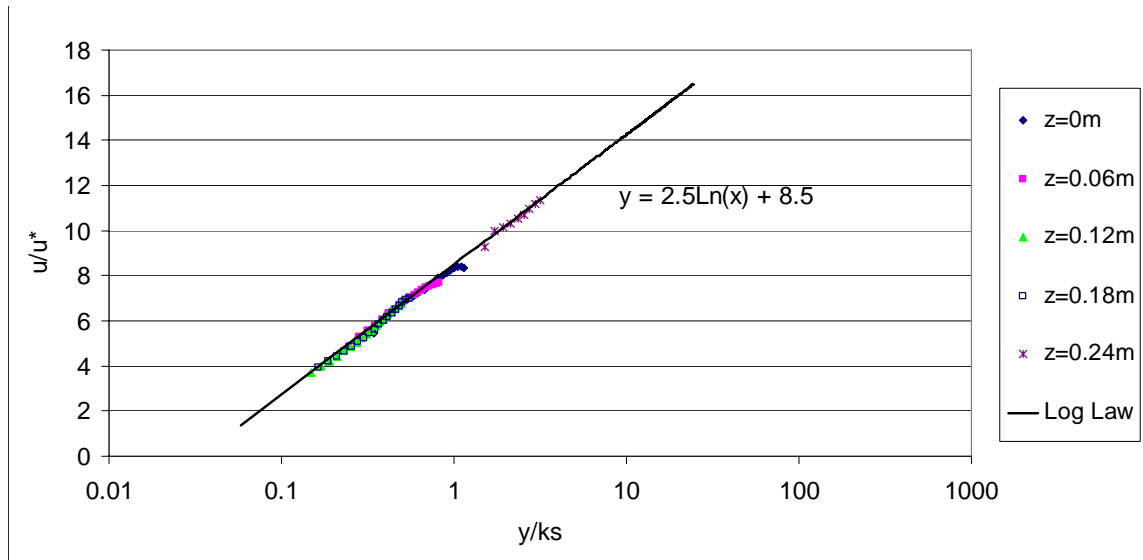


Figure E - 38: Log Law plot for S1Q150, XS8

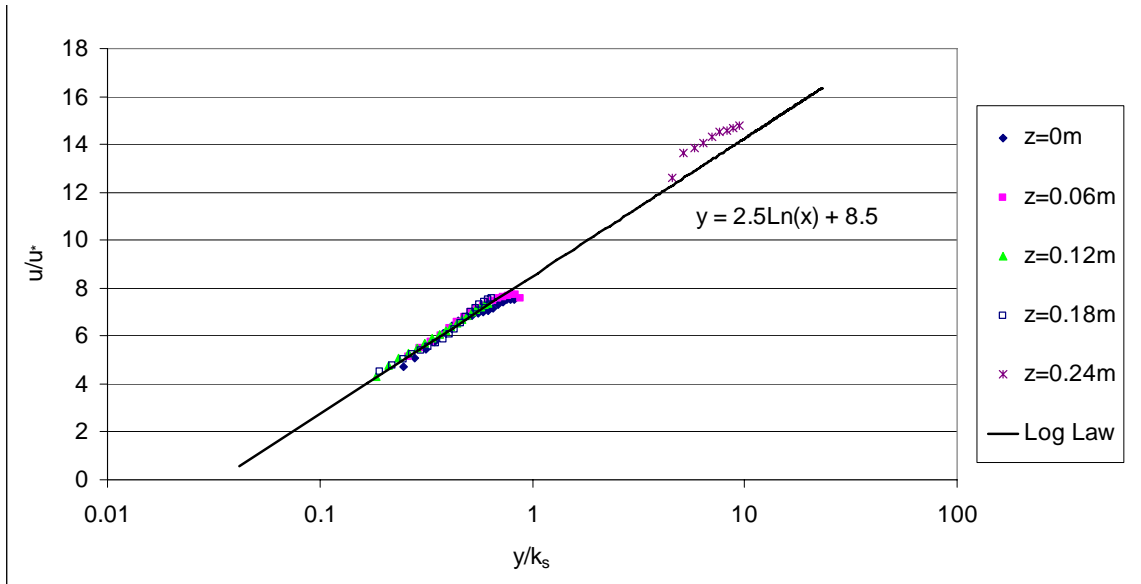


Figure E - 39: Log Law plot for S1Q150, XS10

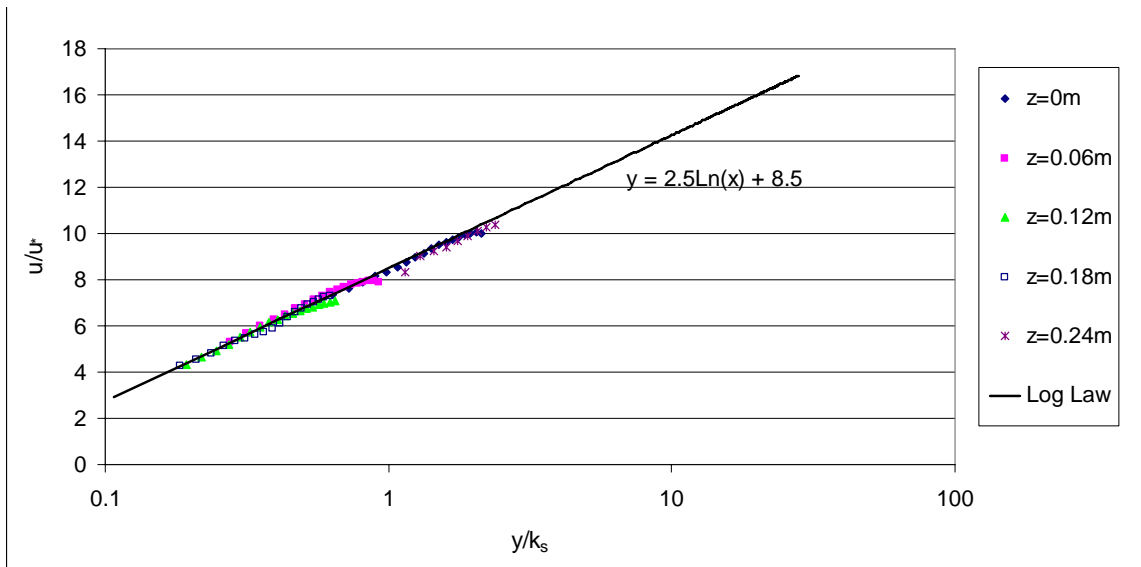


Figure E - 40: Log Law plot for S1Q150, XS12

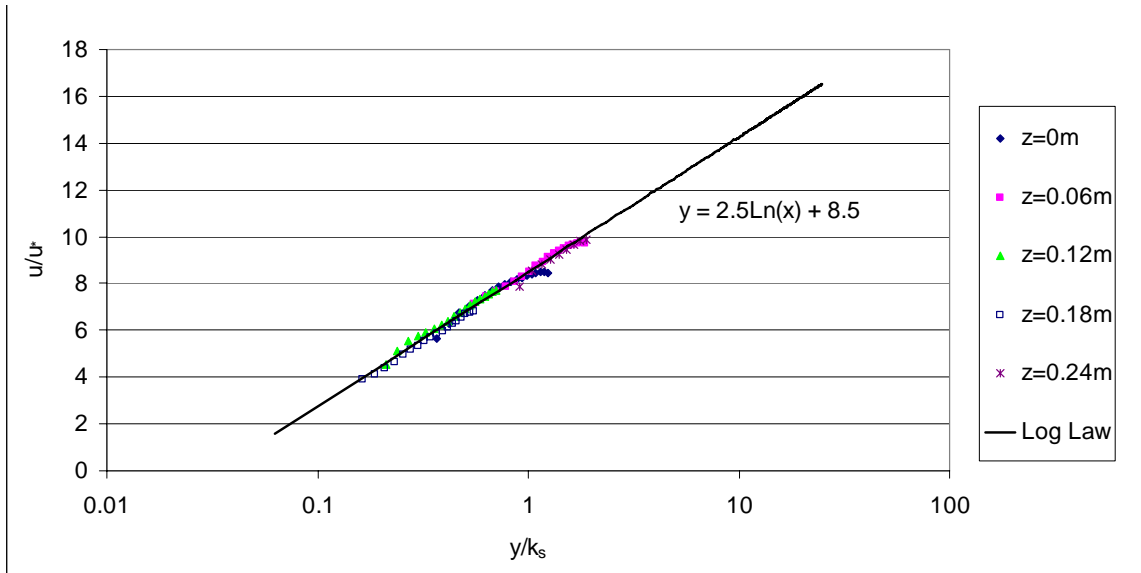


Figure E - 41: Log Law plot for S1Q150, XS14

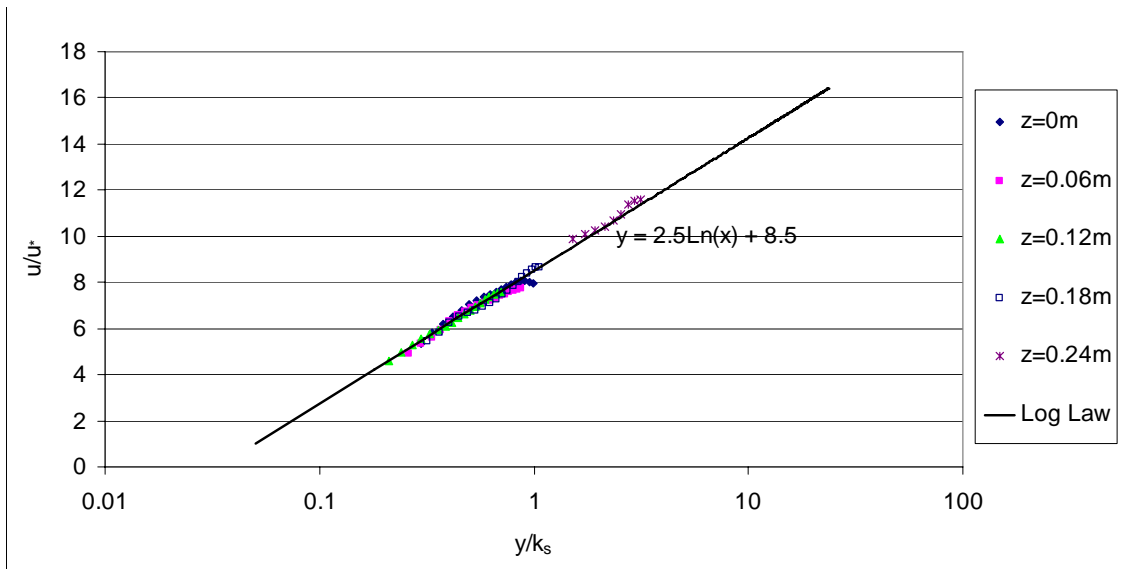


Figure E - 42: Log Law plot for S1Q150, XS17

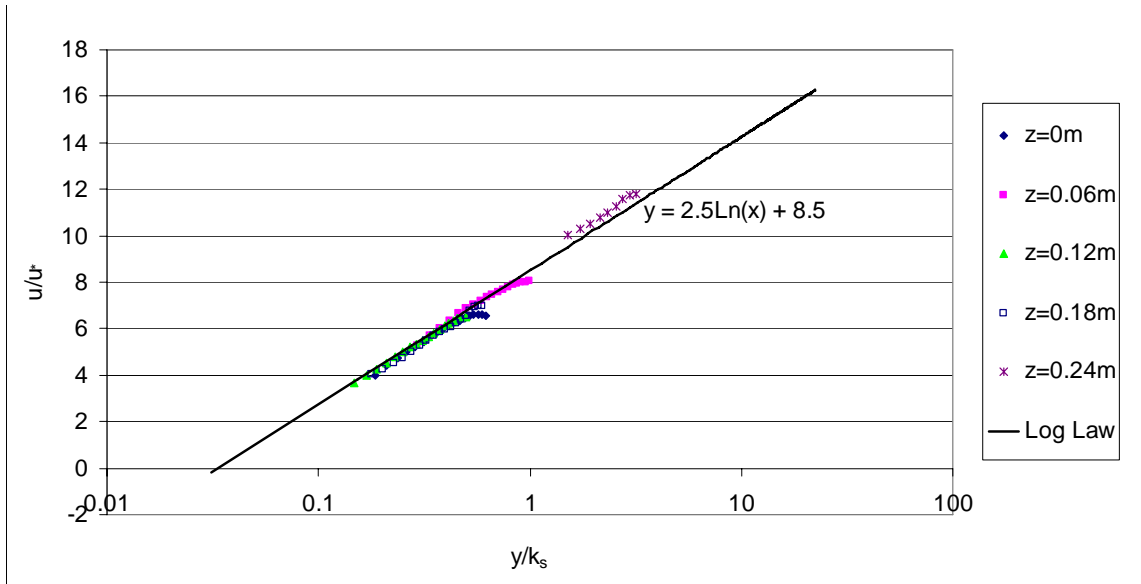


Figure E - 43: Log Law plot for S1Q150, XS20

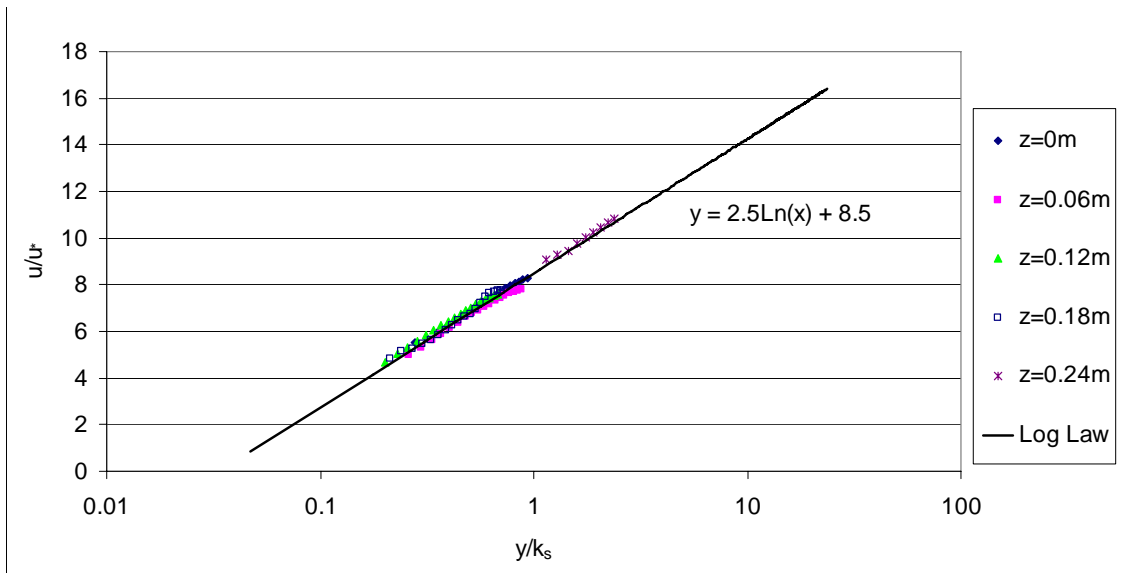


Figure E - 44: Log Law plot for S1Q150, XS23

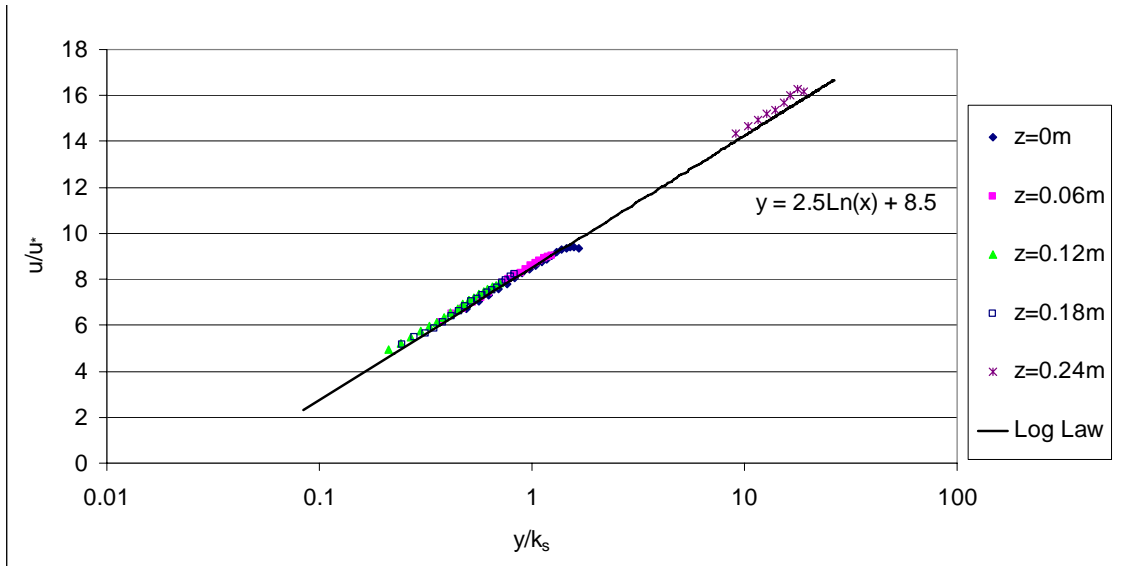


Figure E - 45: Log Law plot for S1Q150, XS26

S1Q254

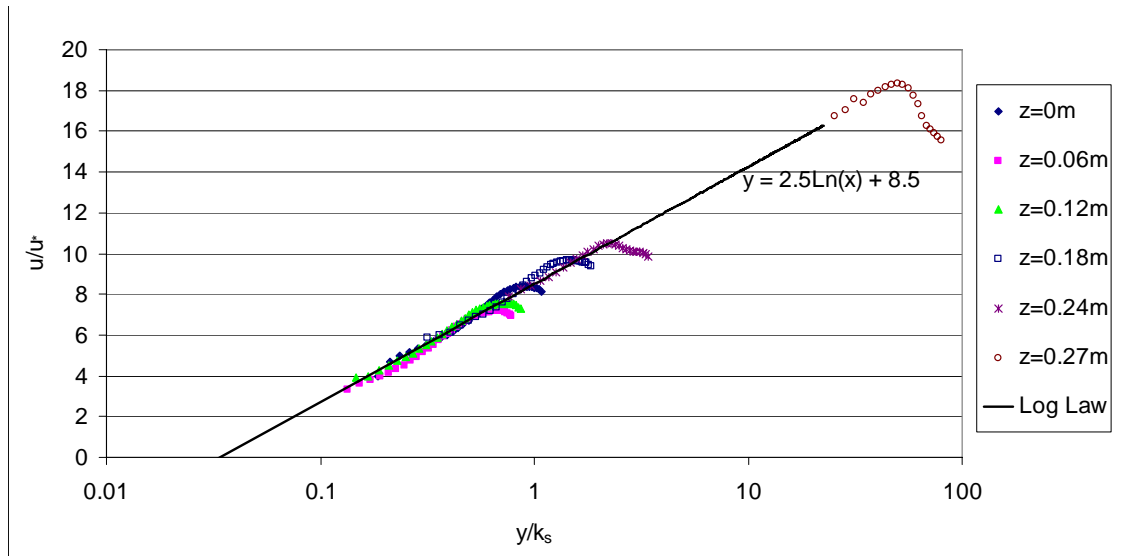


Figure E - 46: Log Law plot for S1Q254, XS6

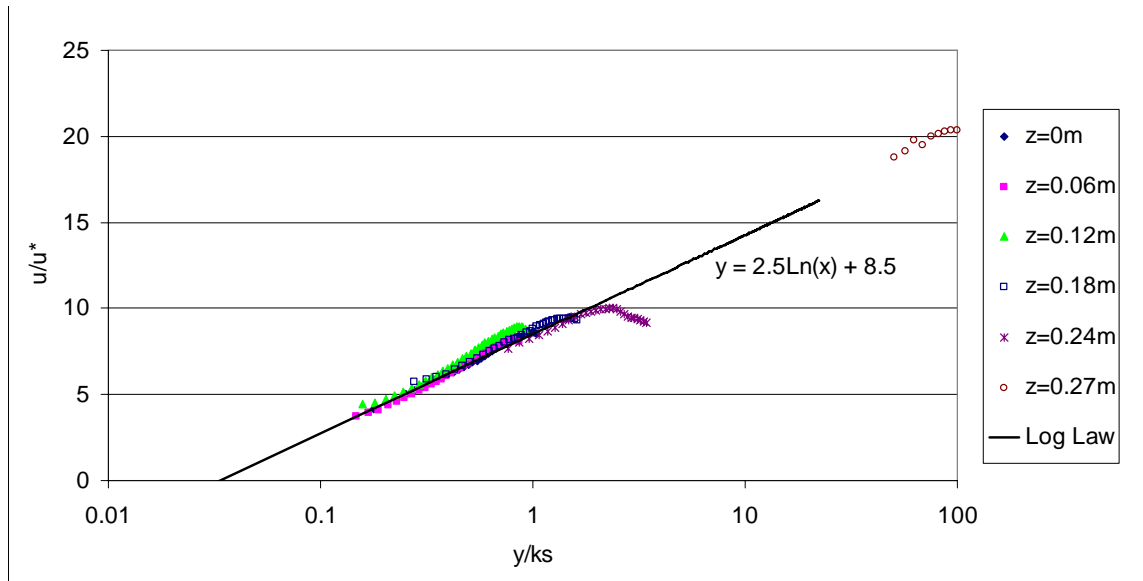


Figure E - 47: Log Law plot for S1Q254, XS8

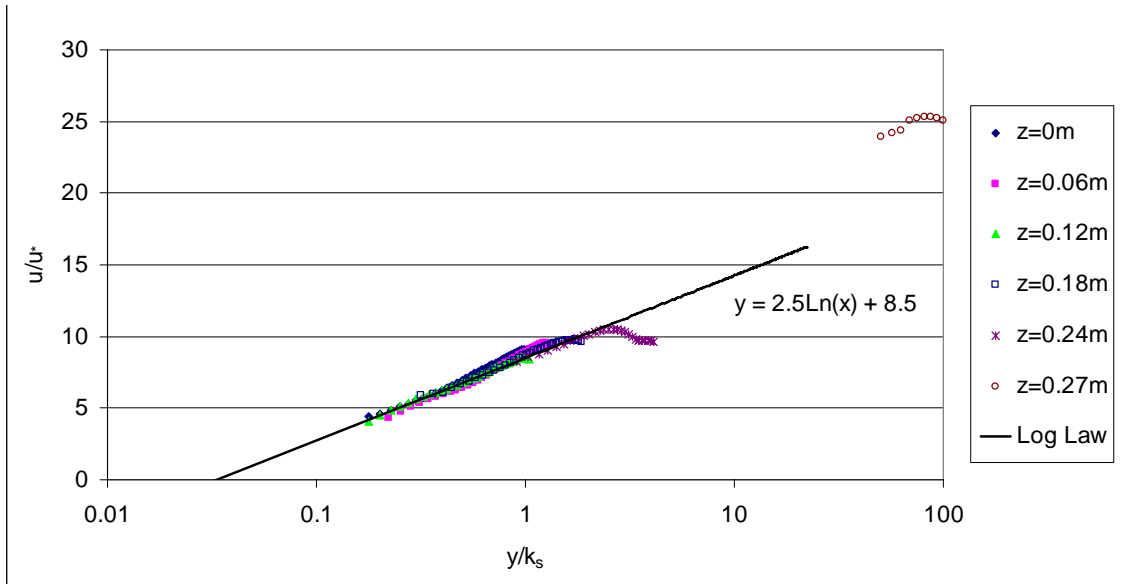


Figure E - 48: Log Law plot for S1Q254, XS10

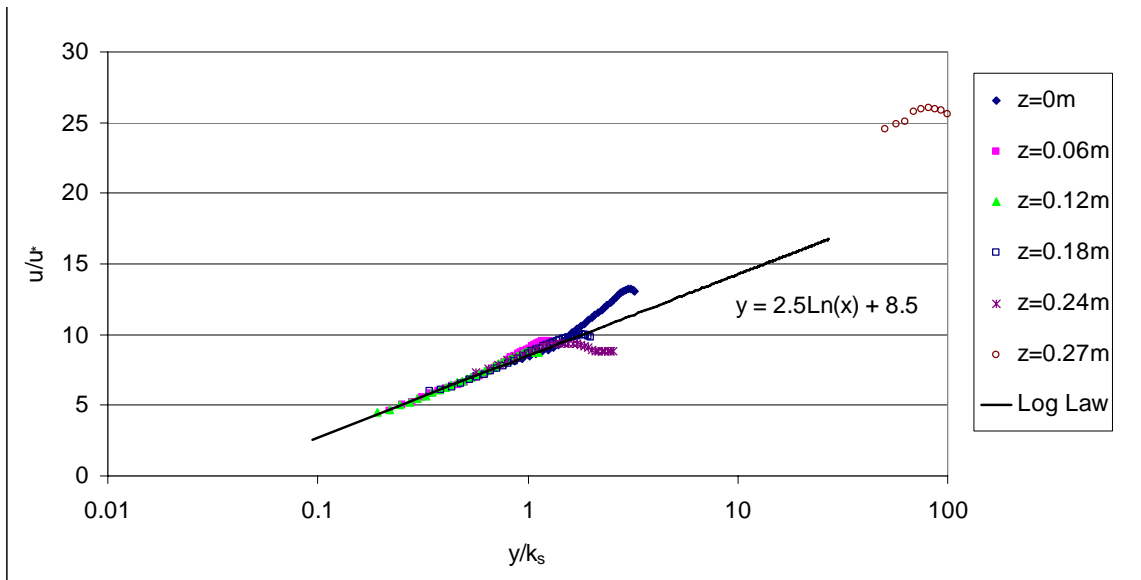


Figure E - 49: Log Law plot for S1Q254, XS12

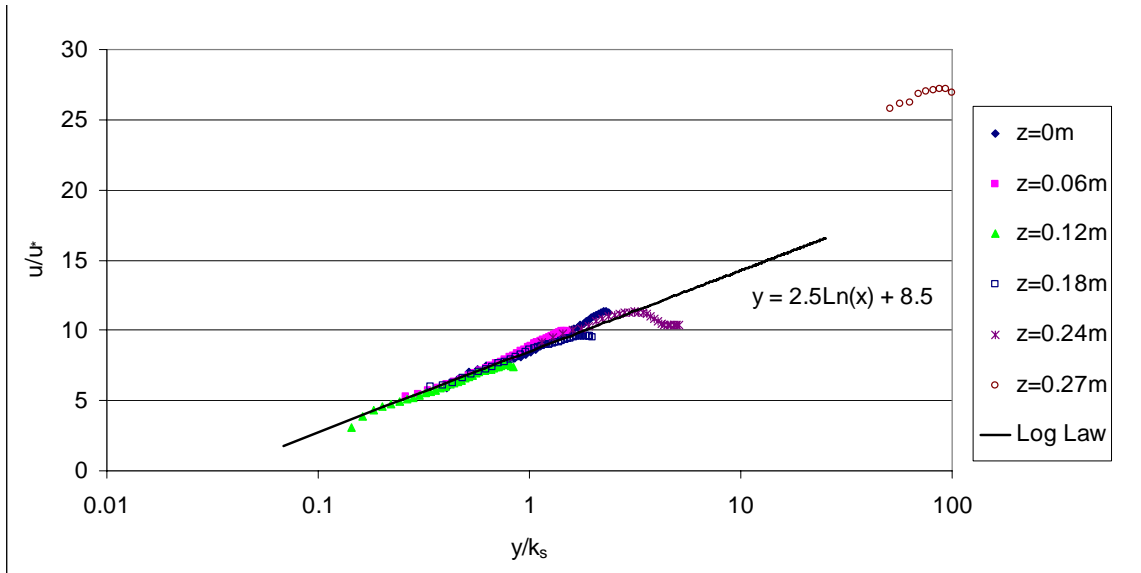


Figure E - 50: Log Law plot for S1Q254, XS14

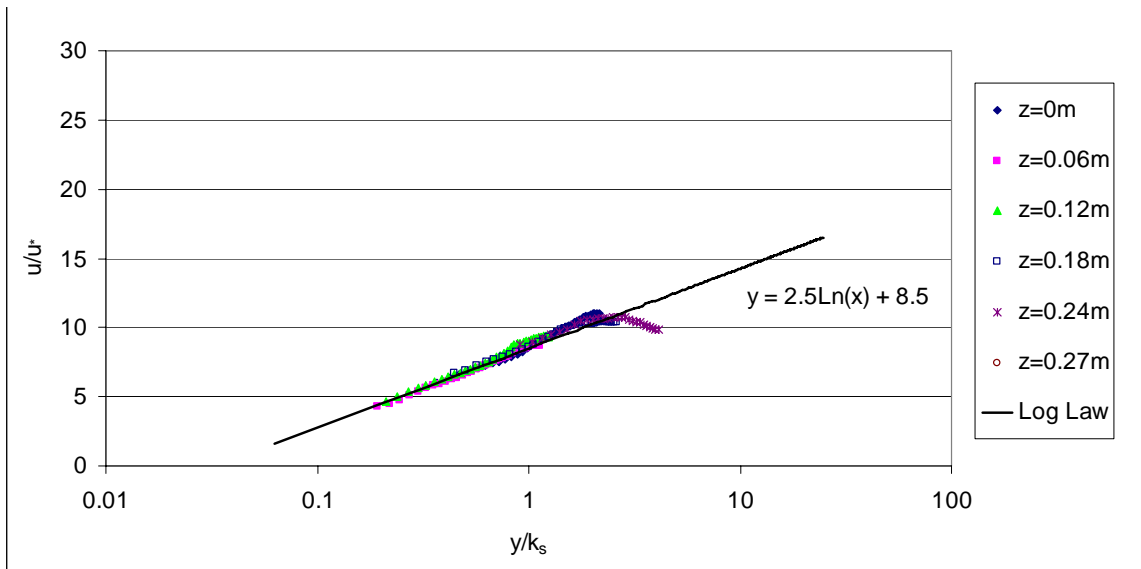


Figure E - 51: Log Law plot for S1Q254, XS17

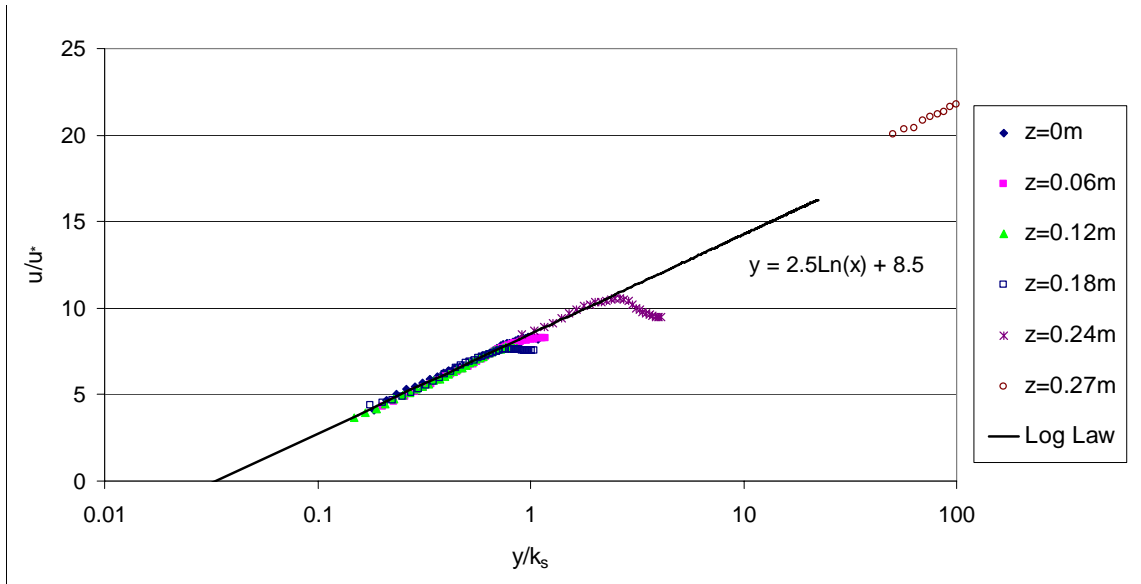


Figure E - 52: Log Law plot for S1Q254, XS20

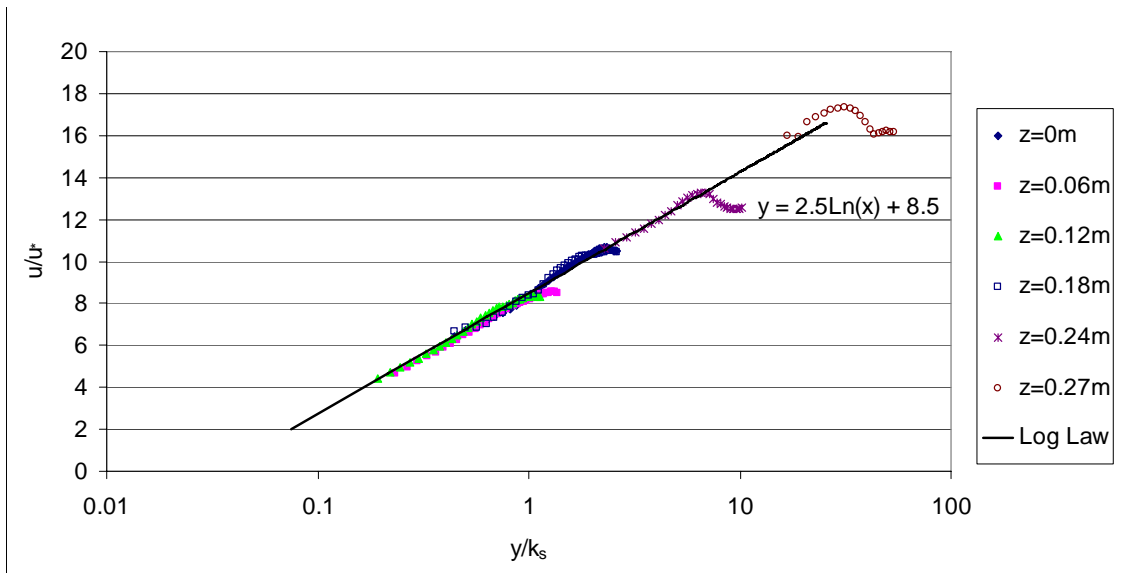


Figure E - 53: Log Law plot for S1Q254, XS23

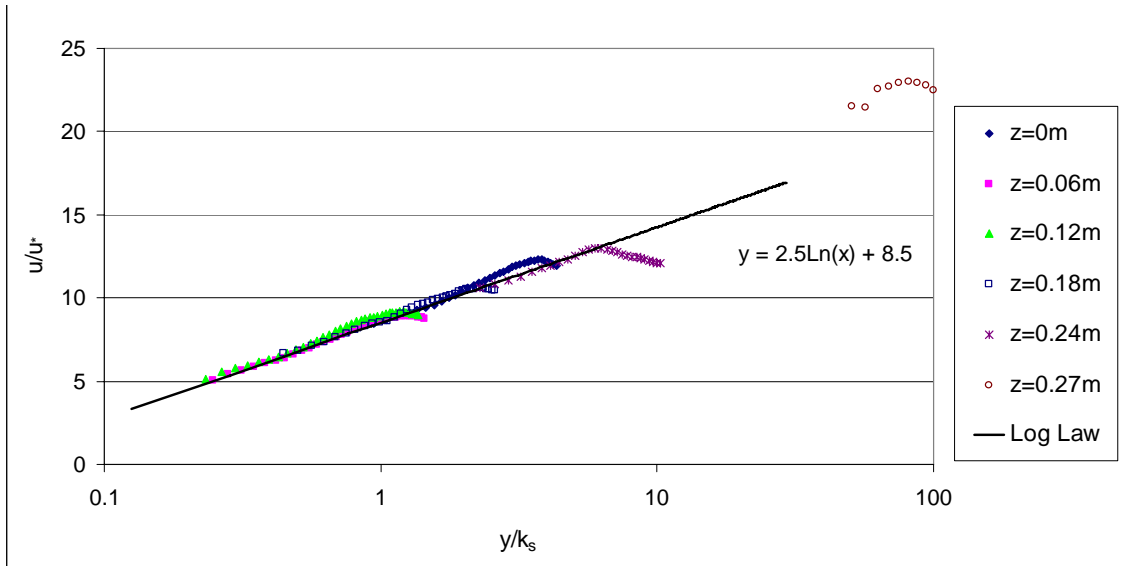


Figure E - 54: Log Law plot for S1Q254, XS26

Appendix F – Individual k_s Values for Experimental Runs

S0Q64

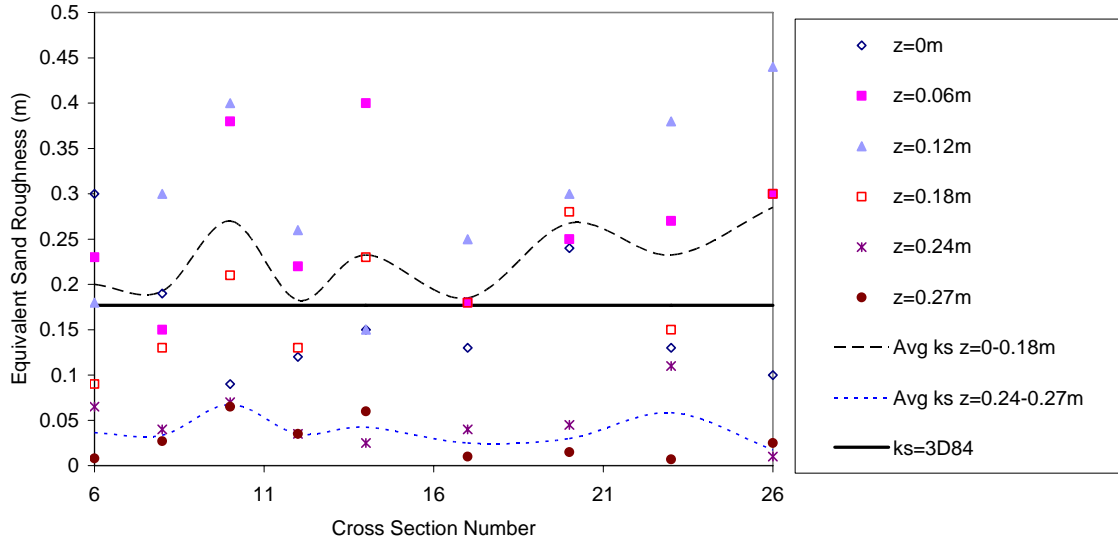


Figure F - 1: Trend in k_s along culvert for S0Q64

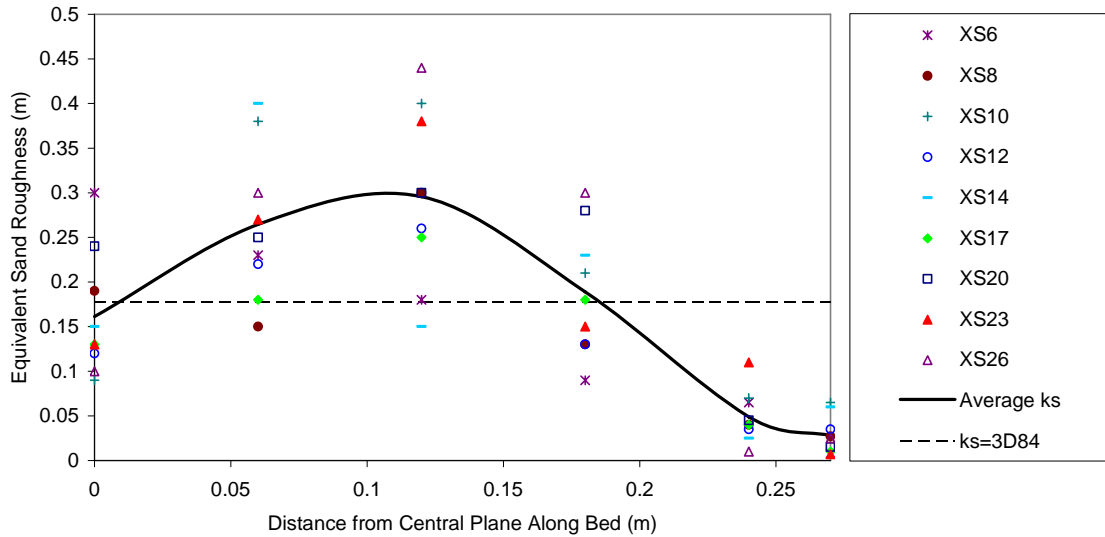


Figure F - 2: Trend in k_s across flow width for S0Q64

SOQ186

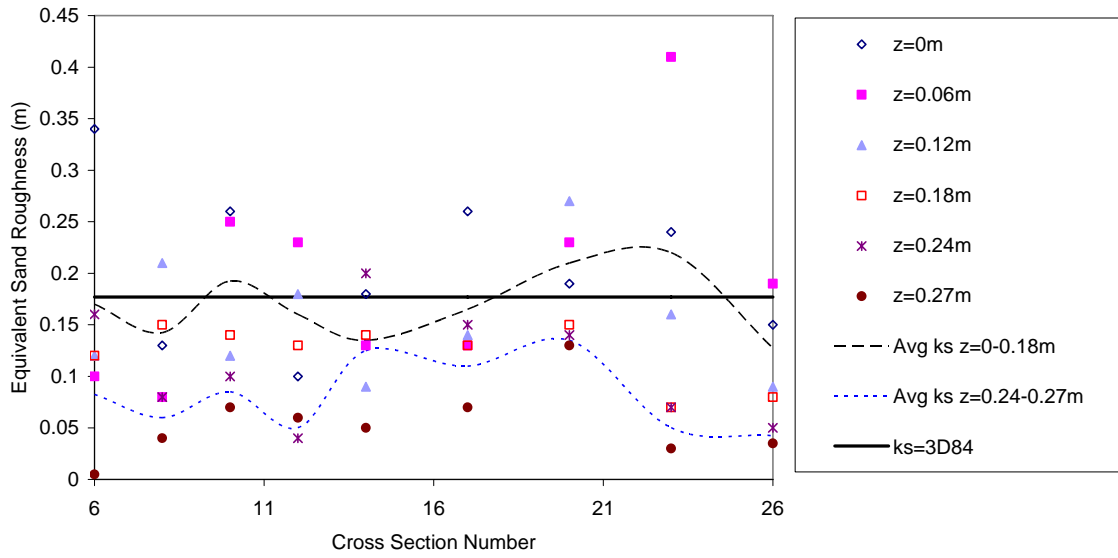


Figure F - 3: Trend in k_s along culvert for SOQ186

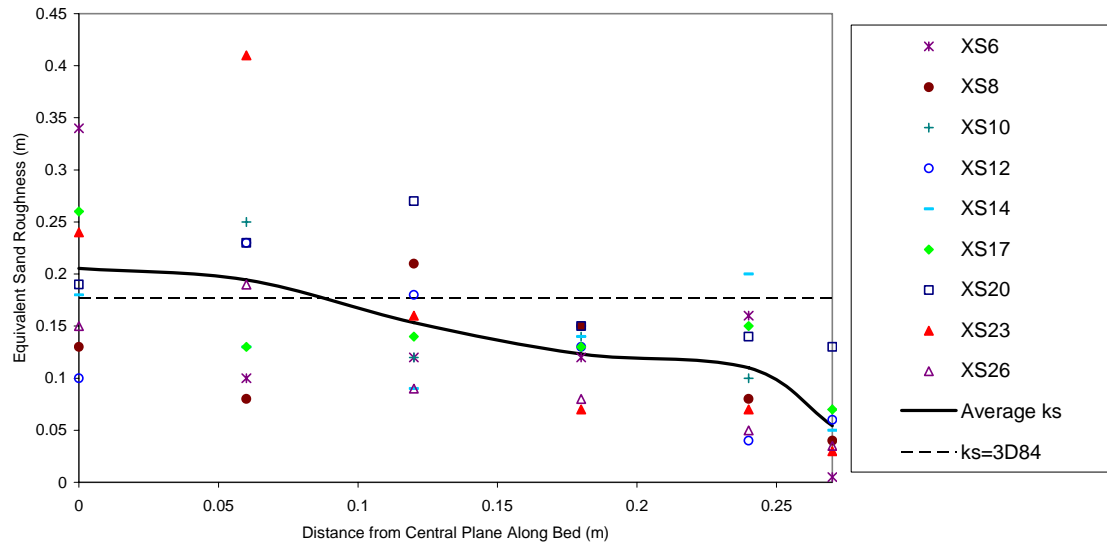


Figure F - 4: Trend in k_s across flow width for SOQ186

S5Q145

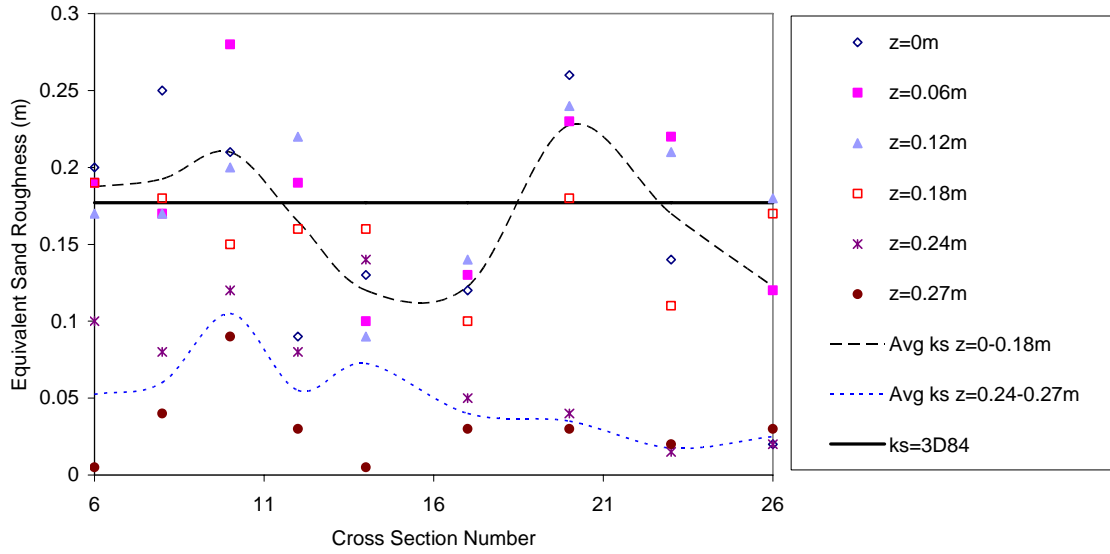


Figure F - 5: Trend in k_s along culvert for S5Q145

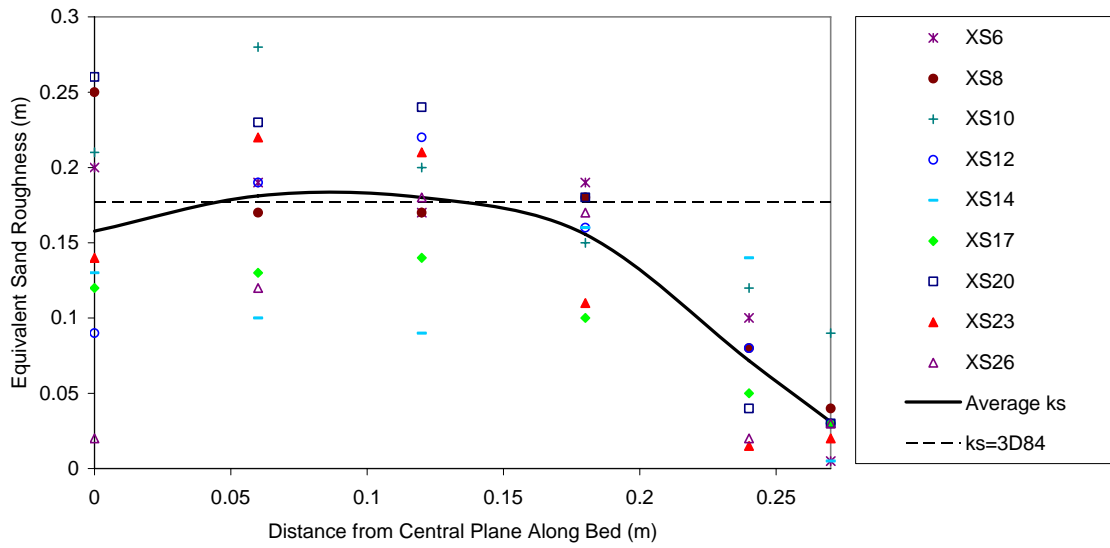


Figure F - 6: Trend in k_s across flow width for S5Q145

S5Q221

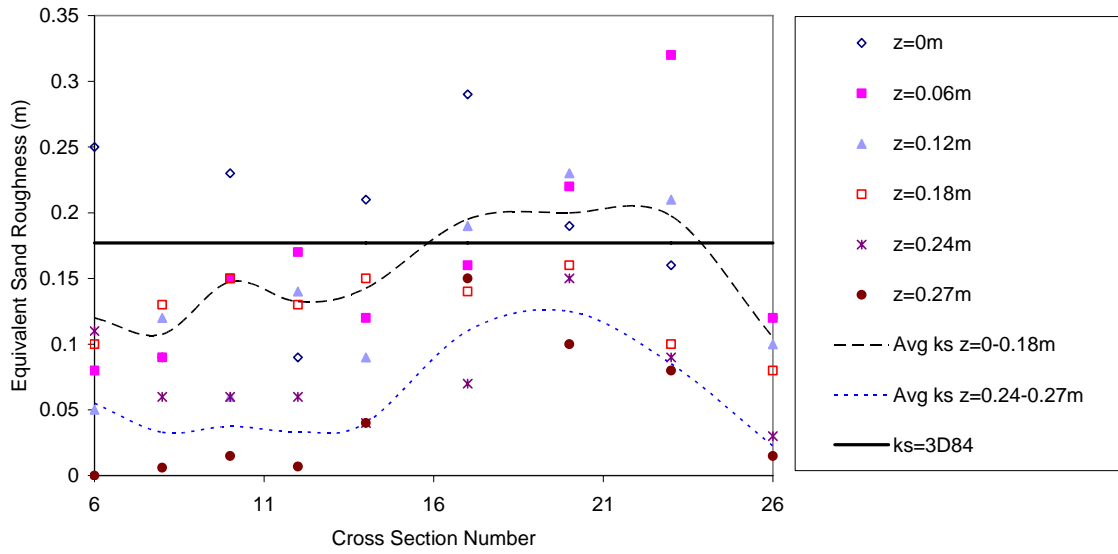


Figure F - 7: Trend in k_s along culvert for S5Q221

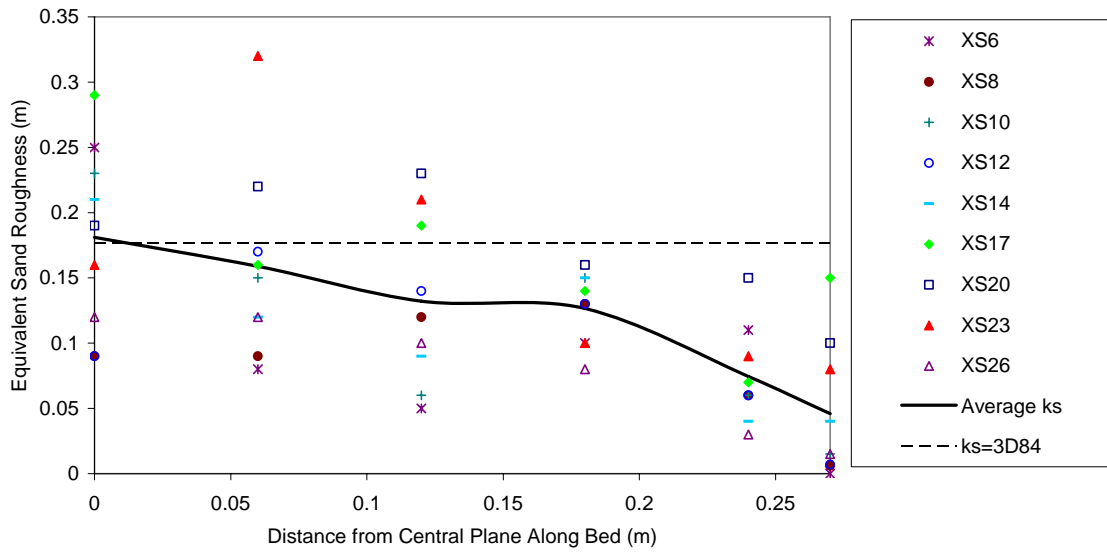


Figure F - 8: Trend in k_s across flow width for S5Q221

SIQ150

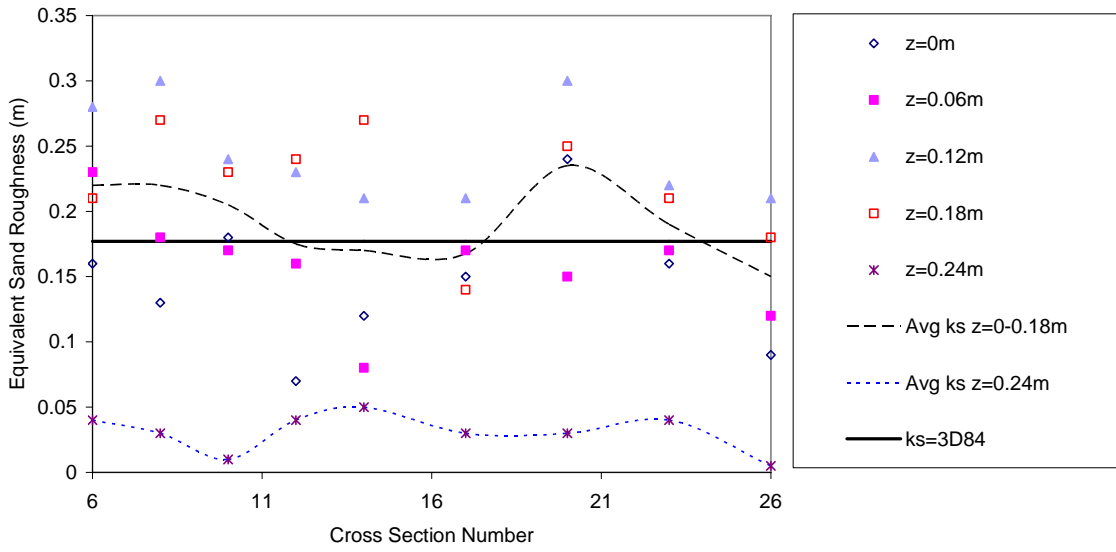


Figure F - 9: Trend in k_s along culvert for SIQ150

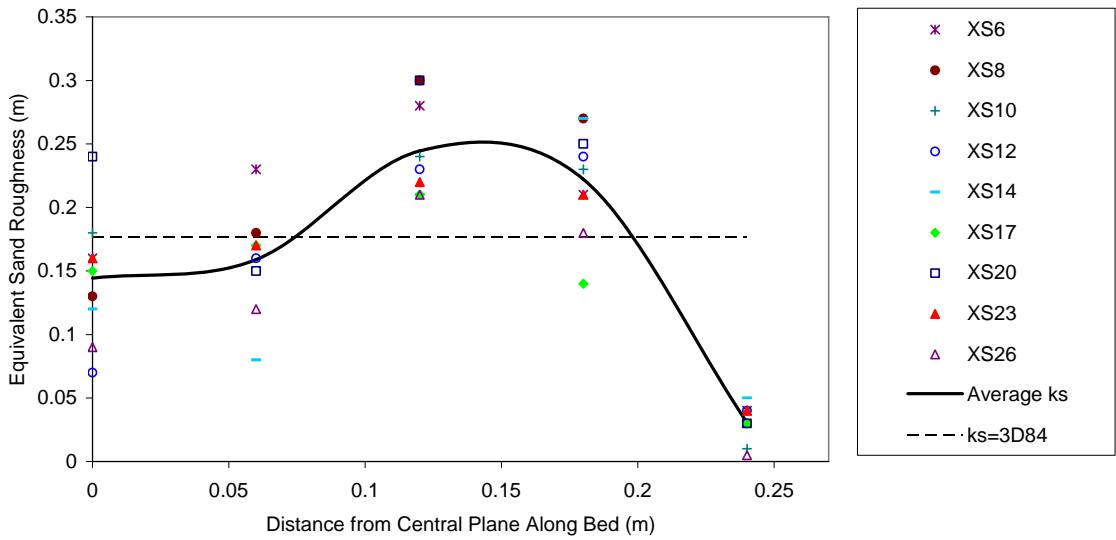


Figure F - 10: Trend in k_s across flow width for SIQ150

SIQ254

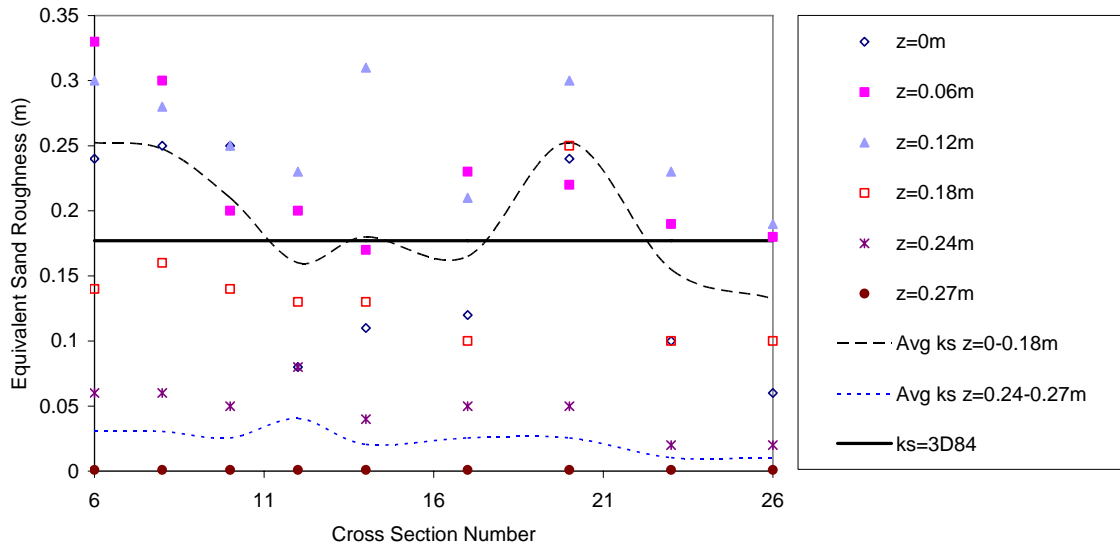


Figure F - 11: Trend in k_s along culvert for SIQ254

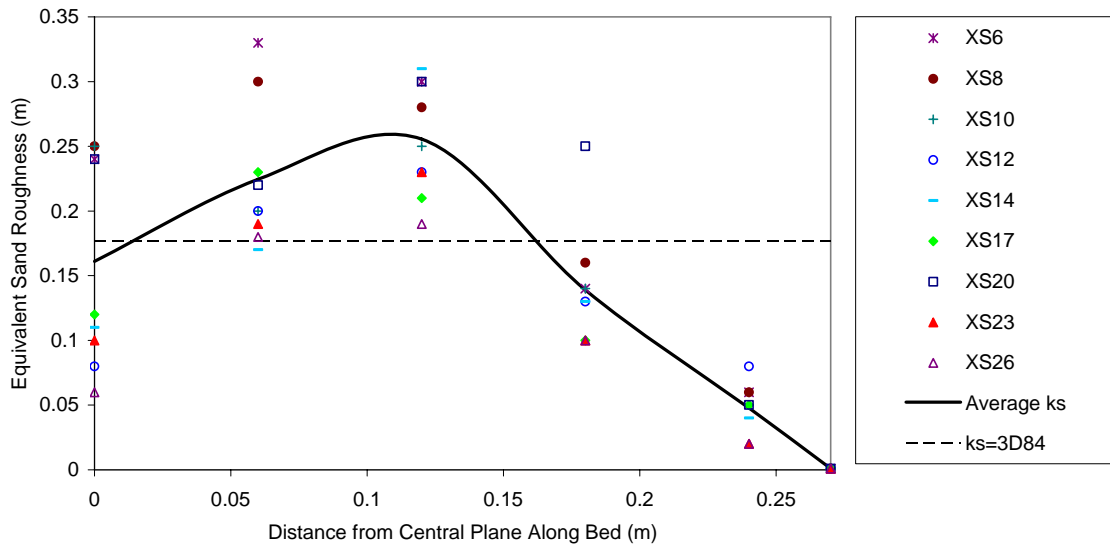


Figure F - 12: Trend in k_s across flow width for SIQ254